INFORMATION TO USERS

This manuscript has been reproduced from the microfilm master. UMI films the text directly from the original or copy submitted. Thus, some thesis and dissertation copies are in typewriter face, while others may be from any type of computer printer.

The quality of this reproduction is dependent upon the quality of the copy submitted. Broken or indistinct print, colored or poor quality illustrations and photographs, print bleedthrough, substandard margins, and improper alignment can adversely affect reproduction.

In the unlikely event that the author did not send UMI a complete manuscript and there are missing pages, these will be noted. Also, if unauthorized copyright material had to be removed, a note will indicate the deletion.

Oversize materials (e.g., maps, drawings, charts) are reproduced by sectioning the original, beginning at the upper left-hand corner and continuing from left to right in equal sections with small overlaps.

ProQuest Information and Learning
300 North Zeeb Road, Ann Arbor, MI 48106-1346 USA
800-521-0600

PETROGENESIS OF THE LATE ARCHEAN QUETICO ALKALINE SUITE INTRUSIONS, WESTERN SUPERIOR PROVINCE, CANADA

by

Birgitte Lassen

Thesis submitted to the
Faculty of Graduate & Postdoctoral Studies
in partial fulfillment of the requirements for the
Ph.D. degree in Earth Sciences

OTTAWA-CARLETON GEOSCIENCE CENTRE
AND
UNIVERSITY OF OTTAWA
OTTAWA, CANADA

May 2004

ABSTRACT

A suite of 13 late Archean subalkaline to alkaline intrusions were studied by major and trace element geochemistry and neodymium, hafnium and lead isotopic methods. The intrusions (2683 - 2678 Ma) are located in the Quetico metasedimentary belt, western Superior Province, and include pyroxene hornblendite, diorite, monzonite, syenite and carbonatite. The samples display arc-like trace element patterns with high Cs, Ba, Sr and light rare earth element abundances and low Zr, Hf, Nb, Ta and Ti. Neodymium and hafnium isotope data reflect derivation from a depleted mantle source with minor contribution from an enriched source. Lead isotope ratios from K-feldspar separates are dominated by a slab fluid or crustal component. Quantitative modeling of trace element and isotope ratios illustrates that a metasomatic event shortly before melting produced the main geochemical signatures, but a contribution from an older crustal source is also required to explain the range in data. Melting models based on rare earth element variations suggest that melting occurred over a range of pressures or took place in the garnet spinel transition zone.

The intrusive complexes can be subdivided into two groups on the basis of high field strength element distribution, which appears to reflect mantle heterogeneities resulting from differences in metasomatic processes. The most abundant group exhibits super-chondritic Nb/Ta and excess Nb relative to magmas produced by melting of a fluid metasomatized mantle. These characteristics are in accord with metasomatism by silicic melts that have left rutile in the residue and the metasomatic agent is thought to be a mixture of slab-derived fluids and melts. The trace element chemistry of the remaining intrusions reflects a source affected by fluid metasomatism.

Carbonatite constitutes a minor part of the Beaverhouse Lake intrusion. Qualitative major and trace element modeling suggests that the carbonatite formed by carbonate-silicate liquid immiscibility. The carbonatite is characterized by highly depleted hafnium isotopic signatures, which are interpreted to result from a previous episode of carbonate metasomatism. Modeling of Lu-Hf partitioning during silicate-carbonate liquid immiscibility suggests that anomalously high hafnium isotopic ratios should develop with time in the carbonate phase, which has potentially important implications for carbonate metasomatism.

Résumé

Une suite de treize plutons tardi-Archéens a été étudié pour ses éléments majeurs et mineurs, et ses isotopes de néodyme, de hafnium et de plomb. Les plutons, âgés de 2683 Ma à 2678 Ma, font partie de la ceinture méta-sédimentaire de Quético, dans la partie occidentale de la province tectonique de Supérieur. Les compositions des plutons comprennent des hornblendite à pyroxène, diorite, monzonite, syénite et carbonatite. Les patrons d'éléments en traces ressemblent au magmatisme de type arc; les teneurs en Cs, Ba, Sr et des terres rares légères sont élevées, tandis que les abondances en Zr, Hf, Nb, Ta et Ti sont faibles. Les données d'isotopes de néodyme et de hafnium témoignent d'une dérivation des magmas à partir d'une source mantellique appauvrie, avec une contribution mineure d'une source plus enrichie. Les rapports d'isotopes de plomb, déterminés pour des concentrations de feldspath potassique, préservent une signature de fluides dérivés d'une plaque subductée, ou bien une signature crustale. La modélisation quantitative de rapports d'éléments en traces et d'isotopes suggère que les signatures géochimiques principales des échantillons sont dues à un événement métasomatique, qui se serait produit peu de temps avant l'événement de fusion partielle en question. Toutefois, les variations dans les compositions chimiques des échantillons nécessitent une contribution venant d'une source crustale ancienne. Selon les résultats de modélisation des variations de terres rares, la fusion aurait eu lieu sous des conditions de pressions lithostatiques assez variables, ou bien sous des pressions correspondants à la zone de transition entre péridotite à spinelle et péridotite à grenat.

Les plutons peuvent être subdivisés en deux groupes, sur la base des distributions de certains éléments de transition, tels Hf, Zr, Nb et Ta, ce qui semble témoigner d'hétérogénéités induites dans la source par des processus métasomatiques. Le groupe le plus important a un rapport Nb/Ta supérieur aux chondrites, et un excès de Nb par rapport aux magmas produits par une fusion partielle d'un manteau métasomatisé. Ces caractéristiques sont en accord avec un métasomatisme induit par des fluides magmatiques riches en silice, laissant du rutile dans le résidu. Il est interprété que des fluides, ou des magmas, dérivés d'une plaque subductée, serait les agents métasomatiques. La composition des autres plutons en éléments en traces indique une dérivation à partir d'une source affectée par un métasomatisme induit par des fluides.

La carbonatite constitue une partie mineure du pluton de Lac Beaverhouse. Une modélisation qualitative d'éléments majeurs et en traces suggère que la carbonatite aurait été formé par une immiscibilité entre magmas carbonaté et silicaté. La carbonatite a un caractère appauvri selon sa signature en isotopes de hafnium, ce qui est interprété comme indicateur d'un événement antérieur de métasomatisme carbonaté. Une modélisation de la partition Lu-Hf entre liquides carbonaté et silicaté suggère un développement potentiel de rapports élevés d'isotopes de hafnium avec le temps, dans la phase carbonatée, ce qui aurait des implications importantes pour le métasomatisme carbonaté.

TABLE OF CONTENTS

Acknowledgements

The work presented in this thesis was supported by a three-year grant from Forskningsstyrelsen (Danish Research Agency).

I wish to thank my advisor John Percival who had the unpleasant task of correcting each version of the thesis, for thorough editorial corrections and many thoughtful and constructive comments and suggestions, which improved the thesis substantially. His help and inspiration is highly appreciated. I am obliged to Brian Cousens for saving my Nd isotope work at a critical stage, for letting me work in his lab and for investing the time to teach me how to run the mass spectrometer. I have also received countless hours of invaluable help and patient instruction with mass spectrometry from John Blenkinsop. I am indebted to both of them for their flexibility and willingness to help and their efforts of trying to fit me into their own busy schedule. A special thank you to Sharon Carr for help and advice on zircon separation, for letting me use the lab at a time when everything was chaotic due to relocation of the lab, and for persistent efforts in trying to arrange that everything was ready for me to get the work done in time. Detailed comments and suggestions by Bruce Kjarsgaard on an earlier version of chapter 4 are also gratefully acknowledged.

I wish to thank the Danish Lithosphere Centre for accepting me in their lab, for analytical support and entrusting me with the MC-ICP-MS. For advice on Hf isotopes and technical assistance with the Axiom I would like to thank Joel Baker, Eirik Krogstad and especially Tod Waight.

A large number of fellow students have provided help, enjoyable company and fruitful discussions in the field. In particular I wish to thank Franck Vally and Neil Pettigrew, who both spent an entire summer working with me. Thanks are also extended to Terry Boerboom, who readily showed his field area in Northern Minnesota, and staff from Pro-Am, who provided logistical help.

A special thank you to Tommy Holm Hansen for always having a friendly email waiting for me in the morning and for keeping me updated on the news and rumors and scandals in Copenhagen, without which the years here would have felt dull and boring, and also to Anne Peschler for many cheerful beer-nights and discussions on almost anything. Finally, I am grateful to Minik Rosing and Robert Frei for willingly accepting to be "contact persons" on the project and Minik for encouragement throughout and hospitality in Copenhagen.

During this study half a year of salary was paid by a Lithoprobe grant to J. Percival and K. Hattori and the analytical work was partially funded by Lithoprobe and NSERC (K. Hattori).

LIST OF FIGURES

LIST OF TABLES

Chapter 1

Introduction and outline of thesis

Some main objectives of current geological research are to identify and quantify the sources contributing to magmatism in present-day and ancient arc settings (e.g. Arculus, 1994; Elliot et al. 1997; Smithies and Champion, 2000). A characteristic suite of high-Mg granitic rocks, the sanukitoid suite, has been described from Archean settings including the Superior Province of Canada (e.g. Shirey and Hanson, 1984; Stern et al., 1989; Stevenson, 1999; Smithies and Champion, 2000). Archean sanukitoids have received much attention because of their compositional similarity to average continental crust. They share geochemical characteristics with high-Mg andesites, which occur in modern arc settings (e.g. Gill, 1981; Tatsumi and Ishizaki, 1982; Kelemen et al., 2001) but occur within cratons and generally in post-collisional settings, which may suggest a petrogenetic process slightly different than that active in modern arcs.

This thesis documents and examines a suite of late Archean sub-alkaline to alkaline intrusions of sanukitoid affinity from the metasedimentary Quetico subprovince in the western Superior Province, for the purpose of constraining the petrogenetic history. Compared to their counterparts in adjacent volcanic-plutonic subprovinces, most intrusions within the Quetico metasedimentary belt have not been investigated in detail. The thesis builds on previous studies of similar rock types, such as those of Stern et al. (1989) and Stevenson et al. (1999) and provides complementary ideas and interpretations.

1.1. Organization

Chapters 2, 3 and 4 have been written in the form of manuscripts to be submitted for publication. This necessitates some overlap, in particular with respect to geological descriptions and methodology. The perceptive reader will also note that a few major and trace element analyses and Nd isotope ratios are used both in chapter 2 and 4, where they serve as input for different types of geochemical models.

The project is the first comprehensive study of large ion lithophile element (LILE) - rich intrusions from the Quetico subprovince and therefore involved extensive time in the field as well as basic petrographic and mineral analyses. For that reason the thesis also includes 3 appendices, which are intended to give a comprehensive description of the geological background and of the samples included in the study. The appendices specify the detailed field relationships of each intrusion, and present mineralogical analyses and petrographic descriptions of individual samples selected for geochemical analyses.

Chapter 2 gives a detailed introduction to the Quetico alkaline suite (QAS) intrusions and presents U-Pb geochronology, major and trace elements and Nd and Pb isotope data. The data are used to describe the differentiation history of the QAS intrusions, including a quantification of high- and low-pressure fractionation, along with degree of crustal contamination and evaluation of conditions of melting. The work includes discovery of ancient Nd model ages beneath the northern Quetico subprovince and infers the presence of a Mesoarchean basement fragment, which is in agreement with recent isotopic work in the southern Wabigoon subprovince by Tomlinson et al. (in press).

Chapter 3 builds on chapter 2, and contains a review of the main geochemical characteristics of the QAS intrusions. It presents Hf isotope data, which are used in conjunction with the data presented in chapter 2 to examine in detail the source components of the QAS intrusions. The chapter aims at quantifying the metasomatizing agent(s) involved in the petrogenesis of the suite as well as the mineralogy of the mantle source. It concludes with a geotectonic framework capable of explaining the geochemical data.

Chapter 4 focuses on a rare Archean carbonatite occurrence within the Beaverhouse Lake intrusion. Geochemical data are presented for silicate and carbonate phases and used to discuss the petrogenesis of the carbonatite. In addition, the wider aspects of carbonate metasomatism in the upper mantle and the possible implications of this process for Lu-Hf isotope systematics are also discussed.

1.2. Statement of original contribution

The present work represents a through examination of the QAS intrusions. The thesis reports new mineralogical and geochemical data, including major, trace element and Nd-Pb-Hf isotope ratios, which are used to qualitatively and quantitatively model the petrogenetic history of the intrusions.

The source region of the studied intrusions is evaluated with respect to metasomatic agents, mineralogy and depth of melt segregation.

U-Pb dating adds to the geochronology database for mantle-derived intrusions of the western Superior Province. Most comparable geochronological work has been carried out on intrusions from adjacent subprovinces, in particular the Abitibi, Pontiac and Wabigoon subprovinces.

Zoned clinopyroxene is described from mafic units of the Gheen intrusion. Zoned clinopyroxene has to my knowledge not previously been reported from sanukitoid suites, but provides important additional constraints on their petrogenesis.

Archean carbonatites are scarce in the geological record and controversy still surrounds carbonatite formation. The thesis documents an Archean carbonatite occurrence and examines its petrogenesis using mass balance calculations and partitioning data.

Evidence is presented that carbonate-silicate liquid immiscibility will have pronounced effects on Lu and Hf partitioning and will result in high Lu/Hf ratios in the carbonate phase. The behavior of Lu-Hf in immiscible carbonate silicate liquids has not previously been demonstrated and may have important implications for carbonate metasomatism.

1.3. Contributions of collaborators

The organization of the thesis, the main interpretations, numerical modeling, writing and drafting is my own work. Dr. John Percival has commented on all chapters and Dr.

Bruce Kjarsgaard provided helpful comments on chapter 4. In addition, a number of people have provided help and guidance with analytical work and data collection.

I have obtained most data presented in the thesis, but some have been done by other people: U-Pb geochronological data were provided by Vicki McNicoll and Julie Perresini (GSC). About half of the major and trace element data come from other labs as specified in Chapter 2, and about half of the electron microprobe data were obtained by Katherine Venance at the GSC.

Chapter 2

Geochemical evolution of late Archean alkaline complexes from the western Superior Province: Insight into complex polybaric differentiation trends

2.1. Abstract

Late Archean igneous activity within the Quetico metasedimentary belt in the western Superior Province produced a chemically diverse alkaline rock suite. Major and trace elements, Sm-Nd and Pb-Pb isotope data are used to model their petrogenesis. Mineral chemistry of clinopyroxene from mafic and leucocratic units implies a complex differentiation history along several liquid lines of descent linked to multiple depths. Alternating reverse and normal zoning in primitive high pressure Cr-diopsides from mafic units indicates complex growth histories and provide direct evidence for magma mixing and disequilibrium crystallization in the deep crust (~ 1.0 - 1.5 GPa) prior to injection into shallow level magma reservoirs and further differentiation by extensive low-pressure fractional crystallization. Qualitative modeling of major and trace element compositional variations confirms the differentiation history implied by mineral chemistry and demonstrates polybaric fractionation, extracting mainly clinopyroxene at depth followed by decompression and fractionation of alkali-feldspar, clinopyroxene, biotite and apatite at shallow levels. Initial $^{143}Nd/^{144}Nd$ isotope ratios vary between 0.50916 and 0.50928 and are partially correlated with differentiation index and other geochemical parameters. The combination of high MgO and older Nd model ages

suggests a role for interaction with older basement. The chemical trends are indicative of mixing with a crustal melt rather than bulk crustal addition. Batch melting models demonstrate that the magmas parental to the intrusions formed by partial melting of a subduction-modified mantle in the garnet-spinel transition zone and that the enrichment event occurred not long before melting. Pb-Pb isotope ratios are entirely dominated by a slab fluid or sediment component and show no detectable contribution from the mantle wedge.

2.2. Introduction

An important feature of the western Superior Province is the widespread syn- to post-tectonic, alkali-rich group of late Archean intrusions collectively referred to as the sanukitoid suite (e.g. Shirey and Hanson, 1984; Stern et al., 1989; Stevenson et al., 1999). Compositionally, the vast majority of Archean sanukitoids have high Mg-number, high abundances of compatible trace elements (Ni, Cr), high abundances of large ion lithophile elements (LILE) and steeply fractionated rare earth element (REE) patterns. These characteristics reflect derivation from an enriched mantle source and most authors assume that this enriched source is metasomatized mantle above a subduction zone (e.g. Stern et al. 1989). The focus of the present work is a group of subalkaline to alkaline intrusions from the Quetico subprovince. The composition of the intrusions corresponds broadly to the sanukitoid suite, although some samples have greater enrichment in LILE and extend to lower Ni and Cr concentrations. In the following, the intrusions will collectively be referred to as the Quetico alkaline suite (QAS) intrusions. The high total

alkali contents of the QAS intrusions and most members of the sanukitoid suite differs from late calc-alkaline to shoshonitic compositions in modern arc settings and may imply a different tectonic setting and/or be linked to differences in H_2O-CO_2 fluid phase. The QAS intrusions are carbonate bearing, which suggest CO_2 enrichment in the source region. Higher X_{CO2} promotes smaller degrees of melting, higher incompatible trace element and lower compatible trace element concentrations in the resulting melt.

Throughout this paper the term "primitive" refers to the definition of Nixon and Johnston (1997): MgO $\geq$8 wt %, Ni and Cr concentrations of minimum 100-150 ppm and 200-300 ppm, respectively, and Mg-number > ~ 60. In contrast to most existing work on late Archean sanukitoids in the Superior Province the QAS intrusions cover a wide compositional range, from primitive to highly evolved rock types and thus offer the opportunity to examine the effects of variable source characteristics, contamination and fractionation with evolution. The occurrence of primitive compositions provides a window on source compositions and conditions of melting and allows resolution of the effects of crustal contamination and subduction processes.

The present study is principally aimed at geochemically characterizing the QAS intrusions in order to place accurate constraints on their magmatic differentiation histories. An accompanying paper (chapter 3) presents a detailed examination of the nature of the source region and the prevailing geotectonic regime during igneous activity. The paper presents new geochemical data including U-Pb geochronology, major and trace elements and Nd and Pb isotope ratios. The observed diversity in trace element concentrations and isotope signatures require multi-stage petrogenetic models including polybaric fractionation, crustal assimilation and magma replenishment.

2.3. Regional geology and age relations

The western Superior Province of Canada is composed of a collage of subprovinces, which form a series of sub-parallel elongated belts. These alternate between volcanic-plutonic belts, metasedimentary belts and high grade gneiss complexes and represent a variety of continental and oceanic environments (e.g. Sage et al., 1996) with a range of terrains in individual subprovinces (e.g. Tomlinson et al., in press.). The subprovinces were progressively accreted from north to south before docking with the Minnesota foreland to the south during the final stages of craton amalgamation at ca 2.68 Ga (e.g. Corfu and Stott, 1986).

The Quetico subprovince is a belt of deformed and metamorphosed sedimentary rocks, located between the Wawa and the Wabigoon greenstone belts (Figure 2.1). The Wabigoon greenstone belt is dominantly composed of volcanic and plutonic rocks with crystallization ages that range from 3.08 to 2.67 Ga in the central and eastern parts to younger ages of 2.78 to 2.66 Ga in the western part (Tomlinson et al., in press). The Quetico subprovince is mainly composed of metagreywacke and derived migmatites. The age and chemical character of the basement to the Quetico sediments is unknown. It may be Marmion (3 Ga) or juvenile 2.75 Ga western Wabigoon. The Quetico sediments were deposited as turbidites under deep water conditions in a collisional basin, which became buried and metamorphosed to greenschist, amphibolite and local granulite facies during collision between the Wabigoon and the Wawa subprovinces (Percival 1989; Percival

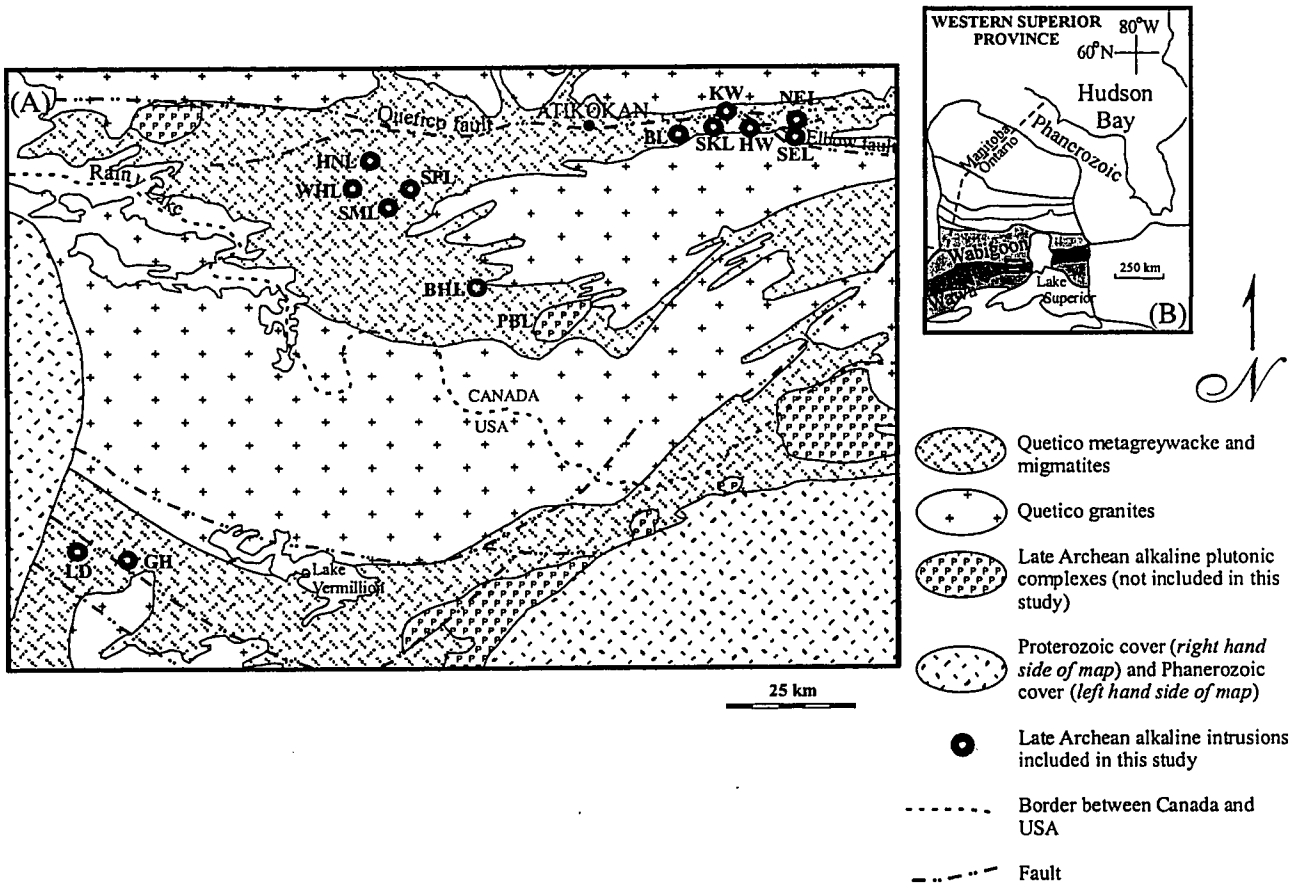

Fig. 2.1. (A) Simplified geological map of the study area showing the location of the QAS intrusions: LD = Linden, GH = Gheen, HNL = Harnett Lake, WHL = Whalen Lake, SPL = Surprise Lake, SML = Samuels Lake, BHL = Beaverhouse Lake, BL = Blalock, SKL = South Kawene Lake, KW = Kawene, HW = Heward, NEL = North Elbow Lake, SEL = South Elbow Lake. Also indicated is PBL = Poohbah Lake intrusion (B) Sketch map, which shows the major subdivision of the western Superior Province highlighting the Quetico metasedimentary belt and surrounding greenstone belts. The black square corresponds to map A. Modified after Stern et al. (1989).

and Williams, 1989; Pan et al. 1994) with metamorphic ages ranging between 2666 and 2650 Ma (Pan et al. 1998). The sources of the Quetico sediments are dominated by ages of <2750 Ma, which has been determined by U-Pb studies on detrital zircons originating from felsic volcanogenic material presumably supplied from the neighboring greenstone belts (Percival and Sullivan, 1988). However, ages as old as 3 Ga have been reported from detrital zircons from the Quetico belt (Davis et al. 1990), which indicate the presence of significantly older crustal material presumably inherited from Wabigoon sources.

The Quetico belt is characterized by the presence of several generations of dykes and small, isolated, compositionally diverse, subalkaline to alkaline intrusions (Figure 2.1), which were emplaced at shallow levels in the crust during the final stages of crustal amalgamation within the Superior Province. The intrusions are late- to post-kinematic with respect to regional deformation and define the classic post-collisional trend of sub-alkalic to alkalic compositions. Ultramafic to mafic intrusions occur mainly along the Quetico fault or as tectonic slivers. These intrusions are commonly composed of variably foliated rock types, especially towards their margins. Intermediate to leucocratic intrusions occur mainly in the south of the subprovince and these are largely tectonically undisturbed. The QAS intrusions cover a wide compositional range and include pyroxene hornblendite, plagioclase-bearing hornblende pyroxenite, hornblende gabbro, quartz syenite, alkali-feldspar quartz syenite, monzonite and syenite with rare carbonatite. Intrusions, consisting dominantly of mafic to ultramafic rock types include Gheen intrusion, North Elbow Lake intrusion, Kawene intrusion, South Kawene Lake intrusion and Samuels Lake intrusion. Intrusions composed mainly of leucocratic rock types

include Linden intrusion, Harnett Lake intrusion, Beaverhouse Lake intrusion, Whalen Lake intrusion, South Elbow Lake intrusion, Blalock intrusion, Surprise Lake intrusion and Heward intrusion (Figure 2.1). Crustally derived biotite- and two-mica-granites postdate the alkaline intrusions and represent the latest stages of igneous activity within the Quetico belt (e.g. Southwick, 1991).

New geochonological data by U-Pb on zircon and titanite gave 2682.6 $^{+8}/_{-2}$ Ma for Gheen intrusion, 2678 ± 6 Ma for Harnett Lake intrusion and 2683 ± 3 Ma for Blalock intrusion. The data are depicted in concordia diagrams in Figure 2.2 and tabulated in Table 2.1. Titanite from Harnett Lake intrusion preserves late stage overgrowths, which give similar ages. Other existing geochronological data include a U-Pb titanite age of 2680 Ma from Whalen Lake intrusion (Percival and Hattori, unpublished data) and a U-Pb zircon age of 2685 $^{+5}/_{-4}$ Ma from Samuels Lake intrusion, which was obtained on zircon separated from a plagioclase-rich segregation, which crystallized from residual liquid during advanced stages of differentiation (N. Pettigrew and V. McNicoll, unpublished data). The important information to extract from these age determinations is that the intrusive complexes were emplaced during a short time interval, establishing a temporal linkage between mafic and leucocratic compositions. Also, there is no detectable age progression across the province as would have been expected from a hotspot trail.

Table 2.1. U-Pb analytical data

Zircon fraction	Weight (μg)	U[a] (ppm)	Pb*[a] (ppm)	$^{206}Pb/^{204}Pb$[c]	Pb (pg)	$^{208}Pb/^{204}Pb$	$^{206}Pb/^{238}U$	Error 1σ	$^{207}Pb/^{235}U$	Error 1σ	$^{207}Pb/^{206}Pb$	Error 1σ	$^{206}Pb/^{238}U$	$^{207}Pb/^{235}U$	$^{207}Pb/^{206}Pb$	Error 2σ	Discordant %
Blalock intrusion																	
Sample # BL0085																	
Z1A	4	143	83	1577	10	0.1849	0.4955	0.00069	12.376	0.0198	0.18119	0.00013	2594.5	2633.6	2663.8	2.4	3.2
Z4A	5	228	137	1426	21	0.2416	0.4915	0.00064	12.226	0.0208	0.18042	0.00018	2577.1	2621.9	2656.7	3.4	3.6
Z6A	8	140	84	9646	4	0.2026	0.5053	0.00081	12.696	0.0216	0.18223	0.00011	2636.6	2657.4	2673.2	1.9	1.7
Z6B	3	137	85	2666	4	0.2111	0.5191	0.00228	13.139	0.0578	0.18356	0.00013	2695.6	2689.7	2685.3	2.3	-0.5
Z7A	4	316	183	6792	5	0.2113	0.4818	0.00087	11.933	0.0227	0.17962	0.00009	2535.1	2599.1	2649.4	1.7	5.2
A1	236	187	159	1327	837	0.9677	0.4579	0.00046	11.449	0.0160	0.18133	0.00013	2430.4	2560.4	2665.0	2.4	10.6
B1	143	221	142	1144	690	0.4667	0.4518	0.00045	11.274	0.0169	0.18098	0.00015	2403.1	2546.0	2661.9	2.6	11.6
C1	125	194	123	1160	565	0.3115	0.4914	0.00049	12.388	0.0186	0.18283	0.00015	2576.7	2634.2	2678.7	2.6	4.6
Gheen intrusion																	
Sample # BL0091																	
Z1A	4	91	57	3923	3	0.1857	0.5299	0.00132	0.530	0.0013	0.19319	0.00016	2741.1	2757.5	2769.6	2.6	1.3
Z1B	5	94	58	7081	2	0.2080	0.5138	0.00077	0.514	0.0008	0.18344	0.00009	2673.0	2679.4	2684.2	1.8	0.5
Z1C	7	93	56	8404	3	0.1832	0.5130	0.00056	0.513	0.0006	0.18324	0.00009	2669.3	2677.0	2682.8	1.6	0.6
Z1D	4	103	64	3452	4	0.2282	0.5118	0.00072	0.512	0.0007	0.18332	0.00011	2664.3	2675.0	2683.2	1.8	0.9
A1	101	49	66	259	556	1.8833	0.5142	0.00072	0.514	0.0007	0.18248	0.00055	2674.5	2675.1	2675.5	9.9	0.0
B1	83	45	58	226	488	1.7503	0.5160	0.00093	0.516	0.0009	0.18291	0.00064	2682.4	2680.7	2679.4	11.6	-0.1
C1	60	40	55	290	245	1.8898	0.5153	0.00082	0.515	0.0008	0.18296	0.00049	2679.1	2679.5	2679.9	8.8	0.0
Harnett Lake intrusion																	
Sample # BL0044																	
Z1A	2	1051	374	11792	4	0.0780	0.3377	0.00034	6.784	0.0081	0.14569	0.00006	1875.8	2083.7	2296.0	1.5	21.1
Z2A	1	1729	885	5191	11	0.0843	0.4728	0.00066	11.359	0.0170	0.17424	0.00009	2495.9	2553.0	2698.8	1.6	4.8
Z2C	1	2102	794	5289	8	0.0878	0.3559	0.00043	7.183	0.0101	0.14637	0.00009	1962.9	2134.4	2303.9	1.9	17.1
Z3A	1	1949	994	1863	14	0.1056	0.4646	0.00051	10.890	0.0142	0.17001	0.00010	2459.7	2513.8	2557.8	2.0	4.6
A1	74	96	75	319	652	0.5791	0.5142	0.00067	12.945	0.0401	0.18259	0.00044	2674.5	2675.6	2676.5	8.0	0.1
B1	35	92	73	630	147	0.6056	0.5135	0.00056	12.921	0.0246	0.18249	0.00024	2671.6	2673.9	2675.6	4.2	0.2
C1	36	83	63	259	336	0.5760	0.5053	0.00086	12.602	0.0504	0.18087	0.00056	2636.7	2650.4	2660.8	10.4	1.1

Errors are 1 std. error of mean in % except 207/206 age errors, which are 2 std. errors in Ma

* Radiogenic Pb

[a] Include sample weight error of ± 0.001 mg in concentration uncertainty

[c] Total common Pb in analysis

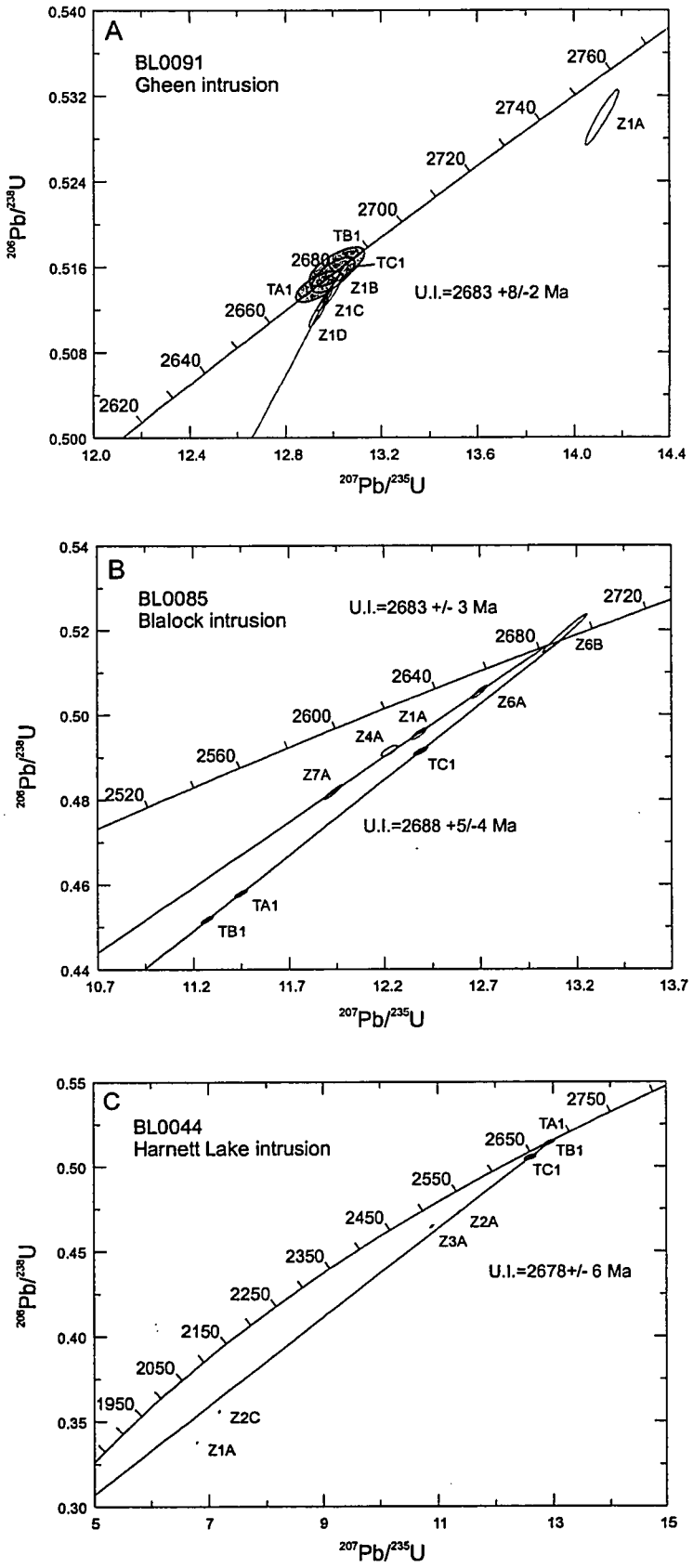

Fig. 2.2. Concordia diagrams of U-Pb zircon and titanite analyses.
Error ellipses are shown at the 2σ(95% confidence) level of uncertainty.

2.4. Field geology

The QAS intrusions range in size from a few hundred metres across to ca 10 km in diameter and commonly have slightly elongate forms with the long axis oriented NE-SW. Contacts to the country rocks vary from sharp to diffuse, but are rarely well exposed. The mafic to ultramafic intrusions are volumetrically small and display relatively simple mineralogy. They commonly contain coarse-grained, plagioclase-rich segregations that may represent filter-pressed residual liquid formed during advanced stages of differentiation combined with the build-up of volatiles. They also show net-veining by millimeter-thick quartz and alkali-feldspar veins. The leucocratic intrusions are larger and more diverse in terms of rock types, and commonly show significant variation in grain size and modal mineral contents on the outcrop scale. Most leucocratic units are equigranular, but blocky megacrysts of alkali-feldspar up to several centimetres across are characteristic of some units. These are commonly flow aligned (Figure 2.3a) or appear to be randomly distributed within the matrix. Where syn-plutonic mafic dykes are present, they are generally partly disaggregated, resulting in aligned trains of angular fragments (Figure 2.3b). Thin syenite dykes (~30 cm) with straight contacts intrude most complexes and crosscut all other units, suggesting late stage emplacement under brittle conditions. For detailed field descriptions see appendix 1.

Numerous field observations suggest that magma mixing and mingling processes occurred at the time of magma emplacement. These include:

(I) Both mafic and leucocratic intrusions preserve field evidence for intrusion of discrete magma batches, either in the form of contacts which illustrate multiple

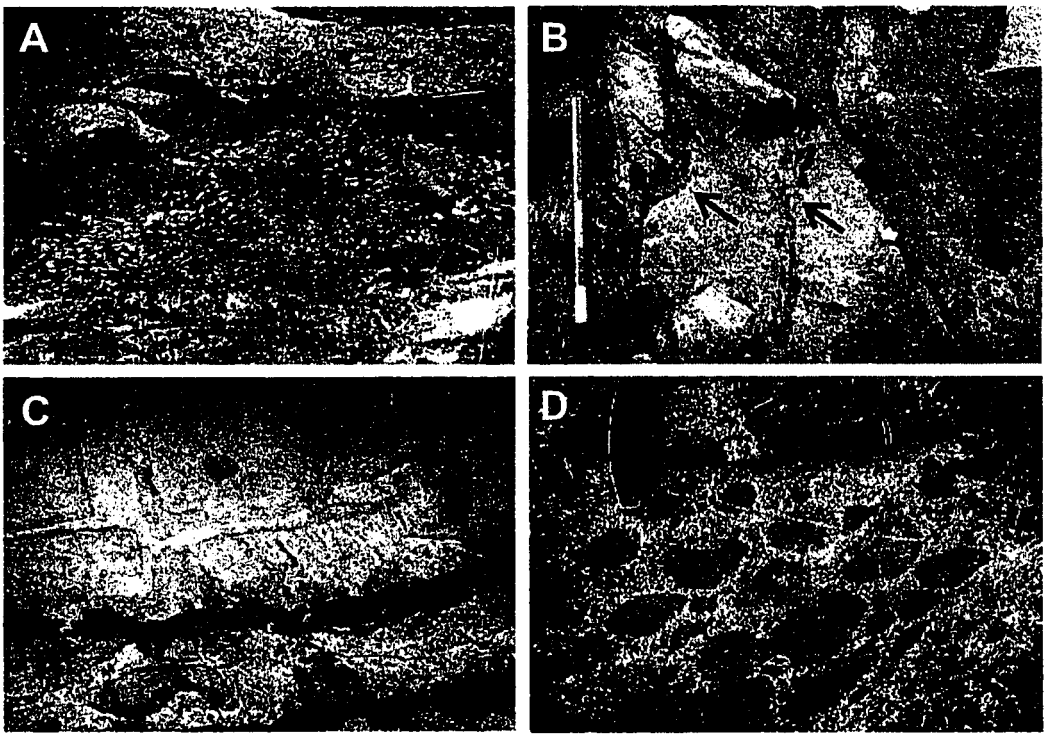

Fig. 2.3. Selected field photos from the QAS intrusions. (A) alkali-feldspar megacystic unit, Whalen Lake intrusion, has flow aligned megacrysts and is intruded by a younger phase of similar composition and cut by later pink dykes with straight contacts (lower part of photo). Note pencil in upper right corner. (B) Partly disaggregated mafic dykes and angular mafic enclaves within monzosyenitic units, Blalock intrusion. Hammer for scale. (C) Evidence for intrusion of several discrete batches of magma with distinctive appearance and composition is present in many intrusions. The photo is from Harnett Lake intrusion and shows an early phase broken up and intruded by a later phase. Note the transition from brittle to more ductile behavior from top to bottom. Hammer for scale. (D) High abundances of elongated, rounded mafic enclaves are locally present within many intrusions, here shown from Harnett Lake intrusion.

intermingling textures and testify to the co-existence of several contemporaneous magmas of contrasting composition, or in the form of crosscutting relationships, where an early unit is broken up and intruded by a younger magmatic phase of similar composition (Figure 2.3c).

(II) A number of intrusions expose abundant fine-grained, (cognate) mafic enclaves, which range in size from about 5 cm to 15 cm (Figure 2.3d). The enclaves are rounded and slightly elongate and commonly dioritic in composition. They have sharp contacts with the host rock with no evidence of mixing or solid-stage diffusion between them, and they contain the same mineral assemblages as the host rock, but have higher modal proportions of ferromagnesian minerals.

(III) *In situ* assimilation of crustal fragments is commonly observed in the field as mingling textures (locally extensive) between intrusive rocks and country rock sediments, especially towards the margins of the intrusions. In contrast, the modal abundance of metasedimentary xenoliths is low within the intrusion interiors, where the xenoliths are commonly angular in form with little or no sign of hybridization.

2.5. Analytical techniques

Major and trace elements have been measured by wavelength dispersive X-ray fluorescence spectrometry (XRF) at the University of Ottawa (UO) and at the Geological Survey of Canada (GSC). Samples were ground in an alumina grinding vessel to a fine powder, fused with lithium metaborate in platinum crucibles and analyzed on the glass discs. Ferrous ion was determined titrimetrically using the Wilson method (GSC) or

calculated from Fe_2O_3 (UO). Volatiles were determined by gravimetry at 900°C (GSC) or by weight difference by heating to 1100°C (UO). Limits of determination are (in %) 0.5 [SiO_2], 0.02 [TiO_2, P_2O_5, $Fe_2O_3^{TOTAL}$], 0.4 [Al_2O_3], 0.1 [MnO, MgO, CaO, Na_2O], 0.05 [K_2O]. Trace elements were analyzed by different methods. Ba, Cr, Ni, Sc, Sr, V and Zn were analyzed by ICP emission spectrometry at the GSC with the following limits of detection: 10 ppm for Ba, Cr, and Ni; 0.5 ppm for Sc and 5 ppm for Sr, V and Zn. Most ICP-MS data were obtained at the GSC and additional data were obtained at UO, and by ACME analytical laboratories in Vancouver, Canada. Detection limits for ICP-MS data (GSC) are 0.02 ppm for Ta, Th, U, Dy, Er, Eu, Gd, Ho, Lu, Pr, Sm, Tb, Tm, Y and Yb; 0.1 ppm for Ce, Ga, La and Nd; 0.5 ppm for Zr; 2 ppm for Pb and 0.05 ppm for Hf, Nb, Rb and Zr. Submitted duplicates show good inter-laboratory agreement, typically 1-5 % for major elements, while trace elements generally agree within ± 5% for concentrations >1 ppm and ± 10-15 % for concentrations in the range 0.1-1 ppm.

U-Pb age determinations were performed at the GSC. Zircon and titanite were separated by standard techniques including crushing, Wilfley table and heavy liquid techniques and hand-picked grains subsequently air abraded using the method of Krogh (1982). U-Pb separations and analytical methods are similar to those of Davis et al. (1997).

Most microprobe analyses were obtained with a Camebax MBX Electron Microprobe at Carleton University using energy dispersive spectrometry (EDS). Natural and synthetic standards were analyzed as unknowns and used for drift correction. The acceleration voltage was 15 kV and the beam current 20 nA. Counting time varied between 20 and 50 seconds for individual elements depending on the mineral analyzed. Additional

microprobe analyses were carried out at the GSC using a Cameca SX-50, an accelerating voltage of 20 kV and a beam current of 10 nA.

Nd and Pb isotopes were analyzed at Carleton University with a MAT 261 thermal ionization mass spectrometer operating in the static mode. Nd and Sm were extracted from whole rock samples through a standard dissolution and two-stage column separation process, and loaded on outgassed double Re filaments with phosphoric acid. Repeated runs of La Jolla standard over a time period of ten months gave 0.511869 ± 0.000014. Isotope ratios are reported without corrections relative to the recommended value. Alkali-feldspar separates were rigorously acid-leached in multiple aliquots [following the method of Carignan et al. (1995)] and Pb and U were extracted from the separates using exchange resins. Pb was loaded on outgassed single Re filaments with silica gel and phosphoric acid and U on double Re filaments with phosphoric acid. Pb isotopic ratios were corrected for U decay. NBS 981 gave $^{206}Pb/^{204}Pb$, $^{207}Pb/^{204}Pb$ and $^{208}Pb/^{204}Pb$ values of 16.898, 15.442 and 36.547, respectively. The average NBS 981 is $^{206}Pb/^{204}Pb$, $^{207}Pb/^{204}Pb$ and $^{208}Pb/^{204}Pb$ of 16.898 ± 0.010, 15.430 ± 0.015 and 36.495 ± 0.050. U500+233U standard gave $^{235}U/^{238}U$ of 1.00868.

2.6. Petrography and mineral chemistry

The vast majority of samples are medium to coarse-grained. Mafic samples generally consist of clinopyroxene, hornblende, plagioclase, magnetite ± phlogopite ± olivine ± orthopyroxene ± titanite. The essential mineralogy of the leucocratic samples includes K-feldspar, plagioclase, clinopyroxene, hornblende, riebeckite, titanite, apatite ± biotite ±

quartz ± calcite ± zircon ± epidote. Monazite is present within calciocarbonatite. Most samples have primary, unaltered mineralogy, but feldspar in mafic samples is commonly altered, and some leucocratic samples show minor feldspar alteration in grain centres.

There is a significant range in mineral compositions both within the igneous province as a whole and within single intrusions, reflective of the diversity in whole rock compositions. Clinopyroxene is present in most plutonic complexes in a wide range of lithological units and its composition is discussed separately below. K-feldspar [$An_0Ab_{0.01\text{-}0.05}Or_{0.95\text{-}0.99}$] occurs as medium-grained, weakly zoned grains and less commonly as flow aligned megacrysts with a blocky habit embedded in a groundmass of fine-grained, faintly twinned plagioclase, microperthitic K-feldspar and mafic minerals. The latter type displays zoning with respect to Ba (BaO up to 1.8 wt %) and is locally fractured or cut by veins filled with micro-crystalline feldspar. Fine-scale concentrically zoned plagioclase is present in moderate proportions in North Elbow Lake intrusion and Gheen intrusion, but is commonly replaced by alteration minerals in cores. Apart from Samuels Lake intrusion, olivine is rare and occurs only in a few samples, where it is rich in Fe and poor in Ni. In North Elbow Lake intrusion large hornblende oikocrysts enclose chadacrysts of olivine, orthopyroxene and clinopyroxene. Phlogopite and/or annite occur in minor modal amounts in all intrusions with the exception of Linden intrusion, which is practically devoid of hydrated mineral phases. Phlogopite contains high F (< 2.7 wt %), but low TiO_2 (0.4 to 1.7 wt %), Ba (< 0.4 wt %) and Cl (below detectable levels). Blue alkali amphibole with high Na contents occurs in Beaverhouse Lake intrusion. Fine-grained Fe-Ti oxides occur in almost all units, but generally in minor modal amounts. Locally, epidote rims ilmenite in mafic units, but within a few leucocratic samples

euhedral epidote occurs as a primary magmatic phase. Apatite shows two textural varieties: euhedral, coarse grains along with ferromagnesian minerals and late crystallizing fine-grained, elongated prisms within groundmass feldspar. Titanite is rich in FeO (<2.6 wt %) and F (<1 wt %) and occurs as wedge-shaped, euhedral grains locally up to 1 cm in length in almost all units except for the ultramafic phases. In evolved rocks anhedral quartz occupies the interstices between feldspar, suggesting late crystallization. Based on texture and chemical composition calcite in leucocratic units is a primary magmatic phase. Its composition is close to end-member calcite with Sr as the most important minor element. SrO concentrations display a limited range between 1.0 and 1.2 wt %, and MgO, MnO and FeO are subordinate components. For detailed petrography and mineral chemistry see Appendix 2 and 3.

2.6.1. Clinopyroxene –zoning and crystallization pressure

Clinopyroxene forms two distinct compositional groups best distinguished by differences in Al_2O_3 and TiO_2 concentrations, and corresponding to clinopyroxene from mafic and leucocratic units (Figure 2.4a and b). In the mafic units, clinopyroxene is characterized by high Mg and Cr and Al_2O_3 contents accompanied by low TiO_2. Compositionally, the majority resembles the low-Ti, moderate-Al Cr-diopside found in mantle xenoliths in the north Kamchatka arc (Kepezhinskas et al., 1995), although they do not appear to be of xenocrystic origin. The leucocratic units contain aegirine-augite with low Al_2O_3 and up to 7 wt % Na_2O, suggesting crystallization under shallow crustal conditions. Using pressure fields of Steward et al. (1996), which are based on a

compilation of experimental work, clinopyroxene from mafic units primarily plot in the 1.0 to 1.5 GPa field, although they do extend to lower pressures. In contrast, crystallization pressures of clinopyroxene from leucrocratic units are restricted to crustal values and plot close to 0.1 GPa (Figure 2.4c).

Clinopyroxene from the Gheen intrusion is optically and chemically zoned, revealing important clues to the magmatic evolution and differentiation history which is not evident from major and trace element data of whole rock samples alone. The distribution of Al^{IV} and Al^{VI} in zoned clinopyroxene is illustrated in Figure 2.4d and is consistent with crystallization at moderate to high pressure according to the pressure fields of Steward et al. (1996). The clinopyroxenes vary from euhedral to euhedral with some resorption, to subhedral. Clean looking, inclusion-free zones alternate with partly resorbed zones, suggesting that the melt was undersaturated during crystallization of the resorbed zones. Representative analyses of zoned clinopyroxene are listed in Table 2.2. Compositionally and texturally, clinopyroxene fall into three main categories:

I. Cr-diopside. Zoning occurs on a large scale as mantles of augite on cores of colorless Cr-diopside, and on a small scale as normal zoning within both rim and core. Clinopyroxene from this group forms clean, inclusion-free grains, which are high in Mg and depleted in Ti (0.04-0.09 p.f.u).

II. Mg-rich augite. These common megacrysts have a wider range in TiO_2 (0.016-0.045 p.f.u) and lower MgO and Cr_2O_3 (<0.5 wt %) relative to Cr-diopsides. Zoning is predominantly normal, but in a few crystals reverse zoning alternates with normal zoning. Zoning occurs within distinct growth zones, interpreted to reflect with periodic injection of fresh magma in a chamber undergoing fractional crystallization (Figure 2.5). In most

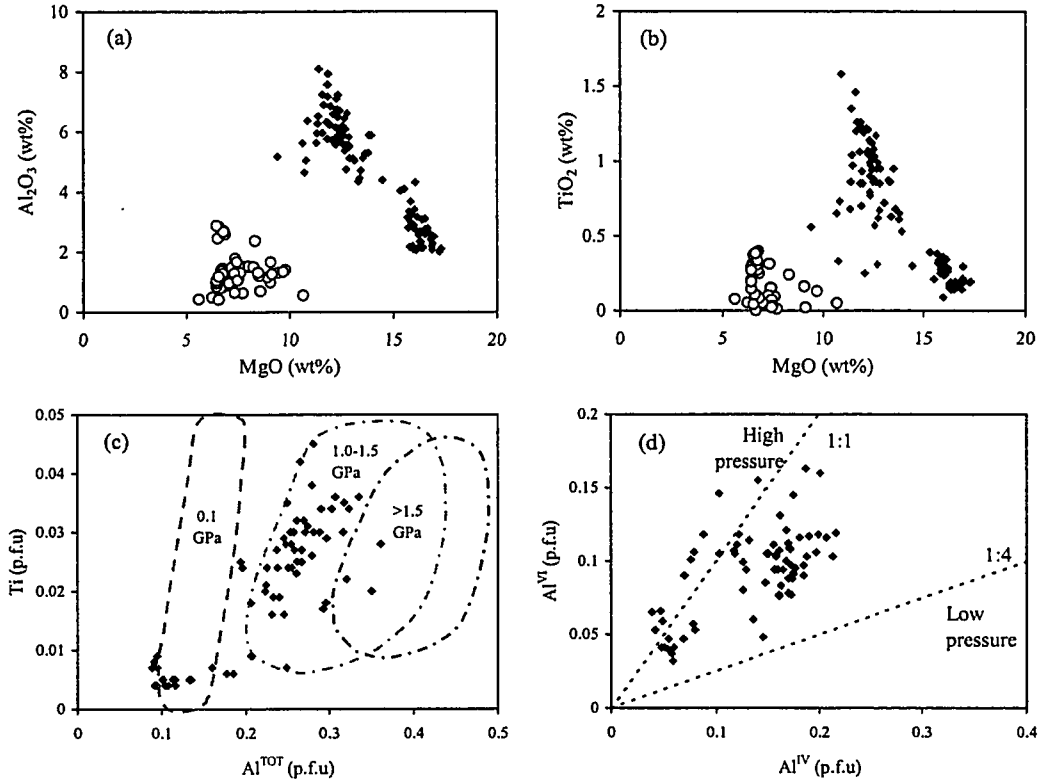

Fig.2.4. (a&b) Clinopyroxenes from mafic to ultramafic units and leucocratic units are distinguished by TiO_2 and Al_2O_3 abundances; open diamonds, leucocratic units; filled diamonds, mafic to ultramafic units. (c) Ti vs. Al^{TOT} (p.f.u) from zoned clinopyroxene in mafic to ultramafic units from Gheen intrusion. Pressure fields after Steward et al. (1996) and references cited within (d) Al^{IV} vs. Al^{VI} for zoned clinopyroxene from Gheen intrusion. A significant portion of aluminum occurs in the octahedrally coordinated sites, suggesting crystallization at high pressure.

Table 2.2. Representative microprobe analyses of zoned clinopyroxene (in wt %)

Analyses #	BL0089-2	BL0089-3	BL0089-12	BL0089-17	BL0089-19	BL0090-13	BL0090-22	BL0090-23	BL0090-24	BL0090-30	BL0090-43	BL0090-44
Pyroxene type	Cr-diopside	Cr-diopside	Mg-augite	augite	Mg-augite	augite	augite	augite	Mg-augite	Cr-diopside	Cr-diopside	Cr-diopside
Zone	mantle	mantle	core	rim	core	rim	rim	rim	core	mantle	mantle	mantle
SiO_2	53.31	52.54	47.39	49.68	52.35	50.76	48.00	50.01	50.42	52.77	53.66	53.80
Al_2O_3	2.06	2.10	7.56	5.17	2.67	4.65	6.84	5.05	4.71	4.32	2.64	2.52
TiO_2	0.26	0.27	1.26	0.56	0.16	0.33	1.19	0.73	0.63	0.24	0.18	0.14
Cr_2O_3	0.37	0.42	0.02	0.04	0.79	0.04	0.18	0.07	0.23	0.29	0.65	0.73
FeO	4.77	4.74	9.13	11.90	4.19	10.19	8.68	10.32	7.33	5.45	4.06	3.92
MgO	16.10	15.95	11.84	9.39	16.26	10.74	11.98	10.81	13.43	16.05	16.72	16.88
MnO	0.08	0.06	0.20	0.22	0.04	0.27	0.14	0.24	0.22	0.17	0.11	0.08
CaO	22.79	23.11	21.82	22.30	22.31	21.59	22.25	21.80	22.61	20.39	21.48	21.90
Na_2O	0.25	0.22	0.53	1.17	0.43	1.14	0.55	0.96	0.54	0.50	0.41	0.34
Total	99.99	99.41	99.74	100.43	99.20	99.71	99.81	99.99	100.12	100.18	99.91	100.31
Si	1.952	1.941	1.784	1.880	1.931	1.912	1.803	1.883	1.874	1.921	1.953	1.951
^{IV}Al	0.048	0.059	0.216	0.120	0.069	0.088	0.197	0.117	0.126	0.079	0.047	0.049
^{VI}Al	0.041	0.032	0.119	0.111	0.047	0.118	0.106	0.107	0.080	0.106	0.066	0.059
Ti	0.007	0.008	0.036	0.016	0.004	0.009	0.034	0.021	0.018	0.006	0.005	0.004
Cr	0.011	0.012	0.001	0.001	0.023	0.001	0.005	0.002	0.007	0.008	0.019	0.021
Fe	0.146	0.146	0.288	0.376	0.129	0.321	0.273	0.325	0.228	0.166	0.124	0.119
Mg	0.879	0.878	0.664	0.530	0.894	0.603	0.671	0.607	0.744	0.871	0.907	0.912
Mn	0.003	0.002	0.006	0.007	0.001	0.009	0.005	0.008	0.007	0.005	0.003	0.003
Ca	0.895	0.914	0.880	0.904	0.882	0.871	0.896	0.879	0.900	0.795	0.838	0.851
Na	0.018	0.016	0.039	0.086	0.030	0.083	0.040	0.070	0.039	0.035	0.029	0.024
Total	4.000	4.008	4.033	4.031	4.010	4.015	4.030	4.019	4.023	3.992	3.991	3.993
Fe/Mg	0.166	0.166	0.434	0.709	0.144	0.532	0.407	0.535	0.306	0.191	0.137	0.130
X_{Fe}^{a}	0.076	0.075	0.157	0.208	0.068	0.179	0.148	0.179	0.122	0.091	0.066	0.063
X_{Mg}^{D}	0.458	0.453	0.362	0.293	0.469	0.336	0.365	0.335	0.397	0.475	0.485	0.485
X_{Ca}^{c}	0.466	0.472	0.480	0.499	0.463	0.485	0.487	0.485	0.481	0.434	0.448	0.452

[a] Ferrosilite component
[D] Enstatite component
[c] Wollastonite component

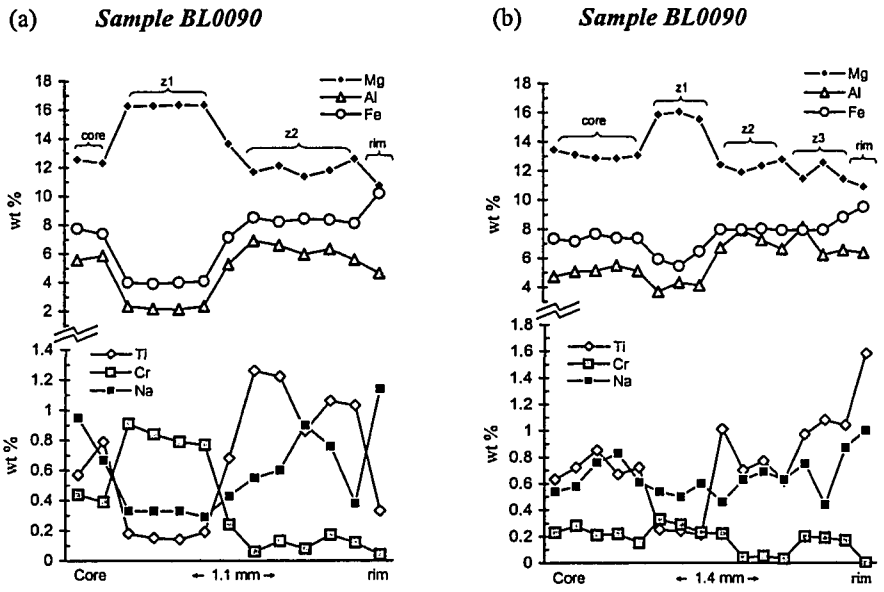

Fig. 2.5. Compositional profiles of clinopyroxene from mafic units in Gheen intrusion.

grains, several cycles of fractional crystallization and magma replenishment are recorded, but some clinopyroxene show evidence for only a single replenishment. Similar zoning patterns in alkaline rocks have been described by Wagner et al. (2003) in nepheline-syenites and carbonatite-rich rocks from northern Morocco and by Neumann et al. (1999) in clinopyroxene from basanitic to phonolitic lavas from Tenerife in the Canary Islands. These authors modeled a petrogenetic history dominated by fractional crystallization in periodically refilled magma chambers.

III. Sector zoned grains ranging from the classic hour-glass zoning to large grains containing a chaotic amalgamation of zones. This type of zoning usually indicates rapid crystallization during strong undercooling presumably related to flow within the magma chamber. No systematic compositional profiles were obtained on sector zoned grains.

2.7. Major and trace elements

2.7.1. Major element variations

The range in chemical compositions of the intrusions both as a suite and within single bodies is remarkable. Variations of selected major elements with respect to MgO as an index of differentiation are illustrated in Figure 2.6 and the data is listed in Table 2.3. Major elements define rather consistent trends with minor departures from the main trend. In general, the QAS intrusions have low TiO_2 contents (only a few samples have $TiO_2 > 1$ wt %), high total alkali contents (K_2O+Na_2O up to 13 wt %, Figure 2.6k) and high but variable Al_2O_3 for a given MgO concentration. In terms of potassium content the

Table 2.3. Whole-rock major element (in wt %) and trace element (in ppm) analyses of the QAS intrusions

Intrusion	Linden intrusion			Gheen intrusion								Harnett Lake intrusion			
Sample #	BL0094	BL0095	BL0099	BL0087a	BL0087b	BL0088	BL0090	BL0091	BL0092	BL0097	BL0098	BL9934	BL9939	BL9955	BL9937
MgO	2.09	2.12	8.12	9.49	9.43	12.23	8.20	2.66	3.05	6.25	2.55	0.86	0.73	1.73	0.74
SiO_2	59.91	59.84	48.13	45.48	45.15	46.80	47.83	55.12	52.81	51.51	54.09	66.30	62.82	56.10	65.90
TiO_2	0.57	0.61	0.76	1.31	1.31	1.05	0.76	0.79	0.87	0.98	0.81	0.31	0.08	0.75	0.32
Al_2O_3	14.55	14.61	14.54	12.90	12.46	10.34	14.51	13.03	12.27	13.09	13.31	16.40	17.06	18.52	16.70
Fe_2O_3T	4.04	4.12	9.60	12.88	13.25	9.88	9.63	6.37	6.00	10.11	6.28	2.80	2.31	6.34	2.90
MnO	0.08	0.07	0.17	0.14	0.14	0.14	0.16	0.13	0.11	0.17	0.12	0.04	0.05	0.11	0.05
CaO	4.51	4.40	9.32	10.44	11.05	12.46	9.23	7.95	9.62	9.14	7.68	1.86	2.53	3.26	1.68
Na_2O	4.12	3.93	1.67	1.93	1.72	1.03	1.56	2.66	2.09	3.48	2.33	6.20	7.30	6.19	5.90
K_2O	7.19	7.37	4.45	1.76	1.79	2.91	4.46	6.66	6.62	2.50	7.00	4.55	4.64	3.92	4.53
P_2O_5	0.45	0.44	0.48	0.65	0.85	0.15	0.49	1.26	2.19	0.67	1.55	0.17	0.22	0.65	0.17
Total	99.75	98.45	99.23	97.26	97.42	99.28	99.43	98.67	96.35	99.63	96.71	99.99	97.96	98.34	99.87
Ba	3652.9	4734	1350	569	561	1458	1273.7	4596.1	5716.2	1369	8882	840	705	1440	710
Cr	36	36	307	132	131	344	289	40	2	134	2	30	17	8	24
Ga	18.6	16.6	13.9	16.7	14.7	10.9	15.7	16.1	15.1	16.2	11.6	22.00	nd	nd	23
Hf	6.5	nd	nd	nd	nd	nd	2.3	7.5	8.5	nd	nd	6.60	nd	nd	5.3
Nb	8	7	6	5	4	3	4.5	15.9	16.7	6	21	28	6	33	27
Ni	31	36	83	69	59	116	84	31	12	29	13	0	3	8	0
Pr	19.6	20	nd	0	nd	nd	5.7	16.6	8.7	2	nd	25	nd	nd	26
Rb	175.1	188	194	36	30	116	157.2	117.4	124.7	53	135	110	101	142	170
Sc	nd	nd	nd	nd	nd	nd	nd	nd	nd	nd	nd	3.4	nd	nd	2.9
Sr	2276.8	2260	722	570	695	332	652.2	2975.6	3191.3	956	2792	640	688	1503	470
Ta	0.4	nd	nd	nd	nd	nd	0.2	0.8	0.9	nd	nd	1.60	nd	nd	1.50
Th	36.4	nd	3.99	2.65		1.63	3.6	11.2	15.6	1.68	5.05	13	nd	nd	10
U	4.7	1.36	nd	nd	nd	nd	1.5	1.9	2		nd	3.10	nd	nd	3.20
V	51	66	nd	363	nd	nd	177	61	46	221	nd	26	26	62	21
Zn	75	70	81	85	84	63	80	110	105	106	98	61	23	91	72
Zr	202.1	213	119	74	80	57	90.2	332.1	390.7	123	569	270	106	365	230
Ce	220	201	52	46	51	42	55.7	395	474.7	41	393	84	74	177	100
Dy	4.33	nd	nd	nd	nd	nd	3.27	9.92	10.88	nd	nd	1.90	nd	nd	2.6
Er	1.48	nd	nd	nd	nd	nd	1.67	2.93	2.91	nd	nd	0.76	nd	nd	1.1
Eu	4.28	nd	nd	nd	nd	nd	1.86	10.33	12.47	nd	nd	1.10	nd	nd	1.5
Gd	10.46	nd	13.9	nd	14.7	10.9	5.3	26.08	30.45	nd	11.6	3.30	16.4	20.2	5.3
Ho	0.63	nd	nd	0.62	nd	nd	1.33	1.34		nd	nd	0.31	nd	nd	0.43
La	99.7	122	32	25	22		24.6	137.1	173.3	27	155	26.0	50	97	48.0
Lu	0.18	nd	nd	nd	nd	nd	0.24	0.32	0.27	nd	nd	0.11	nd	nd	0.13
Nd	116.1	120	19	13	42	27	35.3	254.8	306.4	31	299	29.0	18	96	43.0
Pr	28	nd	nd	nd	nd	nd	7.3	57.43	70.8	nd	nd	8.10	nd	nd	11
Sm	17.5	nd	nd	nd	nd	nd	6.9	45.4	55.8	nd	nd	5.30	nd	nd	7.70
Tb	1.1	nd	nd	nd	nd	nd	0.69	2.64	3.07	nd	nd	0.41	nd	nd	0.62
Tm	0.21	nd	nd	nd	nd	nd	0.25	0.41	0.37	nd	nd	0.11	nd	nd	0.14
Y	20.7	21	nd	19	18	11	18.7	43.2	43.7	22	49	9.20	7	24	13
Yb	1.32	nd	nd	nd	nd	nd	1.6	2.37	2.2	nd	nd	0.74	nd	nd	0.86
Cs	3.5	nd	nd	nd	nd	nd	6.5	1.8	1.3	nd	nd	0.69	nd	nd	6.20

nd = not determined

Table 2.3. Continued

Intrusion	Harnett Lake intrusion						Beaverhouse Lake intrusion								
Sample	BL9940	BL0042	BL0044	BL0045	Harnet P.	Harnet D.	BL9999	BL99101	BL99103	BL99104	BL99108	BL99116	BL0064	BL0065	BL0075
MgO	3.59	0.94	0.88	1.75	1.12	2.71	1.11	0.37	0.51	3.96	0.53	1.08	0.91	0.39	0.07
SiO_2	58.30	59.16	62.95	60.42	59.90	54.05	62.40	1.05	66.40	44.00	63.85	62.10	14.11	1.40	71.59
TiO_2	0.83	0.38	0.36	0.59	0.48	0.85	0.30	0.01	0.05	0.46	0.23	0.19	0.05	0.01	0.03
Al_2O_3	16.90	18.20	16.51	15.80	17.15	17.49	15.60	0.20	17.90	17.17	16.48	15.32	2.89	0.30	13.14
Fe_2O_3T	6.20	4.36	2.42	4.29	3.75	7.83	2.88	0.65	1.30	9.37	2.32	2.86	2.05	0.73	0.92
MnO	0.07	0.08	0.07	0.09	0.07	0.12	0.06	0.21	0.02	0.17	0.07	0.10	0.17	0.19	0.03
CaO	4.50	1.86	2.55	4.39	2.36	3.90	3.30	52.16	0.86	11.92	2.09	4.08	41.42	51.99	0.51
Na_2O	5.00	6.29	4.92	5.82	4.65	6.26	5.80	0.00	6.70	2.04	7.06	5.70	1.38	0.00	5.57
K_2O	3.24	4.72	6.87	3.83	6.68	2.73	6.64	0.08	6.35	3.84	5.34	5.64	0.91	0.14	4.12
P_2O_5	0.51	0.44	0.17	0.33	0.32	1.02	0.35	0.34	0.16	0.42	0.15	0.31	2.19	0.04	0.01
Total	100.50	98.32	98.37	98.28	98.04	98.36	100.50	55.81	100.80	95.65	98.70	98.19	66.99	56.08	96.46
Ba	980	891	1274	2335	2388.7	603.9	1454	460	750	738	517	820	268	56	23
Cr	80	7	16	28	18	6	18	0	18	7	10	11	2	0	5
Ga	23	nd	19.8	nd	20.9	25.4	nd	1.5	24.00	nd	nd	18.4	5.5	1.6	24.6
Hf	3.80	nd	nd	nd	5.9	5.9	nd	7.9	2.10	nd	nd	nd	2.8	0.5	nd
Nb	15	32	30	31	24.2	17.6	19	0.5	3.50	11	15	15	2.8	0.5	11
Ni	51	8	7	14	12	12	15	5	0	31	6	6	12	7	3
Pr	11	0	nd	3	6.5	4.2	nd	27.5	2	nd	nd	nd	17.8	24.1	3
Rb	150	141.1	145	108.4	114.7	164.8	164	2.5	170	198	204	138	26.6	5.6	88
Sc	8.9	nd	nd	nd	nd	nd	nd	nd	0.9	nd	nd	nd	nd	nd	nd
Sr	930	1054.3	725	759	1095.7	1595.5	920	6629.2	330	987	389	558	5211.3	6581.8	35
Ta	0.48	nd	nd	nd	1.5	0.6	nd	0.1	0.27	nd	nd	nd	0.1	0.1	nd
Th	9.20	12.6	2.36	17.5	9.4	5.8	nd	1.1	1.80	nd	nd	4.4	4.1	1.6	10.11
U	1.80	5.7	nd	2.4	2.1	1.8	nd	0.2	0.96	nd	nd	nd	0.9	< .1	7.89
V	77	36	nd	65	39	68	31	< 5	11	54	17	nd	21	< 5	6
Zn	82	87	54	77	50	136	43	8	16	95	47	57	23	10	22
Zr	150		317		313.5	274.8	196	17.6	100	261	79	79	116.5	21.2	51
Ce	130	200	101	188	164.1	155	56	868.3	27	61	87	110	745.8	705.3	nd
Dy	2.10	nd	nd	nd	3.51	3.33	nd	23.8	0.86	nd	nd	nd	22.4	24.84	nd
Er	0.85	nd	nd	nd	1.45	1.41	nd	10.32	0.34	nd	nd	nd	8.96	10.73	nd
Eu	1.70	nd	nd	nd	2.75	2.83	nd	17.94	0.61	nd	nd	nd	17.17	16.64	nd
Gd	4.40	19	19.8	19	6.74	6.89	17.8	49.79	1.80	14.4	19.9	18.4	47.87	48.44	nd
Ho	0.37	nd	nd	nd	0.54	0.56	nd	4.1	0.14	nd	nd	nd	3.72	4.36	nd
La	60.0	106	45	88	77.7	70.5	23	404.3	10	35	36	37	314.2	295	nd
Lu	0.11	nd	nd	nd	0.19	0.19	nd	1.11	0.05	nd	nd	nd	0.97	1.22	nd
Nd	48	98	70	93	78.7	76.3	62	438.1	15	31	57	65	398.2	386.4	nd
Pr	13	nd	nd	nd	20.04	18.83	nd	114.82	3.60	nd	nd	nd	101.48	96.67	nd
Sm	6.90	nd	nd	nd	12	11	nd	77.8	2.60	nd	nd	nd	73.5	72.1	nd
Tb	0.50	nd	nd	nd	0.81	0.79	nd	5.97	0.21	nd	nd	nd	5.5	5.77	nd
Tm	0.12	nd	nd	nd	0.21	0.2	nd	1.38	0.05	nd	nd	nd	1.23	1.46	nd
Y	11	24.6	19	23.5	16.9	17.3	13	130.2	4.40	17	10	10	116.9	136.6	7
Yb	0.68	nd	nd	nd	1.18	1.25	nd	8.45	0.30	nd	nd	nd	7.44	8.89	nd
Cs	4.20	nd	nd	nd	1	6.8	nd	0.1	4.20	nd	nd	nd	1	0.2	nd

Table 2.3. Continued

Intrusion	Whalen Lake intrusion													South Elbow Lake intrusion	
Sample	BL9928	BL9929	BL9930	BL9984	BL99118	BL99120	BL99121	BL99124	BL99160	BL0025	BL0029	BL0033	BL0040	BL00111	BL99135
MgO	18.66	5.38	2.16	1.73	4.32	0.66	1.38	0.15	1.23	2.68	13.21	1.73	2.15	0.23	7.05
SiO_2	46.12	50.48	57.79	62.10	51.20	63.30	58.18	72.66	60.29	57.09	48.85	60.51	55.44	73.18	52.00
TiO_2	0.40	1.28	0.63	0.54	1.07	0.28	0.34	0.11	0.39	0.51	0.53	0.44	0.88	0.08	0.63
Al_2O_3	5.18	15.04	17.32	15.30	14.30	16.90	14.72	13.94	15.86	12.97	9.13	15.02	18.06	14.43	15.50
Fe_2O_3T	11.26	11.27	6.75	4.30	12.50	1.90	3.66	0.85	4.86	5.86	9.50	4.95	6.98	0.61	9.50
MnO	0.17	0.15	0.11	0.09	0.18	0.03	0.08	0.02	0.12	0.13	0.27	0.10	0.11	0.01	0.16
CaO	12.45	7.73	4.03	5.11	7.85	3.28	6.71	0.97	3.81	8.20	12.44	5.04	3.50	1.03	6.46
Na_2O	0.49	4.01	5.58	4.70	4.20	5.20	4.50	4.00	5.76	4.24	0.37	4.13	6.51	2.85	4.20
K_2O	0.18	2.06	3.75	4.82	2.53	7.52	6.38	4.51	4.82	5.08	1.41	5.01	3.54	6.21	1.90
P_2O_5	0.03	0.79	0.44	0.46	0.85	0.14	0.48	0.05	0.46	0.70	0.48	0.37	0.79	0.04	0.45
Total	99.17	101.01	99.96	100.40	100.20	100.80	98.02	98.39	99.46	98.43	98.56	98.35	99.45	98.93	100.90
Ba	0	829	1338	1200	1200	1300	2097	613	1240	2056	317	1537	1333	1494	450
Cr	949	90	37	36	69	12	8	8	7	16	1421	32	7	8	307
Ga	6.4	nd	nd	18	19.00	14.00	nd	nd	n	10.8	10.4	15.5	21.8	21.1	19
Hf		nd	nd	4.2	2.80	1.20	nd	nd	n	nd				nd	2
Nb	2	13	13	30	10.00	19.00	10	12	16.00	18	11	18	34	6	3.90
Ni	210	39	20	12	26	0	10	0	4	14	349	17	12	5	79
Pr	nd	nd	nd	20	8	7	nd	nd	nd	nd	nd	nd	13	14	7
Rb	0	56	90	86	68	160	137	135	74	96	58	87	181	111	88
Sc	nd	nd	nd	5.2	13.0	1.0	nd	nd	nd	nd	nd	nd	nd	nd	22
Sr	147	1298	1292	1400	1500	1300	2206	225	1149	1884	434	1367	1482	451	1000
Ta	nd	nd	nd	1.4	0.27	1.0	nd	nd	nd	nd	nd	nd	nd	nd	0.15
Th	1.44	nd	nd	7.8	3.30	1.60	nd	nd	nd	nd	30.01	3.59	4.43	10.68	1.40
U		nd	nd	2	0.81	0.44	nd	nd	nd	nd			1.17	3.03	0.42
V		212	94	62	211	31	58	12	44	nd			69	2	170
Zn	61	110	94	63	117	18	34	21	70	61	122	76	104	12	91
Zr	23	104	225	170	130	38	112	145	116	131	91	187	347	69	72.0
Ce		123	98	230	150	79	135	21	137	171	386	165	189	20	85.0
Dy	nd	nd	nd	4.5	5.40	2.00	nd	nd	nd	nd	nd	nd	nd	nd	3.20
Er	nd	nd	nd	1.7	2.20	0.68	nd	nd	nd	nd	nd	nd	nd	nd	1.50
Eu	nd	nd	nd	3.2	3.20	1.60	nd	nd	nd	nd	nd	nd	nd	nd	1.90
Gd	6.4	20	20.4	9	10.0	4.10	11.7	21	17.30	10.8	10.4	15.5		nd	5.10
Ho	nd	nd	nd	0.72	0.91	0.32	nd	nd	nd	nd	nd	nd	nd	nd	0.58
La		65	56	116	57.0	36.0	58	10	64.0	79	236	73	120	nd	39.0
Lu	nd	nd	nd	0.2	0.28	0.10	nd	nd	0.18	nd	nd	nd	nd	nd	0.23
Nd		96	56	98	85.0	40.0	82		67.0	82	171	82	90	nd	44.0
Pr	nd	nd	nd	27	20.00	9.90	nd	nd	nd	nd	nd	nd	nd	nd	11.00
Sm	nd	nd	nd	14	15.00	6.60	nd	nd	nd	nd	nd	nd	nd	nd	7.30
Tb	nd	nd	nd	1	1.10	0.46	nd	nd	nd	nd	nd	nd	nd	nd	0.64
Tm	nd	nd	nd	0.23	0.30	0.10	nd	nd	nd	nd	nd	nd	nd	nd	0.22
Y	7	22	20	23	27.00	9.50	14	6	15.00	18	31		23	4	17.00
Yb	nd	nd	nd	1.3	1.70	0.55	nd	nd	nd	nd	nd	nd	nd	nd	1.40
Cs	nd	nd	nd	1.1	1.70	1.40	nd	nd	nd	nd	nd	nd	nd	nd	3.10

Table 2.3. Continued

Intrusion	North Elbow Lake intrusion									Blalock intrusion					
Sample	BL9948	BL9950	BL9952	BL9953	BL9960	BL99155	BL99147	BL0006	BL0017	BL0052	BL0054	BL0076	BL0077	BL0078	BL0082
MgO	17.63	11.86	6.49	7.36	12.98	10.63	7.69	7.14	0.60	6.81	4.21	2.26	4.54	1.77	1.84
SiO_2	49.90	50.40	50.78	40.90	44.30	51.30	47.23	50.45	69.72	49.30	57.49	58.55	55.07	63.30	64.69
TiO_2	0.37	0.71	0.68	1.33	1.66	0.50	0.95	0.40	0.14	1.06	0.76	0.61	0.80	0.43	0.41
Al_2O_3	5.00	10.40	17.40	17.50	11.30	11.50	15.64	17.44	17.01	15.94	15.15	13.97	15.37	15.47	15.57
Fe_2O_3T	10.20	11.30	11.35	15.70	12.20	9.40	12.64	11.57	1.12	9.01	6.75	4.13	8.01	3.69	3.78
MnO	0.18	0.18	0.15	0.15	0.14	0.16	0.16	0.17	0.02	0.13	0.12	0.08	0.12	0.06	0.07
CaO	15.16	10.85	6.39	11.66	12.63	12.47	8.96	6.16	3.40	6.91	4.68	4.95	5.60	2.79	2.94
Na_2O	0.80	1.90	3.22	2.00	1.90	1.90	2.72	3.57	5.53	3.65	3.58	3.67	3.42	4.39	4.24
K_2O	0.42	0.79	1.21	0.98	0.64	0.85	1.49	1.02	1.23	3.22	4.72	7.10	3.72	4.21	4.10
P_2O_5	0.03	0.14	0.33	0.36	0.05	0.22	0.59	0.08	0.05	0.85	0.43	0.50	0.47	0.22	0.22
Total	100.60	100.60	100.60	100.90	100.20	100.50	99.97	100.16	99.18	98.72	98.91	98.53	99.02	98.71	98.74
Ba	120	240	405	310	170	190	482	310	449	1936.9	1726	4717	1474	1391	1210
Cr	1120	690	309	54	583	819	238	343	14	206	194	35	179	53	60
Ga	7	14	18	23	14	14	18.2	19.1	17.6	20.1	16.7	15	17.2	17.5	16.8
Hf	0.89	2	nd	2.10	1.50	1.90	nd	nd	nd	nd	nd	nd	nd	nd	7.9
Nb	1	3.20	1	3.90	3.10	3.10	6	nd	2	15	14	5.8	10	12	8.1
Ni	313	168	79	32	128	120	71	116	13	142	79	31	92	37	40
Pr	1	3	nd	3	2	6	nd	nd	7	2.6	nd	nd	188	24	nd
Rb	10	15	35	24	6	17	66	20	29	95.2	140	192.6	121	141	168
Sc	55.0	46.0	nd	33.0	75.0	46.0	nd	nd	nd	nd	nd	nd	nd	nd	nd
Sr	160	420	998	1000	330	440	636	985	524	1809.3	1203	1998.4	902	1057	1054
Ta	0.06	0.21	nd	0.19	0.16	0.18	nd	nd	nd	0.3	nd	nd	nd	nd	nd
Th	0.50	1.70	nd	0.78	0.30	1.70	3.2	nd	nd	3.5	6.71	11.5	3.05	15.42	19.2
U	0.14	0.41	nd	0.24	0.10	0.46	nd	nd	nd	0.6	nd	6.8	5.95	1.75	1.22
V	182	232	193	356	493	180	nd		16	129		71	143	54	
Zn	53	73	117	92	51	59	99	126	29	113	83	70	81	54	51
Zr	25	70	63	56	38	59	103	36	80	408.2	308	118.4	190	253	248
Ce	16	38	21	44	23	37	47	39		229	148	229	111	124	119
Dy	1.80	2.80	nd	4.3	4.2	2.5	nd	nd	nd	4.2	nd	nd	nd	nd	nd
Er	0.93	1.50	nd	2.1	2.0	1.3	nd	nd	nd	1.69	nd	nd	nd	nd	nd
Eu	0.73	1.10	nd	1.9	1.5	1.1	nd	nd	nd	4.2	nd	nd	nd	nd	nd
Gd	2.50	3.70	18.00	6.20	5.50	3.30	18.2	19.1		9.32	16.7	nd	nd	nd	16.8
Ho	0.34	0.55	nd	0.80	0.81	0.47	nd	nd	nd	0.67	nd	nd	nd	nd	nd
La	5.4	16.0	32.0	15.0	6.9	15.0	13	17		104.3	92	110	56	77	68
Lu	0.13	0.22	nd	0.28	0.25	0.21	nd	nd	nd	0.23	nd	nd	nd	nd	nd
Nd	12.0	22.0	11.0	32.0	22.0	21.0	32	10		121.1	64	132	34	61	56
Pr	2.40	4.90	nd	6.60	4.00	4.90	nd	nd	nd	29.46	nd	nd	nd	nd	nd
Sm	2.70	4.10	nd	6.80	5.40	3.80	nd	nd	nd	17.6	nd	nd	nd	nd	nd
Tb	0.34	0.52	nd	0.79	0.76	0.44	nd	nd	nd	1.05	nd	nd	nd	nd	nd
Tm	0.13	0.22	nd	0.30	0.30	0.19	nd	nd	nd	0.24	nd	nd	nd	nd	nd
Y	10.00	16.00	8.00	23.00	24.00	15.00	21		2	20.6	22	18.4	15	16	
Yb	0.84	1.50	nd	1.80	1.80	1.30	nd	nd	nd	1.5	nd	nd	nd	nd	nd
Cs	0.53	0.42	nd	0.52	0.30	0.95	nd	nd	nd	2.6	nd	nd	nd	nd	nd

Table 2.3. Continued

Intrusion	Blalock intrusion				Surprise Lake intrusion		Heward	Kawene	S.Kawene Lake intrusion		Samuels Lake intrusion			Country rock	
Sample	BL0084	BL0085	BL00103	BL00104	BL9915	BL99130	BL99145	BL9986	BL9993	BL9995	S9901	S9902	S9903	BL9938	BL0039
MgO	6.11	2.07	2.12	4.84	1.00	3.13	6.62	1.06	13.32	13.91	12.29	23.00	24.00	3.05	2.97
SiO_2	57.11	62.50	63.46	54.33	65.30	53.09	50.50	65.50	48.66	48.70	42.50	34.30	36.30	64.90	63.13
TiO_2	0.45	0.50	0.46	0.64	0.22	0.80	0.80	0.43	0.71	0.81	1.51	0.11	0.11	0.54	0.55
Al_2O_3	13.17	15.41	15.81	16.18	16.60	17.50	15.70	17.00	9.62	9.10	13.10	1.50	1.60	14.60	15.64
Fe_2O_3T	5.91	4.26	4.18	8.69	3.30	8.70	11.10	3.70	10.52	10.10	15.10	26.60	23.10	6.30	6.24
MnO	0.14	0.07	0.07	0.14	0.05	0.15	0.15	0.06	0.16	0.14	0.14	0.13	0.12	0.09	0.08
CaO	5.93	3.66	3.35	6.76	3.11	5.41	7.82	3.30	11.51	11.98	10.79	6.07	6.10	3.55	2.72
Na_2O	2.47	3.83	4.18	3.95	7.00	4.58	3.10	4.80	1.89	2.10	2.20	0.16	0.28	3.40	3.86
K_2O	6.07	4.69	4.24	2.06	1.53	4.07	1.78	2.91	1.27	0.85	1.28	0.11	0.13	1.42	2.41
P_2O_5	0.49	0.43	0.25	0.35	0.27	0.59	0.53	0.25	0.16	0.19	0.10	0.04	0.04	0.12	0.15
Total	100.87	98.16	98.53	99.23	99.90	98.48	100.50	100.00	98.11	100.30	101.00	100.80	98.90	100.40	99.06
Ba	1221	2440	1242.1	487	490	1788	600	1100	373	300	260	38	40	460	717
Cr	226	53	65	135	27	30	233	21	818	952	197	808	821	191	147
Ga	14.8	16.6	18.1	16.4	20	19.6	20	22		12	18	1.9	2.2	18	19.3
Hf	nd	nd	5.1	nd	1.80	nd	3	4.7	nd	1.9	1.7	0.3	0.34	4.30	nd
Nb	15	13	11	6	5.30	10	5.7	6.9	4	4.3	3.1	0.37	0.44	6.20	8
Ni	136	31	35	51	0	21	64	0	178	155	79	4230	3900	62	64
Pr	40	nd	9.5	nd	15	nd	6	17	nd	5	2	2	3	25	nd
Rb	224	170	146.9	155	48	109	63	79	23	20	19	33	4.2	43	96
Sc	nd	nd	nd	nd	5.7	nd	24.0	4.7	nd	41.0	58	19	19	14	nd
Sr	1093	1271	1045.4	906	770	1320	590	990	311	310	360	34	51	510	449
Ta	nd	nd	0.8	nd	0.2	nd	0.27	0.41	nd	0.21	0.17	n	0	0.43	nd
Th	11.75	16.94	21.9	6.71	7.9	nd	4.50	7.40	nd	2.10	0.67	0.26	0.33	8.70	5.88
U		4.78	4.9	nd	2.0	nd	0.90	1.70	nd	0.66	0.24	0.08	0.09	2.50	
V	87		52		43	nd	190	38	208	248	443	0.53	53	104	
Zn	92	59	57	87	47	100	94	66	70	53	67	74	53	93	78
Zr	174	306	207.3	132	65	130	100	170	56	52	47	10	13	150	128
Ce	188	185	131.6	107	64	100	75.0	90.0	48	44.0	30	6.4	6.9	70	44
Dy	nd	nd	2.35	nd	2.4	nd	3.9	1.8	nd	3.4	4.6	0.54	0.58	2.50	nd
Er	nd	nd	1.2	nd	1.1	nd	1.8	0.8	nd	1.5	2.1	0.23	0.26	1.30	nd
Eu	nd	nd	1.63	nd	1.5	nd	2.0	1.2	nd	1.5	1.9	0.27	0.29	1.10	nd
Gd	nd	16.6	4.33	16.4	4	19.6	6.2	3.0	13.6	5.1	6.3	0.81	0.84	3.40	19.3
Ho	nd	nd	0.41	nd	0.46	nd	0.73	0.33	nd	0.61	0.81	0.09	0.11	0.48	nd
La	64	85	69.8	50	29.0	67	31.0	39.0	nd	17.0	9.6	2.5	2.7	35.0	32
Lu	nd	nd	0.18	nd	0.23	nd	0.28	0.14	nd	0.20	0.25	0.03	0.03	0.21	nd
Nd	91	95	56.7	34	31.0	49	44.0	35.0	23	28.0	26	4.7	4.9	28.0	18
Pr	nd	nd	15.1	nd	7.60	nd	10.00	9.60	nd	6.20	5	0.99	1.1	7.50	nd
Sm	nd	nd	7.6	nd	5.30	nd	8.10	4.90	nd	5.80	7.1	0.99	1	4.50	nd
Tb	nd	nd	0.5	nd	0.52	nd	0.77	0.36	nd	0.66	0.82	0.11	0.11	0.45	nd
Tm	nd	nd	0.19	nd	0.16	nd	0.29	0.13	nd	0.22	0.28	0.03	0.03	0.19	nd
Y	14	21	13.4	16	13.00	17	22.00	10.00	13	18.00	23	2.5	2.7	15	11
Yb	nd	nd	1.28	nd	0.95	nd	1.80	0.85	nd	1.30	1.7	0.2	0.22	1.40	nd
Cs	nd	nd	7.5	nd	2.20	nd	2.00	3.20	nd	1.50	1.5	0.31	0.29	2.10	nd

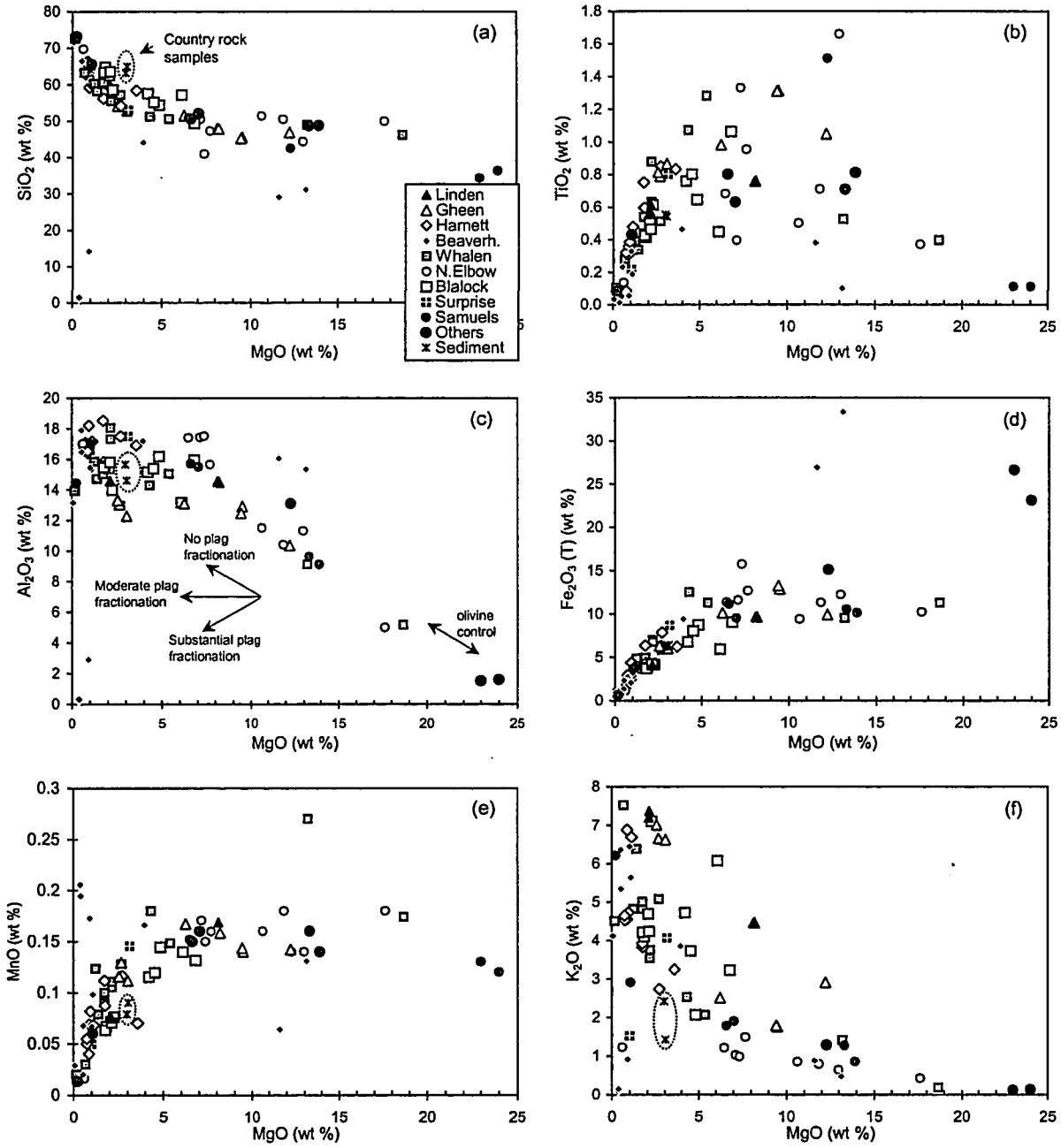

Fig. 2.6. (a through j) Major element variation diagrams with MgO as differentiation index for the QAS intrusions and surrounding country rocks. The country rocks analyses are surrounded by dotted circles. Carbonatite samples are not included in (g), (j), (k) and (l). In the legend "others" refers to intrusions with only one or two geochemical analyses [Kawene Lake intrusion, South Kawene intrusion, Heward intrusion and South Elbow Lake intrusion]. (k) Diagram of SiO_2 *vs*. total alkalis to illustrate the high alkali contents of the QAS intrusions. Note the non-alkaline nature of the county rock samples. Subdivision into subalkaline and alkaline series is from Irvine and Barager (1971). (l) Diagram of SiO_2 *vs*. K_2O with discrimination boundaries from Peccerillo & Taylor (1976).

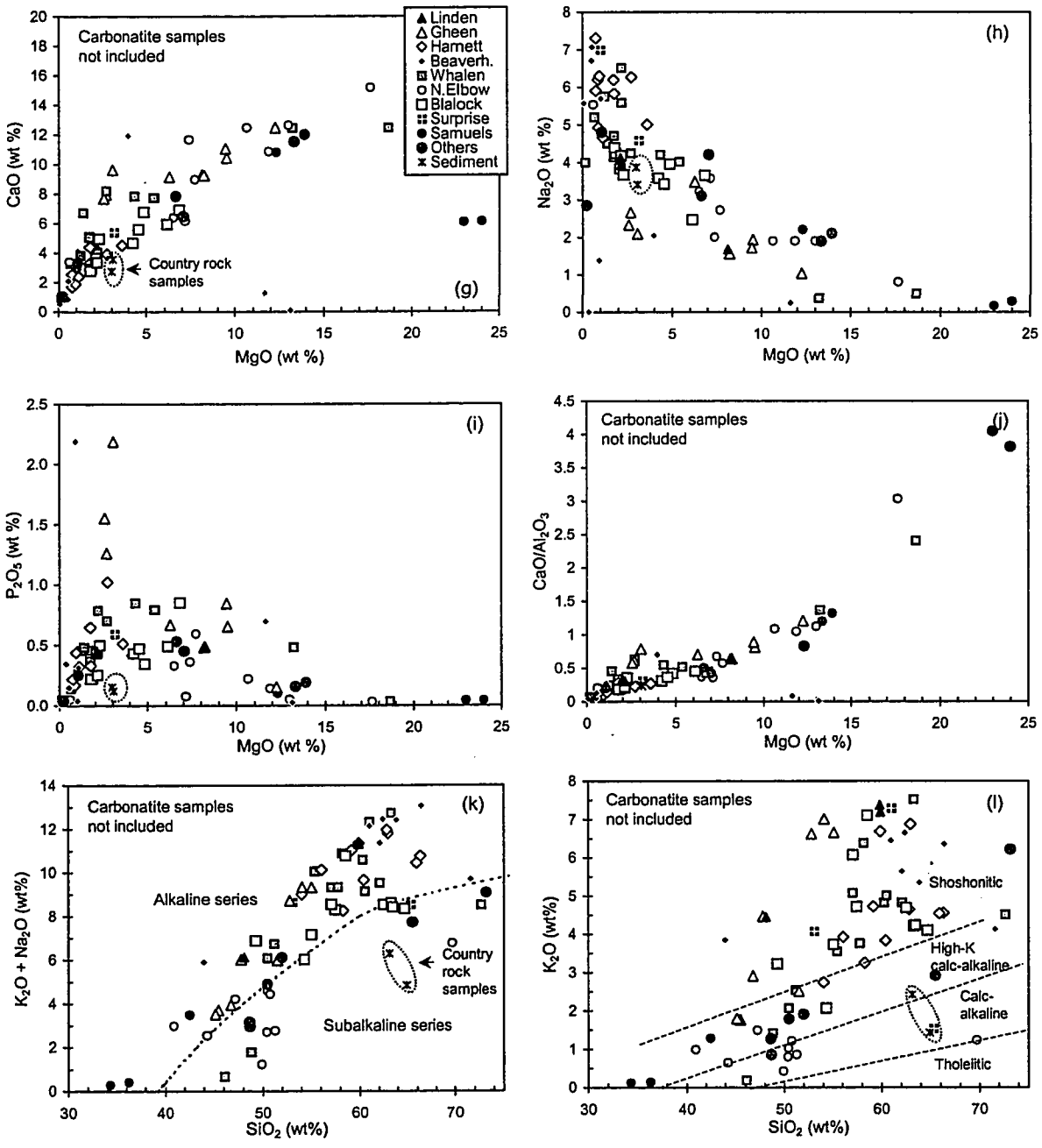

Fig. 2.6 *continued*

majority of samples plots in the shoshonite field in the K_2O *vs.* SiO_2 diagram [according to the classification of Pecerillo and Taylor (1976)] (Figure 2.6l), while a few samples have lower K contents and plot in the high-K calc-alkaline or the calc-alkaline field. K_2O/Na_2O varies significantly from 0.2 to 3.8. The agpaitic index [atomic (K+Na)/Al] increases with decreasing MgO and reaches values just above one in a few samples from Beaverhouse Lake intrusion, falling in the peralkaline field. The QAS intrusions range to higher K_2O and higher total alkalis for a given SiO_2 compared to late Archean LILE rich intrusions from adjacent volcanic belts (Figure not shown). Apart from carbonatite samples, only a few ultramafic samples have elevated LOI values, presumably a consequence of secondary alteration (carbonatization) combined with a high modal proportion of hydrous mineral phases.

Major element variation diagrams can be divided into two broad fields divided by an inflection point for most oxides at MgO ~ 5-6 wt %. For contents below 5 wt % MgO, Si, Na and K increase, Ca, Ti, Mn, P and Ca/Al decrease. There is a large variation in Al abundances, but not consistent trend (Figure 2.6). For compositions with MgO above 5 wt %, Na, K, Al and P increase with MgO, Ca and Ca/Al decrease, and Si and Mn are approximately constant, while Ti displays no clear trend (Figure 2.6).

Even though most samples are moderately to strongly differentiated, several of the high-Mg samples could represent primary melts from the mantle. Compositional criteria used to identify primary mantle melts include Mg-number > 0.7, FeO*/MgO < 1 and Ni and Cr concentrations > 200 and 400 ppm, respectively (Tatsumi and Eggins, 1995). North Elbow Lake intrusion, South Kawene Lake intrusion and Gheen intrusion contain potential near-primary melt compositions. The above criteria are met by sample BL9948,

which is used in the following as assumed parental magma composition for the QAS intrusions.

2.7.2. Trace element variations

2.7.2.1 Multi-element diagrams

Trace element abundances for a representative suite of samples from all intrusions are illustrated in primitive-mantle-normalized diagrams in Figure 2.7 and representative trace element analyses are listed in Table 2.3. One country rock sample (BL9938) is included in all trace element diagrams for reference with respect to potential bulk assimilation effects. Similarly, ocean island basalt (OIB) (Sun and McDonough, 1989) is included for comparison.

Samples from Samuels Lake intrusion have the lowest overall incompatible trace element abundances, probably reflecting the fact that olivine, which is present as a cumulative phase, is practically devoid of incompatible trace elements. In general, LILE are enriched relative to light rare earth elements (LREE) (e.g. high Ba/La) and both groups are moderately to strongly enriched relative to high field strength elements (HFSE) and heavy rare earth elements (HREE) (e.g. high Ba/Nb). These features resemble those observed in arc rocks and contrast strongly with OIB. Samples from Samuels Lake intrusion and Beaverhouse Lake intrusions display absolute HFSE depletion relative to primitive mantle. Variations in fluid-mobile LILE/LILE ratios (e.g.

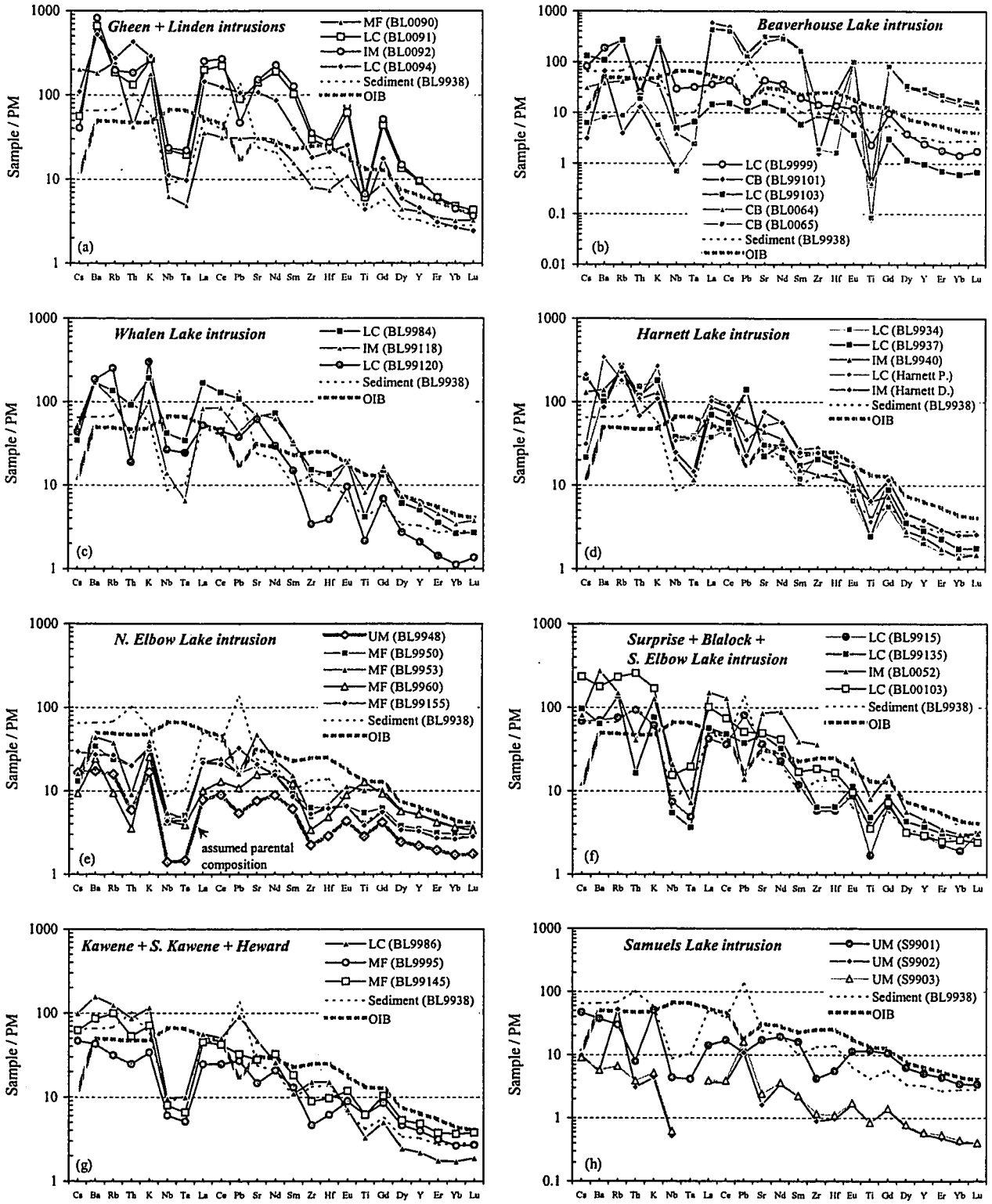

Fig. 2.7. Primitive mantle-normalized incompatible trace element variation diagrams for selected samples from the QAS intrusions and surrounding country rocks. Average OIB is included for comparison. Note that the scale in (b) and (h) extends to values lower than primitive mantle.

Ba/Sr) are generally minor, whereas certain HFSE/HFSE ratios such as Nb/Ta and Zr/Hf extend considerably beyond expected chondritic values. Apart from two samples, primitive mantle-normalized Nb/La is well below unity with the majority having Nb/La ~ 0.2 (cf. 1.006 in chondrite).

Samples from Harnett Lake intrusion, Blalock intrusion and the silicate phases from Beaverhouse Lake intrusion do not show normalized negative Zr and Hf anomalies, whereas all other intrusions and in particular the carbonatite from Beaverhouse Lake intrusion display marked negative Zr and Hf anomalies (Figure 2.7). The carbonatite shows distinct but consistent trace element patterns with larger absolute enrichment in highly incompatible trace elements such as Ba, Sr, Nd and Sm, and more pronounced negative Nb, Ta, Zr and Ti anomalies relative to neighboring elements compared to other samples (Figure 2.7b). These characteristics are interpreted to reflect liquid immiscibility (see Chapter 4).

The Quetico sediments analyzed within this study display incompatible trace element abundances between those of the mafic and leucocratic intrusive rock types, but differ by having lower Ba and Sr contents at equivalent MgO, positive Pb, Th, Zr and Hf anomalies in primitive mantle normalized diagrams and less fractionated heavy rare earth (HREE) patterns. They further contain relatively high concentrations of compatible trace elements (Ni, Cr, Sc and V) compared to leucocratic intrusive rocks, which reflects a source with a high proportion of material supplied from mafic or ultramafic rocks.

Prior to interpreting major and trace element geochemical data it is important to consider the possible effect of hydrothermal alteration on elements, which are easily

mobilized, such as most LILE and Na_2O. Consistent patterns in multi-element diagrams for each intrusion suggest no significant mobilization.

2.7.2.2. Rare earth element (REE) variations

Representative REE data are illustrated in chondrite-normalized diagrams in Figure 2.8. Most samples have steep REE distribution patterns with a distinct break in the slope around Nd and slightly negative Eu anomalies. The magnitude of Eu/Eu* varies between 0.7 and 1.0 (average 0.89) and shows no correlation with weight percent MgO. Within single intrusions, REE patterns are generally parallel and vary only in absolute abundances relative to chondrite. A few exceptions occur in Whalen Lake intrusion and in Gheen intrusion, where patterns for different samples cross, leading to varying LREE / HREE ratios. This feature cannot be produced by different extents of mantle melting or by fractional crystallization of a common mineral assemblage and thereby implies additional complexities such as variable proportions of crustal contamination, magma mingling or mixed mantle sources.

Samples from Blalock intrusion and to a lesser extent North Elbow Lake intrusion are characterized by flat HREE patterns, indicating no major role for garnet as a fractionating or residual phase. The other intrusions show strong fractionation of middle REE (MREE) relative to HREE [Dy/Yb_N up to 3.3] indicating that they were generated at least partly in the presence of residual garnet or reflecting derivation from a metasomatized mantle source. Overall, the REE patterns become steeper with differentiation, which can be explained as a combination of decreasing degrees of partial melting and an increasing

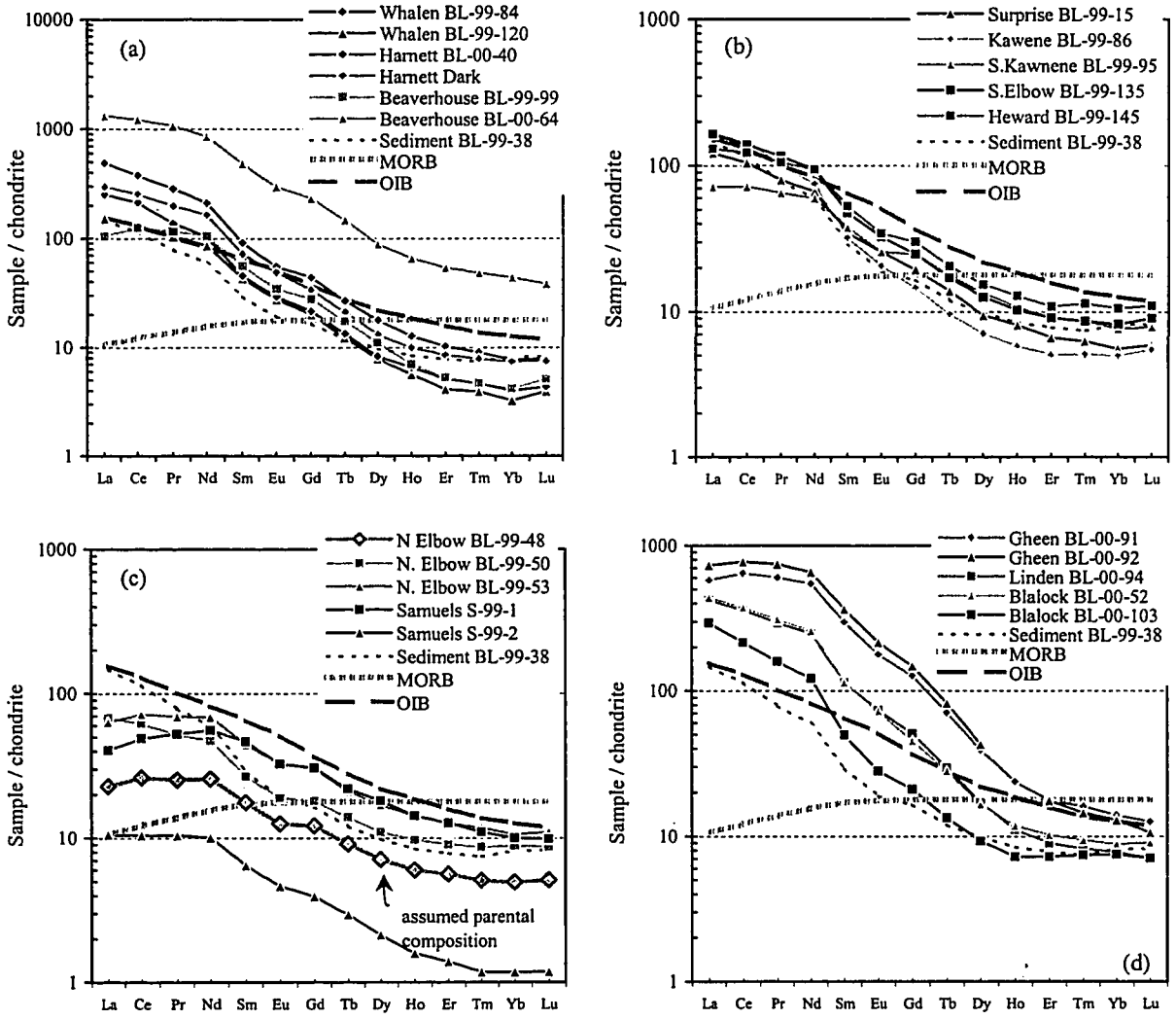

Fig. 2.8. Chondrite-normalized REE variation diagrams for selected samples from the QAS intrusions and surrounding country rocks. Note that each diagram contains data from more than one intrusion. Normalizing factors from Sun & McDonough (1989).

proportion of garnet in the source, where the latter presumably is a consequence of increase in the depth of melting. Total REE contents generally increase with differentiation until MgO equals ~ 3 wt % and decrease at lower MgO contents.

2.8. Isotope variations

2.8.1. Nd isotopic variations

Age corrected $^{143}Nd/^{144}Nd$ of a representative suite of samples show limited variability and define a range between 0.50916 and 0.50928 corresponding to $\epsilon Nd(t)$ between 0.0 and +2.3. There is no significant difference in Nd isotopic composition between mafic and leucocratic samples. All analyzed samples have Nd model ages older than their crystallization age (T_{DM} = 2704 - 2911 Ma). The data are illustrated in Figure 2.9a and b and listed in Table 2.4.

Henry et al. (1998) report $\epsilon Nd(t)$ between -0.1 and +1.1 for eight sediment samples from the Quetico belt and Vervoort et al. (1999) report $\epsilon Nd(t)$ of -0.5 for one sediment sample. Thus the country rocks extend to marginally more enriched Nd isotopic compositions relative to the QAS intrusions, although there is significant overlap. The Nd isotopic ratios of the QAS intrusions lie in the range of previously published data from late Archean alkaline intrusions in the western Superior Province [$\epsilon Nd(t)$ between ~ +0.1 and +3.1, Stevenson, 1999; Bédard and Ludden, 1997; Henry et al. 1998] and overlap with data from the nearby Poohbah Lake intrusion [ϵNd = +0.8, Tilton and Bell, 1994] but Nd model ages are somewhat older than for alkaline intrusions of similar age from

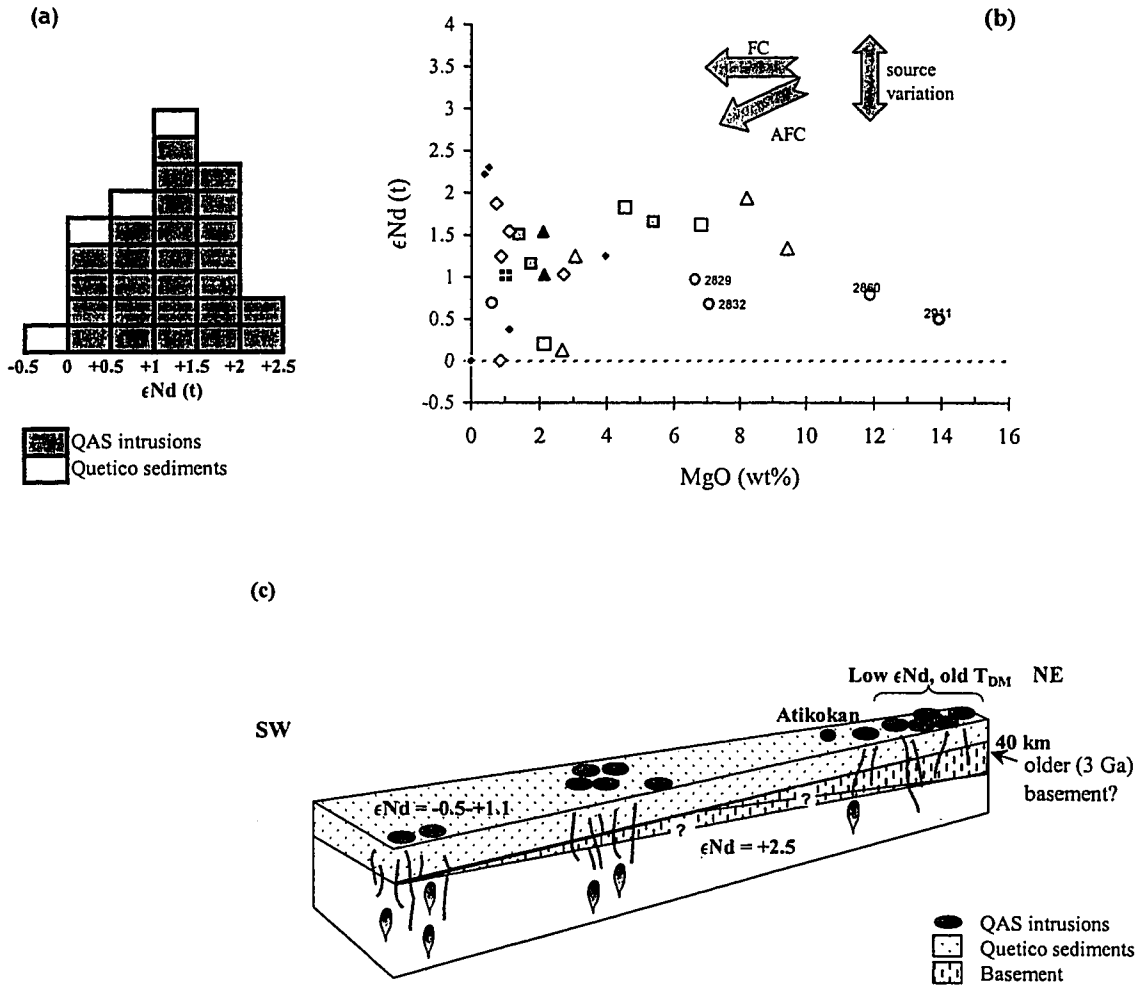

Fig. 2.9. (a) Histogram of εNd(t) for QAS intrusions and the Quetico sediments. Sediment isotope compositions from Henry et al. (1998) and Vervoort et al. (1999). (b) Diagram of initial $^{143}Nd/^{144}Nd$ expressed as εNd(t) *vs*. MgO (wt %) used to assess the role of crustal contamination. Symbols as in Figure 2.6. The numbers next to samples indicate depleted mantle model ages in Ma. Schematic vectors indicate the effect of source variation and trajectories of chemical change during fractional crystallization (FC) and assimilation + fractional crystallization (AFC), assuming a contaminant compositionally similar to the Quetico metasediments. CHUR = chondritic uniform reservoir (c) Simplified cross section of the central Quetico subprovince with QAS intrusions (corresponds to SW – NE part of Figure 2.1). The intrusions in the northeastern part of the province have relatively low εNd combined with old Nd model ages, which may suggest the presence of older basement beneath the sediment pile. Other intrusions show no or only minor contribution from such a source.

Table 2.4. Whole-rock Sm-Nd isotope ratios of the QAS intrusions

Sample #	IN	Sm[a] (ppm)	Nd[a] (ppm)	$^{147}Sm/^{144}Nd$	$^{143}Nd/^{144}Nd$[b]	$^{143}Nd/^{144}Nd_i$	$\epsilon Nd(T)$[c]	$f_{Sm/Nd}$[d]	T_{DM}[e]
BL0094	LN	18.07	112.61	0.09703	0.510954	0.509238	1.54	-0.51	2757
BL0095	LN	4.86	23.57	0.10141	0.511008	0.509213	1.03	-0.48	2797
BL0087	GN	5.25	22.43	0.14155	0.511734	0.509228	1.34	-0.28	2824
BL0090	GN	8.56	39.95	0.12964	0.511554	0.509259	1.94	-0.34	2732
BL0091	GN	42.42	240.85	0.10645	0.511051	0.509167	0.13	-0.46	2881
BL0092	GN	60.90	348.41	0.10563	0.511093	0.509223	1.25	-0.46	2785
BL9934	HAR	4.90	26.73	0.11037	0.511112	0.509160	0.00	-0.44	2904
BL9937	HAR	6.89	38.79	0.10449	0.511071	0.509255	1.87	-0.47	2787
BL0044	HAR	8.95	54.04	0.10003	0.510991	0.509223	1.24	-0.49	2784
Harnett D.	HAR	10.85	70.06	0.09357	0.510867	0.509213	1.03	-0.52	2794
Harnett P.	HAR	11.21	70.90	0.09557	0.510927	0.509238	1.54	-0.51	2758
BL9999	BHL	8.16	43.96	0.11226	0.511164	0.509179	0.37	-0.43	2875
BL99103	BHL	2.38	13.47	0.10607	0.511153	0.509278	2.30	-0.46	2697
BL99104	BHL	5.79	29.69	0.11798	0.511310	0.509224	1.25	-0.40	2801
BL0065	BHL	72.46	416.86	0.10505	0.511131	0.509274	2.22	-0.47	2704
BL9929	WHL	12.60	70.80	0.10757	0.511149	0.509245	1.66	-0.45	2749
BL99121	WHL	10.45	63.18	0.10005	0.511006	0.509237	1.51	-0.49	2761
BL0033	WHL	11.66	74.17	0.09500	0.510899	0.509219	1.16	-0.52	2785
BL99135	SEL	7.30	42.70	0.10334	0.511022	0.509195	0.68	-0.47	2832
BL9950	NEL	4.87	23.57	0.12484	0.511408	0.509201	0.79	-0.37	2860
BL0017	NEL	0.41	2.41	0.10601	0.511070	0.509196	0.69	-0.46	2835
BL0052	BL	17.45	114.76	0.09192	0.510870	0.509240	1.62	-0.53	2745
BL0077	BL	7.74	49.07	0.09535	0.510941	0.509253	1.83	-0.52	2731
BL00103	BL	7.31	56.31	0.08606	0.510694	0.509171	0.20	-0.56	2843
BL9915	SPL	5.11	28.52	0.10820	0.511125	0.509212	1.02	-0.45	2810
BL99145	HW	7.61	40.90	0.11252	0.511194	0.509209	0.97	-0.43	2829
BL9995	SKL	5.39	24.83	0.13130	0.511507	0.509185	0.50	-0.33	2911

[a] Isotope dilution determinations

[b] $^{143}Nd/^{144}Nd$ analyses are measured to ± 0.0030% (2σ) or better, except for sample BL99145, which has an error of 0.0045

[c] Calculated at U-Pb crystallization age where available and otherwise assuming 2680 Ma

[c] Uncertainty is ± 1

[d] $f_{Sm/Nd} = [(^{147}Sm/^{144}Nd_{sample})/(^{147}Sm/^{144}Nd_{CHUR})]-1$

[e] Mantle evolution curve from Nelson and DePaolo (1985) defined as $\epsilon_{Nd}(t) = 0.25t^2 - 3t + 8.5$

adjacent subprovinces (data sources: Bédard and Ludden, 1997; Tomlinson et al. in press) and there is a tendency towards lower Nd isotope values at equivalent MgO relative to samples from the Wabigoon subprovince, presumably a consequence of contamination by the more enriched country rocks within the Quetico belt. Tomlinson et al. (in press) reported T_{DM} and U-Pb ages of 2.8-3.1 Ga from the south-central part of the Wabigoon subprovince, indicating the presence of an older crustal fragment in the area. T_{DM} values up to 2911 Ma for QAS samples may reflect a contribution from such a component. Older Nd model ages are mainly from intrusions in the northeastern part of the subprovince. A possible model to account for this feature is shown schematically in Figure 2.9c.

In general, correlations between ϵNd and incompatible trace element concentrations are limited as are correlations between ϵNd and LILE/HFSE and LILE/LREE ratios (Figures not shown). Taken as a whole, there is no clear correlation between ϵNd and MgO, although a faint positive correlation exists between 8 and 1 wt % MgO (Figure 2.9b) which may imply contamination by the more enriched Quetico sediments in some way linked to fractionation. There is no obvious correlation between ϵNd and SiO_2.

Although total variation in Nd isotopic composition is restricted it does exceed analytical uncertainty, so the range in data either requires some input from a crustal component or the spread is related to source heterogeneity. Even the most depleted ϵNd value of +2.3 is more enriched than published estimates of 2.68 Ga depleted mantle values within the Superior Province (e.g. Shirey and Hanson, 1986). The fact that all samples are dispersed to more enriched compositions rules out direct derivation from a depleted mantle source and requires some input from long-term LREE-enriched material.

Arc rocks generally have low Nd isotopic signatures compared to depleted N-MORB, which is usually interpreted to reflect a contribution from subducted sediment (e.g. Hawkesworth et al., 1991) or related to the presence of enriched OIB-type material in the mantle wedge (e.g. Vroon et al., 1993).

2.8.2. Pb isotopic variations

Initial Pb isotope ratios of leached alkali-feldspar separates range between $^{206}Pb/^{204}Pb$ = 13.090-13.464, $^{207}Pb/^{204}Pb$ = 14.590-14.815 and $^{208}Pb/^{204}Pb$ = 33.433-33.993. In all samples the leachates are more radiogenic than the residues, which implies the presence of labile radiogenic Pb resulting from *in situ* decay of U and Th, so even after rigorous leaching the residues should still be considered maximum estimates of initial values. The residues were corrected for U decay based on U contents determined by isotope dilution. Pb isotope data is presented in Table 2.5 and illustrated in Figure 2.10a. The data plot in a narrow field on or slightly above the Stacey-Kramers crustal evolution curve at cà 2750 Ma, which is significantly older than their crystallization age as determined by U-Pb on zircon (ca 2680). The small dispersion in Pb isotope ratios results in essentially horizontal correlations between $^{207}Pb/^{204}Pb$ and fractionation index (MgO) (Figure 2.10b) and the data plot close to the field for crustal Pb from the western Superior Province from Henry et al. (1998) and Carignan et al. (1995). The data are largely similar to published Pb isotope data from other alkaline intrusions within Quetico subprovince and surrounding greenstone belts, which also display mainly crustal values (Stevenson et al. 1999; Henry et al., 1998; Tilton and Bell, 1994). This could be the result of crustal

Table 2.5. Pb isotopes of alkalifeldspar separates from the QAS intrusions

Sample #	a	$^{206}Pb/^{204}Pb$	$^{207}Pb/^{204}Pb$	$^{208}Pb/^{204}Pb$
BL0095	R	13.434	14.590	33.433
BL0095	L	14.876	15.047	34.719
BL0091	R	13.464	14.613	33.513
BL0091	L	14.788	14.397	34.669
BL9939	R	13.293	14.815	33.993
BL9939	L	15.451	18.053	37.002
BL99103	R	13.342	14.631	33.938
BL99103	L	16.191	22.233	36.934
BL99120	R	13.090	14.599	33.303
BL99120	L	15.798	19.747	36.171

a: R = residue, L = leachates

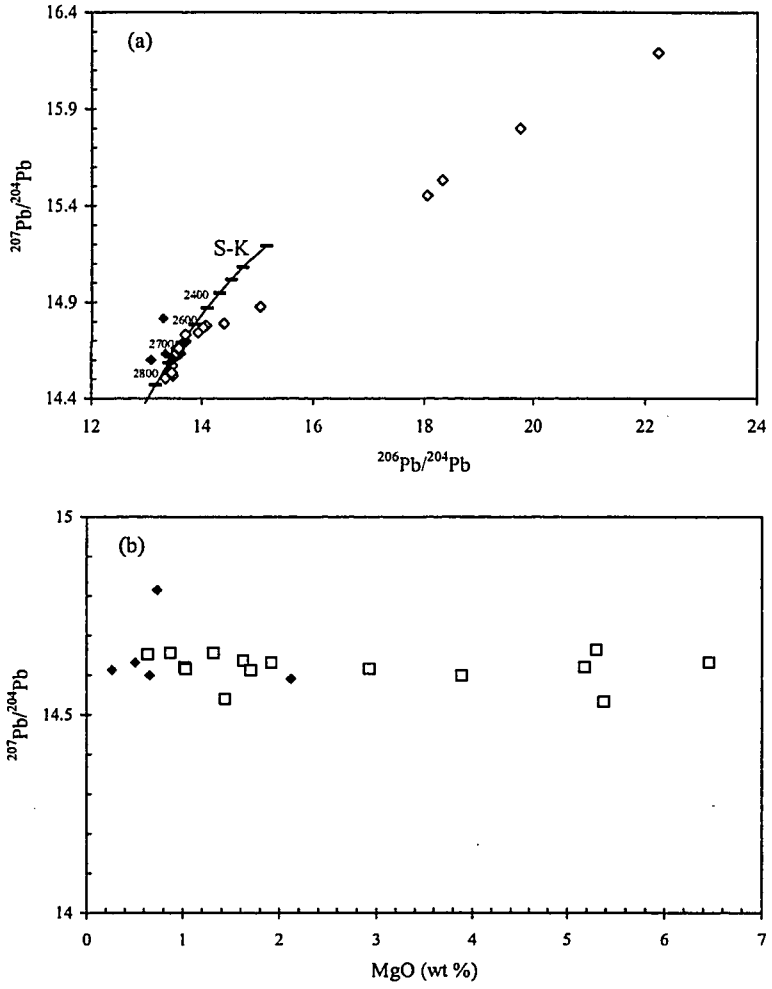

Fig. 2.10. Pb isotope ratios for feldspar separates from the QAS intrusions and late Archean complexes from surrounding subprovinces: (a) $^{207}Pb/^{204}Pb$ *vs*. $^{206}Pb/^{204}Pb$ including a portion of the Stacey-Kramers crustal evolution curve (Stacey and Kramers, 1975). Filled symbols indicate data from this study, black diamonds are initial Pb isotope data, grey squares are leachates; open diamonds, data from Henry et al. (1998), Tilton and Bell (1994), Stevenson et al. (1999) and Carignan et al. (1993). (b) $^{207}Pb/^{204}Pb$ vs. MgO. Filled symbols indicate data from this study; open squares, Stevenson et al. (1999).

contamination in the form of AFC as proposed by Stevenson et al. (1999). Alternatively, enriched Pb isotopic signatures could be ascribed to inheritance from a subduction-modified mantle source formed by aqueous fluid transport of sediment Pb into the mantle wedge. Such fluids are known to selectively enrich Pb relative to Nd. These models are difficult to distinguish geochemically, because no Pb isotope data are available for the Quetico sediments, and because the tight range in Pb isotope data shows no significant correlations with fractionation indices or other geochemical parameters.

2.9. Discussion

The intrusions included in this study define a wide compositional range, but are closely related in age and geographic location. Despite compositional diversity, in part related to differing state of differentiation, all intrusions possess a number of characteristic geochemical signatures such as high LILE/HFSE and high LILE/LREE ratios compared to melts from a primitive mantle. These characteristics suggest a common origin and evolution, although each intrusion must have evolved in an independent magma chamber most likely under slightly different pressure and temperature conditions.

Figure 2.11 shows a comparison between the QAS intrusions, Archean sanukitoids from the western Superior Province and modern sanukitoids from the Setouchi belt in Japan. As stated earlier, the composition of the QAS intrusions overlap broadly with these rocks suggesting a similar origin. Enrichment of LILE combined with depletion of HFSE are typical features of Phanerozoic subduction-related magmas and are generally

(a)	QAS intrusions (this study)	Archean sanukitoids1,2,3	Setouchi high-Mg andesite4,5
Age (Ma)	2685 - 2678	~ 2680	12.4 - 14.8
Mg-number	0.77 - 0.26	0.71 - 0.35	0.79 - 0.66
SiO_2 (wt %)	41 - 73	41 - 73	49 - 56
Ni (ppm)	350 - 0	188 - 12	306 - 32
Ce/Yb	24 - 215	39 - 323	13 - 20

[1] Stern et al. (1989), [2] Stern & Hanson (1991), [3] Stevenson et al. (1999),
[4] Shimoda et al. (1998) and references within, [5] Tatsumi & Ishizaka (1982)

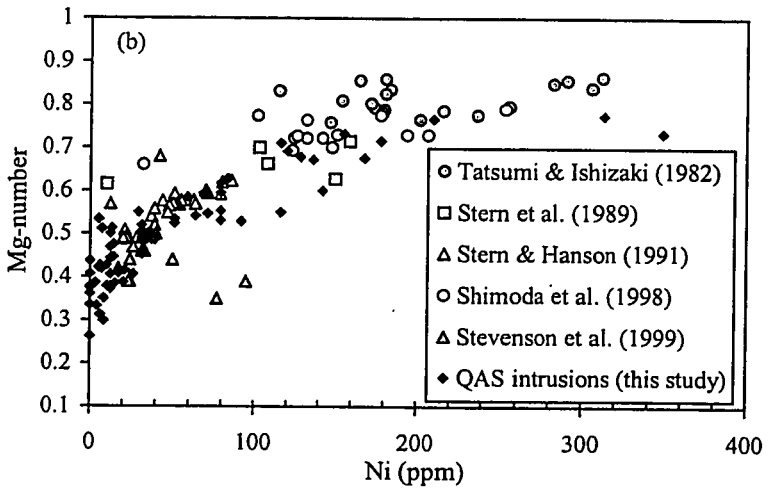

Fig. 2.11. (a) Comparison between QAS intrusions, Archaean sanukitoids and modern sanukites. (b) Ni (ppm) *vs*. Mg-number for QAS intrusions, sanukitoids from the western Superior Province [Data sources: Stern et al. (1989), Stern & Hanson (1981), Stevenson et al. (1999)] and modern sanukites from the Setouchi belt in Japan [Shimoda et al. (1998), Tatsumi & Ishizaka (1982)]. The QAS intrusions overlap with these rocks, but also extent to more evolved compositions. Olivine cumulate samples are not included. Ni-rich QAS samples are lamprophyre dykes.

attributed to addition of metasomatic fluids released by dehydration of subducted oceanic lithosphere to depleted mantle wedge materials (e.g. Gill, 1981; Saunders et al., 1991). Given the relatively high LILE and LREE concentrations and HFSE depletion of the Quetico metasediments, and considering the presence of xenocrystic zircons and high $^{207}Pb/^{204}Pb$ ratios in the intrusive rocks, a critical question is whether the arc signature is inherited from a metasomatized mantle source or reflects crustal contamination with possible addition from the Quetico basement or a combination of these possibilities. The low Mg-numbers and the slightly more enriched Nd isotopic compositions of the country rocks preclude their being the main source of the intrusive complexes.

In the following discussion, several models are evaluated to account for the compositional diversity observed among the QAS intrusions. Judging from major and compatible trace element variations much of the geochemical heterogeneity is consistent with broad control by fractional crystallization, which may have been accompanied by crustal contamination. The presence of spectacular mingling textures within many intrusions combined with disequilibrium textures in clinopyroxene further implies the influence of mixing or replenishment processes.

2.9.1. Fractional crystallization

2.9.1.1. Qualitative constraints

Decrease in abundances of MgO, Ni, Cr and Sc of whole-rock samples combined with decreasing Mg-numbers of ferromagnesian minerals from mafic to leucocratic units

suggest that fractional crystallization played an important role in controlling major element variations within the QAS intrusions. This is also indicated by linear trends in log log plots based on compatible trace elements such as Ni and Cr. When plotted against a fractionation index, here defined as MgO, a number of major and trace elements show distinct inflection points, which rule out simple mixing as the cause of the geochemical variations, and indicate the onset of fractionation of various mineral phases e.g. TiO_2 (Fe-Ti oxide), CaO (clinopyroxene), P_2O_5 (apatite) (Figure 2.6) and Sr (feldspar) (Figure 2.12). The first order observations can be explained qualitatively by sequential fractionation of common ferromagnesian minerals, joined later by Fe-Ti oxides, feldspar and apatite. An exception to the general trend is samples from the Gheen intrusion for which most elements continuously increase with differentiation in accordance with accumulation of alkali feldspar and apatite.

The transition elements Ni, Cr and Sc decrease abruptly with differentiation, accompanied by a strong decline in CaO/Al_2O_3 throughout the differentiation interval. The trends suggest accumulation of olivine and clinopyroxene in samples with MgO > 14 wt % and extensive fractionation of clinopyroxene ± olivine ± amphibole during later stages of differentiation. Samples from Samuels Lake intrusion are characterized by very high MgO concentrations (23-24 wt %) combined with high CaO/Al_2O_3, moderate Cr and extreme Ni concentrations (3900 - 4200 ppm) suggesting control by olivine accumulation. As olivine has very low concentrations of incompatible trace elements its presence as a cumulative phase results in a diluting effect, which decreases the concentration of all incompatible trace elements, but does not affect trace element ratios. CaO/Al_2O_3 declines abruptly until MgO ~ 5-6 wt % and decreases more gradually for

lower MgO concentrations. Since CaO/Al_2O_3 primarily measures the amount of clinopyroxene relative to other phases in the fractionating assemblage (e.g. Presnall et al., 1978; Mahood and Baker, 1986) the trend defined by the Quetico samples indicates an initially large proportion of fractionating clinopyroxene, followed by a fractionating assemblage involving less clinopyroxene. Even the most evolved samples exhibit a steady decline in Ni, Cr and Sc with MgO, implying that clinopyroxene was a fractionating mineral throughout the differentiation interval, which is consistent with its modal presence. A major role for amphibole fractionation is unlikely in the early stages of differentiation despite its common modal occurrence, because amphibole separation results in depletion in MREE relative to HREE, which is not observed. Also, Y and HREE increase with differentiation for the mafic to ultramafic samples, a trend which cannot be explained by substantial hornblende extraction. Steadily decreasing TiO_2, Fe_2O_3 and V for MgO concentrations lower than 5-6 wt % necessitate fractionation of an Fe-Ti oxide and indicate high oxygen fugacity of the parental magma.

Al_2O_3 strongly increases with decreasing MgO until MgO ~ 8 wt %, which indicates that plagioclase was not an important fractionating mineral phase until the derivative liquids approached high Al_2O_3 concentrations (Figure 2.6c). Initial increase in Sr contents also implies that plagioclase was subordinate to ferromagnesian minerals in the crystallization sequence (Figure 2.12). Suppression of early plagioclase crystallization may result from high initial water content of the magma, which contracts the liquidus field of plagioclase (e.g. Sisson and Grove, 1993; Gaetani et al., 1993). Sr and Ba behave incompatibly until MgO ~ 3 wt %, but show a strong decline at lower MgO contents, consistent with extraction of alkali-feldspar and/or plagioclase and apatite (Figure 2.12).

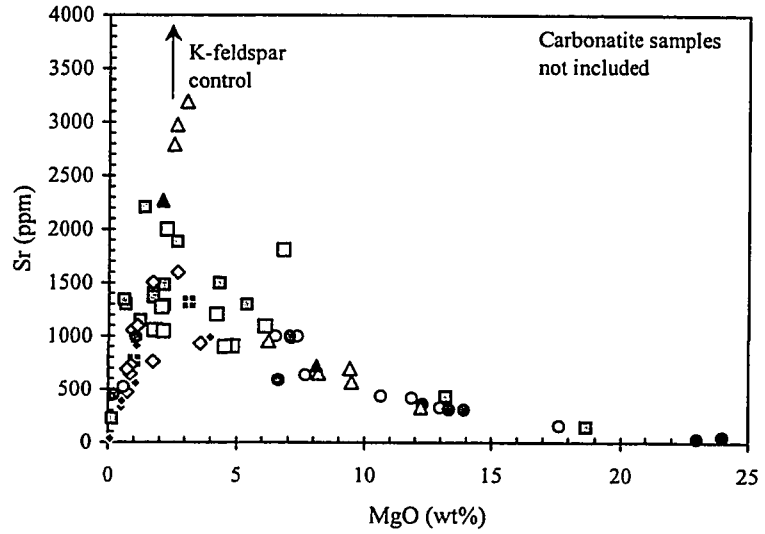

Fig. 2.12. Mg (wt %) *vs*. Sr (ppm) for samples < 2.5 wt % MgO. Symbols as in Figure 2.6.

A large proportion of alkali-feldspar must be removed from the liquid in order to generate the decrease in Sr and Ba, and a high degree of fractionation is required to deplete the melt from very high concentrations of Sr and Ba within intermediate samples to very low concentrations in the most evolved samples. Apatite joined the fractionating assemblage at MgO ~ 3 wt % as indicated by decreasing P_2O_5, Y and Sr. Decreasing ΣREE for low MgO contents underlines the importance of alkali amphibole ± titanite ± apatite fractionation at advanced stages of differentiation. Compatibility of Zr and Hf at low MgO contents is likely to reflect incorporation of these elements in alkaline clinopyroxene and / or amphibole in highly evolved liquids, rather than indicating zircon fractionation.

2.9.1.2. Quantitative constraints

For quantitative modeling of fractionation trends the sample set has been divided into two sections: one comprising the ultramafic to mafic samples and the other containing the intermediate to leucocratic rock types. The reason for this division is twofold: (1) Mineral chemistry of clinopyroxene suggests polybaric differentiation and shows that mafic and leucocratic complexes (and mafic and leucocratic units within a single intrusion) differentiated at different levels in the crust and (2) The inflection point observed for most oxides at ~ 5 wt % MgO indicates a significant change in fractionating mineral phases and proportions at this stage.

2.9.1.2.1. Mafic to ultramafic samples

The mafic to ultramafic samples differentiated at relatively high pressure (~ 1.0-1.5 GPa) as suggested by the mineral chemistry of clinopyroxene (Figure 2.4). At this depth, replenishment of the magma chamber by primitive magma occurred concomitantly with fractional crystallization, as indicated by zoning textures in clinopyroxene. Such mixing events are likely to have caused deviations from the liquid line of descent and imply that closed system fractional crystallization models are an oversimplification. The trace elements Zr, Ba and Sr behave perfectly incompatibly (assuming K_D of zero) for MgO contents above 5 wt %, which suggests either a high-pressure (plagioclase-absent) fractionating assemblage or that these elements were buffered by repeated injection of new magma. Small negative Eu anomalies in some of the most magnesian samples may imply extraction of plagioclase in the early stages of differentiation, but could also be attributed to residual plagioclase in the source of metasomatic fluids or melts.

In order to evaluate the proposed fractionating assemblage simple mass balance calculations by least-squares major element calculations and trace element modeling were undertaken. The modeling was performed in multiple-steps to allow for changes in the fractionating assemblage and mineral chemistry and carried out using both observed mineral assemblages and assemblages predicted from experimental work. The quality of the model is measured by the sum of squares of the residuals (R^2), where $R^2<1$ is considered acceptable.

Most experimentally determined phase proportions at high pressure include mainly clinopyroxene, olivine and plagioclase. Experiments by Grove et al. (1992) at 1.0 GPa on

a high-Mg tholeiite yielded a fractionating mineral assemblage of 0.55 cpx - 0.32 ol - 0.13 plag, and Thy (1991) determined 0.47 cpx - 0.35 ol - 0.18 plag on mildly alkaline basalts at 1.0 - 1.25 GPa. Sisson and Grove (1993) reported a fractionating assemblage of 0.4 cpx - 0.3 ol - 0.29 plag - 0.01 Fe-Ti, which differs slightly from other experimentally determined high-pressure assemblages in that Fe-Ti oxide is a fractionating phase, but may be more appropriate for the QAS intrusions, which exhibits strong decreases in Fe and Ti with differentiation. The experimentally determined phase proportions are in overall agreement with qualitative observations, but no acceptable fits were obtained with least squares modeling, despite attempting a large number of models. Lack of support from least squares modeling for the mafic to ultramafic samples as representative of parental magma compositions probably reflects the interplay of several processes such as polybaric fractionation, cumulative processes, magma replenishment and crustal contamination, rather than contradicting the quantitative constraints on fractionation trends.

2.9.1.2.2. Leucocratic samples

The intrusions dominated by intermediate to leucocratic rock types differentiated at shallow levels in the crust as indicated by clinopyroxene compositions. The lower pressure significantly changed the sequence, composition and cotectic proportions of the fractionating mineral phases. At low pressures, feldspar becomes the first and dominant liquidus phase to crystallize in derivative liquids that are enriched in alumina and alkalis. In contrast to mafic and ultramafic samples, mass balance calculations by least squares

modeling produced good results for individual intrusions when modeling small fractionation steps. For leucocratic samples typical mineral compositions and fractionating mineral assemblages approximately equal to the observed petrographic assemblages were used in modeling. When considering large fractionation intervals or trying to link samples from different intrusions the sum of squared residuals increased significantly, indicating small differences in fractionation trends between intrusions. Sample BL0095 from Linden intrusion can be modeled by extracting 5 % of the observed mineral assemblage (cpx, ksp, plag, bio, ap, mt) from sample BL0094, which gives minimal deviations between observed and calculated compositions with ΣR^2 equal 0.02. A small degree of intersample fractionation for the Linden intrusion is confirmed by trace element concentrations, in particular limited differences in Sr and Ba contents.

The strong decrease in Sr with decreasing MgO observed for leucocratic samples is consistent with a high proportion of plagioclase and / or alkali-feldspar in the fractionating assemblage (Figure 2.12). Corresponding decline in Ba with decreasing MgO indicates that alkali-feldspar dominated as a fractionating mineral, while plagioclase was subordinate, an inference which is collaborated by a higher modal proportion of alkali-feldspar relative to plagioclase in evolved samples. Preceding from sample BL0095 the strong decrease in Ba and Sr can be modeled adequately by extraction of various proportions of alkali-feldspar and plagioclase along with minor amounts of other minerals, which requires between 30 and 55 % fractional crystallization (Fig. 2.13).

Numerous attempts were made to link the microgranular, mafic enclaves, which occur in many intrusions (Figure 2.3d) with the respective leucocratic host rocks by mass

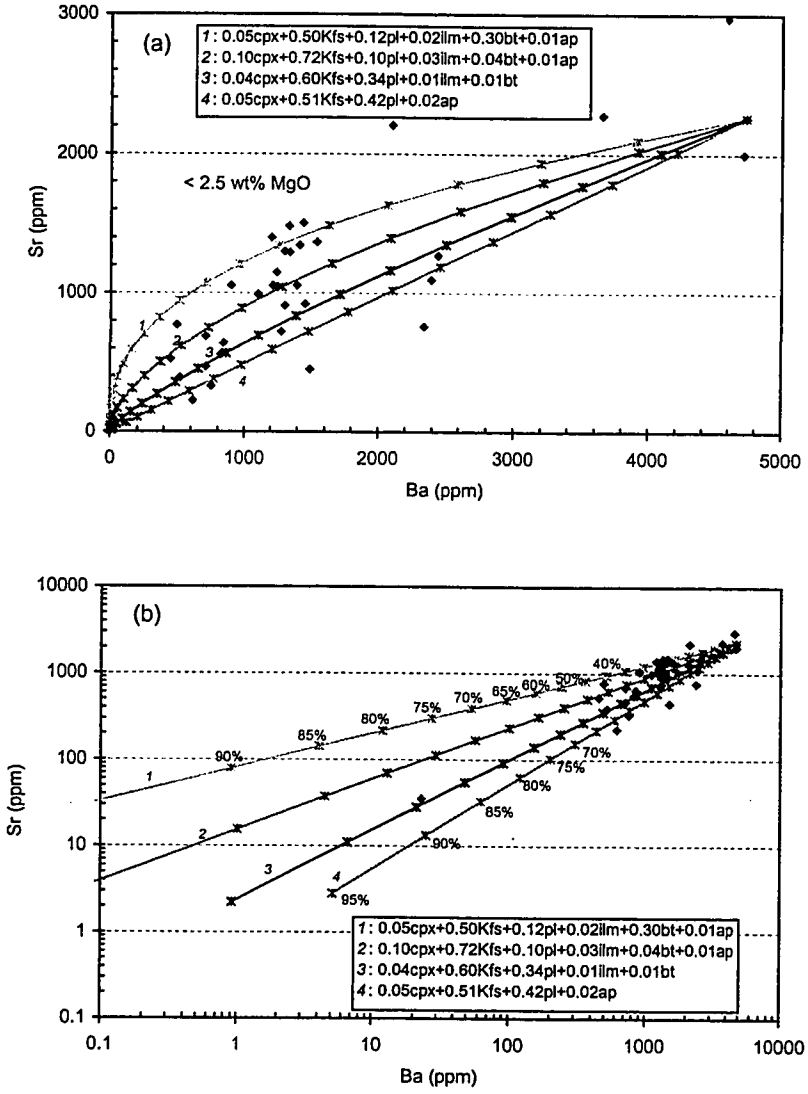

Fig. 2.13. (a) Diagram of Ba against Sr for samples < 2.5 wt % MgO compared with fractional crystallization models, which show the effect of Rayleigh fractionation of varying proportions of the main rock-forming minerals: (cpx) clinopyroxene, (Kfs) K-feldspar, (pl) plagioclase, (bt) biotite, (ilm) ilmenite and ap (apatite). Numbers in italic denote fractionating assemblages as indicated in the text box. Path 2 corresponds to the mineral assemblage obtained by least-squares modeling of major elements. Sample BL0095 is used as parental magma and tick marks correspond to 5%. Numbers next to tick marks correspond to degrees of fractional crystallization. (b) Similar to (a) but with logarithmic scales to illustrate degrees of fractional crystallization needed to produce the most differentiated samples. Partition coefficients from compilation of Rollinson (1993) and from Edward & Griffin (1994), Watson & Green (1981) and Paster et al. (1974).

balance calculations, but these models were generally unsuccessful. Leucocratic samples from most intrusions can be modeled satisfactorily by least squares, when ΣR^2 of maximum 1.0 is considered acceptable, but they give slightly higher residuals for SiO_2 and in some cases CaO relative to other elements. The modes improve substantially if accumulation of small amounts of quartz is included in the computation, but it seems more reasonable to include assimilation of small amounts of the local Quetico sediments, as these rocks are characterized by higher SiO_2 and lower CaO for equivalent MgO relative to the intrusive rocks (Figure 2.6a and g) (discussed further below).

2.9.2. Crustal contribution

2.9.2.1. Qualitative constraints

Interaction between intrusive rocks and the metasedimentary country rocks is evident from field observations of partly hybridized sediment rafts within a number of intrusions and is further constrained by the presence of older xenocrystic zircons within Harnett Lake intrusion (B. Lassen and J. Perresini, unpublished data, 2002). The question therefore is not whether contamination occurred, but merely whether it occurred to a sufficient extent to explain the overall pattern of the isotopic and elemental variations within the intrusive complexes. The heat introduced by the emplacement of the magmas into the crust is likely to have been at least partly responsible for the widespread mingling textures observed along the margins in some intrusions. Support for crustal contamination comes from Nd isotope ratios, Nd model ages and in particular Pb isotope ratios, which

cannot be produced by fractional crystallization alone, but requires either mixing with isotopically contrasting material or source heterogeneity. The range in Nd isotope composition of the sediments precludes definition of a simple isotopic end-member for mixing calculations.

The exact amount of crustal contamination is difficult to evaluate and is further not likely to be similar in all intrusions. Compared to most of the intrusive rocks, multi-element patterns for the country rocks peak at Pb and display positive Th, Zr and Hf anomalies (Figure 2.7). Sample BL00103 from Blalock intrusion displays positive anomalies for Th, Zr and Hf and undepleted Pb thereby resembling the local sediments (Figure 2.7f). It is also characterized by a Nd model age of 2843 Ma. Sample BL0052, also from Blalock intrusion, has deep negative troughs for Th and Pb, in strong contrast to the sediment samples (Figure 2.7f) and is characterized by a younger Nd model age, suggesting large differences in amount of contamination within a single intrusion. Judging from multi-element diagrams and Nd model ages, contamination appears to have been important in the Kawene, Heward, Linden, Surprise and Harnett Lake intrusions.

2.9.2.2. Quantitative constraints

To place quantitative constrains on the style and degree of crustal contamination Figure 2.14 plots ϵNd versus Th/Yb. The advantage of this plot is that Th and Yb are relatively immobile in subduction fluids, and high Th/Yb is likely to be controlled by the input of sediment or sediment melt in the petrogenesis. The broad negative correlation indicated by the arrow could therefore imply progressive crustal contamination. In Figure

2.14a are also shown calculated assimilation and fractional crystallization (AFC) curves (DePaolo, 1981) and a grid of mixing curves (mixing equation of Langmuir, 1978) using sample BL9938 as crustal end-member. Fine lines are mixing curves, dashed lines contour degree of mixing. Because of the uncertainties surrounding the composition of the parental magma and the contaminant, the models do not yield definite results. To account for the range of Nd isotope composition of the country rocks (see section 7.1) AFC and mixing trajectories are shown for country rock end-members with ϵNd equal to -0.5, 0, +0.5, +1 and +1.1, but any composition within that range is possible. For AFC modeling the fractionating assemblage is 35 % plagioclase, 30 % K-feldspar, 25 % clinopyroxene, 5 % amphibole and 5 % ilmenite, but the position of the calculated AFC curves is almost insensitive to variations in the mineral extract as long as it does not include phases which strongly fractionate Yb such as garnet. Higher r values result in increasing Th/Yb, but has little effect on Nd isotope ratios. Samples characterized by low Th/Yb follow the model curves in support of an AFC or mixing model (Figure 2.14a) but it is also clear from the figure that bulk addition of country rock fails to explain the trend towards high Th/Yb. This holds true even for the improbable case of AFC where the ratio of the mass assimilated to the mass crystallized r exceeds 1.0 (not illustrated) and implies that an additional process must be controlling the Th/Yb budget.

Partial melts of sediments have significantly more fractionated trace element ratios than their protoliths, so the trend towards high Th/Yb could result from assimilation in the form of an anatectic melt rather than bulk crustal addition. Figure 2.14b and c illustrates a grid of mixing between the initial magma and two crustal end-members that correspond to 30 % and 10 % batch partial melting of sediment sample BL9938. Specific

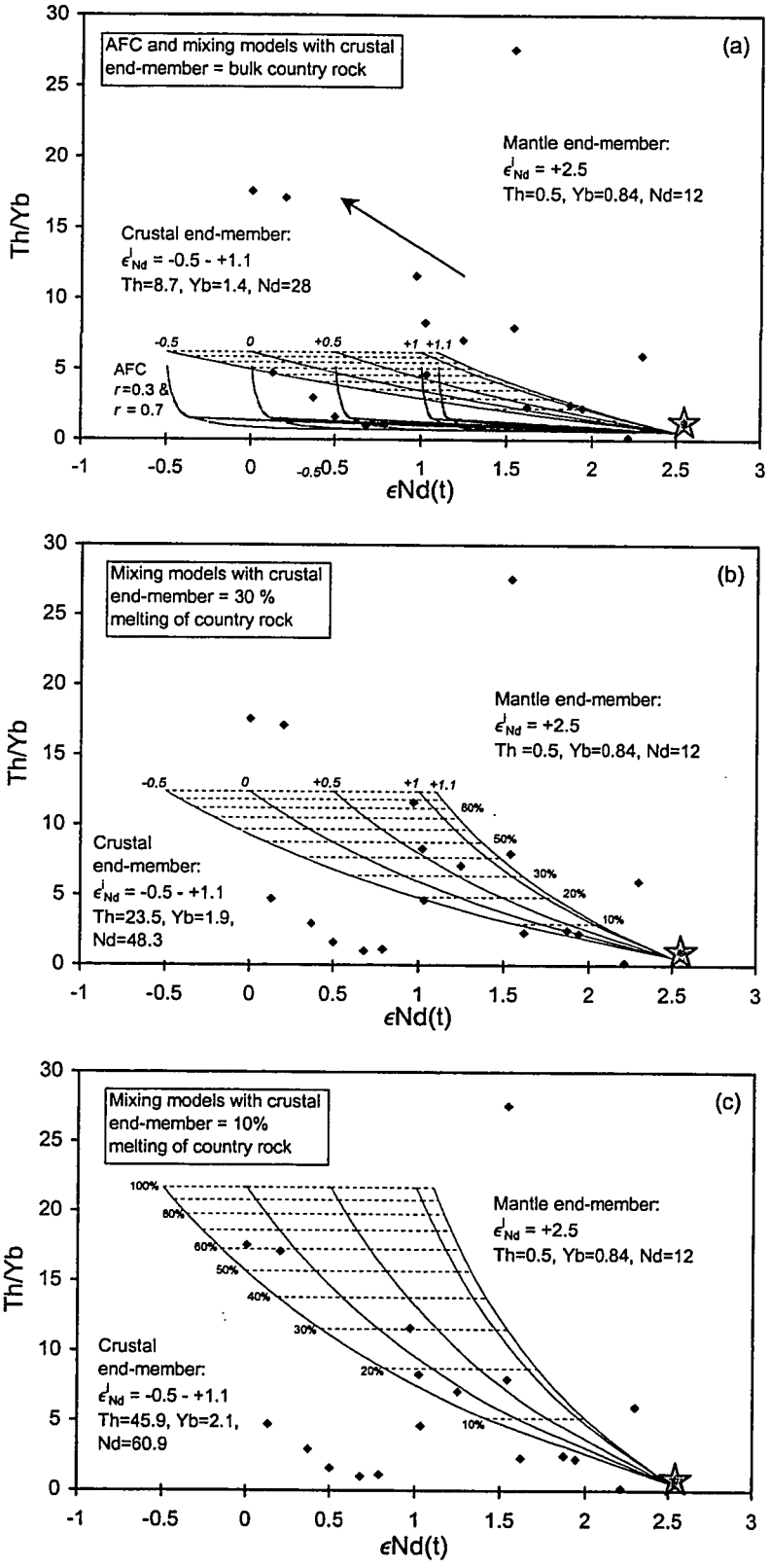
AFC and mixing models with crustal end-member = bulk country rock
(a)
Mantle end-member:
ϵ^{i}_{Nd} = +2.5
Th=0.5, Yb=0.84, Nd=12
Crustal end-member:
ϵ^{i}_{Nd} = -0.5 - +1.1
Th=8.7, Yb=1.4, Nd=28
-0.5
0
+0.5
+1
+1.1
AFC
r=0.3 &
r = 0.7
Th/Yb
εNd(t)
Mixing models with crustal end-member = 30 % melting of country rock
(b)
Mantle end-member:
ϵ^{i}_{Nd} = +2.5
Th =0.5, Yb=0.84, Nd=12
80%
50%
30%
20%
10%
Crustal end-member:
ϵ^{i}_{Nd} = -0.5 - +1.1
Th=23.5, Yb=1.9,
Nd=48.3
Mixing models with crustal end-member = 10% melting of country rock
(c)
100%
80%
60%
50%
40%
30%
20%
10%
Mantle end-member:
ϵ^{i}_{Nd} = +2.5
Th=0.5, Yb=0.84, Nd=12
Crustal end-member:
ϵ^{i}_{Nd} = -0.5 - +1.1
Th=45.9, Yb=2.1,
Nd=60.9

Figure 2.14.

Fig. 2.14. Plots of ϵNd against Th/Yb for QAS intrusions. The negative trend indicated by the arrow may be explained by crustal contamination. Diagram (a) shows the effect of bulk addition of country rock (sample BL9938) in the form of coupled assimilation fractional crystallization (AFC) (DePaolo, 1981) for *r* values of 0.3 and 0.7. Curves run from 0.95 to 0.05 %, but increments are left out for simplicity. To illustrate the range of Nd isotope composition of the country rocks curves are shown for ϵNd of -0.5, 0, +0.5, +1 and +1.1. Mantle end-member is sample BL9948 assuming ϵNd of +2.5. Crustal extract is 35 % plagioclase, 30 % K-feldspar, 25 % clinopyroxene, 5 % amphibole and 5 % ilmenite. Also shown is a grid for bulk mixing. Fine lines are mixing curves, dashed lines contour degree of mixing. Number at end of curve denotes Nd isotope composition of country rock end-member. Low Th/Yb values are reproduced by AFC and bulk mixing, but require advantaged degrees of differentiation. (b) and (c) show that high Th/Yb can be explained by simple mixing models between a mantle-derived magma and a crustal end-member composed of 30 % and 10 % anatectic melt, respectively, of the country rock. Trace element concentrations of end-members are in ppm. Partition coefficients from compilation of Rollinson (1993).

parameters in the melting process are indicated in the figure text. Mixing is obviously a simplification of the actual process as it does not take into account chemical changes during fractional crystallization, but it can be justified in the present case, because Th/Yb undergoes minimal changes until advanced stages of fractional crystallization and radiogenic isotope ratios remain unchanged. The models assume perfect melt extraction from the country rock and that the contaminant in the molten stage mixes with the mantle-derived magma. The data is reproduced significantly better than by bulk addition. Figure 2.14c shows that addition of a relatively small proportion of anatectic melt can explain most compositions.

In summary, a combination of AFC and digestion of partial melts of the country rocks could produce the isotopic variability within the QAS intrusions. Further quantification of the amount of crustal contamination is not possible given the uncertainties regarding the variability in Nd isotopic composition of the contaminant and trace element evidence for variable amounts of contamination within single intrusions.

2.9.3. Magma mingling / mixing

2.9.3.1. Qualitative constraints

Macroscopic evidence for coexistence of magmas occurs in several intrusions, which raises the possibility that magma mixing accompanied fractional crystallization. In addition to this, Harnett Lake, Whalen Lake, North Elbow Lake, South Elbow Lake, Blalock and Gheen intrusions display clear mingling textures, which are observed in the

field as rounded to sub-rounded microgranular enclaves of various sizes and compositions present both within mafic and leucocratic units (Figure 2.3d and see appendix 1).

Evidence for periodic magma chamber replenishment in the middle to deep crust is observed in high pressure clinopyroxenes from mafic units in the Gheen intrusion, but is restricted to this intrusion. As described in section 5.1 these exhibit distinct zoning patterns in the form of growth zones, interpreted to record open system processes with repeated injection of fresh, less differentiated liquid into the magma reservoirs. The presence of several populations of clinopyroxene with different Mg/Fe ratios within single samples further supports a mixing model. The distinct variation in crystallization pressure inferred for mafic and leucocratic units from single intrusions suggests polybaric clinopyroxene crystallization. High pressure clinopyroxene must have been carried in the magma during ascent.

In typical arc settings, magma ponds at the base of the crust or within the lower crust and is modified by a combination of fractional crystallization, assimilation and recharge or MASH (= mixing, assimilation, storage, homogenization; Hildred and Moorbath 1988) processes. The evidence presented here may suggest that such a MASH setting was present beneath the Quetico crust in the Late Archean. Lack of obvious mixing trends on Harker diagrams (Figure 2.6) either reflects that mixing was subordinate to differentiation by fractional crystallization or that evidence for high pressure replenishment processes has been overwhelmed by subsequent low pressure differentiation signatures.

2.10. Constraints on mantle melting and source compositions

The mafic and ultramafic units have high concentrations of compatible trace elements, such as Ni, Cr and Sc, combined with high MgO and low SiO_2, which rule out substantial modification by crustal contamination. Even primitive samples, including sample BL9948 which is compositionally close to a primary mantle melt, display pronounced negative Nb, Ta and Ti anomalies and are invariably enriched in LILE and LREE relative to primitive mantle. Simple mass balance requires > 25 % bulk crustal addition to a primitive mantle starting composition to reach the LILE concentrations of sample BL9948. Even if crustal material was added in the form of a strongly enriched partial melt, the proportion would have to be substantial, causing considerable enrichment in SiO_2 and thereby resulting in whole rock compositions that were no longer primitive. In addition, noteworthy differences exist between the trace element pattern defined by the country rocks and primitive samples. The latter exhibit negative anomalies at Zr, Hf, Th and Pb (Figure 2.7e), suggesting that these characteristics are not caused by crustal contamination unless the contaminant was not the local Quetico sediments, but the underlying basement for which the composition is not known. Consequently, the LILE and LREE enriched and HFSE depleted nature of the most primitive intrusive rocks is believed to primarily reflect a source characteristic and thereby implies the influence of a metasomatic agent acting on depleted mantle. In modern arcs these characteristics are attributed to mantle wedge fertilization by liberation of LILE-rich fluids and / or small-degree partial melts emanating from the subducting slab. Lack of correlation between Nd isotope ratios and incompatible trace element concentrations, along with time-integrated

depleted Nd isotopic signatures suggest that the metasomatic event occurred not long before melting. Older enrichment events would have permitted development of larger Nd isotopic heterogeneities and dispersion towards more enriched compositions. Since the intrusions are carbonate bearing, the metasomatizing agent appears to have contained a mixture of H_2O and CO_2. The trace element variations of intermediate to leucocratic samples appear to reflect a combination of metasomatic processes and crustal contamination (section 8.3.2). The nature of the metasomatic event is examined thoroughly in an accompanying paper (see Chapter 3).

Estimating the mineral assemblage of the source region is difficult due to the variable enrichment effects caused by subduction processes. In particular, it is difficult to verify whether the high Dy/Yb results from small degrees of melting in the garnet stability field as judged qualitatively from REE diagrams (section 6.2.2) or is inherited from a subduction component. Following the approach of Borg (1997) Figure 2.15 intends to match calculated batch melting curves with incompatible trace element concentrations of primitive samples, which show minimal overprint of fractional crystallization and crustal contamination processes. To simulate a subduction modified mantle a source composition was constructed by mixing primitive mantle (Sun and McDonough, 1989) and a subduction component (Reiners et al., 2000) in the proportions 0.995:0.005. The models were computed applying the equation for batch melting (Albarède, 1995) and initially assuming a residual mineral assemblage of 50 % olivine, 25 % orthopyroxene, 15 % clinopyroxene and 10 % garnet. The compositions of the calculated melts exhibit progressive LILE and LREE enrichment and HFSE depletion with decreasing degrees of melting, with little change in HREE, and replicate the data fairly well, although Nb and

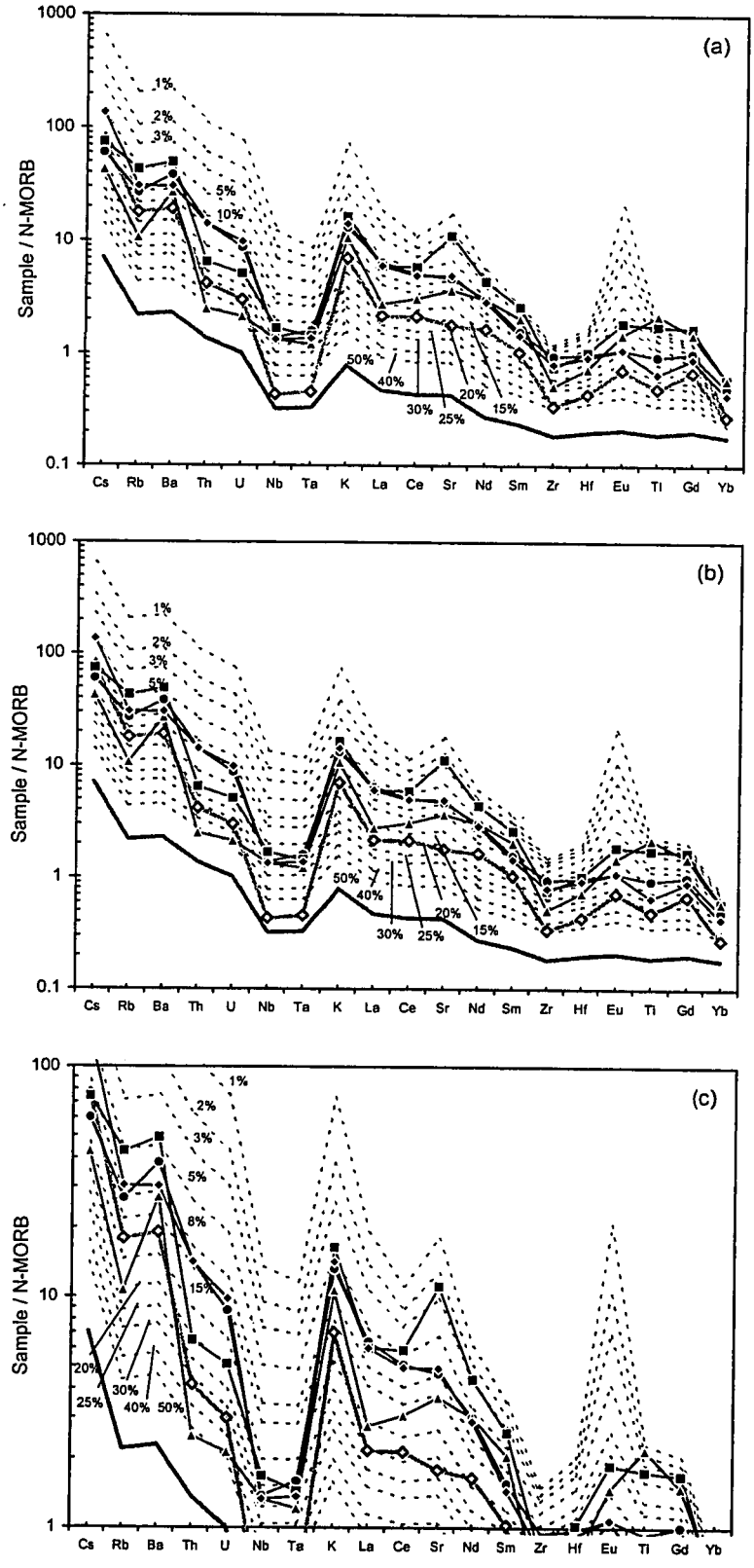
(a)
Sample / N-MORB
1000
100
10
1
0.1
1%
2%
3%
5%
10%
50%
40%
30%
25%
20%
15%
Cs Rb Ba Th U Nb Ta K La Ce Sr Nd Sm Zr Hf Eu Tl Gd Yb
(b)
Sample / N-MORB
1000
100
10
1
0.1
1%
2%
3%
5%
50%
40%
30%
25%
20%
15%
Cs Rb Ba Th U Nb Ta K La Ce Sr Nd Sm Zr Hf Eu Tl Gd Yb
(c)
Sample / N-MORB
100
10
1
1%
2%
3%
5%
8%
15%
20%
25%
30%
40%
50%
Cs Rb Ba Th U Nb Ta K La Ce Sr Nd Sm Zr Hf Eu Tl Gd Yb

Fig. 2.15

Fig. 2.15. (a) MORB-normalized incompatible trace element diagram comparing high-Mg samples of the QAS intrusions with calculated batch melting models (grey dashed curves). The models use a starting composition composed of a mixture of primitive mantle (Sun and McDonough, 1989) and a subduction component (Reiners et al., 2000) in the proportions 0.995:0.005 and assuming a residual mineralogy consisting of 50 % olivine, 25 % orthopyroxene, 15 % clinopyroxene and 10 % garnet. Heavy grey curve corresponds to the source. Melting curves are shown for 50, 40, 30, 25, 20, 15, 10, 8, 5, 3, 2 and 1 % melting. Partition coefficients from Rollinson (1993) and Borg (1997) and references within. (b) Similar to (a) but with a source mode of % 50 % olivine, 25 % orthopyroxene, 15 % clinopyroxene, 3 % garnet and 7 % spinel. (c) Close-up of middle portion of (b) for better visual estimation of fit.

Ta contents of some samples are lower than calculated values (Figure 2.15a). Adding small amounts of sediment to the starting composition prevents the development of negative Zr-Hf anomalies and delays the growth of negative Nb-Ta anomalies. Somewhat surprisingly, a starting composition composed of MORB and the same subduction component is not as suitable and failed to closely reproduce the observed compositions. The resulting pattern is not as fractionated as the QAS samples and shows only minor depletion in Nb and Ta and no depletion in Zr and Hf (Figure not shown).

A second group of models using spinel in the residue in place of garnet does not produce significantly different patterns, except that it fails to replicate the low HREE concentrations, suggesting that a subduction component alone is not able to sufficiently lower HREE concentrations (Figure not shown, but examined in detail below). Published subduction components indeed have high MREE/HREE and low HREE concentrations (e.g. Keppler, 1996, Reiners et al. 2000), but it requires addition of an unreasonably large quantity of subduction component ($X^{fluid} \sim 0.2$) to lower HREE concentrations through dilution in the derivative melts to the degree observed in the QAS intrusions. Despite recent arguments by Ayers (1998) for large fluid additions, it does not provide a reasonable fit in the present case as it raises LILE and LREE in the derivative melts to absurdly high values. Similar arguments apply if the metasomatic agent was a melt derived from a descending slab. Best results were obtained with a residual mineralogy consisting of 50 % olivine, 25 % orthopyroxene, 15 % clinopyroxene, 3 % garnet and 7 % spinel (Figure 2.15b and c), although it should be noted that the ratio of garnet to spinel is strongly influenced by the partition coefficients used in modeling. The partition coefficients used here have approximately similar Gd/Yb as those of Fujimaki et al.

(1984). In contrast, the partition coefficients used by Borg (1997) would place the melting process almost entirely in the garnet stability field.

As discussed by Thirlwall et al. (1994) variations in REE ratios are particularly useful in determining the melt contributions from garnet and spinel facies upper mantle. Figure 2.16 shows plots of representative ratios of LREE, MREE and HREE for samples with Mg-number > 0.5. Superimposed on the plots are calculated batch melting curves for garnet lherzolite, spinel lherzolite, mixed garnet-spinel lherzolite and an amphibole-bearing peridotite for 50 to 0.1 % partial melting using the same starting composition as above. Depletions in the form of previous melt extractions would shift the starting composition to lower La/Yb, La/Sm, Zr and Gd/Yb. The mineral modes are 50 % olivine, 25 % orthopyroxene, 15 % clinopyroxene and 10 % garnet for garnet lherzolite, 55 % olivine, 25 % orthopyroxene, 15 % clinopyroxene and 5 % spinel for spinel lherzolite and 50 % olivine, 25 % orthopyroxene, 15 % clinopyroxene, 3 % garnet and 7 % spinel for the mixed lherzolite (similar mode as modeled above). These modes do not contain metasomatic minerals, but the relatively high degrees of melting required to produce primitive magmas would have exhausted any metasomatic minerals. The metasomatic mineral most likely to be present in large amounts is pargasitic amphibole, so an amphibole-bearing mixed garnet - spinel peridotite is included for comparison. It contains olivine, 12 % orthopyroxene, 6 % clinopyroxene, 7 % garnet, 4 % spinel and 15 % amphibole (pargasite) (after MacKenzie and Canil, 1999). On the other hand, the role of amphibole in the source is debatable, since degrees of melting needed to produce the most primitive compositions imply temperatures too high for amphibole to have been a residual phase and thereby have significantly influenced trace element partitioning. The

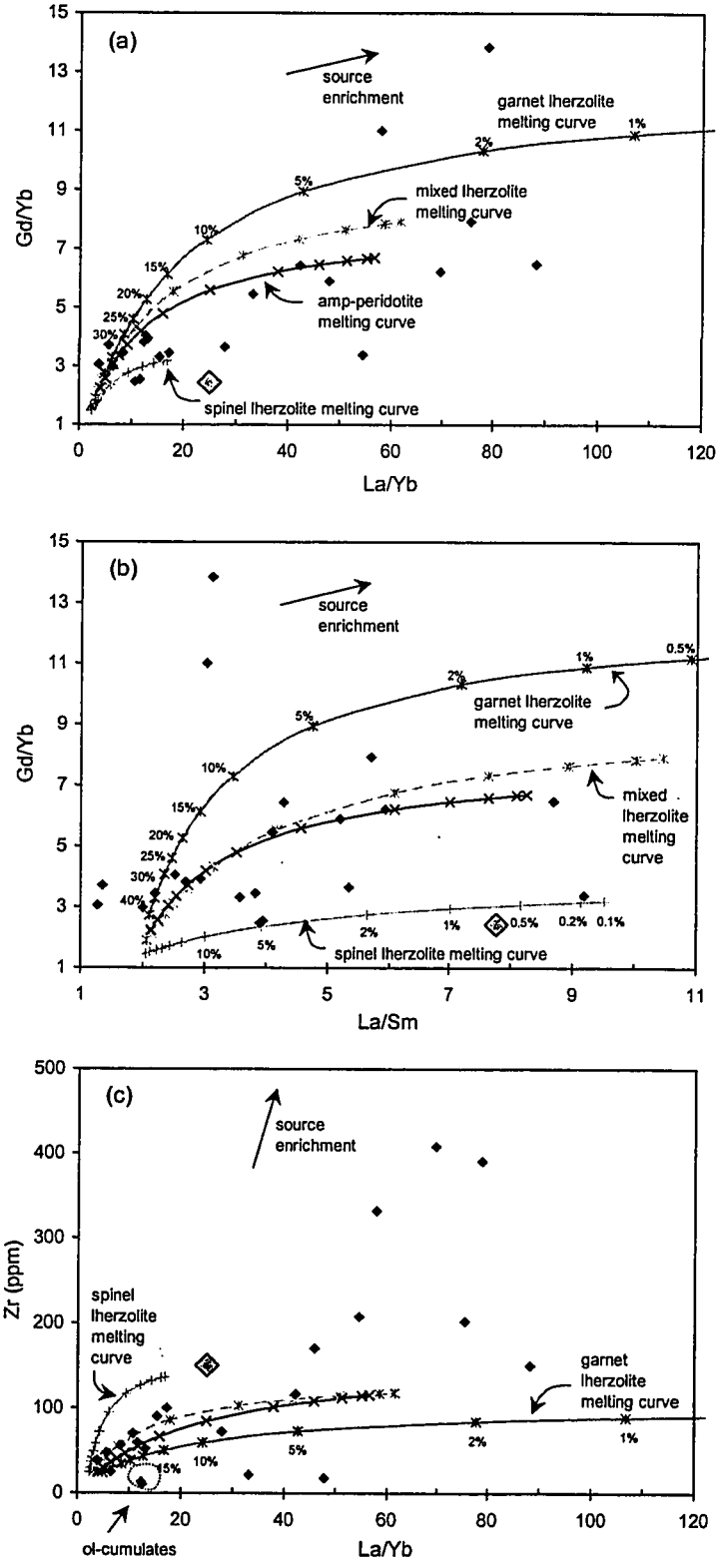
(a)
source enrichment
garnet lherzolite melting curve
mixed lherzolite melting curve
amp-peridotite melting curve
spinel lherzolite melting curve
Gd/Yb
La/Yb
(b)
source enrichment
garnet lherzolite melting curve
mixed lherzolite melting curve
spinel lherzolite melting curve
Gd/Yb
La/Sm
(c)
source enrichment
spinel lherzolite melting curve
garnet lherzolite melting curve
ol-cumulates
Zr (ppm)
La/Yb

Figure 2.16

Fig. 2.16. Variations of (a) La/Sm with Gd/Yb (b) La/Yb with Gd/Yb and (c) La/Yb with Zr concentration (in ppm) for QAS samples with *mg*-number > 0.5. Superimposed are calculated batch melting curves for garnet lherzolite (dark grey curve), spinel lherzolite (light grey curve with crosses), mixed spinel-garnet lherzolite (light grey dot-and-dash curve with stars) and amphibole-bearing mixed peridotite (black curve). The models use a starting composition composed of a mixture of primitive mantle (Sun and McDonough, 1989) and a subduction component (Reiners et al., 2000) in the proportions 0.995:0.005. The mineral modes of garnet lherzolite, spinel lherzolite and mixed garnet-spinel lherzolite are 50 % olivine, 25 % orthopyroxene, 15 % clinopyroxene and 10 % garnet, 55 % olivine, 25 % orthopyroxene, 15 % clinopyroxene and 5 % spinel, and 50 % olivine, 25 % orthopyroxene, 15 % clinopyroxene, 3 % garnet and 7 % spinel, respectively. The mode for amphibole-bearing peridotite is 56 % olivine, 12 % orthopyroxene, 7 % clinopyroxene, 8 % garnet, 4 % spinel and 15 % amphibole (pargasite) (after MacKenzie and Canil, 1999). Numbers next to the curves denote degrees of melting. When the full length of the curve is plotted, tick marks correspond to 50, 40, 30, 25, 20, 15, 10, 5, 2, 1, 0.5, 0.2 and 0.1 %. A sediment sample (BL9938) is included for reference with respect to possible crustal contamination effects. In (c) the circled samples correspond to olivine cumulates and can not be regarded as melt compositions in terms of Zr concentrations. Partition coefficients from Rollinson (1993) and Borg (1997) and references within.

latter is collaborated by high K contents combined with the absence of negative K anomalies in multi-element diagrams and relatively high normalized Ba and Rb concentrations (Figure 2.7) which suggest that a K-enriched phase such as phlogopite or amphibole was not residual during mantle melting. Amphibole was most likely present in the source, but melted out and thereby contributed to the composition of the derivative melt.

Overall, the data do not follow any melting curve closely, but the majority of the data form an array that parallels the garnet melting curve at somewhat lower Gd/Yb. Melting within the spinel stability field alone produces limited increase in Gd/Yb, La/Sm and La/Yb in strong contrast to the observed variations. Adding sediment or sediment melts to the starting composition shifts the curves to higher La/Yb, but has little effect on Gd/Yb and furthermore cannot account for the highest La/Yb values. Samples with >10 wt % MgO either follow the garnet lherzolite melting curve, but for unreasonably high degrees of partial melting (30-40 %), or plot below the garnet lherzolite melting curve. Because melting in the spinel stability field alone is unable to produce the high Gd/Yb ratios, a mixing model involving melt batches from spinel and garnet stability fields is required to explain the range in data. Similar conclusions from REE modeling have been inferred for Miocene basanitic to tholeiitic volcanic rocks from Vogelsberg (Bogaard and Wörner, 2003) and for intraplate volcanism in Yemen (Baker et al., 1997). Melting either took place in the garnet-spinel transition zone at pressures of 2.5-3 GPa, or melt batches from the garnet stability field were diluted by melts generated at lower pressures during ascent. The lack of systematic variation for the most primitive samples in Figure 2.16 suggests a heterogeneous mantle source combined with variable degrees of melting.

In summary, the mantle source appears to be a trace-element enriched garnet-bearing lherzolite with moderately depleted Nd isotopic composition. A comprehensive examination of the source(s) for the Quetico igneous complexes is presented in an accompanying paper (chapter 3).

2.11. Conclusions

1) The QAS intrusions contain a wide range of rock types, but display compositionally continuous major element systematics combined with similar overall trace element patterns such as high LILE and LREE and low HFSE and HREE concentrations, combined with limited variation in Nd and Pb isotope ratios. They are essentially contemporaneous and appear to have a common origin.

2) Mineral composition of multiple populations of clinopyroxene indicate that the magmas parental to the QAS differentiated by a number of processes at a range of pressures along several liquid lines of descent. High pressure, zoned Cr-diopsides reveal internal variation trends consistent with replenishment of primitive magma in deep-seated magma reservoirs.

3) Mafic to ultramafic magmas fractionated at high pressure during stagnation in periodically refilled magma chambers at the base of the crust. The most magnesian samples are olivine cumulates, but the main extracted mineral phase was clinopyroxene plus lesser amounts of olivine, phlogopite, plagioclase and Fe-Ti oxide. Lack of support

from least squares major element modeling probably reflects a combination of polybaric fractionation and magma replenishment.

4) Low-pressure fractionation controlled the evolution of the derivative magmas. The major compositional changes were driven by removal of clinopyroxene, alkali-feldspar and plagioclase and lesser amounts of amphibole, biotite, magnetite and apatite. Least squares major element modeling calculations give good matches to the data and suggest that each intrusion evolved along an independent differentiation trend.

5) Crustal contamination by isotopically more enriched material, presumably identical to the Quetico metasediments, is recorded by Nd and Pb isotopic signatures. Trace element systematics support a model which includes bulk addition in the form of AFC, combined with incorporation of various degrees of anatectic melt from the country rocks. It remains unclear whether the crustal Pb isotope ratios reflect crustal assimilation or fluid transport of sediment Pb via subduction zone fluids.

6) The magmas parental to the QAS intrusions formed by partial melting of a source that had been metasomatized by LILE and LREE- rich fluids and / or melts liberated from a subducting slab not long before melting. Quantitative modeling of REE shows that high-Mg samples can be generated by partial melting in the spinel-garnet transition zone.

Chapter 3

Fingerprinting source components and the role of fluid and slab melt metasomatism in the origin of late Archean alkaline complexes, western Superior Province Canada

3.1. Abstract

A suite of late Archean igneous complexes within the Quetico metasedimentary belt in the western Superior Province can be subdivided into two groups on the basis of Nb enrichment and REE distribution patterns, here referred to as Group I (Nb-depleted) and Group II (Nb-enriched). New Hf isotope data give initial $^{176}Hf/^{177}Hf$ between 0.281030 and 0.281340. Group I intrusions plot above to slightly below the depleted mantle evolution curve, while Group II intrusions are dispersed to more enriched Hf isotope compositions. The source of Group I intrusions is composed of three components: depleted MORB, enriched slab-derived fluids and a sediment component. Group II intrusions have adakitic affinities, and require a more complex scenario involving addition of small degree melts. We evaluate several models and show that integration of trace element and isotope data favor a model of wedge-modified slab melts and/or slab-melt metasomatism. Superchondritic Nb/Ta of Group II is attributed to metasomatism by silicic melts that have left rutile in the residue.

3.2. Introduction

A central issue in interpreting modern and ancient subduction related rocks is estimating the relative contribution from the mantle wedge, subducted sediments and slab components. In particular, evaluating the role of transfer agents from the subducting plate to the mantle wedge (fluids versus melts) and estimating the mineralogy of the sources from which these arise, are critical factors in interpreting the geochemical signatures of arc lavas. The distribution of high field strength elements (HFSE) is particularly useful in identifying the nature of the subduction components as HFSE are largely immobile in slab fluids, but compatible in slab melts.

Controversy remains as to whether subducted sediments and oceanic crust are partially melted and to what extent the melts are incorporated into the overlying mantle wedge and contribute to arc petrogenesis. For oceanic crust, geophysical models show that partial melting is unlikely to take place in modern arcs except under special circumstances with unusually high slab temperatures (e.g. Peacock, 1990). On the other hand a rapidly growing body of new geochemical data favors slab melting in certain present-day arc settings (e.g. Sajona et al., 2000; Castillo et al., 1999; among many others). In a recent study of the Aleutian arc Kelemen et al. (2001) proposed that previously published thermal models have systematically underestimated the temperature in parts of the mantle wedge, which could explain the discrepancies between geophysical and geochemical models.

It is commonly inferred that slab melting was more important in the Archean, because of the assumed hotter mantle and correspondingly steeper geotherms in the early Earth

(e.g. Martin, 1994). Slab melting in the Archean may also have been enhanced as a result of prolonged heating time as a result of flat subduction (e.g. Karsten et al., 1996). In cooler mantle wedges, slab melts may be involved in the petrogenesis of arc rocks as metasomatizing agents rather than being erupted at the surface (e.g. Rapp et al., 1999; Defant and Kepezhinskas, 2001). Wedge-modified slab melts are compositionally very similar to modern high-Mg andesites and high-Mg diorites or "sanukitoids" (Smithies and Champion, 2000), which occur within the Superior Province (e.g. Stern et al., 1989; Stevenson et al., 1999; Chapter 2, this work). Moyen et al. (2001) recently proposed that by the end of the Archean the geotherm may have been such that almost all slab melts were absorbed within the mantle and that sanukitoids represent derivatives of a slab melt metasomatized mantle.

The primary objective of this paper is to place constraints on the geodynamic setting and the nature of the source region for the late Archean Quetico alkaline suite (hereafter abbreviated QAS) intrusions of sanukitoid affinity within the western Superior Province (Figure 3.1). The complex nature of tectonic assembly of the western Superior Province provides the potential for heterogeneous mantle domains and different subduction components (fluids and melts), leading to a wide variety of possible magma-types parental to the QAS intrusions. The suite is described with respect to magmatic differentiation history in an accompanying paper (see chapter 2) in which it was also concluded that the QAS intrusions are derived from a metasomatized mantle wedge. Mantle metasomatism may involve a number of agents, including silicate and carbonate melts, H_2O- and CO_2-rich fluids (e.g. Ionov et al., 2002). In this paper, a more thorough

investigation of the metasomatic media involved in the petrogenesis of the QAS intrusions is presented.

3.3. Geological framework and review of geochemistry

The QAS intrusions (Figure 3.1) are volumetrically small bodies, which range from ultramafic rock types to syenite and rare carbonatite. They intrude metasedimentary rocks of the Quetico subprovince, a belt of deformed, metamorphosed flysch (Percival and Williams, 1989), which is located between the Wawa and the Wabigoon greenstone belts in the western Superior Province (Figure 3.1). The geological relationships are described in more detail in Chapter 2 and in appendix 1. Five intrusions were dated by U-Pb on zircon and / or titanite and gave ages between 2678 and 2685 Ma, which are indistinguishable considering uncertainty (Chapter 2 and references therein) and establish a temporal linkage between mafic and leucocratic intrusions. The QAS intrusions are late- to post-kinematic with respect to regional deformation and define a trend from subalkalic to alkalic rock types, as is common in post-collisional settings.

In MORB-normalized diagrams most samples are enriched in Cs, Ba, Sr, K, La, Ce, Pb and Rb relative to Nb, Ta, Ti, Zr and Hf, leading to characteristic high ratios of large ion lithophile elements (LILE) relative to HFSE, as is commonly reported from subduction related rocks (e.g. Arculus, 1994) (Figure 3.2). Most samples show distinct Pb and Sr spikes relative to rare earth elements (REE) of similar compatibility. There is considerable variation between highly fluid-mobile LILE, such as Ba, Rb, Cs, K and U, and the less fluid-mobile LILE, such as Th and the light rare earth elements (LREE).

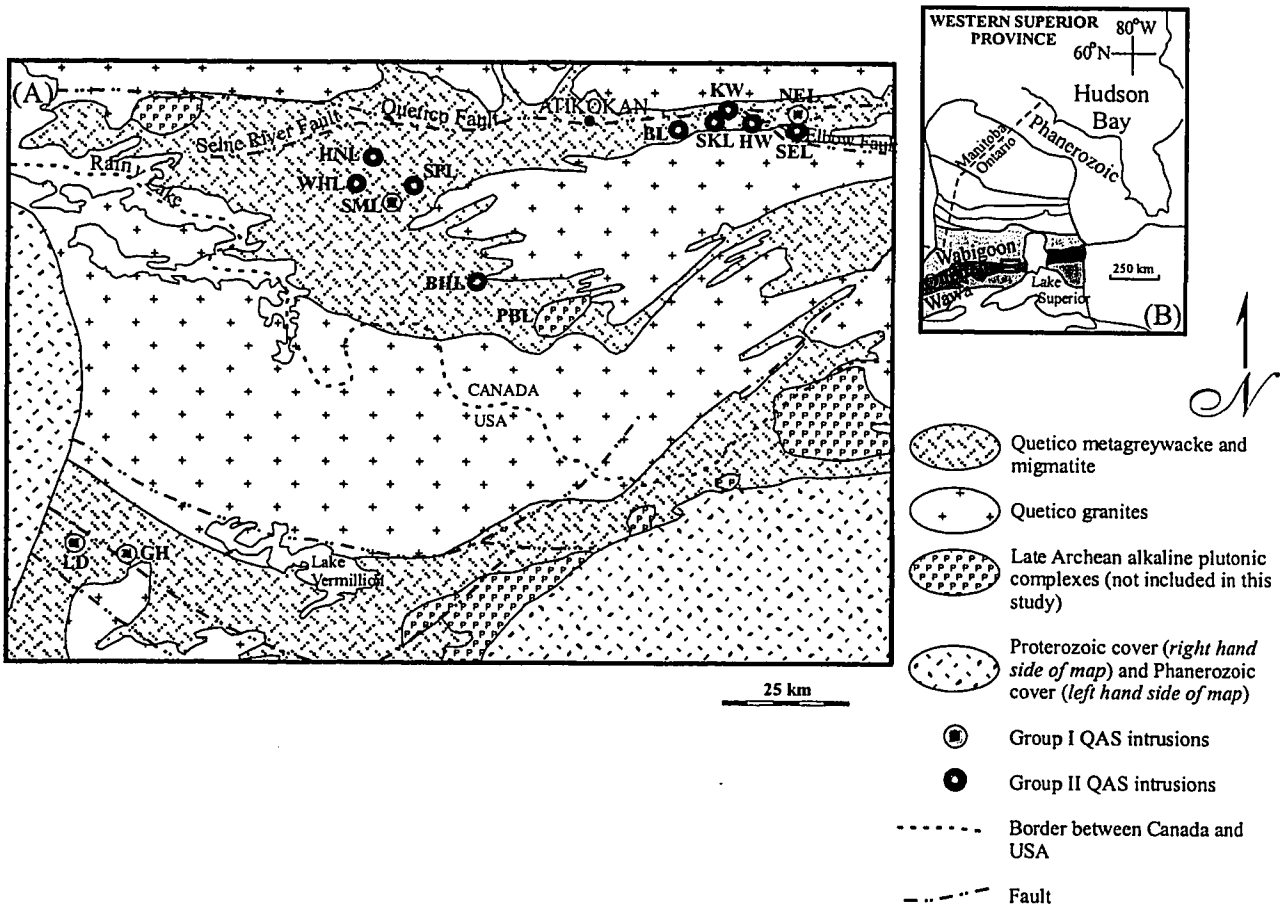

Fig. 3.1. (A) Simplified geological map of the Quetico subprovince and surrounding greenstone belts, showing the location of the studied intrusions: LD = Linden, GH = Gheen, HNL = Harnett Lake, WHL = Whalen Lake, SPL = Surprise Lake, SML = Samuels Lake, BHL = Beaverhouse Lake, BL = Blalock, SKL = South Kawene Lake, KW = Kawene, HW = Heward, NEL = North Elbow Lake, SEL = South Elbow Lake. Also indicated is PBL = Poohbah Lake intrusion. The division into Group I and II intrusions is discussed later in the text (B) Outline of the western Superior Province with location of map (A) indicated by the small black frame. Modified from Stern et al. (1989).

These are also common characteristics of arc rocks, but some QAS intrusions are unusual in that they display deep negative Zr-Hf anomalies, which are more pronounced than Nb-Ta anomalies in MORB-normalized diagrams (Figure 3.2). For these intrusions Zr and Hf display absolute depletion relative to MORB, while Nb and Ta are depleted relative to neighboring elements, but not relative to MORB. Within any single intrusion there is no major change in pattern shape with differentiation.

Nd isotopic ratios span a small range with initial $^{143}Nd/^{144}Nd$ between 0.509160 and 0.509278 corresponding to ϵ^{Nd} between 0.0 and +2.3 (chapter 2). Initial Pb isotope ratios of leached alkali-feldspars show even less relative variation and plot in a narrow field on or slightly above the Stacey-Kramers crustal evolution curve at *ca* 2750 Ma, similar to the age of the country rocks, but significantly older than the crystallization age of the intrusions as determined by U-Pb on zircon. This implies that their Pb isotopic signatures are dominated by crustal sources, in the form of Pb from subducted sediments transferred to the mantle by fluids or by contamination of mantle-derived magmas by an older, lower crustal source.

Prior to examining the source characteristics of the QAS intrusions it is important to evaluate the types of deep and shallow crustal level differentiation processes and the degree to which these have modified initial trace element and isotopic compositions. An accompanying paper (Chapter 2) modeled a complex differentiation history of the QAS intrusions that included fractional crystallization at moderate pressure mainly by extraction of clinopyroxene concomitant with replenishment by fresh magma batches into the magma reservoirs. Derivative magmas rose and differentiated at shallow crustal levels by low pressure fractional crystallization as they were contaminated by the local Quetico

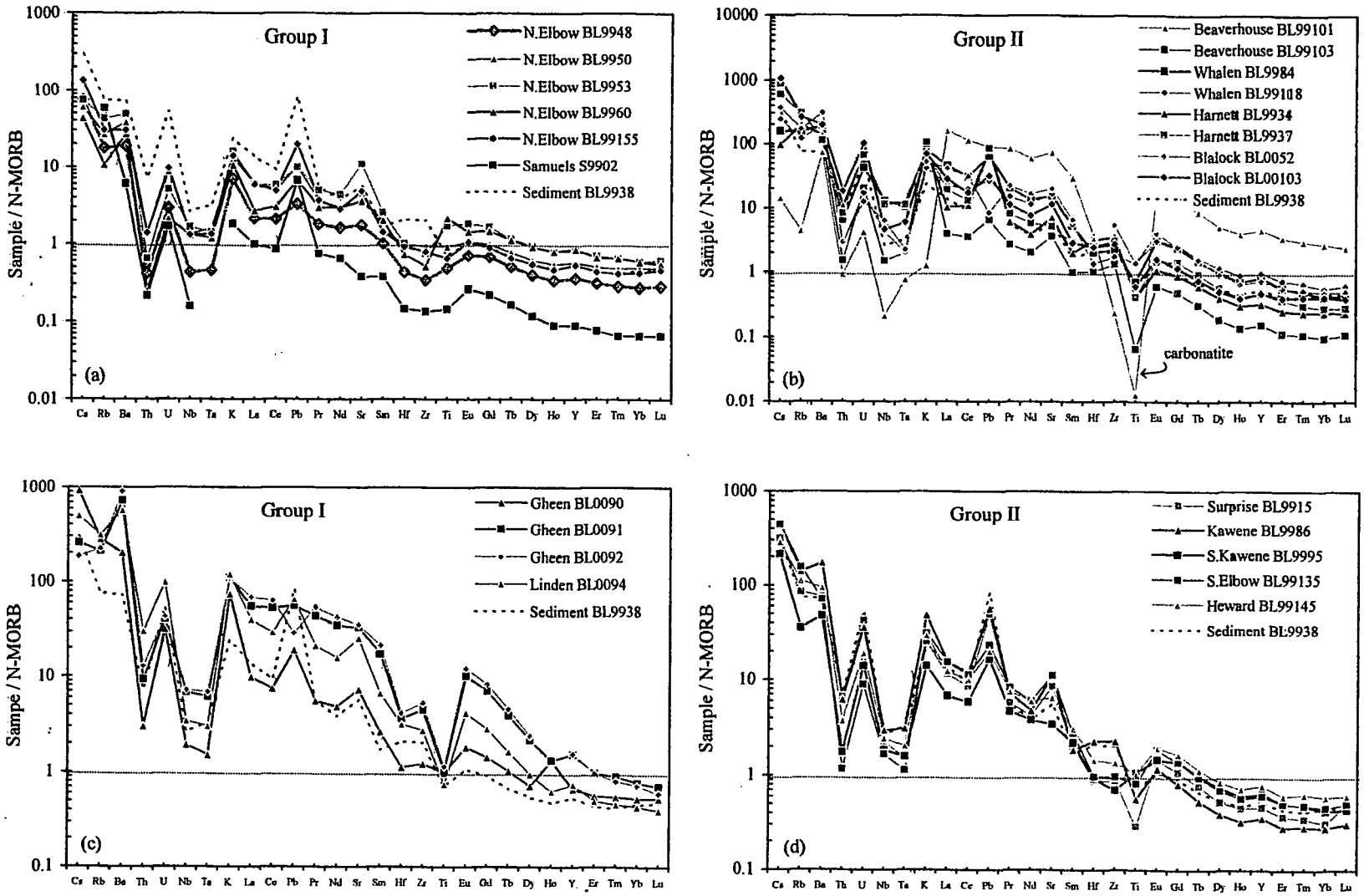

Fig. 3.2. MORB-normalized trace element diagrams for representative samples from the QAS intrusions and surrounding country rocks. Division into Group I and II is discussed later in the text.

metasediments. Lassen et al. (chapter 2) further concluded based on batch partial melting models, that the high LILE and LREE, and low HFSE concentrations primarily reflect derivation from a metasomatized mantle wedge.

3.4. Subdivision of intrusive complexes

In Figure 3.3 the incompatible trace elements are normalized to N-MORB and arranged in the order of expected enrichment in slab-derived fluids from left to right after Maury et al. (1992) [following Bourdon et al. (2002)] where the order of enrichment is determined by experimental work. The diagram subdivides the QAS intrusions into two groups: Most samples from the QAS intrusions possess distinct positive Nb anomalies relative to neighboring elements and these anomalies occur in both primitive and evolved samples (Figure 3b). A regional survey reveals that LILE-rich intrusions throughout the southwestern Superior Province do not show similar Nb enrichment patterns, except for the Cone Lake intrusion in the Wawa subprovince (data from Boerboom, 1994). Samples from four QAS intrusions (Gheen, Linden, Samuels Lake and North Elbow Lake intrusions) lack positive Nb anomalies relative to Eu and Dy and thereby resemble other LILE-rich intrusions in the southwestern Superior Province (Figure 3.3a). These differences in Nb enrichment patterns are important and have petrogenetic significance as detailed below. The other critical element to consider in Figure 3.3 is Sr. All samples display relatively flat patterns for Sr relative to Ce and Nd, which suggests a role for plagioclase as a residual or fractionating phase, and which thereby places limits on depth

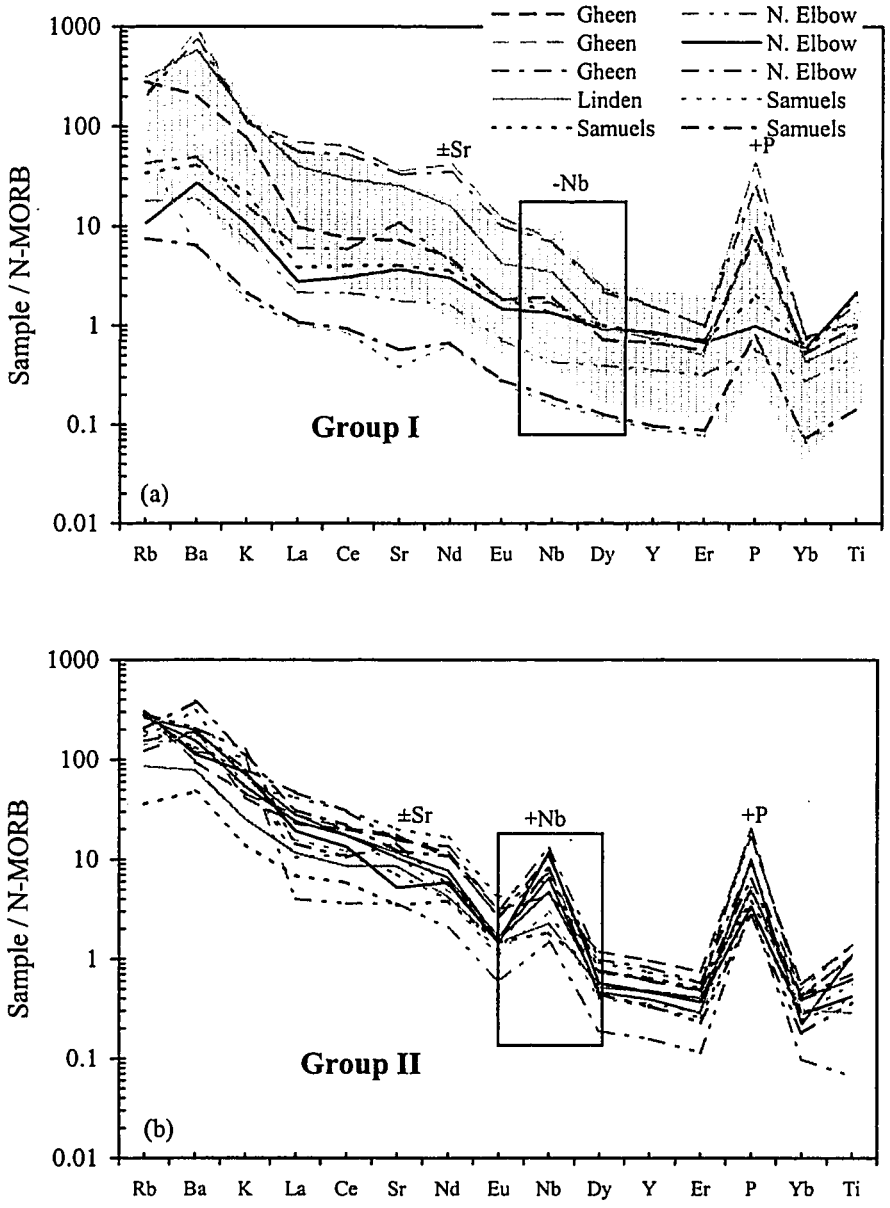

Fig. 3.3. Subdivision of the QAS intrusions (a) "Nd-depleted" intrusions or Group I (b) "Nb-enriched" intrusions or Group II. There are no obvious anomalies for Sr in either group, suggesting a role for plagioclase in the source.

of segregation and differentiation to <1.5 GPa. A positive anomaly would indicate the absence of plagioclase in the source.

In the following discussion, the two groups of intrusions will be treated separately and referred to as Group I (Nb-depleted) and Group II (Nb-enriched), respectively. There is no detectable age difference between the two groups and no apparent link between the groups and their geographic distribution within the Quetico subprovince (Figure 3.1) but the subdivision is further highlighted when considering other geochemical parameters. In general, samples from Group II are more fractionated than those of Group I and display significantly higher LREE/HREE ratios. Group I intrusions have chondritic Nb/Ta, while Group II intrusions show strong Nb/Ta fractionation and extend to superchondritic values (examined in detail below). Most Group II samples contain high abundances of Nb (up to 34 ppm Nb) relative to normal arc suites. Some, but not all, have Al_2O_3 > 15 wt %, low heavy rare earth elements (HREE) (Yb < 1.9 ppm) and low Y, Sr > 400 ppm and high Sr/Y, thereby resembling adakites according to the original definition outlined by Defant and Drummond (1990) and experimentally simulated slab melts, such as those of Sen and Dunn (1994). The most evolved samples generally carry the strongest adakite signatures, but intermediate samples have the highest Nb abundances.

There is substantial overlap between the two groups in major element composition, but they are to some extent distinguished in K variation. Group I can be divided into a low, almost horizontal K trend (North Elbow and Samuels) and a steeply inclined K trend (Gheen and Linden) with K_8 (K_2O at 8 wt % MgO) values of 1.5 and 4.5, respectively, whereas Group II has K contents between these two trends (Figure 3.4a). Group II generally has higher Na_2O and Al_2O_3 concentrations relative to Group I at equivalent

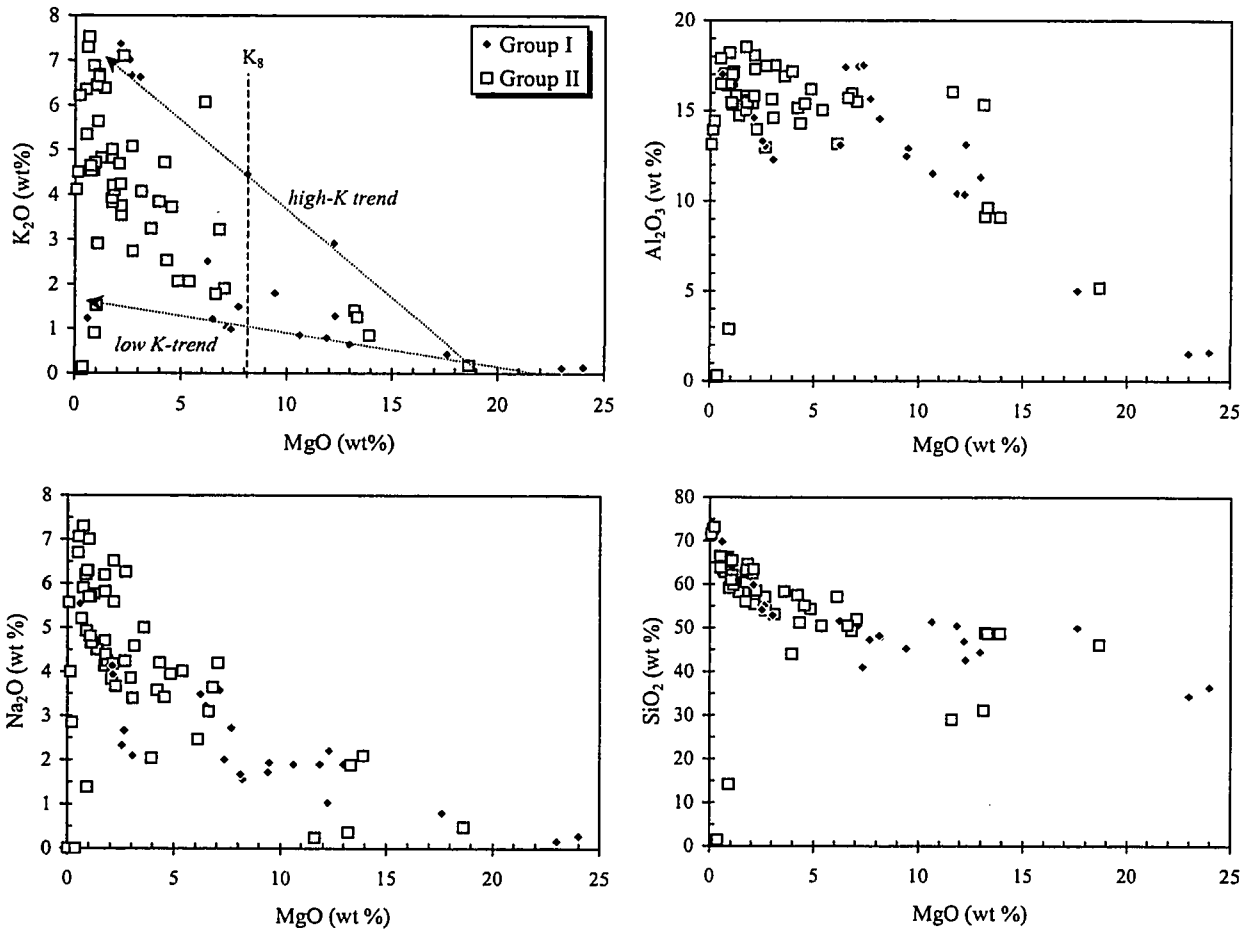

Fig. 3.4. Major element variation diagrams for Group I and II QAS intrusions

MgO (Figure 3.3b and 3.3c). Group I defines an overall positive trend between SiO_2 and Y, while Group II shows a negative trend in this diagram (Figure 3.5a). There is a positive correlation between La/Y and Ba/Nb for Group I and a slight negative correlation between these element ratios for Group II (Figure 3.5b). A regional review indicates that Group II indeed has very low Ba/Nb compared to LILE-rich intrusions of the southwestern Superior Province sanukitoid suite, while Group I displays a trend similar to those intrusions. The low ratios result from a combination of lower Ba and higher Nb for a given MgO relative to other intrusions. They occur in both primitive and evolved Group II samples and are therefore not related to fractionation processes. Group I also exhibits strong positive correlations between Na_2O and Yb and Al_2O_3 and Yb, while Group II defines negative correlations between these elements and extends to low Yb abundances for high Na_2O and Al_2O_3 abundances (Figure 3.5c and 3.5d). The divergence in major and trace element characteristics resembles what has been observed in young Ecuadorian lavas and interpreted to reflect the transition between calc-alkaline and adakitic magmatism (see Samaniego et al., 2002).

A positive correlation exists between $^{143}Nd/^{144}Nd$ and Dy/Yb for Group II, which suggests mixing between an isotopically depleted source with fractionated REE and a less depleted source characterized by less fractionated REE. No correlation is observed between these ratios for Group I. In addition, there is a wider spread in Nd isotope ratios for Group II relative to Group I, but this could simply reflect the larger amount of Nd isotope data.

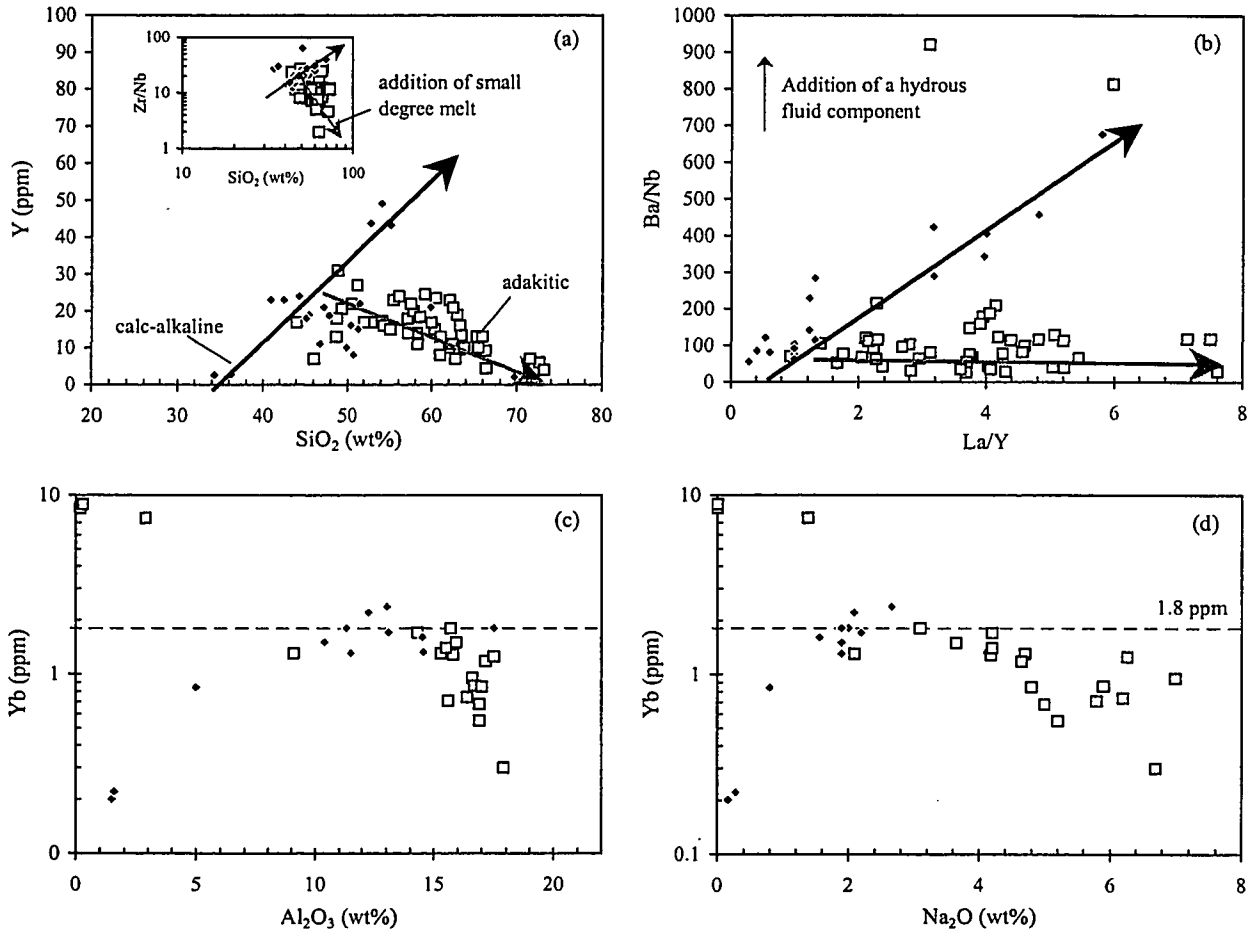

Fig. 3.5. Geochemical variation diagrams for Group I and II QAS intrusions. (a) Group I defines a positive and Group II a negative trend between SiO2 and Y. Inset shows decreasing Zr/Nb with evolution for Group II intrusions, suggesting addition of small degree melt, because Nb is a highly incompatible and Zr a moderately incompatible trace element (b) Group I is a hydrous fluid component, whereas a fluid component is less apparent in Group II. (c and d) All samples are characterized by low Y and Yb, but Group II further trends toward high Al_2O_3 and high Na_2O. See text for discussion.

3.5. Analytical work

3.5.1. Hf isotopes

Hf isotope analyses were obtained on zircon using a VG-Elemental Axiom MC-ICPMS located at the Danish Lithosphere Centre in Copenhagen, Denmark. Zircons were separated following standard mineral separation techniques including crushing, magnetic separator, Roger's table, heavy liquids and hand picking under binocular microscope. Zircons containing visible cores, inclusions or cracks were avoided.

The MC-ICPMS is equipped with eight movable faraday cups and one fixed axial faraday cup. The cups were set up to monitor mass ^{173}Yb through to ^{182}W with mass ^{178}Hf in the Axral collector. ^{173}Yb and ^{175}Lu were monitored to correct for isobaric interferences on mass ^{176}Hf and were corrected on-line using the following ratios: ^{176}Yb/^{173}Yb = 0.79323 and ^{176}Lu/^{175}Lu = 0.026528. Isobaric interferences of Ta and W on ^{180}Hf were corrected for by monitoring masses ^{181}Ta and ^{182}W and ratios of ^{180}Ta/^{181}Ta (= 0.0001) and ^{180}W/^{182}W (= 0.004943). These ratios were determined by progressively adding the elements in question as a standard solution. Data was corrected for mass fractionation using normalization ratios of ^{179}Hf/^{177}Hf (=0.7325) and ^{178}Hf/^{177}Hf (=1.46717) according to the exponential law. Correct instrument set-up was monitored by ensuring that the same ratios were achieved by both mass fractionation corrections.

The Axiom is equipped with a LSX-200 CETAC quadrupled Nd-Yag laser with a wavelength of 266 nm. Analyses were carried out using a 50 μm laser spot size, operating at a pulse rate of 20 Hz. Ablated material was passed into the MC-ICPMS using a flow of

Ar carrier gas with a flow rate of ca 1 L/minute. Backgrounds were measured for ca 20 seconds before ablation was started. Data acquisition began after a few seconds of initial ablation, when a stable signal was attained, and data was collected as one block of 150 to 200 0.5 second integrations depending on zircon size. During ablation the laser was slowly tracked along the length of the zircon. For smaller zircons, this resulted in complete ablation of the zircon interior. In some larger zircons replicate and triplicate analyses were performed. Duplicate analyses of NIST 610 to determine Lu/Hf ratios were carried out using the same lasering procedure. The typical uncertainty on a single analysis of $^{176}Lu/^{177}Hf$ is ± 0.5-2% and the mean 2SE uncertainty on $^{176}Hf/^{177}Hf$ is ± 0.000049. Seven runs of standard JMC-475 gave 0.282147 ± 0.000006. Other details on laser instrument set-up are presented in Willingers et al. (2002).

Hf isotope ratios are tabulated in Table 3.1. ϵ_{Hf} were calculated assuming CHUR $^{176}Hf/^{177}Hf = 0.282772$ and $^{176}Lu/^{177}Hf$ of 0.0332 (Blichert-Toft and Albarède, 1997) and using a ^{176}Lu decay constant of $1.865 \cdot 10^{-11}$ year^{-1} (Scherer et al., 2001). It should be noted that these values are not yet well constrained, which may affect interpretations based on calculated Hf isotope ratios. Depleted-mantle (T_{DM}) model ages were calculated assuming present-day ratios for the depleted mantle reservoir of $^{176}Hf/^{177}Hf = 0.28325$ and $^{176}Lu/^{177}Hf = 0.0384$ (Griffin et al., 2000).

3.5.2. Results

The number of intrusions and the range in rock types characterized for Hf isotopes are limited to those in which zircon is present and forms sufficiently large grains to obtain

reliable data. Therefore it has been possible to obtain Hf data only on one mafic-ultramafic intrusion (North Elbow Lake intrusion), where zircon was extracted from a plagioclase-rich segregation. Age corrected $^{176}Hf/^{177}Hf$ of the analyzed zircons range between 0.281030 and 0.281340, which corresponds to εHf(t) of -1.42 and +9.59, although except for three outliers the data range between +1.7 and +8.32 and hence have $^{176}Hf/^{177}Hf$ higher than chondritic ratios (Table 3.1, Figure 3.6). Most grains have model ages (T_{DM}) older than the emplacement ages of the QAS intrusions. The one zircon with negative εHf is clearly inherited. Its T_{DM} model age is 3.02 Ga, remarkably close to the age of the Marmion terrane (Tomlinson et al. (in press.), which may extend into the Quetico basement (see chapter 2, this work). Data from Beaverhouse Lake intrusion is discussed separately in a subsequent paper (chapter 4).

The majority of Group I data range from depleted mantle values to lower values of ~ +4. The spread towards lower values indicates some contribution from an enriched, probably crustal, source. Some are dispersed to slightly higher values relative to previously reported late Archean Hf data from the Superior Province (Davis et al., 2000; Vervoort and Blichert-Toft, 1998; Corfu and Noble, 1992; Corfu and Stott, 1993; Corfu and Stott, 1996). The tectonic setting of the QAS intrusions is not accurately known, but they are post-collisional and most probably formed in a back-arc setting. Woodhead et al. (2001) analyzed the Hf isotopic composition of arc/back-arc pairs and reported systematically higher $^{176}Hf/^{177}Hf$ in back-arc assemblages than in the corresponding arc.

Zircons from Group II intrusions are dispersed to lower Hf isotope ratios relative to Group I. Except for a few outliers they totally overlap with the sanukitoid suite from southern Uchi and central Abitibi greenstone belt analyzed by Corfu and Stott (1996) and

Table 3.1. Hf isotope data for Group I and II intrusions

Sample #	IN	$^{176}Lu/^{177}Hf$ (meas.)	$^{176}Lu/^{177}Hf$ (T)	$^{176}Hf/^{177}Hf$ (meas.)	$^{176}Hf/^{177}Hf$ (init.)	ϵ(Hf) (init.)	T(DM) Ga
BL0091 zr.1	GH	0.000638	0.000558	0.281235	0.281206	4.83	2.78
BL0091 zr.2	GH	0.000635	0.000555	0.281258	0.281230	5.67	2.75
BL0091 zr.3	GH	0.000769	0.000672	0.281242	0.281207	4.86	2.78
BL0091 zr.5	GH	0.000775	0.000677	0.281216	0.281181	3.94	2.82
BL0091 zr.8	GH	0.000473	0.000413	0.281198	0.281177	3.78	2.82
BL0092 zr.1	GH	0.000743	0.000627	0.281336	0.281304	8.32	2.65
BL0092 zr.3	GH	0.001000	0.000843	0.281301	0.281258	6.66	2.71
BL0092 zr.5	GH	0.000644	0.000543	0.281314	0.281286	7.67	2.67
BL0092 zr.11	GH	0.001127	0.000950	0.281325	0.281276	7.31	2.69
BL0092 zr.11	GH	0.001118	0.000943	0.281319	0.281271	7.14	2.69
Harnett P. zr.4	HAR	0.001351	0.001218	0.281228	0.281165	3.37	2.84
Harnett P. zr.6	HAR	0.001391	0.001255	0.281304	0.281240	6.04	2.74
Harnett P. zr.9	HAR	0.001195	0.001077	0.281256	0.281201	4.65	2.79
Harnett P. zr.10	HAR	0.001466	0.001322	0.281353	0.281285	7.63	2.68
Harnett P. zr.12	HAR	0.001479	0.001334	0.281345	0.281276	7.32	2.69
BL9934 zr.2	HAR	0.001004	0.000930	0.281258	0.281210	4.98	2.78
BL9934 zr.4	HAR	0.001133	0.001049	0.281284	0.281230	5.68	2.75
BL9934 zr.6	HAR	0.001094	0.001013	0.281292	0.281240	6.04	2.74
BL9934 zr.7	HAR	0.000945	0.000875	0.281220	0.281175	3.71	2.83
BL9934 zr.9	HAR	0.001341	0.001242	0.281309	0.281245	6.22	2.73
BL9934 zr.13	HAR	0.001012	0.000937	0.281239	0.281191	4.29	2.80
BL0044 zr.1	HAR	0.001605	0.001353	0.281325	0.281256	6.59	2.72
BL0044 zr.3	HAR	0.000600	0.000506	0.281056	0.281030	-1.43	3.02
BL0044 zr.4	HAR	0.000782	0.000660	0.281221	0.281188	4.17	2.81
BL0044 zr.5	HAR	0.001035	0.000873	0.281252	0.281207	4.88	2.78
BL0044 zr.7	HAR	0.000629	0.000567	0.281194	0.281165	3.35	2.84
BL0037 zr.2	HAR	0.000825	0.000743	0.281291	0.281253	6.48	2.72
BL0037 zr.4	HAR	0.001127	0.001016	0.281270	0.281218	5.23	2.77
BL0037 zr.7	HAR	0.000450	0.000406	0.281181	0.281160	3.18	2.84
BL0037 zr.10	HAR	0.000752	0.000678	0.281250	0.281215	5.15	2.77
BL0037 zr.11	HAR	0.000982	0.000885	0.281278	0.281233	5.78	2.75
BL0033 zr.1	WHL	0.000999	0.000900	0.281265	0.281218	5.26	2.77
BL0033 zr.3	WHL	0.000922	0.000831	0.281252	0.281209	4.94	2.78
BL0033 zr.4	WHL	0.000940	0.000847	0.281218	0.281175	3.71	2.83
BL0033 zr.5	WHL	0.001007	0.000908	0.281245	0.281198	4.54	2.79
BL0017 zr.1	NEL	0.000561	0.000470	0.281291	0.281267	7.00	2.70
BL0017 zr.1	NEL	0.000557	0.000467	0.281247	0.281223	5.43	2.76

Table 3.1. Continued

Sample #	IN	$^{176}Lu/^{177}Hf$ (meas.)	$^{176}Lu/^{177}Hf$ (T)	$^{176}Hf/^{177}Hf$ (meas.)	$^{176}Hf/^{177}Hf$ (init.)	ϵ(Hf) (init.)	T(DM) Ga
BL0017 zr.2	NEL	0.000448	0.000376	0.281285	0.281266	6.95	2.70
BL0017 zr.3	NEL	0.000587	0.000492	0.281298	0.281273	7.20	2.69
BL0017 zr.4	NEL	0.000765	0.000642	0.281271	0.281238	5.96	2.74
BL0017 zr.5	NEL	0.000566	0.000475	0.281365	0.281340	9.60	2.60
BL0017 zr.1	NEL	0.000571	0.000479	0.281267	0.281243	6.13	2.73
BL0017 zr.1	NEL	0.000817	0.000585	0.281308	0.281278	7.38	2.69
BL0017 zr.2	NEL	0.000395	0.000331	0.281198	0.281181	3.92	2.82
BL0017 zr.3	NEL	0.000435	0.000375	0.281260	0.281241	6.07	2.73
BL0017 zr.3	NEL	0.000286	0.000247	0.281217	0.281204	4.75	2.78
BL0017 zr.4	NEL	0.000556	0.000480	0.281231	0.281206	4.82	2.78
BL0017 zr.4	NEL	0.000630	0.000544	0.281258	0.281230	5.69	2.75
BL0017 zr.15	NEL	0.000470	0.000405	0.281260	0.281240	6.02	2.74
BL0017 zr.15	NEL	0.000717	0.000618	0.281292	0.281261	6.77	2.71
BL0017 zr.15	NEL	0.000559	0.000482	0.281261	0.281236	5.89	2.74
BL0017 zr.14	NEL	0.000644	0.000556	0.281276	0.281247	6.29	2.73
BL0017 zr.12	NEL	0.000618	0.000542	0.281232	0.281205	4.77	2.78
BL0017 zr.10	NEL	0.001106	0.000969	0.281311	0.281261	6.78	2.71
BL0017 zr.8	NEL	0.000691	0.000606	0.281290	0.281259	6.71	2.71
BL0085 zr.1	BL	0.000589	0.000494	0.281186	0.281161	3.21	2.84
BL0085 zr.5	BL	0.000364	0.000305	0.281137	0.281121	1.80	2.89
BL00103 zr.1	BL	0.000905	0.000816	0.281205	0.281163	3.28	2.84
BL00103 zr.2	BL	0.001131	0.001020	0.281242	0.281189	4.22	2.81
BL00103 zr.5	BL	0.000880	0.000793	0.281210	0.281169	3.50	2.83
BL00103 zr.8	BL	0.000572	0.000515	0.281173	0.281146	2.70	2.86
BL00103 zr.9	BL	0.000811	0.000731	0.281207	0.281170	3.54	2.83
BL00103 zr.10	BL	0.000612	0.000566	0.281191	0.281162	3.26	2.84
BL00103 zr.13	BL	0.000531	0.000491	0.281185	0.281160	3.19	2.84
BL00103 zr.14	BL	0.000814	0.000751	0.281202	0.281163	3.30	2.84
BL00103 zr.16	BL	0.001089	0.001006	0.281221	0.281169	3.52	2.83
BL00103 zr.17	BL	0.000561	0.000518	0.281189	0.281162	3.25	2.84

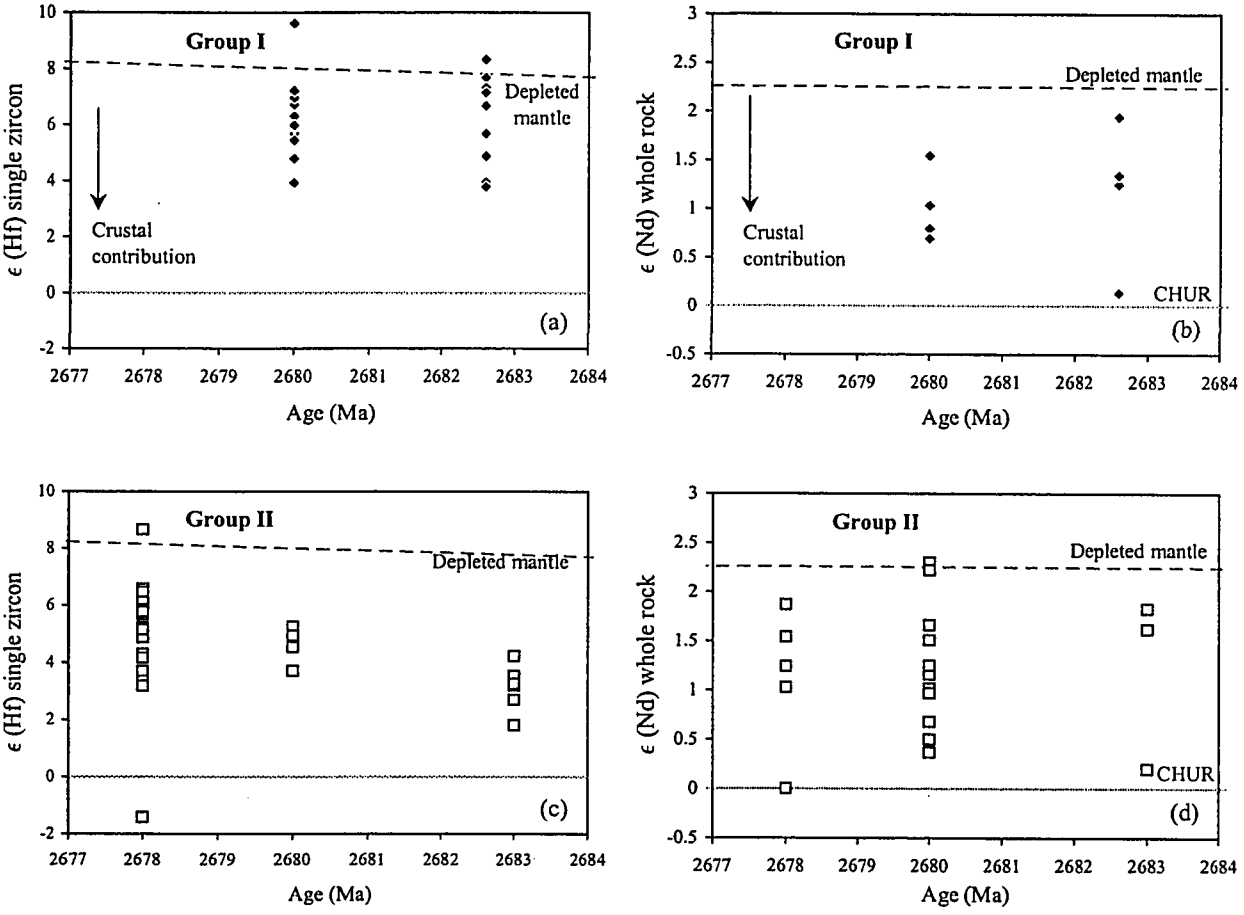

Fig. 3.6. Plot of ϵHf versus time in Ma for zircons from Group I (a) and Group II (c) intrusions. Group II intrusions are dispersed to more enriched Hf isotope compositions relative to Group I. For comparison (b) and (d) show ϵNd versus time for Group I and II intrusions. Note that the data at 2680 Ma represent more than one intrusion. In (c) the one sample with negative ϵHf is most likely an inherited zircon. In (a) and (c) depleted mantle curve is after Davis et al. (2000).

sanukitoids from the western Superior analyzed by Davis et al. (2000). Corfu and Stott (1996) report ϵHf from +5 to +1.7 and argue that +5 corresponds to the metasomatized mantle, while Davis et al. (2000) report a limited range in ϵHf (+4.5 to +6.5) and argue that sanukitoids from the western Superior Province are derived from a mantle source with ϵHf of +6.5.

3.6. Discussion

3.6.1. The Nb/Ta budget

Group I intrusions collectively define a fairly narrow range in Nb/Ta (~ 17-22), while Group II intrusions display a much wider compositional range of 5-37 plus one remarkably high value of 50 [after the data set has been screened for samples with > 55 wt % SiO_2] cf. Nb/Ta of 16.8 ± 3.1 in chondrite (Hofmann et al., 1986) (Figure 3.7). Similar high values have been reported from present day arcs, for example lavas from the Bismark and Tongan arcs have Nb/Ta up to 33 (Stolz et al. 1996) (Figure 3.7). Also included in the figure is the field of late Archean LILE-rich intrusions (sanukitoids) from adjacent volcanic-plutonic subprovinces. Sanukitoid data from the metasedimentary Pontiac subprovince are shown separately. The latter display strong Nb/Ta fractionation, whereas superchondritic Nb/Ta are uncommon in sanukitoid suites from other areas in the western Superior Province. This suggests that a different set of processes than these involved in the production of the sanukitoid suite is responsible for the QAS Group II intrusions.

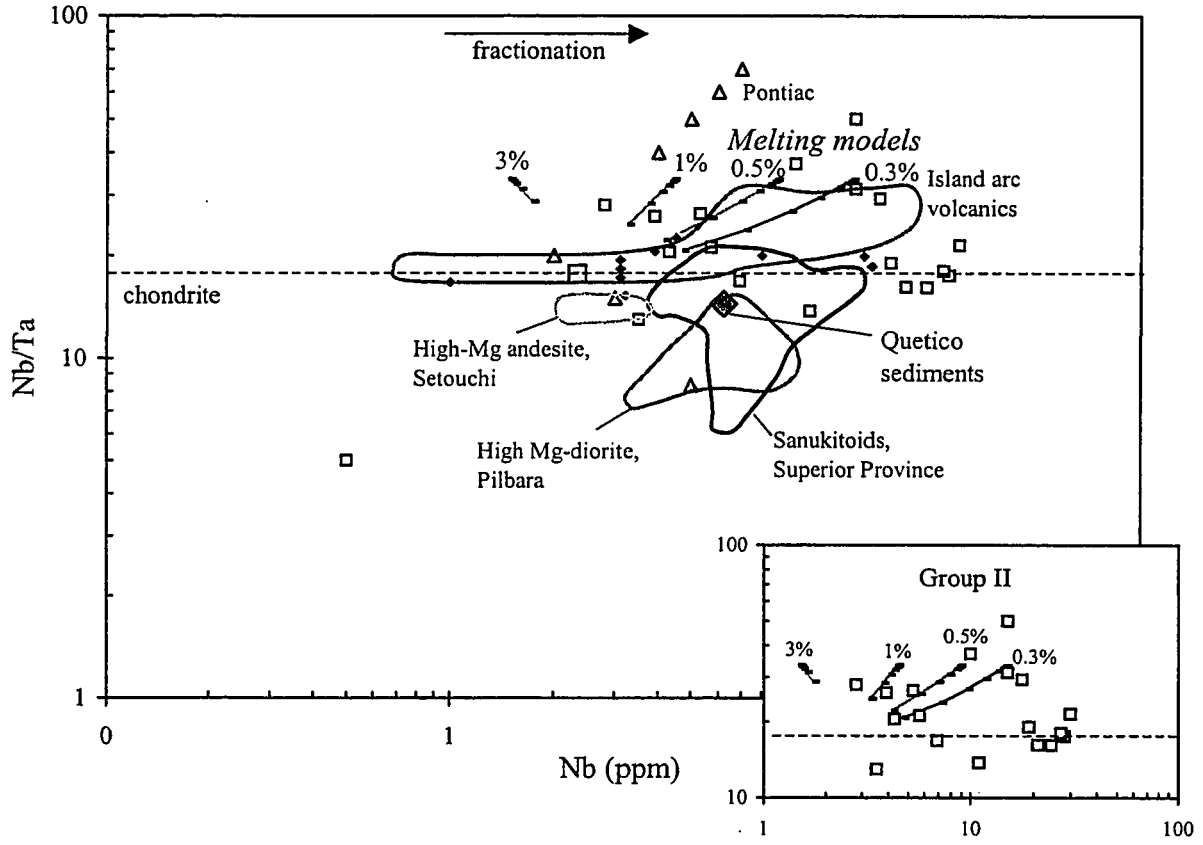

Fig. 3.7. Plot of Nb/Ta versus Nb comparing Group I and II with literature data. Symbols as in Figure 3.4. Also shown are data from LILE-rich intrusions from Pontiac subprovince (grey triangles). Data sources: late Archean sanukitoid suites from adjacent volcanic-plutonic belts in the western Superior Province (Stevenson et al. 1999), high-Mg diorite from Pilbara in western Australia (Smithies and Champion, 2000), high-Mg andesite from Setouchi, Japan (Shinjo, 1999) and island arc volcanics (Stoltz et al., 1996), Pontiac intrusions (Feng and Kerrich, 1992). Also indicated are batch melting models which show degree of Nb/Ta fractionation produced by melting in the presence of residual rutile. The number next to the model indicates percent rutile in the source. The models were computed applying the equation for batch melting (Albarède, 1995). The models use a MORB starting composition and assume a residual mineralogy consisting of olivine, orthopyroxene, clinopyroxene and garnet in addition to rutile. Increments are shown for 40, 20, 10, 5, 2, 1, 0.5, 0.2, 0.1 % degrees of melting. More than 1 % residual rutile bends the melting curve to the left and results in strong Nb-depletion in the melt. Partition coefficients from Jenner et al. (1994). For clarity, the inset shows Group II samples and melting models only. Note the dispersion to highly fractionated Nb/Ta.

Sub-chondritic Nb/Ta within Group II mainly occurs in carbonatite, whereas silicate rocks from Group II are characterized by chondritic to super-chondritic Nb/Ta. The high Nb/Ta of Group II intrusions cannot be produced by shallow level crustal contamination, because the Quetico sediments have Nb/Ta ~ 14, similar to sediments worldwide, which generally have ratios slightly below the chondritic value. If the high Nb/Ta were produced by fractionation of titanite or some other titanium-rich mineral phase, a correlation should be observed between this ratio and a fractionation index. Extraction of titanite strongly increases Nb/Ta in the residual melt fraction, as titanite incorporates Ta with respect to Nb (Green and Pearson, 1997). On the contrary, the highest ratios are observed in the most primitive Group II samples, which are unlikely to have fractionated even minor titanite.

Fractionation of Nb/Ta in potassic arc-related rocks has been attributed to addition of silicate melts from either subducted oceanic crust or subducted sediments in the presence of residual rutile (e.g. Stolz et al., 1996; Elliott et al. 1997). Ryerson and Watson (1987) experimentally showed that rutile is unlikely to be residual in the mantle wedge, where it would also have been extracted by previous melting events. If rutile was involved in the melt production process, it must therefore reside in the subducting slab, in subducting sediments or in the lower crust. Foley et al. (2000) presented new trace element partition coefficients and demonstrated that contrary to the common belief, Nb/Ta fractionation applies equally to dehydration and melting in the presence of residual rutile. If the partition coefficients of Foley et al. (2000) are correct, a possible explanation for the observed variation between Group I and II is metasomatism with two distinct fluids that have been extracted from different reservoirs, one of which contained rutile. This could

be an eclogitic MORB source and an eclogitic sediment source as suggested by Grove et al. (2002) for primitive andesites from Mt. Shasta. If the partition coefficients of other experimental studies are assumed correct (e.g. Brenan et al., 1994) the observed data variation definitely requires a melt contribution from a rutile-bearing reservoir.

Melting models were performed to illustrate the extent to which residual rutile fractionates Nb from Ta in the derivative melts. A MORB source was used as starting composition and other parameters used in modeling are specified in the figure caption. The three models superimposed on Figure 3.7 illustrate the extent of Nb/Ta fractionation during melting with varying percentages of residual rutile in the source, where the number next to the curve denotes the percentage of residual rutile. When the source contains more than 2 % rutile the melting curve bends to the left such that the derivative melts become strongly depleted in Nb. Note that the scale is logarithmic, so even 1 % rutile strongly suppresses the Nb abundance of the derivative melt. The combination of high Nb abundances and superchondritic Nb/Ta in Group II requires derivation from a source with low percentages of rutile and/or strong Nb addition from an independent source.

3.6.2. Fingerprinting source components

Trace element and isotope variations suggest that a multi-component source is required to explain the petrogenesis of the QAS intrusions. The main differences between Group I and II are in key trace element ratios such as Nb/Ta, Ba/Nb and to a lesser extent Nd and Hf isotope ratios. Whatever the model, it will have to account for the close spatial

and temporal location of the two groups of intrusions. Below, the petrogenesis of each group is evaluated separately.

3.6.3. Group I intrusions

The strong enrichment in fluid-mobile LILE, such as Ba, K, Sr and Rb, relative to the less fluid-mobile LILE, such as Th and the LREE, implies significant mass transfer into the source region in the form of a fluid component (e.g. Brenan, 1995; Ayers, 1998). This is also supported by the trend towards high Ba/Nb in Figure 3.5b. The fairly smooth pattern displayed by these intrusions is Figure 3.3a is approximately similar to the pattern produced by hydrous metasomatism (see Bourdon et al., 2002). The absence of excess Nb relative to normal arc rocks (Figure 3.3a) along with increasing Y (and Yb) for increasing SiO_2 (Figure 3.5a) suggests an overall calc-alkaline differentiation path. The trace element variations displayed by Group I in this diagram are similar to most other LILE-rich intrusions from the western Superior Province. Chondritic Nb/Ta implies the absence of rutile in the source. The compositional spectrum of Group I intrusions can to a first approximation be modeled by partial melting of a mantle wedge that had previously been modified by the introduction of variable flux of water-rich fluids liberated by dehydration reactions in a downgoing plate. According to this hypothesis, the fluids were enriched in trace elements that are mobile in such fluids, in particular LILE, relative to trace elements that are immobile in metasomatic fluids, in particular HFSE. The source of the fluids was not rutile-bearing. All samples from Group I have Mg-number $\geq$0.45, which is the maximum attainable Mg-number during melting of basalt (Evans and Hanson, 1997) and

the intrusions can therefore not represent partial melts from the lower crust, but have an ultimate origin in the mantle.

In order to evaluate the magnitude of sediment addition, we first attempted to remove the effect of the subduction component by plotting ratios of non-fluid-mobile elements, thereby as much as possible "seeing through" the subduction imprint. Figure 3.8 is based exclusively on elements and isotope ratios not expected to be added or fractionated by subduction fluids and it shows mixing lines between a MORB source and a sediment component (in this case assumed similar to the Quetico sediments). Tick marks correspond to 5 percent. In (a) is also shown a melting model of a MORB source for comparison. Mixing curves in ratio-ratio diagrams can be straight or hyperbolic, depending on the relative incompatibility of the elements in question (e.g. Langmuir et al., 1978). The hyperbolic mixing curve in (a) and (c) suggests mixing of sources rather than crustal contamination, although minor crustal contamination must have also contributed (see chapter 2). A sedimentary component may have been added in the form of a melt, in which case the end-member is dispersed to the right. The diagrams illustrate that a three-component mixture involving a depleted mantle source, sediments, and slab-derived fluids is required to explain the range in data for Group I intrusions. Slab-derived fluids selectively carry Pb with respect to Nd, which explains the crustal Pb isotope ratios and depleted Nd isotope ratios for Group I intrusions, although a small amount of crustal contamination probably also contributed to the Nd isotopic compositions (see also Chapter 2). Only small volumes of sediment could have mixed with a primitive mantle or a MORB starting composition and still have produced the most magnesium-rich samples.

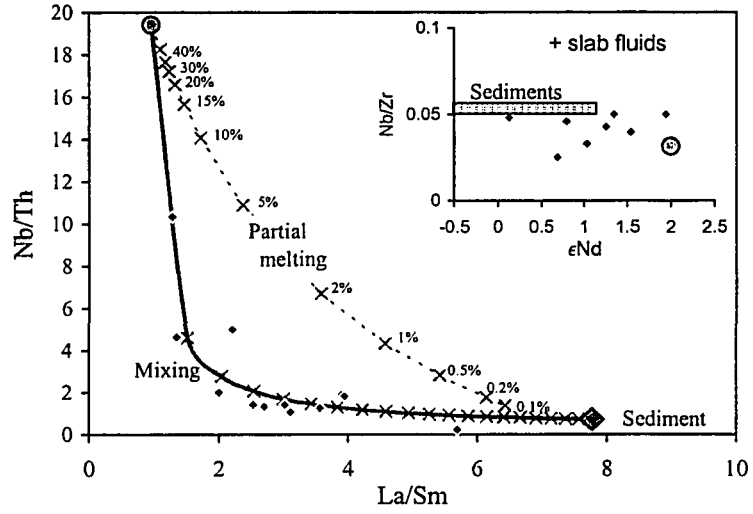
Nb/Th
La/Sm
40%
30%
20%
15%
10%
5%
Partial
melting
2%
1%
0.5%
0.2%
0.1%
Mixing
Sediment
+ slab fluids
Sediments
Nb/Zr
εNd

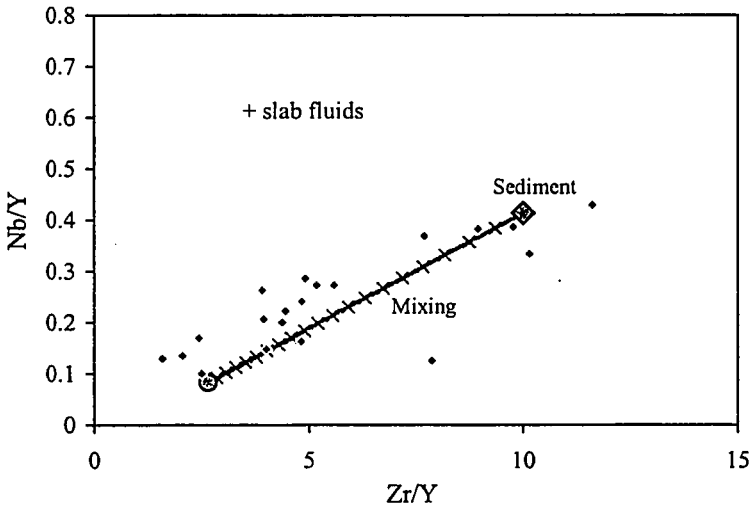
Nb/Y
Zr/Y
+ slab fluids
Sediment
Mixing

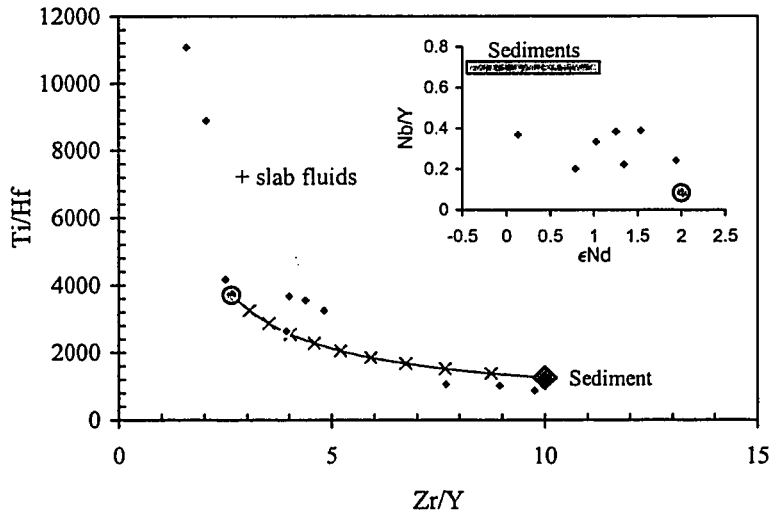
Ti/Hf
Zr/Y
+ slab fluids
Sediments
Nb/Y
εNd
Sediment

Fig. 3.8

Fig. 3.8. Variations of (a) La/Sm with Nb/Th (b) Zr/Y with Nb/Y and (c) Zr/Y with Ti/Hf for Group I intrusions. Superimposed on all diagrams are mixing lines between a MORB source and a sediment component. Tick marks correspond to 5%. In (a) is also shown a calculated batch melting curve for a mixed garnet-spinel lherzolite with MORB as starting composition. In addition (a) and (c) show plots of ϵNd versus Nb/Zr and ϵNd versus Nb/Y for Group I samples. Partition coefficients from Rollinson (1993) and references within.

The petrogenetic model for Group I has similarities to many studies of recent arcs where it is inferred that mixing processes occurred in the mantle wedge between a depleted MORB source, slab-derived fluids and a sediment component (e.g. Ellam and Hawkesworth, 1988; Turner et al., 1996; Elliot et al., 1997). The model is summarized schematically in Figure 3.11a.

3.6.4. Group II intrusions

Group II shares geochemical characteristics of high-Mg diorite and belongs to the "sanukitoid-suite" defined by Stern et al. (1989) and Shirey and Hanson (1984). Experimental work has shown that such rocks can be produced by partial melting of a hydrous, metasomatized upper mantle (Tatsumi, 1981, 1982; Hirose, 1997). However, Group II intrusions display two geochemical characteristics that distinguish them on a regional scale: they extend to superchondritic Nb/Ta and have distinct Nb enrichment patterns. Positive Nb anomalies in Figure 3.3b imply excess Nb relative to "normal" arc rocks, such that Nb has been added to the mantle wedge in larger amounts than expected from fluid metasomatism alone and thus requires input from an additional component.

Several models have been put forward in order to explain excess Nb relative to common arc rocks. Excess Nb can stem from an OIB contribution (Reagan and Gill, 1989) or from an input in the form of a slab melt [an adakite, as defined by Defant and Drummond (1990)] (e.g. Sajona et al., 2000) or a melt derived from subducted sediments (e.g. Shimoda et al., 1998). A slightly different setting is partial melting of a mantle wedge previously metasomatized by slab melts (e.g. Kepezhinskas et al., 1996; Sajona et

al., 1996) or metasomatized by sediment melts. Deep subduction fluids (>100 km depth) are also known to carry higher concentrations of HFSE relative to "normal" subduction fluids (e.g. Churikova et al., 2001, and references therein). Finally, excess Nb may stem from carbonate metasomatism, which causes depletion in HFSE relative to REE with the sole exception of Nb (Rudnick et al., 1993). The most important arguments for and against these models are presented below.

3.6.4.1. Model 1 - OIB

In Figure 3.9 is illustrated average OIB (Sun and McDonough, 1989) along with samples from Group II intrusions. The overall good match could imply the presence of an enriched component in the source of Group II intrusions. An OIB source component has been invoked in several arc studies to explain relatively high Nb/La (e.g. Vroon et al., 1993). Intuitively this is an attractive model as thermal perturbations from incoming OIB in the form of passive upwelling sub-slab asthenosphere could have triggered the onset of partial melting within the mantle wedge. It is also possible that OIB source type material existed as small domains of enriched material within a MORB source mantle wedge. The OIB model explains the presence of positive Nb anomalies combined with the absence of positive Sr anomalies for Group II samples in Figure 3.3b. However, chapter 2 argues against the involvement of OIB source material, mainly on trace element grounds. Trace element pattern of primitive Group II samples, which show minimal effect of fractional crystallization and crustal contamination processes, differ substantially from the OIB pattern. The same argument applies to leucocratic samples. For example, positive Nb

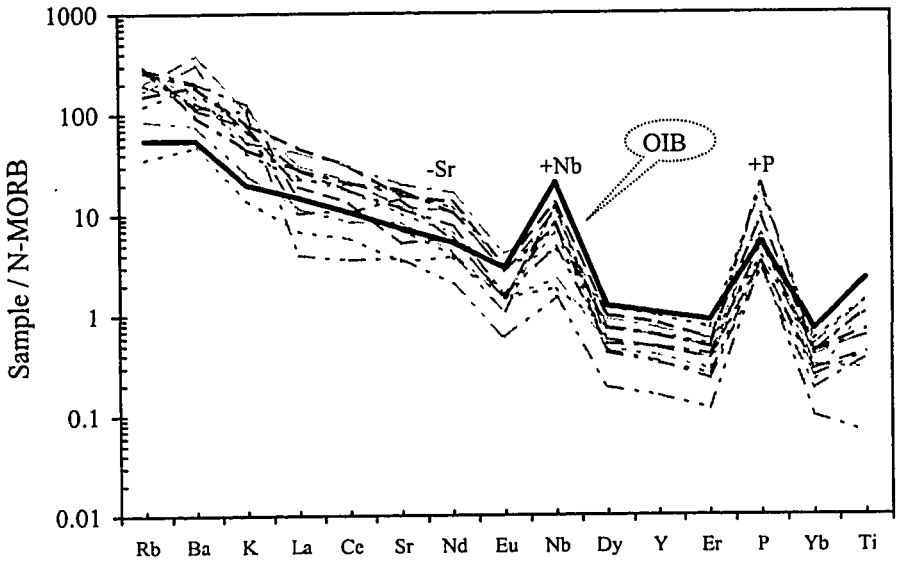

Fig. 3.9. MORB-normalized trace element diagrams for OIB and representative samples of Group II.

anomalies relative to La and K in primitive mantle normalized diagrams are an established characteristic of OIB. Contrary to this, almost all samples show pronounced negative Nb anomalies relative to these elements ($Nb/Nb^* < 1$) and in general the patterns of the Quetico samples in mantle normalized diagrams differ strikingly from that of OIB. In particular, LILE and LREE are more enriched and HFSE significantly more depleted than OIB. As a result, many incompatible trace element ratios fall completely outside established OIB ranges and also outside the compositional range produced by mixing of OIB with a MORB or a primitive mantle starting composition. The latter is particularly true for Th/Yb and Ba/La, which are usually higher, and Nb/U, Ce/Pb and Rb/Cs, which are usually lower. A final argument against OIB control is that Nb/Ta ranges to superchondritic ratios, whereas OIB is limited to chondritic and sub-chondritic values.

3.6.4.2. Model II – Slab fluids

It has been known for some time that deep subduction fluids, liberated where HFSE-rich phases are no longer stable, may carry excess HFSE (e.g. Churikova et al., 2001). As emphasized by these authors, partitioning data also suggest that such fluids have enhanced capability to carry HFSE relative to slab fluids liberated at lower pressures. As stated in section 3.6.1 a possible explanation for the spatial and temporal coincidence of Group I and II could be metasomatism with two distinct fluids that have been extracted from different reservoirs, one of which contained rutile. However, the excess Nb of Group II is too large to result from deep subduction fluids alone. As an example, Nb/Dy

of Group II ranges to 28 times N-MORB, which is not compatible with this model. The trend towards low Ba/Nb in Fig. 3.5b does not suggest significant input from a fluid component and there is further no correlation between Nb/Ta and fluid-controlled trace element ratios such as Ba/La or Cs/Ce (figure not shown).

3.6.4.3. Model III - Carbonate metasomatism

Rudnick et al. (1993) discussed the geochemical effects of carbonate metasomatism and suggested that it leads to fractionation of Nb from other HFSE. Their rationale was that in most carbonatites Nb is slightly enriched relative to REE, when normalized to primitive mantle, whereas other HFSE are strongly depleted relative to REE. Geochemical features of carbonate metasomatism also include fractionation of Nb/Ta and Zr/Hf, which results in superchondritic Nb/Ta and Zr/Hf (Rudnick et al., 1993).

The first argument against carbonate metasomatism as the cause of the enriched Nb signature in Group II intrusions is that there is no obvious difference in Zr/Hf between Group I and II (figure not shown). If carbonatite metasomatism had been involved, a correlation would be expected between Nb/Ta and Zr/Hf, as well as between Ba/La and Zr/Hf, as these ratios behave similarly during carbonate metasomatism, and such correlations are not observed.

The effect of carbonate metasomatism on Lu/Hf is discussed in detail in chapter 4. If carbonate metasomatism was the cause of the Nb peaks in Figure 3.3b, strongly depleted Hf isotope ratios would be expected within Group II samples even if carbonate metasomatism happened shortly before melting. In contrast, ϵHf(T) values overlap with

other intrusions of sanukitoid affinity from the western Superior Province and range between depleted mantle values and those expected for zircons crystallized from magmas with a significant crustal input (Figure 3.6b).

3.6.4.4. Model IV – Slab melt

The presence of samples with trace element characteristics similar to slab melts may be suggestive of the involvement of slab melts in the petrogenesis of Group II. Recently, late Archean adakites were documented in the Wawa subprovince immediately south of the Quetico subprovince (Polat and Kerrich, 2001; Polat and Kerrich, 2002) (see Figure 3.1b) and late Archean Nb-enriched basalts (NEB) were documented in Wabigoon subprovince immediately north of Quetico subprovince (Wyman et al., 2000) (see Figure 3.1b) and interpreted by these authors to be derived from an adakite metasomatized mantle wedge. Like Group II intrusions, the Nb-rich basalts have positive Nb anomalies relative to Eu and Dy (Figure 3.10) and range to superchondritic Nb/Ta. Incorporation of slab melts is in agreement with fractionated Nb/Ta, if the slab was rutile-bearing. Adakitic dacites from the Wabigoon subprovince also have positive Nb anomalies, but display sub-chondritic Nb/Ta (data from Wyman et al., 2000).

An argument against involvement of direct slab melts in the petrogenesis of Group II is that slab melts form during active subduction, and this process is difficult to reconcile with the timing of the QAS intrusions, because they have been interpreted, based on tectonic and geochemical grounds, as having formed after subduction ceased. The problem can be overcome by considering melting of a detached slab of oceanic crust,

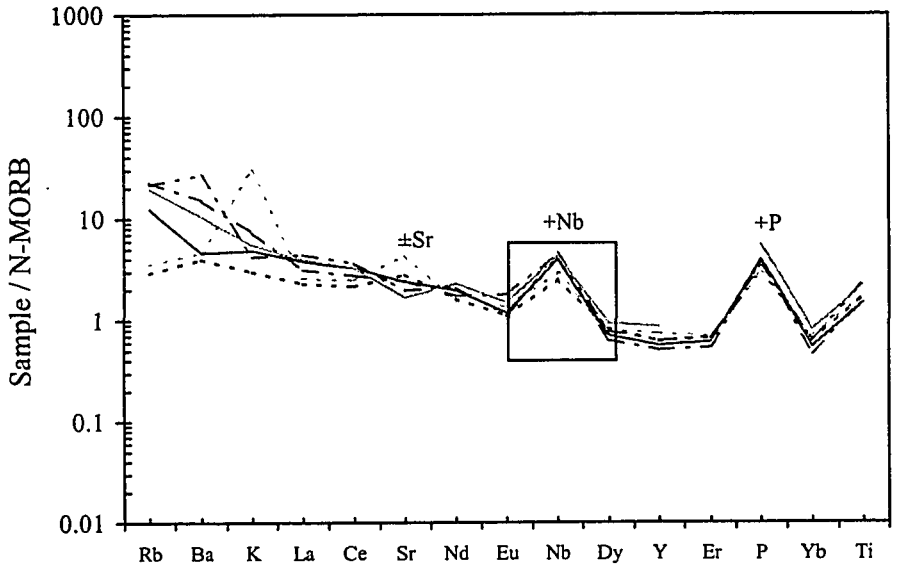

Fig. 3.10. Nb-enriched basalts from the Wabigoon Subprovince (Wyman et al., 2000)

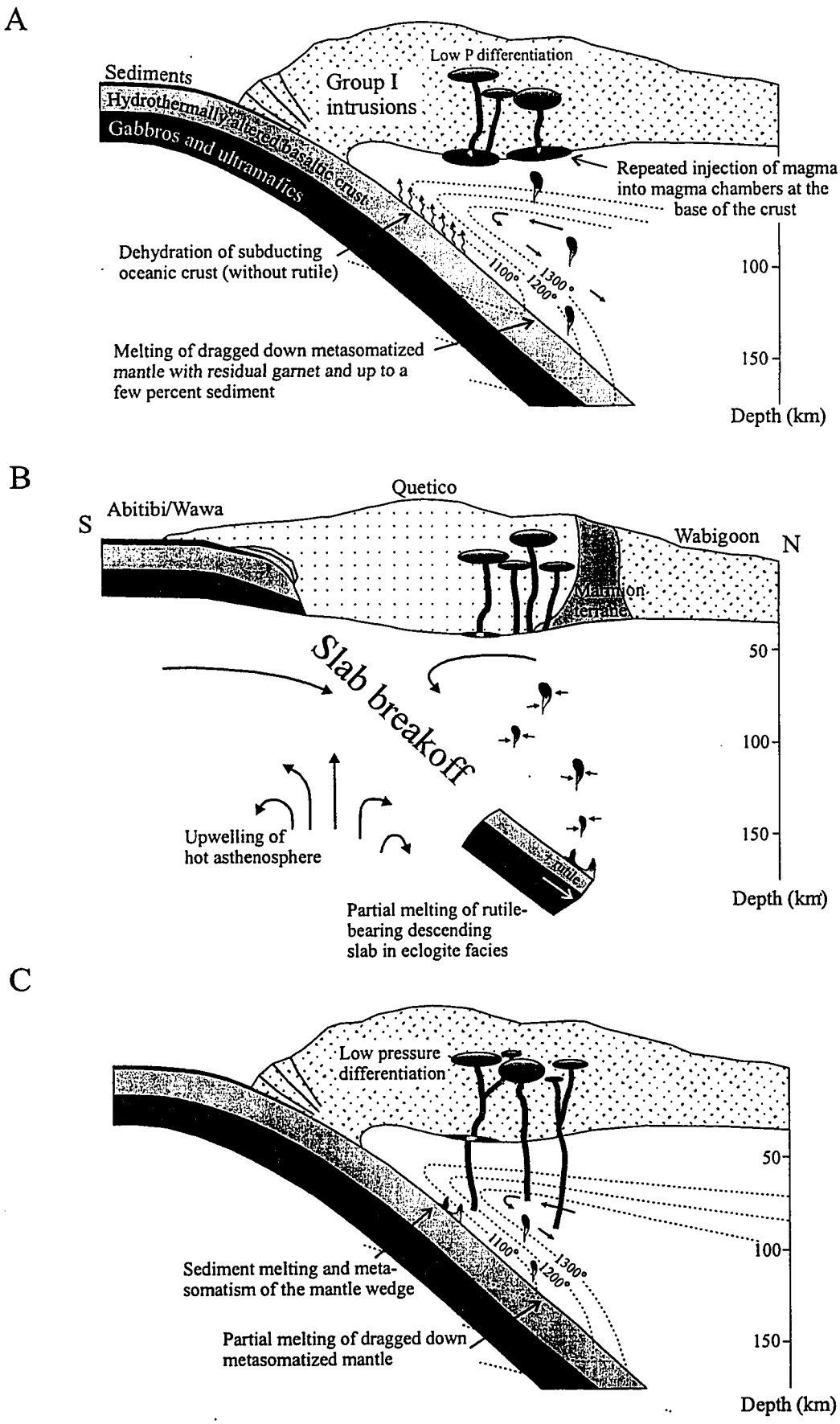
A
Sediments
Hydrothermally altered basaltic crust
Gabbros and ultramafics
Group I intrusions
Low P differentiation
Repeated injection of magma into magma chambers at the base of the crust
Dehydration of subducting oceanic crust (without rutile)
1100°
1200°
1300°
Melting of dragged down metasomatized mantle with residual garnet and up to a few percent sediment
100
150
Depth (km)
B
S
Abitibi/Wawa
Quetico
Wabigoon
N
Marmion terrane
Slab breakoff
50
100
150
Upwelling of hot asthenosphere
rutile
Partial melting of rutile-bearing descending slab in eclogite facies
Depth (km)
C
Low pressure differentiation
50
100
Sediment melting and metasomatism of the mantle wedge
1100°
1200°
1300°
Partial melting of dragged down metasomatized mantle
150
Depth (km)

Fig. 3.11.

Fig. 3.11. Illustration of the possible petrogenetic models for Group I and II intrusions. (a) Group I, which has a narrow range in Nb/Ta close to the chondritic value, originates from a mantle wedge (with originally unfractionated Nb/Ta) which was fluxed by abundant hydrous fluids derived from a slab at pressures where rutile was not stable (b) Group II displays a wide range in Nb/Ta and may originate from melts of a detached slab of oceanic crust with residual rutile that reacted with mantle peridotite en route to the surface (c) A less likely possibility for the generation of Group II is partial melting of a mantle wedge that had been metasomatized by small-degree sediment melts.

where melting can occur some time after the cessation of subduction, when the slab detaches and sinks into the mantle, similar to the model envisaged by Sajona et al. (2000) for the Philippines (Figure 3.11b). This model is in agreement with a back-arc setting for the QAS intrusions. Slab melts may also have been involved in the petrogenesis of group II magmas without being erupted as adakites, because the reaction between slab melt and mantle peridotite is melt consuming (Rapp et al., 1999). The mantle wedge may absorb slab melts as they rise toward the surface, forming a melt-modified mantle wedge, which will be characterized by, among other attributes, high LILE and HFSE (Rapp et al., 1999). Partial melting of such a melt-metasomatized mantle can produce melts with certain slab-melt characteristics, although they do not represent true slab melts (e.g. Schiano et al., 1995). Positive Nb-anomalies in Figure 3.3b and super-chondritic Nb/Ta are in accord with partial melting of a mantle wedge, which had been metasomatized by silicic melts that left rutile in the source. It is not possible with the present data set to determine whether the slab-melt signatures resulted from slab melts that reacted with peridotite on their way to the surface, or were produced by later melting of a slab-melt-metasomatized mantle wedge.

The first melt from a detached slab in the eclogite facies will have $SiO_2 < 63$ % combined with low Mg-number, Ni and Cr concentrations (Yogodzinski et al., 1995) in reasonable agreement with the most SiO_2-rich Group II samples, but the detached slab model requires that the slab melts rose through (and reacted with) at least some mantle peridotite, which would result in significant increases in Mg-number, Ni and Cr concentrations and lower SiO_2 (Caroll and Wyllie, 1989). Such processes could have produced the less SiO_2-rich Group II samples, although most samples have only

moderately high Mg, Ni and Cr contents. Mass balance requires that reaction with peridotite results in lower LILE and LREE abundances relative to pristine slab melts, because the reactions are strongly melt consuming, but trace element ratios such as La/Yb and Sr/Y remain almost unchanged (Rapp et al., 1999), in agreement with the compositional range of Group II samples.

It was shown by Atherton and Petford (1993) that rocks with certain adakite characteristics can be produced by partial melting of underplated, garnet-bearing, mafic lower crust. Such rocks will display low Mg-number, Ni and Cr contents compared to wedge-modified adakites as they have not interacted with mantle peridotite. However, it is difficult to integrate this model with the occurrence of rocks with high Mg-number that are part of Group II. When compared to rocks that have been interpreted as partial melts of underplated basaltic crust, such as the Cordillera Blanca batholith from the South American Cordillera (Petford and Atherton, 1996), Group II samples display significantly lower SiO_2 combined with higher MgO, Al_2O_3 and alkali contents.

3.6.4.5. Model VI - Sediment melt model

An important characteristic of present-day adakites is their MORB-like isotope signatures, which results from melting of depleted basaltic crust without sediment involvement. The enriched Pb isotopic compositions of the QAS intrusions contrast with MORB-like isotopic compositions for high Mg-andesites from the western Aleutians (Kersting and Arculus, 1995) and with modern sanukitoid-like rocks from the Lassen region in California (Borg et al., 2002), but resemble those of Setouchi high-Mg

andesites, which contain a sediment melt component according to Shimoda et al. (1998) and Tatsumi (2001). Both Group I and II intrusions are characterized by enriched Pb isotope compositions, which have been attributed to crustal contamination (see chapter 2). However, the dispersion to more crustal-like Hf isotope compositions for Group II relative to Group I (Figure 3.6b) may indicate that the melt component did not originate from a depleted oceanic slab. The important question is how much of the enriched component resulted from low-pressure crustal contamination and how much is inherited from the source. A possible sediment-melt model is illustrated in Figure 3.11c.

Hf isotope ratios of Group II samples range between depleted mantle values and those expected for zircons crystallized from magmas with a significant crustal input. In support of the slab melt model, samples with Hf isotope ratios close to depleted mantle values are characterized by strong positive Nb anomalies, suggesting that a sediment melt is not the cause of excess Nb. Other parameters also suggest that sediment melt was not involved in the formation of Group II parental magmas. All but 5 samples from Group II intrusions have Th/Ce lower than 0.1, which was considered the lower limit for sediment melt interaction by Hawkesworth et al. (1997). Group II has lower Th/Nb, Th/Ce and Th/Yb relative to late Archean LILE-rich intrusions (sanukitoids) from adjacent greenstone belts (data from Stevenson, 1999) (figure not shown), suggesting a smaller role for a sediment melt in the petrogenesis. On the other hand, LILE-rich intrusions with superchondritic Nb/Ta appear to occur only within the metasedimentary Quetico and the metasedimentary Pontiac subprovinces (Figure 3.7), pointing to the possibility that residual rutile was a characteristic of the sediments. However, there is an anti-correlation between Nb/Ta and Th/Yb for Group II samples, suggesting that superchondritic Nb/Ta

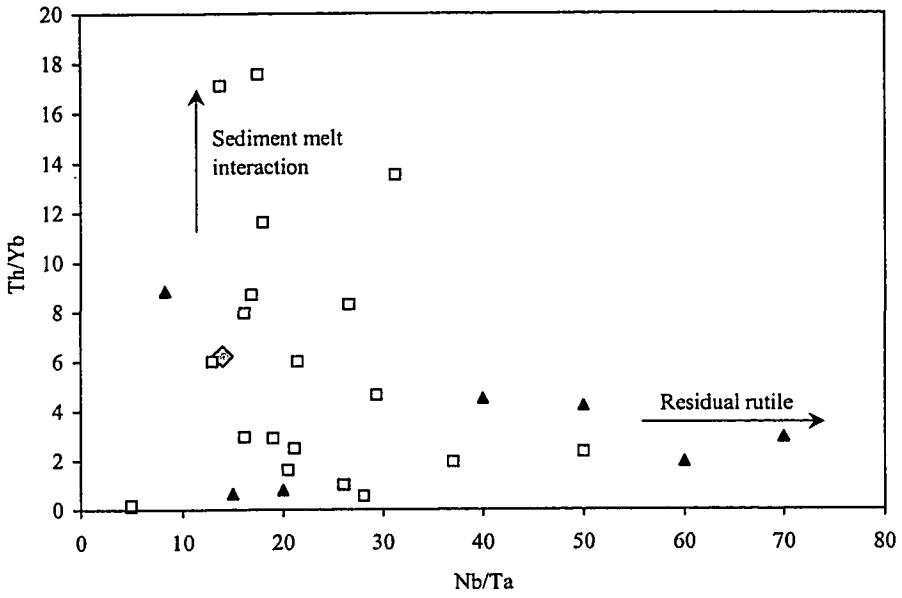

Fig. 3.12. Th/Yb versus Nb/Ta. Symbols as in Fig. 3.4. Black triangles are Pontiac samples. The anticorrelation suggests that sediment interaction is not the cause of superchondritic Nb/Ta.

is not caused by a sediment (melt) component (Fig. 3.12) and supporting the interpretations based on the Hf isotope ratios.

3.7. Summary and conclusions

The QAS intrusions can be subdivided into two groups on the basis of Nb enrichment relative to Dy and Eu in MORB-normalized diagrams. The intrusions are derived from a heterogeneous mantle source that had been variably metasomatized by slab fluids and slab melts. Group I intrusions do not show Nb anomalies with respect to Dy and Eu. The magmas were generated by fluid-enhanced melting of depleted sub-arc mantle wedge and involved three components: MORB-source mantle, slab-derived fluids and a sedimentary component. The latter may have been introduced into the source region in the form of subducted sedimentary material, but some crustal contamination could also account for some of the same geochemical features.

Rocks of Group II are characterized by positive Nb anomalies with respect to Dy and Eu, along with high (superchondritic) Nb/Ta. Their geochemical characteristics resemble those of the sanukitoid suite and several models were evaluated to explain their petrogenesis. It is unlikely that Group II rocks were derived from pockets of enriched material (OIB source) within a mantle wedge because many fractionation-insensitive trace-element ratios, particularly Nb/Ta, are inconsistent with OIB compositions. Different metasomatic agents were considered on the basis of their characteristic trace-element ratios and isotopic compositions. Slab-derived fluids are implausible to explain Nb enrichment and there is poor correlation with fluid-controlled ratios such as Ba/La

and Cs/Ce. Metasomatism by carbonate influx produces fractionation of Nb from Ta as well as Zr from Hf, but Group I and II have indistinguishable Zr/Hf. Mantle metasomatism by a sediment melt derived from a rutile-bearing source could explain the Nb/Ta character of the Group II rocks, but an expected correlation with Th/Yb is not observed. Furthermore, depleted Hf isotope ratios do not favor input of evolved crustal sources. The model that best explains excess Nb, superchondritic Nb/Ta and depleted Hf isotope ratios involves metasomatism by a small-degree melt derived from an isotopically juvenile source leaving residual rutile. The most likely melt source is an oceanic slab, and the process may have involved rise and interaction with the mantle wedge, or wedge metasomatism followed by subsequent melting.

Chapter 4

Evidence for polybaric immiscibility in Archean carbonatite and implications for Lu-Hf isotopic systematics

4.1. Abstract

The late Archean Beaverhouse Lake intrusion is a bimodal syenite carbonatite complex exposed within the western Superior Province. The carbonatite is a high CaO - low alkali sövite with high concentrations of large ion lithophile elements and rare earth elements. It has moderately depleted Nd isotopic signatures ($\epsilon Nd_{2680\ Ma} = +2.2$) and strongly depleted Hf isotopic signatures ($\epsilon Hf_{2680\ Ma} = +10$ to $+18$). Mass balance by least squares major element calculations suggests evolution along a carbonate silicate field boundary. Trace element modeling points to an origin of the carbonatite by liquid immiscibility at shallow crustal levels, which is in keeping with partitioning of trace elements into carbonate and silicate phases. Carbonate-silicate liquid immiscibility at mantle pressures will have pronounced effects of Lu and Hf partitioning and result in high Lu/Hf ratios in the mantle. We present a model in which the highly depleted Hf isotope signatures of the carbonatite result from strong fractionation of Lu/Hf ratios during an episode of carbonate metasomatism.

4.2. Introduction

Despite decades of research, controversy still surrounds the petrogenesis of carbonatites and their genetic relation to associated silicate rocks. In short, experimental studies have focused on three main models, which can explain the origin of carbonatites: (I) Small degrees of melting of carbonated mantle peridotite at pressures greater than 2.5 GPa (e.g. Sweeney, 1994; Harmer and Gittins, 1998); (II) Extreme degrees of fractional crystallization of a carbonated silicate melt at low pressures (e.g. Wyllie, 1987; Lee and Wyllie, 1994); and (III) Immiscible separation of carbonate-rich and silicate-rich liquids from an intermediate parent also at low pressures (Koster van Groos and Wyllie, 1963; Kjarsgaard and Hamilton, 1989; Brooker and Hamilton, 1990; among many others). Over the years, a wealth of experimental studies has been published arguing for and against these processes, even though they all have evidence from both experimental studies and field observations. In particular, liquid immiscibility has been widely debated, including the size of the miscibility gap, the compositional spectrum of carbonatites which can be produced by immiscibility, and the possible extension of an immiscibility field to mantle pressures. Some workers have maintained that immiscibility is restricted to alkali-rich systems (e.g. Harmer, 1999, and references therein) whereas others argued that calcium-rich and alkali-poor compositions can be produced by immiscibility (Kjarsgaard, 1998). Kjarsgaard and Hamilton (1988, 1989) concluded that compositions containing virtually no alkalis, such as sövites, are likely to represent cumulates of immiscible carbonate liquids and Kjarsgaard (1998) showed that silicate-carbonate liquid immiscibility exists

between high CaO - low alkali carbonatite melt and evolved nephelinite between 0.2 and 0.5 GPa and 900-1000°C.

The characteristic intimate association of carbonate and silicate rocks in many alkaline complexes has often been cited in support of liquid immiscibility, while arguments against liquid immiscibility operating in such complexes include the observation that the carbonate-rich phase is generally the last to intrude. This is in conflict with its low density, which should lead to its intrusion before the silicate phase (e.g. Twyman and Gittins, 1987). The density problem in bimodal carbonate-silicate complexes has been addressed by several workers. Brooker and Hamilton (1990) showed experimentally that at 1.5 GPa an immiscible calciocarbonate phase is denser than a nephelinitic melt and thus is likely to intrude after the silicate phase. In addition, Minarik (1998) studied microstructures in immiscible silicate and carbonate melts and demonstrated that due to higher melt-solid interfacial energy the carbonate melt is prevented from migrating independently of the silicate melt and the limited mobility leads the carbonate phase to intrude after the silicate phase has solidified.

The carbonate-bearing Beaverhouse Lake (BHL) intrusion belongs to a suite of late Archean alkaline intrusions within the western Superior Province in Canada (Figure 4.1). It is exposed within the metasedimentary Quetico subprovince about 40 km SW of Atikokan, Ontario. The Quetico subprovince is a belt of deformed, metamorphosed flysch, which is located between the Wawa and the Wabigoon greenstone belts (Percival and Williams, 1989) (Figure 4.1). The BHL intrusion differs from adjacent late Archean alkaline intrusions of the suite by the presence of calcio-carbonatite (sövite) and further displays a number of minor geochemical differences, which can be shown to originate

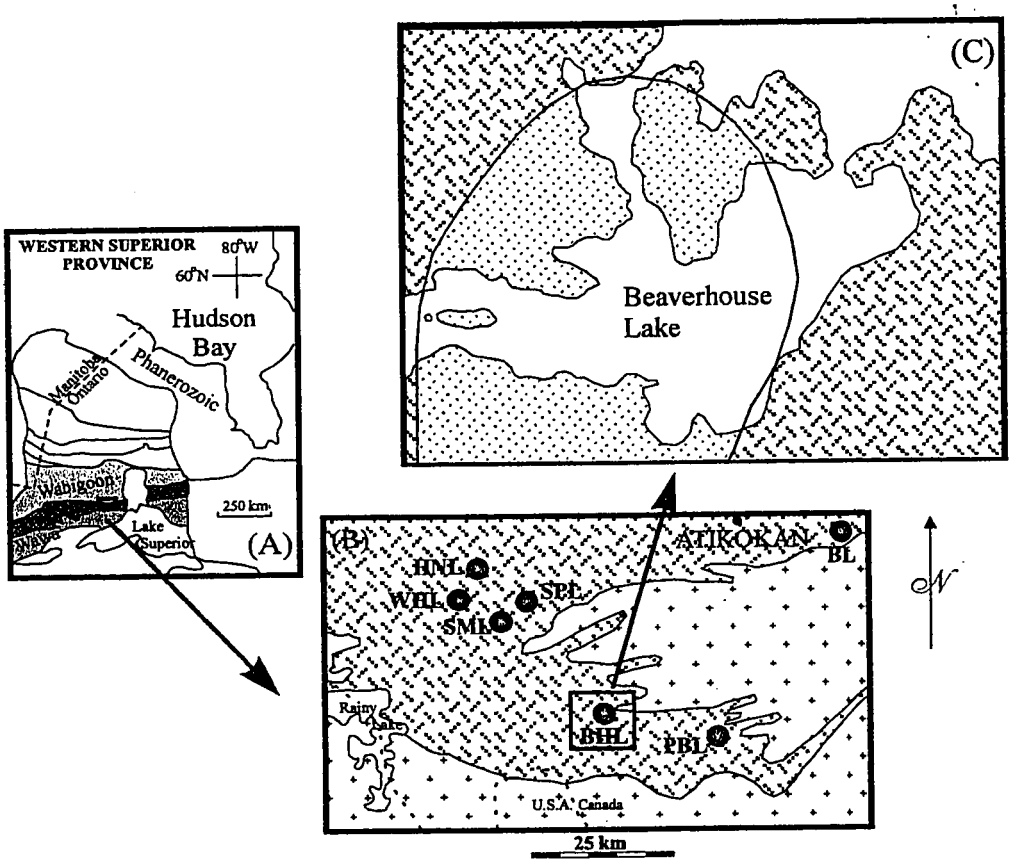

Fig. 4.1. (A) Outline of the western Superior Province. (B) Simplified geological map of part of the Quetico Subprovince. BHL= Beaverhouse Lake intrusion, HNL=Harnett Lake intrusion, WHL=Whalen Lake intrusion, SML=Samuels Lake intrusion, SPL=Surprise Lake intrusion, BL=Blalock intrusion, PBL=Poohbah Lake intrusion. Modified after Stern et al. (1989). Dark grey dotted pattern = Quetico metagreywache and migmatite, black crosses = Quetico granites. (C) Close up of the BHL intrusion.

from the separation of a carbonatite phase. This paper explores the geochemical relationship between the carbonatite and the silicate rocks present within the BHL intrusion and demonstrates the likelihood of liquid immiscibility as the dominant petrogenetic process. It further discusses the potential effect of carbonate-silicate liquid immiscibility on Lu/Hf fractionation and the wider implications of the process. The studied carbonatite differs from other examples in the literature in that two stages of liquid immiscibility may be required to explain both trace element and isotope variations. Other aspects of the petrogenesis of the intrusion, such as the nature of the mantle source(s), are covered in a subsequent paper.

4.3. Geology

4.3.1. The BHL intrusion

The age of the BHL intrusion is not accurately known, but it appears to be about 2680 Ma based on abundant precise U-Pb age determinations on zircon and titanite from other intrusions within the Quetico alkaline suite intrusions, all of which have ages within uncertainty of 2680 Ma (B. Lassen and V. McNicoll, unpublished data). The BHL intrusion is a small alkaline intrusion, which is in clear intrusive contact with slightly older metasediments of the Quetico subprovince. It is circular in outline and approximately 3 km in diameter based on its positive aeromagnetic anomaly, but is mainly exposed in the centre. The BHL intrusion was emplaced at shallow levels in the crust during the final stages of crustal amalgamation within the Superior Province in an

overall compressional tectonic regime, demonstrated by earlier D_1 and later D_2 regional deformation events. The intrusion consists predominantly of syenite with subordinate calcio-carbonatite (~5 %). It is a heterogeneous body, which shows a wide range of textures with significant variation in grain size and modal mineral proportions on outcrop scale. Where the contact to the metasedimentary country rocks is exposed, it is sharp and only minor sedimentary enclaves occur within the intrusion.

4.3.2. The BHL silicate rocks

The silicate rocks are mostly quartz-free syenites, but nepheline-syenites and quartz-syenites are also present. They are medium grained to locally coarse grained, and consist predominantly of variable proportions of strongly twinned microcline, intergrown with sodic plagioclase, euhedral bright green pleochroic aegirine-augite, and two primary amphiboles: sodium-rich hornblende and acicular blue amphibole. Biotite, calcite, quartz, apatite, rare magnetite and titanite are accessory phases. Calcite locally occurs as aggregates of grains. Pseudomorphs after nepheline are common in some parts of the intrusion, but the main part consists of nepheline-free syenite, locally with small amounts of modal quartz. In some outcrops, coarse blocky alkali-feldspar megacrysts are aligned and in others, centimetre-scale layering is defined by alternating alkali-feldspar and biotite-rich zones. Thin syenitic dykes (2-30 cm) with straight contacts and no systematic orientation cut the silicate rocks and net-veining by mm-thick quartz and alkali-feldspar veins is common.

4.3.3. The BHL carbonatite

The carbonatite is in intrusive contact with the syenite, has internal intrusive contacts and contains small fragments of the surrounding syenite. It is medium- to coarse grained, with slightly finer-grained margins. On fresh surfaces, it is white to light grey with a light bluish tint, but it weathers dark brown. The carbonatite consists mainly of calcite and displays igneous textures with coarse, tabular calcite crystals, interpreted as phenocrysts, dispersed in a matrix of medium-grained calcite. Interstitial non-carbonate minerals are irregular patches of sodic amphibole (riebeckite) and sporadically distributed monazite (> 1 %). Ferromagnesian minerals occur in small clusters that are unevenly distributed within the calcite matrix. These consist of bright green euhedral aegirine-augite, intergrown with bright green amphibole and blue riebeckite, perthitic alkali-feldspar, fluor-apatite, rare magnetite and titanite. Apatite locally forms coarse elongate grains. In places, crystals in the calcite matrix are weakly flow aligned, probably due to emplacement as a crustal mush. No carbonate minerals other than calcite were observed.

4.4. Analytical methods

The coarse-grained texture of the carbonatite, combined with erratic distribution of ferromagnesian minerals, complicates representative sample taking, but large amounts of sample were crushed in order to overcome this problem.

Whole rock major and selected trace elements were measured by wavelength dispersive X-ray fluorescence spectrometry (XRF) at the University of Ottawa or the

Geological Survey of Canada. After removal of weathered surfaces, samples were ground to a fine powder in an aluminum oxide ceramic shatterbox, fused with lithium metaborate in platinum crucibles and analyzed on glass discs. Volatiles were determined as loss on ignition by gravimetry at 900°C. A subset of samples were analyzed for H_2O (total) and CO_2 (total) using combustion followed by infrared spectrometry (GSC). FeO was determined by titration (GSC) or calculated from Fe_2O_3 (OU). Estimated errors of major element analyses are ± 1 % of the quoted values. For the silicate rocks, Sc, Hf, Ta, U, Pb, Th and the rare earth elements were determined by inductively coupled plasma mass spectrometry (ICP-MS) at the Geological Survey of Canada, while the carbonatite samples were analyzed for these elements by ACME analytical laboratories, Vancouver, Canada, using similar methods. Detection limits are 0.02 ppm for Ta, Th, U, Dy, Er, Eu, Gd, Ho, Lu, Pr, Sm, Tb, Tm, Y and Yb; 0.1 ppm for Ce, Ga, La and Nd; 0.5 ppm for Zr; 2 ppm for Pb and 0.05 ppm for Hf, Nb, Rb and Zr. Duplicates indicate precision and accuracy for trace element concentrations to be ± 5 % for values greater than 10 times detection limits. Microprobe analyses were obtained with a Cameca SX-50 at the Geological Survey of Canada using wavelength-dispersive X-ray spectrometry, a beam current of 10 nA and a voltage of 20 kV. Natural and synthetic standards were analyzed as unknowns and used for calibration.

Whole rock Nd isotope data were analyzed at Carleton University with a MAT 261 thermal ionization mass spectrometer operating in the static mode. Rock powder was spiked with an appropriate amount of a mixed ^{148}Nd-^{149}Sm tracer and the samples dissolved in sealed Teflon beakers in an HF-HNO_3 solution for 48 hours. Nd and Sm were extracted from whole rock samples through a conventional two stage column

separation procedure and loaded on outgassed double Re filaments with phosphoric acid. Isotope ratios were normalized to a value of $^{146}Nd/^{144}Nd = 0.72190$ to correct for instrumental mass fractionation effects. LaJolla standard gave $^{143}Nd/^{144}Nd$ of 0.511869 ± 0.000014. Isotope ratios are reported without corrections relative to the recommended value for the standard.

Hf isotope data were obtained *in-situ* on zircon with a laser ablation microprobe coupled to a MC-ICPMS at the Danish Lithosphere Centre in Copenhagen. The instrument is a VG-Elemental Axiom equipped with a LSX-200 CETAC quadrupole Nd-Yag laser with a wavelength of 266 nm. Zircons were separated from the carbonatite by standard separation techniques and handpicked under binocular microscope. The extreme low Lu/Hf ratios in zircon make calculation of initial Hf isotope compositions basically insensitive to minor age uncertainties. Analyses were carried out using a 50 μm laser spot size, operating at a pulse rate of 20 Hz. Data was corrected for mass fractionation according to the exponential law using normalization ratios of $^{179}Hf/^{177}Hf = 0.7325$ and $^{178}Hf/^{177}Hf = 1.46717$. The NIST-610 was used as external calibration standard. The typical uncertainty on a single analysis of $^{176}Lu/^{177}Hf$ and $^{176}Yb/^{177}Hf$ is ±0.5-2%. Seven runs of standard JMC-475 gave 0.282147 ± 0.000006.

For calculation of ϵ_{Hf} we assume $^{176}Hf/^{177}Hf = 0.282772$ and $^{176}Lu/^{177}Hf = 0.0332$ of CHUR (Blichert-Toft and Albarède, 1997) and use a ^{176}Lu decay constant of $1.865 \cdot 10^{-11}$ $year^{-1}$ (Scherer et al., 2001). A complete description of instrument setup is published by Willingers et al. (2002) and further details on Hf isotope analyses including interference corrections are presented in chapter 3.

4.5. Mineral chemistry

Calcite within carbonatite contains significant SrO (1.0-1.16 wt %, average 1.05 wt %). It has minor substitution of MgO, FeO and MnO, which reach maximum concentrations of 0.4, 0.6 and 0.3 wt %, respectively. Apatite in silicate and carbonatite rock types contains high F (maximum 4.6 wt %) and has Cl contents below detection limits, but apatite in carbonatite also contains high SrO (~0.6 wt %) compared to apatite within syenite (~0.1 wt %). Aegirine-augite in both rock types is depleted in TiO_2, but accommodates considerable Na_2O (5-7 wt %). The composition of pyroxene in both rock types generally overlap, but aegirine-augite from carbonatite extends to slightly higher MgO and Cr_2O_3 concentrations relative to aegirine-augite from silicate rocks. Two kinds of amphibole are present in both rock types: bright green hornblende, and blue riebeckite with high alkali contents. Like aegirine-augite, amphibole extends to slightly more magnesian compositions within carbonatite. Representative mineral analyses are listed in Table 4.1.

4.6. Geochemistry

4.6.1. Major and trace elements

According to the IUGS recommendation for plutonic rock names (Le Maitre, 1989) the silicate rocks of the BHL intrusion classify as syenites. They have high, but variable, total alkalis (Na_2O+K_2O) ranging from 6 to 13 wt %, and K_2O/Na_2O ratios between 0.8

Table 4.1. Representative mineral analyses of the BHL intrusion

Phase	cpx[1]	cpx[2]	cpx[3]	cpx[4]	amp[5]	amp[1]	amp[4]	Kfs[3]	cal[5]	cal[5]	cal[4]	ap[2]	ap[4]	ap[4]
SiO_2	52.38	53.02	52.81	52.02	43.51	53.70	52.98	65.72	–	–	–	0.46	0.11	0.07
Al_2O_3	0.42	0.89	2.71	1.09	8.68	0.53	1.11	18.74	–	–	–	–	–	–
TiO_2	0.04	0.09	0.31	0.09	0.95	0.02	0.08	–	–	–	–	–	–	–
FeO	19.87	18.53	16.78	16.93	17.76	23.93	16.62	n.d.	0.51	0.36	0.29	0.16	0.06	0.05
MgO	6.55	6.65	6.79	7.55	10.80	8.78	13.29	n.d.	0.36	0.27	0.16	0.03	n.d.	0.03
MnO	0.36	0.50	0.35	0.19	0.51	0.33	0.20	–	0.27	0.25	0.29	0.07	0.03	0.05
CaO	12.80	14.78	14.89	15.20	11.47	2.26	7.19	0.03	52.30	51.54	54.54	55.46	55.17	55.18
Na_2O	6.40	5.05	5.75	5.40	1.23	5.72	3.66	0.72	–	–	–	n.d.	0.17	0.04
K_2O	n.d.	n.d.	0.02	n.d.	1.09	0.23	0.72	16.17	–	–	–	n.d.	n.d.	0.01
P_2O_5	–	–	–	–	–	–	–	–	–	–	–	41.36	40.84	40.69
Cr_2O_3	n.d.	0.06	n.d.	0.11	0.11	0.05	0.03	–	–	–	–	n.d.	0.06	0.03
NiO	–	–	–	–	–	–	–	–	–	–	–	0.06	0.02	0.07
SrO	–	–	–	–	–	–	–	–	1.16	1.00	1.05	–	–	–
BaO	–	–	–	–	–	–	–	0.37	0.09	0.12	0.14	0.05	0.14	0.02
V_2O_5	–	–	–	–	–	–	–	–	–	–	–	0.01	n.d.	0.04
As_2O_3	–	–	–	–	–	–	–	–	n.d.	n.d.	n.d.	–	–	–
ZnO	–	–	–	–	–	–	–	–	n.d.	n.d.	n.d.	–	–	–
SO_3	–	–	–	–	–	–	–	–	0.12	n.d.	n.d.	–	–	–
CO_2	–	–	–	–	–	–	–	–	44.07	44.35	43.64	–	–	–
F	–	–	–	–	–	–	–	–	–	–	–	3.59	3.89	3.66
Cl	–	–	–	–	–	–	–	–	–	–	–	0.01	n.d.	n.d.
Total	99.27	99.59	101.41	98.91	97.13	95.92	96.84	101.75	98.88	97.88	100.15	99.89	101.18	100.58

[1]Syenite BL-99-99, [2]Syenite BL-99-103, [3]Syenite BL-99-104, [4]Carbonatite BL-00-64, [5]Carbonatite BL-00-101

and 1.9. For these samples, MgO, TiO_2, MnO, CaO and P_2O_5 are negatively correlated with SiO_2, while Al_2O_3 and the alkalis show scattered trends. The carbonatite is characterized by elevated CaO, very low total alkalis and low alumino-silicate components. P_2O_5 contents are highly variable (0.03 to 2.1 wt %) and presumably controlled by apatite fractionation or accumulation. The compatible trace elements Ni, Cr, V and Sc are low for all analyzed samples, suggesting that at least the silicates are derived from an evolved magma, which has undergone significant fractionation of ferromagnesian minerals. Representative major and trace element data for silicate and carbonate phases is presented in Table 4.2.

Trace element abundances are illustrated in primitive mantle normalized spider diagrams in Figure 4.2a and b. A country rock analysis (BL-99-38) is included in the trace element diagrams for reference with respect to potential bulk assimilation effects. This is mainly relevant for the silicates, because the strong trace element enrichment in the carbonatite samples is likely to outweigh the effect of any crustal contamination. The carbonatite displays a spiky pattern with strong enrichments and depletions relative to primitive mantle. It has highly elevated concentrations for most large ion lithophile elements (LILE) with enrichment factors reaching 300 times primitive mantle for Sr (Figure 4.2a). This corresponds to Sr contents between 3000 and 6000 ppm. It displays positive anomalies for Th, but extreme depletions in high field strength elements (HFSE) in particular Ti, which reaches values as low as 0.08 times primitive mantle. Nb, Ta, Zr and Hf show less pronounced negative peaks, but are likewise present in very low abundances. The trace element patterns for the carbonate samples are overall similar except that sample BL-99-101 is distinctly enriched in Ba relative to the other samples

Table 4.2. Major element (in wt %) and trace element (in ppm) data for silicate and carbonate phases from the BHL intrusion

Sample #	BL9999	BL99103	BL99104	BL99108	BL99116	BL99101	BL0064	BL0065
Rock type	syenite	syenite	syenite	syenite	syenite	carbonatite	carbonatite	carbonatite
SiO_2	62.40	66.40	44.00	63.85	62.10	1.05	14.11	1.40
TiO_2	0.30	0.05	0.46	0.23	0.19	0.01	0.05	0.01
Al_2O_3	15.60	17.90	17.17	16.48	15.32	0.20	2.89	0.30
FeO_T	2.88	1.17	8.43	2.08	2.58	0.58	1.84	0.66
MnO	0.06	0.02	0.17	0.07	0.10	0.21	0.17	0.19
MgO	1.11	0.51	3.96	0.53	1.08	0.37	0.91	0.39
CaO	3.30	0.86	11.92	2.09	4.08	52.16	41.42	51.99
Na_2O	5.80	6.70	2.04	7.06	5.70	0.00	1.38	0.00
K_2O	6.64	6.35	3.84	5.34	5.64	0.08	0.91	0.14
P_2O_5	0.35	0.16	0.42	0.15	0.31	0.34	2.19	0.04
CO_2	0.2	1.2	n.a	n.a	n.a	n.a	n.a	n.a
H_2O	0.3	0.2	n.a	n.a	n.a	n.a	n.a	n.a
LOI	1.50	0.40	1.20	0.40	0.82	-	-	-
Total	100.50	100.80	95.65	98.70	98.19	55.81	66.99	56.08
Cs	2.60	4.20	n.a	n.a	n.a	0.1	1	0.2
Rb	170	170	198	204	138	2.5	26.6	5.6
Ba	1300	750	738	517	820	460	268	56
Pb	3	2	n.a	n.a	n.a	27.5	17.8	24.1
Sr	910	330	987	389	558	6629.2	5211.3	6581.8
Y	11.0	4.4	17	10	10	130.2	116.9	136.6
Th	2.10	1.80	n.a	n.a	4.4	1.1	4.1	1.6
U	0.72	0.96	n.a	n.a	n.a	0.2	0.9	<0.1
Zr	160	100	261	79	79	18	117	21
Hf	4.20	2.10	n.a	n.a	n.a	7.9	2.8	0.5
Nb	21.0	3.5	11	15	15	0.5	2.8	0.5
Ta	1.30	0.27	n.a	n.a	n.a	0.1	0.1	0.1
Zn	41	16	95	47	57	8	23	10
Ni	12	0	31	6	6	5	12	7
Sc	3.0	0.9	n.a	n.a	n.a	n.a	n.a	n.a
V	34	11	54	17	n.d	< 5	21	< 5
Cr	32	18	7	10	11	0	2	0
Ga	19.0	24.0	n.a	n.a	18.4	1.5	5.5	1.6
La	25.0	10.0	35	36	37	404.3	314.2	295
Ce	76.0	27.0	61	87	110	868.3	745.8	705.3
Pr	11.00	3.60	n.a	n.a	n.a	114.82	101.48	96.67
Nd	49.0	15.0	n.a	n.a	n.a	438.1	398.2	386.4
Sm	8.60	2.60	n.a	n.a	n.a	77.8	73.5	72.1
Eu	2.00	0.61	n.a	n.a	n.a	17.94	17.17	16.64
Gd	19.0	24.0	n.a	n.a	18.4	1.5	5.5	1.6
Tb	0.65	0.21	n.a	n.a	n.a	5.97	5.5	5.77
Dy	2.80	0.86	n.a	n.a	n.a	23.8	22.4	24.84
Ho	0.40	0.14	n.a	n.a	n.a	4.1	3.72	4.36
Er	0.87	0.34	n.a	n.a	n.a	10.32	8.96	10.73
Tm	0.12	0.05	n.a	n.a	n.a	1.38	1.23	1.46
Yb	0.71	0.30	n.a	n.a	n.a	8.45	7.44	8.89
Lu	0.13	0.05	n.a	n.a	n.a	1.11	0.97	1.22

n.a. (not analyzed); n.d (not detected) .

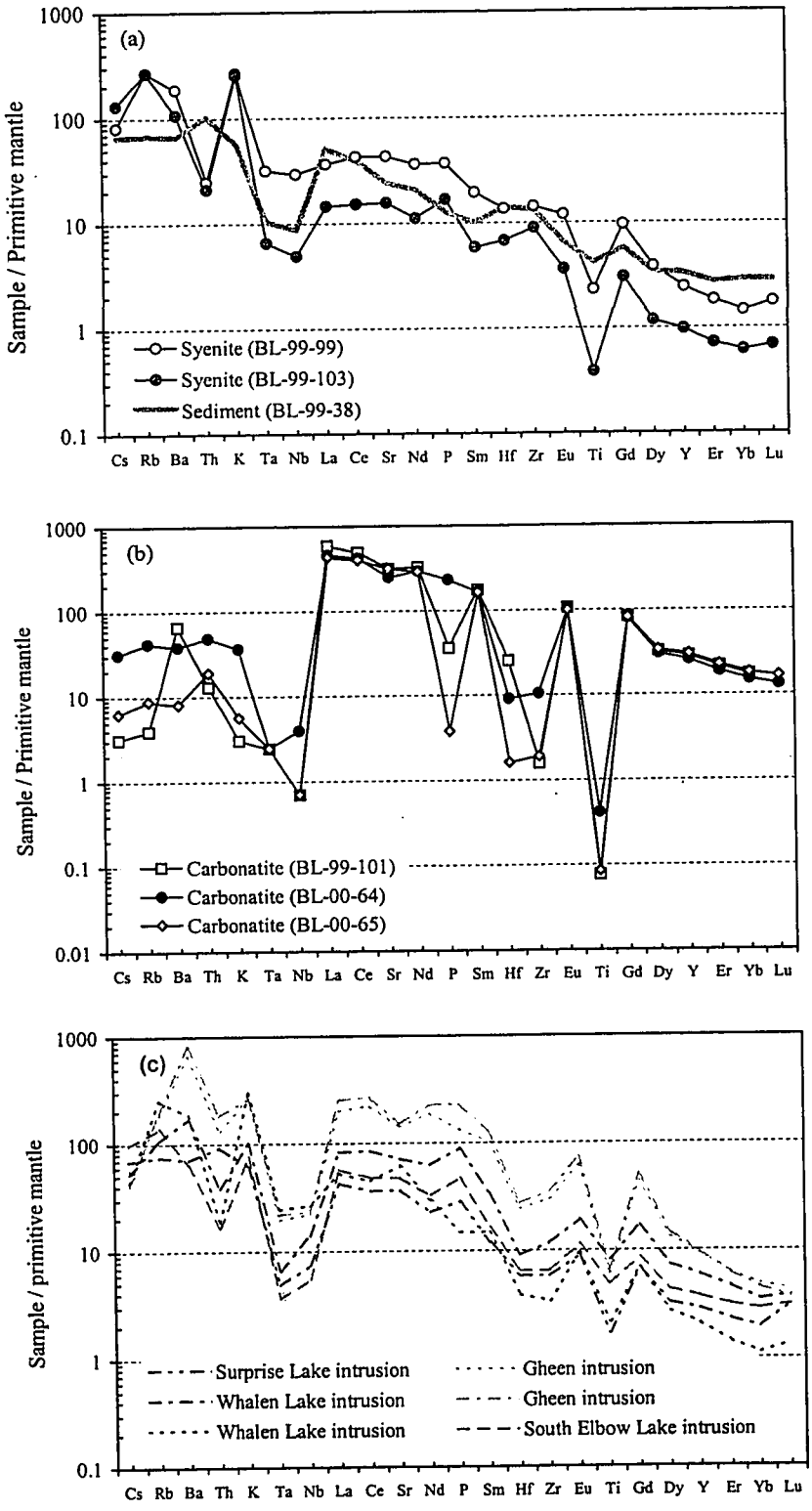
(a)
Sample / Primitive mantle
1000
100
10
1
0.1
Syenite (BL-99-99)
Syenite (BL-99-103)
Sediment (BL-99-38)
Cs Rb Ba Th K Ta Nb La Ce Sr Nd P Sm Hf Zr Eu Ti Gd Dy Y Er Yb Lu
(b)
Sample / Primitive mantle
1000
100
10
1
0.1
0.01
Carbonatite (BL-99-101)
Carbonatite (BL-00-64)
Carbonatite (BL-00-65)
Cs Rb Ba Th K Ta Nb La Ce Sr Nd P Sm Hf Zr Eu Ti Gd Dy Y Er Yb Lu
(c)
Sample / primitive mantle
1000
100
10
1
0.1
Surprise Lake intrusion
Whalen Lake intrusion
Whalen Lake intrusion
Gheen intrusion
Gheen intrusion
South Elbow Lake intrusion
Cs Rb Ba Th K Ta Nb La Ce Sr Nd P Sm Hf Zr Eu Ti Gd Dy Y Er Yb Lu

Fig. 4.2.

Fig. 4.2. Primitive mantle-normalized incompatible trace element variation diagrams for BHL samples and surrounding country rocks (a) BHL silicate samples (b) BHL carbonatite samples (c) syenites and related rock types from other late Archean alkaline intrusions exposed within the Quetico subprovince. Note the differences in patterns between the BHL silicate and the BHL carbonatite samples, and between the BHL silicate rocks and silicate rocks from other intrusions.

and has no negative Hf anomaly. These differences probably reflect erratic distribution of the accessory phases that host these elements. Secondary alteration seems to be an implausible explanation as Hf is highly immobile at surface conditions.

The trace element patterns of the syenites differ strikingly from those of the carbonatite. The syenites have relatively smooth patterns, which are gently sloping from left to right, and notably they display significantly less marked positive and negative anomalies (Figure 4.2b). The most prominent features are peaks at Rb and K and low relative Th and Ti concentrations. These syenites also show differences in trace element patterns relative to syenites and related rock types from other late Archean alkaline intrusions exposed within the Quetico subprovince. In particular, they have less marked depletions in Nb, Ta, Zr and Hf relative to neighboring elements and overall lower trace element abundances, including REE abundances, relative to silicate rocks from other intrusions (Figure 4.2c). These differences are important and have petrogenetic significance as detailed below.

Rare earth element (REE) distribution patterns for carbonate and silicate phases, respectively, from the BHL intrusion are illustrated in Figure 4.3. In general, the REE patterns are strongly fractionated with $(La/Yb)_N$ ratios ranging between 23.8 and 34.3 [where the subscript N denotes chondrite normalized] and $(Dy/Yb)_N$ ratios between 1.8 and 2.6. All samples have very minor negative Eu anomalies. The silicate rocks display moderately high REE contents, while the carbonatite samples have systematically higher REE concentrations, and their REE spectrum lies entirely within the carbonatite field as defined by Nelson et al. (1988). The carbonatite and the silicate units have approximately similar REE distribution patterns, but vary in absolute abundances relative to chondrite,

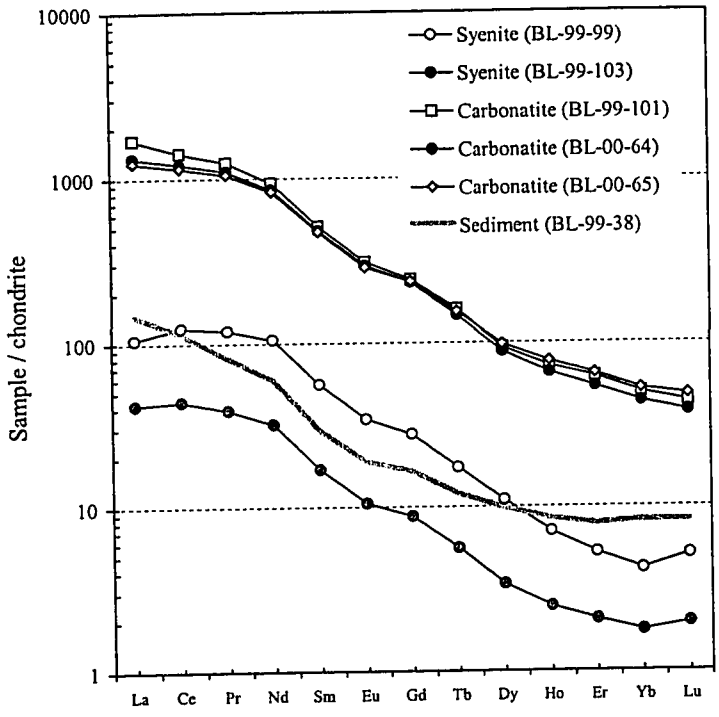

Fig. 4.3. Chondrite-normalized REE compositions of carbonatite and syenite from the BHL intrusion. Sediment sample BL-99-38 is included for comparison. Note the similarity in patterns of silicate and carbonatite phases. Normalizing values taken from Sun & McDonough (1989).

which is typical for carbonatite-bearing complexes worldwide (Möller et al. 1980). On closer inspection, the silicate rocks do, however, show slight convex patterns for the light REE and slight concave patterns for the heavy REE (in particular sample BL-99-99). Such patterns are likely to reflect minor fractionation of aegirine-augite and / or riebeckite consistent with its modal appearance. The closely parallel patterns within each rock type suggest that there has been no significant secondary mobilization of REE. The Quetico sediment BL-99-38, which represents a potential crustal contaminant, has different REE pattern with an overall flat profile for elements heavier than Dy.

With the exception of one carbonatite sample, both the carbonatite and the syenite rocks display sub-chondritic Nb/Ta combined with super-chondritic Zr/Hf, but there is no correlation between Nb/Ta and Zr/Hf. $(Lu/Hf)_N$ are approximately 0.1 for the silicate rocks, but extend to values as high as 10 for the carbonatite. The carbonatite displays extreme Hf depletion relative to middle REE with $(Hf/Sm)_N$ between 0.009 and 0.1. In contrast, the syenites do not show notable Hf depletions and have $(Hf/Sm)_N$ close to unity.

4.6.2. Isotope data

Whole rock Nd isotope data were obtained on both the syenite phases and the carbonatite. The silicate rocks display a restricted range in initial Nd isotope compositions (calculated at 2680 Ma) between 0.50918 and 0.50928 (Table 4.3). This corresponds to ϵ_{Nd} between +0.77 and +2.30 and signifies time-integrated LREE depletion of the source region. The sövite gives ϵ_{Nd} of +2.22 and thus overlaps with the

Table 4.3. Whole-rock Nd data for syenite and carbonatite rocks of the BHL intrusion. Hafnium isotope data are from the carbonatite and obtained by laser ablation on zircon.

Sample #	BL9999	BL99103	BL99104	BL0065	Sample #	BL0065	BL0065	BL0065	BL0065
Rock type	syenite	syenite	syenite	carbonatite		ZR1	ZR2	ZR3	ZR4
$^{147}Sm/^{144}Nd$	0.11226	0.10607	0.11798	0.10505	$^{176}Lu/^{177}Hf$	0.00126	0.00089	0.00142	0.00172
$^{143}Nd/^{144}Nd$ (meas.)	0.511164	0.511153	0.511310	0.511131	$^{176}Yb/^{177}Hf$	0.062569	0.046430	0.075756	0.098327
$^{143}Nd/^{144}Nd$ (init.)	0.511184	0.509278	0.509224 ± 40	0.509274 ± 19	$^{176}Hf/^{177}Hf$ (meas.)	0.281642 ± 88	0.281407 ± 63	0.281443 ± 51	0.281583 ± 59
ϵNd	0.77	2.30	1.25	2.22	$^{176}Hf/^{177}Hf$ (init.)	0.281578	0.281361	0.281370	0.281494
Sm (ppm)	8.2	2.4	5.8	72.5	ϵHf	18.03	10.33	10.66	15.08
Nd (ppm)	44.0	13.5	29.7	416.9					

more radiogenic silicate rocks. These isotope compositions are entirely within the range of previous estimates from other late Archean alkaline complexes within the western Superior Province (e.g. Tilton and Bell, 1994; Stevenson et al., 1999; Henry et al., 1998; Chapter 2, this work). The data is illustrated versus time in Figure 4.4 along with data from other alkaline intrusions and available data on the Quetico sediments. Overlap among Nd isotopic ratios of the carbonatite and the associated silicates permits, but does not prove, a petrogenetic link between them by derivation from a common parental magma by either liquid immiscibility or fractional crystallization.

Henry et al. (1998) report ϵNd(t) between -0.1 and +1.1 for eight sediment samples from the Quetico belt and Vervoort et al. (1999) report ϵNd(t) of -0.5 for one sample, so the country rocks extend to more enriched Nd isotope compositions relative to the intrusive rocks. Digestion of country rock may therefore be responsible for the dispersion towards slightly more enriched compositions of the silicate rocks. The presence of minor sedimentary xenoliths within the BHL intrusion would support such an interpretation. In a study of comparable rocks, the formation of cogenetic quartz and nepheline syenite was attributed by Foland et al. (1993) to the effect of crustal contamination. Crustal contamination should mainly affect isotopic compositions of the silicates (see Ray, 1998).

Initial $^{176}Hf/^{177}Hf$ isotope ratios of the zircons in carbonatite are strongly depleted with respect to CHUR and range between 0.28136 and 0.28157, corresponding to $\epsilon Hf_{(2.68\ Ga)}$ between +10.3 and +18. Nd isotope ratios of carbonatites are believed to closely reflect those of their sources (e.g. Bell and Blenkinsop, 1989), and the highly depleted Hf isotope ratios suggest decoupling between Sm-Nd and Lu-Hf in the source region.

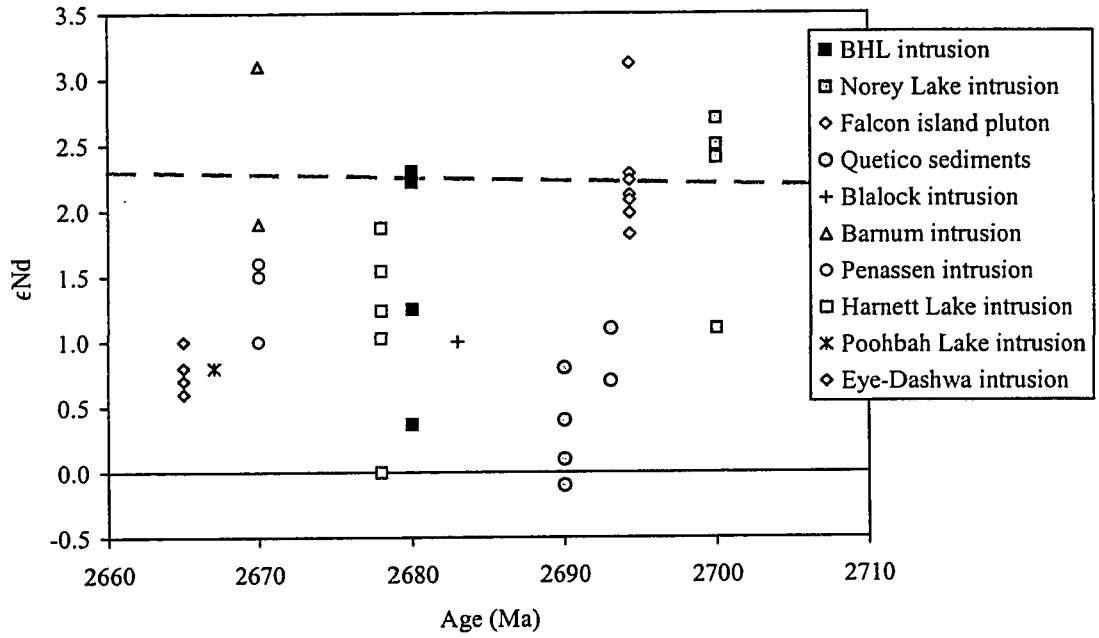

Fig. 4.4. Age versus εNd for the Beaverhouse Lake intrusions and similar type intrusions from the western Superior Province and data on the Quetico sediments. Data compiled from several sources: Poohbah Lake intrusion (Kwon 1986); Falcon Island pluton (Ayer, 1999); Blalock intrusion, Eye-Dashwa intrusion, Penassen intrusion and Quetico sediments (Henry et al., 1998); Barnum intrusion and Norvey Lake intrusion (Stevenson et al., 1999). CHUR = chondrite uniform reservoir.

Hafnium isotope ratios are tabulated in Table 4.3 and the data is displayed in Figure 4.5 along with published Hf isotope data from other late Archean igneous complexes within the western Superior Province. The BHL carbonatite displays Hf isotope ratios which are significantly more depleted than estimated depleted mantle values in the Superior Province at 2680 Ma [ϵHf = +6.5, Davis et al., 2000; Corfu and Noble, 1992]. Hafnium isotope data were not obtained on the silicate rocks, as no zircons were found in them, but syenitic intrusions of similar age from the Quetico subprovince and adjacent greenstone belts have distinctly less depleted Hf isotope ratios and mostly cluster around depleted mantle values, but also range to more enriched compositions (Davis et al. 2000; Corfu and Stott 1993; Chapter 3 this work). The origin of the strongly depleted Hf isotopic signatures of the carbonatite is discussed in a later section.

4.7. Discussion

4.7.1. Origin of carbonatite

This section evaluates whether the BHL carbonatite and silicate rocks are likely to be petrogenetically related. The presence of interstitial primary calcite in the BHL syenites indicates that they originate from a CO_2-bearing parental melt. Stable isotope compositions of calcite in syenite are mantle-like [$\delta^{18}O$ = +8.29 ‰ to +10.57 ‰ relative to SMOW, and $\delta^{13}C$ = -2.91 ‰ to -4.46 ‰ relative to PDB (Hattori and Percival, 1999)] and the analyzed silicate samples have high $CO_2/(H_2O+CO_2)$ ratios, with bulk rock CO_2 contents between 0.2 % and 1.2 % (Table 4.2).

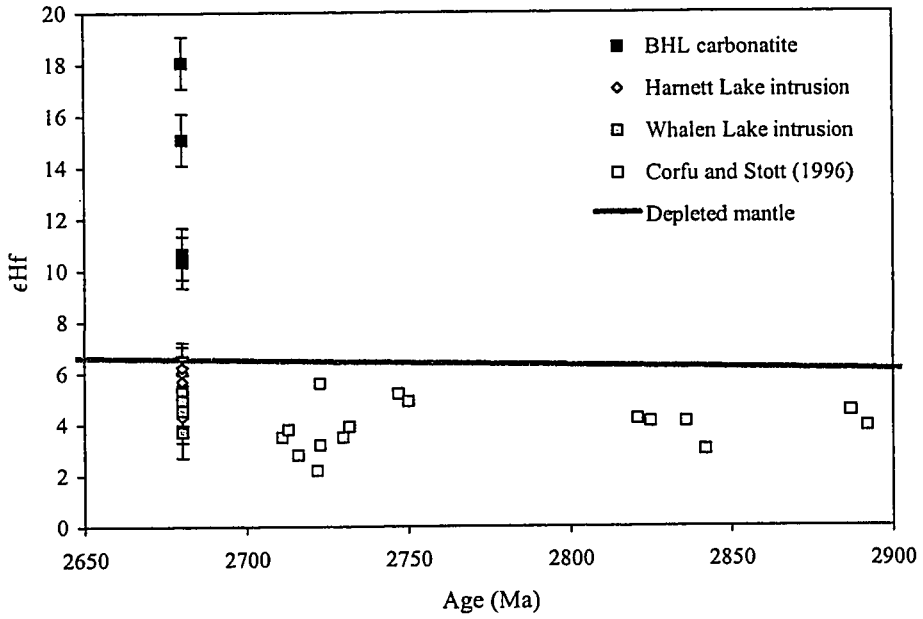

Fig. 4.5. Age versus εHf for the BHL carbonatite and syenites from nearby syenitic Harnett and Whalen Lake intrusions (B. Lassen, unpublished data). Data from the Uchi subprovince (Corfu and Stott, 1996) is included for comparison. The BHL carbonatite is distinctly depleted relative to silicate samples. Depleted mantle curve after Davis et al. (2000),

For the BHL silicate rocks CaO strongly decreases with evolution, which can only be explained by extraction of a carbonate phase during differentiation. Simple mass balance calculations indicate that the decrease in CaO is too large to result from clinopyroxene fractionation alone and substantial albite fractionation can be excluded on the basis of Al_2O_3 and Eu variations. Extraction of apatite and/or melilite can also drastically affect CaO concentrations, but increasing P_2O_5 with evolution renders apatite fractionation not viable to account for the rapid decrease in CaO, and melilite is not likely to be part of the fractionating assemblage, because it has not been observed within the BHL intrusion and in general requires more SiO_2-undersaturated conditions. Assimilation of country rock cannot dilute CaO, because the Quetico sediments have CaO contents as high as the intrusive rocks.

Mass balance calculations were used to model the evolution of the BHL silicate rocks. The modeling is rather complex, because CO_2 is an important constituent of calcite and the system may not have remained closed with respect to CO_2. Therefore the calculations do not provide unique solutions. Water was not included in the calculations. Samples BL-99-99 and BL-99-103 were used as starting and end-composition. If CO_2 is ignored the differentiation interval between 61 and 66.4 wt % SiO_2 is best replicated with a fractionating assemblage including ~ 8 % calcite along with clinopyroxene (aegirine-augite) and alkali-feldspar plus minor amounts of alkali amphibole, biotite and Fe-Ti oxides (Table 4.4). The proportion of fractionated silicate phases corresponds largely to the observed modal assemblages and the best result gives $r^2 = 0.37$, where r^2 is the sum of squared residuals. If CO_2 is included in the mass balance calculations it is necessary to

Table 4.4. Summary of mass balance calculations

Starting composition sample BL-99-99
End composition sample BL-99-103

FC	Excluding CO_2 % liquid left = 0.79 0.37cpx - 0.49Kfs - 0.02 Fe-Ti - 0.02bio - 0.02amp - 0.08cal	$\Sigma r^2 = 0.37$	
FC	Including CO_2 % liquid left = 0.78 0.39cpx - 0.46Kfs - 0.01FeTi - 0.01bio - 0.01amp - 0.14cal	$\Sigma r^2 = 0.62$	
IMM[1]	Excluding CO_2 % liquid left = 0.78 Separation of 16 % carbonatite liquid	$\Sigma r^2 = 0.34$	$[0.94]^2$
IMM[1]	Including CO_2 % liquid left = 0.8 Separation of 15 % carbonatite liquid	$\Sigma r^2 = 0.39$	$[1.01]^2$

FC = fractional crystallization; IMM = immiscibility
[1] Carbonatite from from Cooper and Reid (1998) sample AFC084
[2] Carbonatite from Brooker (1998) sample RB641

add 1.5 wt % CO_2 to the starting composition and the best result involves extraction of 13 % calcite, which gives $r^2 = 0.62$ (Table 4.4).

Regardless of the CO_2 budget the range of data can only be explained if a carbonate phase is being extracted from the system during magmatic differentiation. This suggests that the magma followed a path along a silicate-carbonate field boundary (cotectic) and co-precipitated calcite and silicate phases. The carbonatite could therefore have formed as a result of gravity settling of calcite. However, according to simple mass balance, it is also possible to explain the data by carbonate-silicate liquid immiscibility, concomitant with fractionation of the above mentioned silicate phases, as long as the immiscible carbonate phase is a sövite, which gives $r^2 = 0.94$ (Table 4.4). Below, these models are examined by trace element modeling.

4.7.2. Trace element modeling

Simple fractional crystallization models involving calcite extraction demonstrate that the decrease observed for Ba, Sr and LREE with evolution is not well replicated by trace element modeling. In most cases, the models fail to reproduce the variations and result in insufficient decrease in these elements with evolution. Following the results of major element modeling and using appropriate abundances for Ba in biotite (from McMurry, 2001) and observed Ba concentrations in alkali-feldspar from the BHL intrusion (obtained by electron microprobe), as much as 14000 ppm Ba in calcite is needed to obtain a reasonable match to the model. This is in strong contrast to the range of reported Ba concentrations from trace element studies of calcite in carbonatite complexes (328

ppm to 1395 ppm) (Hornig-Kjarsgaard, 1998) and an order of magnitude higher than the highest value of Ba in calcite actually measured within the BHL carbonatite (~1400 ppm, see appendix 3). Sr variations can be modeled satisfactorily when using the highest reported value for Sr in calcite in carbonatite complexes (12500 ppm, Hornig-Kjarsgaard, 1998), which also corresponds well to the highest measured value from the BHL carbonatite ~ 11100 ppm (Appendix 3). In contrast, results for LREE are ambiguous. Reported La concentrations of calcite in carbonatite complexes range from 115-389 ppm (Hornig-Kjarsgaard, 1998), but it takes ~700 ppm of La in calcite to obtain a reasonable fit. Likewise, the average reported value of Ce in calcite is 368 ppm and the highest reported value 616 ppm (Hornig-Kjarsgaard, 1998), but it requires ~ 2200 ppm Ce to obtain a reasonable match.

These above results suggest that the carbonatite was not formed by fractional crystallization of a carbonated parental magma, but it is nevertheless difficult to totally exclude the model, because minor fractionation of titanite or another REE-bearing mineral would have strongly affected the REE budget.

4.7.3. Liquid immiscibility

Assuming that the silicate and the carbonate phases were in equilibrium, distribution coefficients, K_D, can be used in conjunction with trace element concentrations of the carbonatite and the associated silicate rocks to determine whether the two could be related through liquid immiscibility. Wendtland and Harrison (1979) presented limited K_D data including Ce, Sm and Tm for immiscible carbonate – silicate liquids. A decade

later, K_D's for Ba, Zr, Hf, Ta and certain REE were resolved by Hamilton et al. (1989), and the study of Jones et al. (1995) added K_D for the important element Nb, as well as Th, Pb, U and P to the list. Finally, a newer study by Veksler et al. (1998) extended the range with a number of trace elements, such as Sr, Ti and certain REE not yet determined by others. Using K_D's from several experimental studies obtained under different pressure and temperature conditions and with a variety of methods undoubtedly present a problem. There are minor internal discrepancies between these studies for certain elements as detailed below.

As stated in section 4.1 and illustrated in Figure 4.2, the silicate rocks from the BHL intrusion have certain distinct geochemical characteristics compared to silicate rocks from other LILE-rich intrusions exposed within the metasedimentary Quetico subprovince. These differences include considerably lower REE contents (by a factor of ten) and significantly less marked negative Nb, Ta, Zr and Hf anomalies with respect to adjacent incompatible elements in primitive mantle normalized diagrams. The moderate enrichment in REE in the silicate phases combined with the presence of carbonatite with extremely high REE concentrations is likely to reflect carbonate-silicate liquid immiscibility, according to the experimental results of Bedson (1984) and Hamilton et al. (1989). Alternatively, REE may have been extracted from the system by fractionation of a REE-bearing mineral such as apatite, calcite or monazite. As stated above there is no obvious correlation between P_2O_5 and REE, suggesting that apatite is not controlling the REE budget and the one carbonatite sample with elevated P_2O_5 concentration of 2 wt % does not have the highest REE contents. REE concentrations are higher in the carbonatite by a factor of approximately ten and present in approximately similar quantities in the

various carbonatite samples. These levels are generally significantly lower than those of the average intrusive carbonatite (~ 4000 ppm; Wooley and Kempe, 1989). The limited K_D for REE determined by Hamilton et al. (1989) fit reasonably well with the data, and according to Bedson (1984) higher pressures promote REE partitioning into the carbonate melt.

The observed distribution of HFSE and LILE between carbonate and silicate phases within the BHL intrusion in general matches published K_D values well and explains the observed differences in trace element patterns for the BHL intrusion relative to other alkaline intrusions exposed within the Quetico subprovince. The distribution of Zr and Ta between the carbonatite and the silicate phases is in accord with the absence of negative Zr and Ta anomalies relative to neighboring elements in the silicate phases and the presence of pronounced negative Zr and Ta anomalies, which are an order of magnitude lower than primitive mantle, in the carbonatite (Figure 4.2). Prominent negative Nb anomalies in the carbonatite, combined with no or minor negative Nb anomalies in the associated syenites, can likewise qualitatively be explained by liquid immiscibility. Partition coefficients from Veksler et al. (1998) and Jones et al. (1995) indicate that Nb preferentially partitions into the silicate phase, in accordance with the data. Published partition coefficients match well for U, Ta and Sr and are in reasonable agreement with the relative distribution of Hf and Ba. The difficulty of measuring very low Hf concentrations at the time of writing led to imprecise K_D^{Hf}, but Hamilton et al. (1989) were nevertheless able to conclude that Hf strongly partitions into the silicate phase during immiscibility. Sample BL0064 is enriched in Th relative to the other carbonate

samples and has significantly higher Th contents than expected, but this probably reflects erratic distribution of monazite, which strongly concentrates this element.

The carbonatite is highly enriched in Pb, while the silicate rocks have very low Pb contents (2-3 ppm). These relative Pb concentrations strongly contrast with expected behavior of Pb during silicate-carbonate liquid immiscibility according to partition coefficients of Jones et al. (1995), however Pb is the only element which varies from the expected behavior, in fact behaving oppositely to that expected. Pb is easily mobilized at shallow conditions and may be added or removed during low-grade hydrothermal alteration.

The above discussion suggests that the BHL carbonatite formed by liquid immiscibility, but a fractional crystallization model cannot be totally excluded based on trace element modeling.

4.8. The effect of carbonate – silicate liquid immiscibility on Hf isotope ratios

Within the mantle, garnet is the only mineral known to significantly fractionate the radioactive decay pair Lu-Hf. The only other mineral which fractionates these elements to a lesser degree is orthopyroxene. As a result, the maximum fractionation of Lu/Hf within the mantle has been assumed to be limited by the amount of garnet and orthopyroxene present. The discovery of carbonate – silicate liquid immiscibility textures within mantle xenoliths (e.g. Kogarko et al., 1995) raises an important issue for the Lu-Hf isotope system and potentially has wide implications for the interpretation of Hf isotope data of rocks derived from a carbonated metasomatized upper mantle. In contrast to

mantle melting processes, silicate-carbonate liquid immiscibility strongly decouples Lu from Hf [following the partition coefficients of Hamilton et al., 1989] (Lassen et al., 2002), so that during immiscibility the carbonate liquid becomes highly enriched in Lu relative to Hf, with the degree of enrichment depending on Lu/Hf of the melt prior to immiscibility. Over time, the carbonate fraction will develop radiogenic Hf isotope ratios. The immiscible silicate phase acquires very low Lu/Hf ratios and generates unradiogenic Hf isotope compositions with time. In contrast, carbonate-silicate liquid immiscibility cannot significantly fractionate Sm from Nd (See Veksler et al., 1998) and the process will therefore lead to decoupling of Nd and Hf isotope ratios.

It is well known that the extreme low viscosity of carbonatite melts makes them highly mobile and efficient agents for mantle metasomatism (e.g. Hunter and McKenzie, 1989). High pressure phase relations suggest that the mantle is capable of storing large amounts of carbonate at depths beneath 100 km (Wyllie, 1987 and references cited therein) and the scarcity of carbonatite in mantle xenoliths brought to the surface probably reflects the instability of carbonate at low crustal pressures rather than representing the amount of carbonate actually present within the mantle. Examples of carbonated mantle xenoliths with textural evidence for carbonate-silicate liquid immiscibility are relatively rare in the literature (Amundsen, 1987; Chalot-Prat and Arnold, 1999; Ionov et al., 1993; Kogarko et al., 1995; Pyle and Haggerty, 1994) and significant controversy surrounds these results (e.g. Wyllie and Lee, 1998), but the process has tentatively been suggested on the basis of trace element chemistry of mantle xenoliths (Ionov et al., 1996). Criticism also surrounds the fact that most experimental support for carbonate-silicate liquid immiscibility is found at low pressures and although

it has been known for some time that an immiscibility gap exists at mantle pressures (e.g. Brooker and Holloway, 1997) some workers have questioned how realistic carbonate immiscibility in the mantle really is (e.g. Wyllie and Lee, 1998; Harmer and Gittins, 1998). These authors argue that there is a large gap between plausible liquid paths and the carbonate-silicate liquid immiscibility volume at mantle pressures. Finally, Brooker (1998) demonstrated that the extent of the two liquid field is strongly dependent on degree of CO_2 saturation and that at 2.5 GPa it may require only 6-7 wt % CO_2 for silicate-rich melts to exsolve small amounts of carbonatite liquid. The implication is that if an immiscible origin exists for carbonatites in the mantle, which is now supported by experimental work, this may have pronounced effects on Lu/Hf fractionation and thereby Hf isotope composition of carbonate metasomatized mantle given sufficient time to develop highly radiogenic Hf isotopic signatures. Along comparable lines of reasoning, a recent study by Bizimis et al. (2003) uses experimental partitioning between carbonatite melt and peridotite mineralogy to demonstrate that the mantle source of carbonatites should have approximately similar or higher Lu/Hf than primary carbonatite melts. They measured Lu and Hf concentrations of carbonate fractions of carbonatites and obtained Lu/Hf between 83 and 1160 times that of primitive mantle. The authors concluded that carbonatite sources must be short-lived features, because of the lack of carbonatites with highly radiogenic Hf isotope compositions, but state that this hypothesis awaits acquisition of more Hf data on carbonatites.

The partition coefficient experiments by Hamilton et al. (1989) were conducted at low pressures equivalent to upper and mid crustal conditions and the effect of higher pressures corresponding to upper mantle conditions on Lu and Hf partitioning between

carbonate and silicate melts remains unknown at present. The lack of high-pressure partition coefficients indeed represents an important limitation and additional data is needed to conclusively establish the effect of liquid immiscibility on Lu and Hf partitioning and thereby Hf isotope ratios in metasomatized carbonated upper mantle. However, the experiments by Hamilton et al. (1989) show that within the pressure range analyzed (0.1 – 0.6 GPa) Lu/Hf fractionation strongly increases with increasing pressure at constant temperature. Indirect evidence for Lu/Hf fractionation at mantle pressures can be found in mantle xenolith studies such as those of Dautria et al. (1992), who report distinct positive Hf anomalies relative to Nd in mantle xenoliths, which they interpret to reflect equilibration of garnet lherzolite with a carbonate phase in the upper mantle. They argue that this pattern fits well with the partition coefficients of Hamilton et al. (1989), supporting the concept that REE are held in the carbonate phase while Hf is sequestered in the silicate phases.

4.9. A petrogenetic model

Several models are evaluated to explain the highly radiogenic Hf isotope signatures of the BHL carbonatite. Model I examines whether this signature can be produced simply by derivation from a time-integrated depleted mantle reservoir (i.e. with a large proportion of garnet in the source). If so, this process must be followed by carbonate-silicate liquid immiscibility at crustal pressures to account for the trace element characteristics.

A second group of models considers the effect on Lu/Hf of extracting or adding carbonatite melt to the mantle source. The radiogenic Hf isotope ratios may result from

partial melting of a mantle reservoir that had been modified by previous carbonate melt extraction (*i*); partial melting of a mantle reservoir, which had been modified by carbonate metasomatism, either primary carbonatite melts (*ii*) or secondary carbonatite melts formed by immiscibility from a carbonated parental melt (*iii*). The first two scenarios correspond largely to those described in detail by Bizimis et al. (2003). Both processes require subsequent liquid immiscibility at crustal pressures to account for the trace element signatures. The last scenario leaves a veined mantle consisting of metasomatic phases, which are easily fusible and melt out preferentially, producing melts with high $^{176}Hf/^{177}Hf$, given sufficient time after metasomatism. An initial depletion event is still required to explain the positive epsilon Nd isotope ratios. To explain the coexistence of carbonatite and silicate rocks with trace element pattern of an immiscible liquid combined with highly depleted Hf isotopic signatures in the carbonatite, it is necessary to propose two episodes of carbonate – silicate liquid immiscibility; the first at mantle pressures, causing Lu/Hf fractionation, and the second at crustal pressures, leading to trace element characteristics of immiscible liquids for both carbonate and silicate fractions of the BHL intrusion. This model is illustrated schematically in Figure 4.6. The model largely follows the ideas described by Davies and von Blankenburg (1995) [their Figure 1]. Narrow rifting immediately prior to slab breakoff leads to upwelling asthenosphere, which provides heat for melting at shallow levels. The temporal and spatial proximity to LILE-rich intrusions, which do not show effect of carbonate metasomatism (see chapter 3) suggests this is a one time local event. An initial CO_2-rich melt derived by partial melting of carbonate-bearing peridotite (1) splits into two

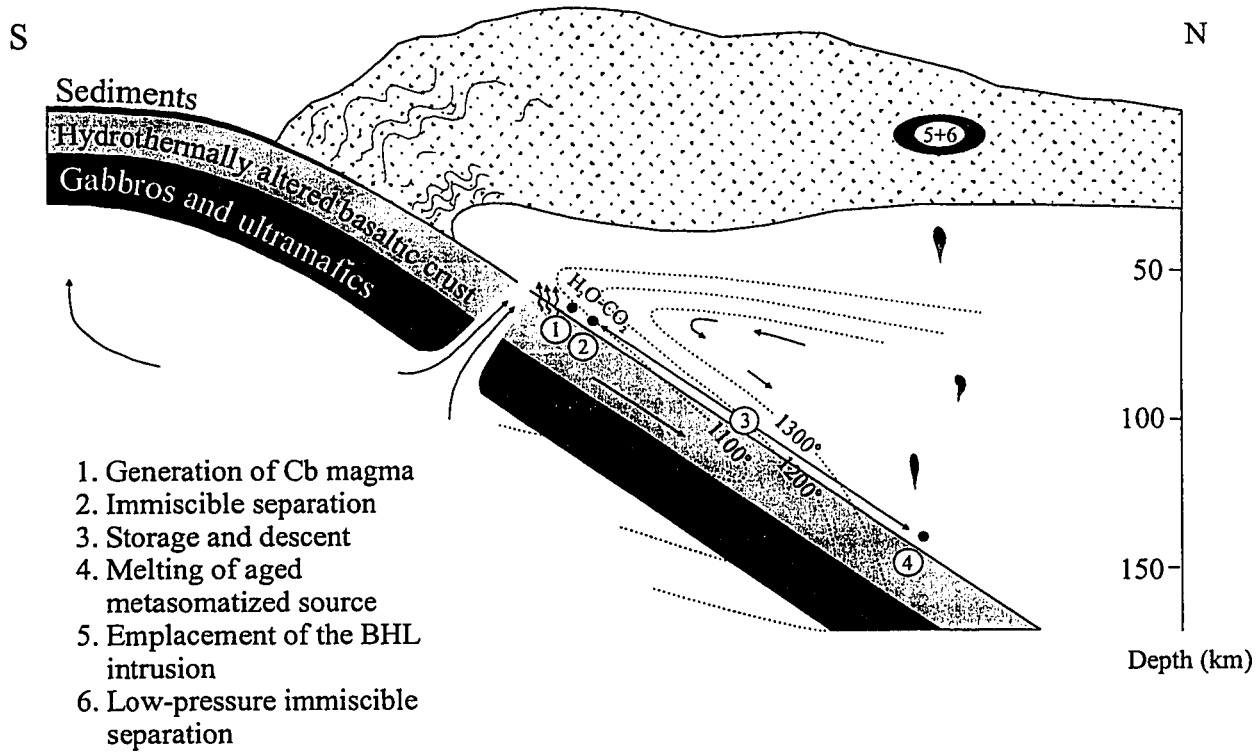

Fig. 4.6. Schematic illustration of the possible tectonic setting for the BHL intrusion. (a) follows the shallow rifting model of Davies and Blanckenburg (1995). The incoming heat source facilitates melting at shallow levels and the melt metasomatized the overlaying mantle wedge. Vertical scale and isotherms are approximate. See text for discussion.

fractions during liquid immiscibility and metasomatizes the upper mantle (2). The immiscibility process fractionates Lu from Hf within the metasomatized mantle. After storage and descent as the slab sinks deeper into the mantle (3) small degrees of melting of the veined lithosphere results in a carbonated silicate melt (4) which rises and finally separates by immiscibility at lower crustal pressures (5).

One critical parameter of all models is time. The BHL intrusion was formed in a recently active tectonic environment; it is post-collisional and about 2680 Ma. Judging from the latest stage of calc-alkaline igneous activity, subduction ended at ~ 2695 Ma, which leaves a maximum of 15 m.y. plus possibly the time from metasomatism or immiscible separation to final descent (path 3 in Figure 4.6) to develop isotopic compositions outside the ordinary range. Assuming that path 3 is ~ 100 km and the down-dip velocity ~ 5 cm/year, storage time will be ~ 2 m.y., which yields a maximum of 17 m.y. for growth of radiogenic Hf. If a very slow down-dip subduction rate is used in modeling (~ 1 cm/year) storage time will increase to ~ 10 m.y. and total time to maximum 25 m.y. If carbonate metasomatism occurred as a result of carbonatites derived from a deeper asthenospheric source, time would be limited to ~ 15 m.y. For a time span of 17 m.y. and assuming a chondritic Hf isotope ratio at the time of metasomatism (2697 Ma), the process would require a source with a minimum $^{176}Lu/^{177}Hf$ of 1.5501 to produce the observed Hf isotope ratios. This corresponds to Lu/Hf of 10.871 [Lu/Hf = 0.238 in chondrite].

The age of the basement to the Quetico sediments is unknown. It may be Marmion (~ 3000 Ma) or juvenile western Wabigoon (~ 2750 Ma). The time dilemma may be accounted for by invoking an old cratonic lithospheric mantle reservoir beneath the

western Superior Province in the late Archean, although there is no supporting evidence that such a reservoir existed. The oldest zircons reported from the Quetico metasedimentary belt are 3100 Ma and presumably supplied from neighboring greenstone belts. However, if 3100 Ma is taken as the upper time limit for mantle fractionation events in the Quetico area and considering the 2680 Ma age of the BHL intrusion, a maximum elapsed time of 420 m.y. can be assumed. If this is valid, a source with a minimum $^{176}Lu/^{177}Hf$ of 0.0963 is needed to produce the observed Hf isotope ratios. This corresponds to a Lu/Hf of 0.6753 [Lu/Hf = 0.238 in chondrite].

Calculations were performed to test the suitability of each model for various time spans. The models assume a chondritic Hf isotopic composition at the time of depletion or metasomatism. With an elapsed time of 15-17 m.y., Model 1, which concerns fractionation produced by garnet residual from a previous melting event, is inadequate. Even in the geologically unrealistic case of a pure garnet residue, a primitive mantle starting composition modified by high degrees of melt extraction cannot generate the observed initial Hf isotope ratios in such a short time span. For an elapsed time of 420 m.y. the Hf isotope ratios can develop within an extremely garnet-rich residual mantle reservoir (> 50 % garnet) with a primitive mantle starting composition, which has been modified by extraction of ~ 40 % melt. For lower degrees of melt extraction (~30 %) as much as 70 % residual garnet is needed to account for the isotope ratios for the same amount of time. We do not consider these cases realistic. Incorporation of subducted material with unusually high REE/Hf contents in the source can help explain the high Hf isotope ratios. Such material includes red clays, which are distinctly enriched in REE, but depleted in Hf, and can have $^{176}Lu/^{177}Hf$ up to 2.6 times chondritic (Patchett et al., 1984),

but this model requires an unrealistically large amount of material with unusual Lu/Hf ratios to explain the data. It seems beyond doubt that some other process controls the Hf isotope signatures of the BHL carbonatite.

Following the ideas presented in Bizimis et al. (2003), model (*i*) assumes that Lu/Hf of a mantle source modified by extraction of carbonatite melt is equal to or greater than that of primary carbonatites. The authors report Lu/Hf of the carbonate fraction of carbonatites from 15.8 to 95.1, which correspond to $^{176}Lu/^{177}Hf$ between 2.2530 and 13.5609, and which they argue is similar to or lower than $^{176}Lu/^{177}Hf$ of the source. Thus for an elapsed time of 17 m.y. the Hf isotope signatures of the BHL carbonatite can easily be accommodated by this model. Using the highest reported value, the Hf isotope ratios can be generated within a time frame of < 2 m.y. after metasomatism. Model (*i*) would, however, result in enriched Nd isotope ratios, which are not observed.

Model (*ii*) involves carbonatite metasomatism and requires a longer time span compared to model (*i*) because the ratio of carbonatite melt to primitive mantle composition will be relatively small. The highest reported Lu/Hf of carbonate by Bizimis et al. (2003) was used in modeling, which is justified because the authors argue that the source should have Lu/Hf equal to *or higher* than the metasomatizing agent. For an elapsed time of 17 m.y. addition of 11 % carbonatite to a primitive mantle starting composition is required to generate the observed initial Hf isotope ratios. The number is fairly large, but not necessarily unrealistic, as a veined mantle may be strongly heterogeneous and the metasomatic phases are most fusible and likely to melt out first. Assuming larger time spans of 50, 100 and 420 m.y., the process requires ~ 4, 2 and 0.5

% carbonatite addition, respectively, to generate the observed initial Hf isotope ratios. Model (*ii*) would also result in enriched Nd isotopic signatures, which are not observed.

The outcome of model (*iii*) is critically dependent on input parameters such as Lu/Hf of the metasomatic melt prior to immiscibility, D_{Lu}/D_{Hf} of immiscible carbonate silicate liquid at mantle pressures (which is not known at present) as well as the proportion of added carbonate to the mantle during metasomatism. The evolution of a primitive mantle starting composition (Sun and McDonough, 1989), modified by addition of various proportions of carbonate formed by immiscibility with various Lu/Hf of the metasomatizing agent prior to immiscibility was modeled using experimental data of Hamilton et al. (1989) obtained at 0.6 GPa. For an elapsed time of 17 m.y. this process requires addition of 8 % carbonate to explain the range in data. If Lu/Hf of the initial metasomatic melt prior to immiscibility was similar to the BHL carbonatite, addition of less than 1 % carbonate melt is required to explain the range in data. In principle, Model (*i*), (*ii*) and (*iii*) can all explain the Hf isotope data, but Model (*iii*) is also in agreement with Nd isotope data.

As stated above, fractionation of Lu/Hf during silicate-carbonate immiscibility at crustal pressures strongly increases with increasing pressure at constant temperature. If this trend continues at mantle pressures, addition of significantly less carbonate would be needed to produce the observed Hf isotope ratios, or alternatively, unusual Hf isotope signatures may develop during very short time spans.

4.10. Summary

Mass balance calculations combined with trace element modeling have shown that carbonate-silicate liquid immiscibility qualitatively explains the geochemical variations among the magmatic components of the BHL intrusion. Overlapping Nd isotope ratios between carbonatite and the more primitive silicates are in agreement with derivation from a common parental magma. Highly depleted Hf isotopic signatures of the carbonatite combined with the moderately depleted Nd isotopic signatures is best explained by involving an episode of carbonate metasomatism in the upper mantle by an immiscibly separated carbonate melt or by derivation from a source which had undergone extraction of carbonatite. Strong fractionation of Lu from Hf during carbonate-silicate liquid immiscibility raises an important issue for the Hf isotope system and potentially has wide implications for the interpretation of Hf isotope data of rocks derived from a carbonate metasomatized upper mantle. These results suggest that high Lu/Hf ratios may be expected in part of the subcontinental lithospheric mantle.

Chapter 5

Summary and conclusions

The late Archean QAS intrusions within the Quetico metasedimentary belt in the western Superior Province contain a wide range of rock types, but display compositionally continuous major-element systematics combined with similar trace element patterns such as high LILE and LREE, along with low HFSE and HREE abundances. These characteristics are typical of subduction-related magmatism and contrast with trace element characteristics in intraplate rift associations.

New U-Pb geochronology adds to the database on late-to post-tectonic, mantle-derived Archean magmatism and establishes a temporal link to sanukitoid suites within the western Superior Province. Previous geochronological data are sparse in the Quetico subprovince, as most work was carried out on intrusions from adjacent subprovinces in particular the Abitibi, Pontiac and Wabigoon subprovinces. Three intrusions (Harnett, Gheen and Blalock) yield U-Pb ages between 2678 and 2683 Ma.

Major and trace element variations of the QAS intrusions are to a large degree controlled by fractional crystallization and can be explained qualitatively by sequential extraction of common ferromagnesian minerals, joined later by Fe-Ti oxides, feldspar and apatite. Zoned, high-pressure clinopyroxene implies mixing due to repeated injection of magma into lower crustal magma chambers. Four intrusions in the northern part of the Quetico belt have low ϵNd values that yield Nd model ages in excess of 2.9 Ga, which suggest the presence of a fragment of ancient crust at depth. This inference builds on the

results of Tomlinson et al. (in press) from the southern Wabigoon subprovince and suggests that the 3.0 Ga Marmion terrain extends at least 10 km southward beneath the Quetico belt. Pb-Pb isotope ratios are entirely dominated by crustal contamination or by a slab fluid component derived from subducting sediments. Quantitative melting models demonstrate that the magmas parental to the igneous complexes formed by partial melting of a trace-element-enriched mantle with distinct garnet signature, but a contribution from melt generated in the spinel stability field is also required to explain the range in REE patterns. Depleted Nd isotope compositions indicate that the enrichment event occurred shortly before magma generation.

The QAS intrusions have been subdivided into two main groups on the basis of their Nb enrichment patterns. Group I intrusions have chondritic Nb/Ta and high Ba/La and chemically resemble late Archean LILE-rich intrusions (sanukitoid suite) from other subprovinces in the Superior Province. These rocks formed by partial melting of a mantle wedge which had undergone fluid metasomatism. The composition of the most abundant group, referred to as Group II, extends to super-chondritic Nb/Ta, has low Ba/Nb and defines a trend towards low Y and Yb for increasing Na and Al. Group II is generally more enriched in terms of incompatible trace elements and isotope compositions, but also contains primitive members. The trace element characteristics of Group II require contributions from small degree melts, either as slab melt additions to the mantle wedge, or as sediment melts from a descending slab, presumably as a mixed fluid-melt metasomatic agent. Super-chondritic Nb/Ta is attributed to addition of melt which left rutile in its source.

Results of field work in the Quetico metasedimentary belt include the discovery of an Archean carbonatite within the Beaverhouse Lake intrusion. The mineral and trace element characteristics of silicate and carbonate composition from the Beaverhouse Lake intrusion were investigated in detail to obtain a model for the petrogenesis of the carbonatite. Using measured trace-element partitioning coefficients between syenite and carbonatite compositions, mass balance calculations of major and trace elements suggest that the carbonatite formed by liquid immiscibility. The petrogenetic model is supported by Nd isotope ratios, which overlap between the silicate and carbonatite compositions, and with the relative volume of carbonatite and silicate phases.

Hf isotope ratios of zircon separated from the carbonatite gave significantly more depleted values than depleted mantle at 2680 Ma. Some evidence has now arisen that carbonatite melts can fractionate Lu from Hf (Lassen et al., 2002; Bizamis et al., 2003), which is important because trace-element enriched carbonatite generated in the upper mantle is thought to be an effective metasomatic agent. Modeling of Lu-Hf partitioning during silicate-carbonate liquid immiscibility suggests that anomalously high $^{176}Hf/^{177}Hf$ should develop with time in the carbonate phase. The Hf isotope signatures of the carbonatite can be explained by invoking a carbonate metasomatic event in the mantle prior to 2680 Ma. The metasomatizing agent that initiated the process could have been either a primary carbonatite melt or a carbonatite formed by high-pressure liquid immiscibility at mantle depths.

List of references

Albarède, F., 1995. Introduction to geochemical modeling. Cambridge University Press pp. 543.

Amundsen, H.E.F., 1987. Evidence for liquid immiscibility in the upper mantle. Nature 327, 692-695.

Arculus, R.J., 1994. Aspects of magma genesis in arcs. Lithos 33, 189-208.

Atherton, M.P., Petford, N., 1993. Generation of sodium-rich magmas from newly underplated basaltic crust. Nature 362, 144-146.

Ayer, J.A., 1999. Petrogenesis of tectonic evolution of the Lake of the Woods greenstone belt, western Wabigoon subprovince, Ontario, Canada. Unpublished Ph.D. thesis University of Ottawa pp. 207.

Ayers, J., 1998. Trace element modeling of aqueous fluid – peridotite interaction in the mantle wedge of subduction zones. Contributions to Mineralogy and Petrology 132, 390-404.

Baker, J.A., Menzies, M.A., Thirlwall, M.F., Macpherson, C.G., 1997. Petrogenesis of Quaternary intraplate volcanism, Sana'a, Yemen: Implications for plume-lithosphere interaction and polybaric melt hybridization. Journal of Petrology 38 1359-1390.

Bèdard, L.P., Ludden, J.N., 1997. Nd-isotope evolution of Archean plutonic rocks in southeastern Superior Province. Canadian Journal of Earth Sciences 34, 286-298.

Bedson, P., 1984. Rare earth element distribution between immiscible silicate and carbonate liquids. Prog. Exp. Petrol. NERC 6th Rep, pp 12-19.

Bell, K., Blenkinsop, J., 1989. Neodymium and strontium geochemistry of carbonatites. In: Bell K (ed.) Carbonatites – genesis and evolution. Unwin Hyman, Boston, pp 278-300.

Bizimis, M., Salters, V.J.M., Dawson, J.B., 2003. The brevity of carbonatite sources in the mantle: evidence from Hf isotopes. Contributions to Mineralogy and Petrology 145, 281-300.

Blichert-Toft, J., Albárede. F., 1997. The Lu-Hf isotope geochemistry of chondrites and the evolution of the mantle-crust system. Earth and Planetary Science Letters 148, 243-258.

Boerboom, T.J., 1994. Alkalic plutons in northwestern Minnesota. *In*: Report of investigations, Minnesota Geological Survey pp. 20-38.

Bogaard, P.J.F., Wörner, G., 2003. Petrogenesis of basanitic to tholeiitic volcanic rocks from the Miocene Vogelsberg, Central Germany. Journal of Petrology 44, 569-602.

Borg, L.E., 1997. The variable role of slab-derived fluids in the generation of primitive calc-alkaline lavas from the southernmost Cascades, California. The Canadian Mineralogist. 35, 425-452.

Borg, L.E., Blichert-Toft, J., Clynne, M.A., 2002. Ancient and modern subduction zone contributions to the mantle sources of lavas from the Lassen region of California inferred from Lu-Hf isotopic systematics. Journal of Petrology 43, 705-723.

Bourdon, E., Eissen, J-P., Monzier, M., Robin, C., Martin, H., Cotten, J., Hall, M.L., 2002. Adakite-like lavas from Artisana volcano (Ecuador): Evidence for slab melt metasomatism beneath the Andean northern volcanic zone. Journal of Petrology 43, 199-217.

Brenan, J.M., Shaw, H.F., Phinney, D.L. and Ryerson, F.J., 1994. Rutile-aqueous fluid partitioning of Nb, Ta, Hf, Zr, U and Th: implications for high field strength element depletions in island arc basalts. Earth and Planetary Science Letters 128, 327-339.

Brenan, J.M., Shaw, H.F., Ryerson, F.J., Phinney, D.L., 1995. Mineral-aqueous fluid partitioning of trace elements at 900°C and 2.0 GPa: constraints on the trace element chemistry of mantle and deep crustal fluids. Geochimica Cosmochimica Acta 59, 3331-3350.

Brooker, R.A., 1998. The effect of CO_2 saturation on immiscibility between silicate and carbonate liquids: an experimental study. Journal of Petrology 39, 1905-1915.

Brooker, R.A., Hamilton, D.L., 1990. Three-liquid immiscibility and the origin of carbonatites. Nature 346, 459-462.

Brooker, R.A., Holloway, J.R., 1997. The role CO_2 saturation in silicate-carbonatite magmatic systems. Geological Association of Canada-Mineralogical Association of Canada Annual Meeting Ottawa, Ont., Abstract A34.

Carignan, C., Gariépy, C., Machado, N., Rive, M., 1993. Pb isotope geochemistry of granotoids and gneisses from the late Archean Pontiac and Abitibi Subprovinces of Canada. Chemical Geology 106, 299-316.

Carignan, C., Machado, N., Gariépy, C., 1995. Initial lead isotopic composition of silicate minerals from the Mulcahy layered intrusion : implications for the nature of the Archean mantle and the evolution of greenstone belts in the Superior Province, Canada. Geochemica et Cosmochimica Acta 59, 97-105.

Carroll, M.R., Wyllie, P.J., 1989. Experimental phase relations in the system tonalite-peridotite-H2O at 15 kb; implications for assimilation and differentiation processes near the crust-mantle boundary. Journal of Petrology 30, 1351-1382.

Castillo, P.R., Janney, P.E., Solidum, R., 1999. Petrology and geochemistry of Camiguin Island, southern Philippines: Insights to the source of adakite and other lavas in a complex arc tectonic setting. Contributions to Mineralogy and Petrology 134, 33-51.

Chalot-Prat, F., Arnold, M., 1999. Immiscibility between calciocarbonate and silicate melts and related wall rock reactions in the upper mantle: a natural case study from Romanian mantle xenoliths. Lithos 46, 627-659.

Churikova, T., Dorendorf, F., Wörner, G., 2001. Sources and fluids in the mantle wedge below Kamchatka, evidence from across-arc geochemical variation. Journal of Petrology 42, 1567-1593.

Cooper, A.F., Reid, D.L., 1998. Nepheline sövites as parental magmas in carbonatite complexes: Evidence from Dicker Willem, Southwest Namibia. Journal of Petrology 39, 2123-2136.

Corfu, F., Noble, S.R., 1992. Genesis of the southern Abitibi greenstone belt, Superior Province, Canada: evidence from zircon Hf-isotope analyses using a single filament technique. Geochimica et Cosmochimica Acta. 56, 2081-2097.

Corfu, F., Stott, G., 1993. Age and petrogenesis of two late Archean magmatic suites, northwestern Superior Province, Canada: zircon U-Pb and Lu-Hf isotopic relations. Journal of Petrology 34, 817-838.

Corfu, F., Stott, G., 1986. U-Pb ages for late magmatism and regional deformation in the Shebandowan Belt, Superior Province, Canada. Canadian Journal of Earth Sciences 23, 1075-1082.

Corfu, F., Stott, G.M., 1996. Hf isotopic composition and age constraints on the evolution of the Archean central Uchi Subprovince, Ontario, Canada. Precambrian Research 78, 53-63.

Davies, J.H., von Blanckenburg, F., 1995. Slab breakoff: A model of lithosphere detachment and its test in the magmatism and deformation of collisional orogens. Earth and Planetary Science Letters 129, 85-102.

Davis, D., Pezutto, F., Ojakangas, R., 1990. The age and provenance of metasedimentary rocks in the Quetico Subprovince, Ontario, from single zircon analyses: implications for Archean sedimentation and tectonics in the Superior Province. Earth and Planetary Science Letters 99, 95-105.

Davis, W.J., McNicoll, V.J., Bellerive, D.R., Santowski, K., Scott. D.J., 1997. Modified chemical procedures for the extraction and purification of uranium from titanite, allanite and rutile in the Geochronology Laboratory, Geological Survey of Canada. Radiogenic Age and Isotopic Studies. Report 10, Geological Survey of Canada 1997-F, 33-35.

Davis, D.W., Amelin, Y., Nowell, G.M., Parrish, R.R., 2000. Constraints on crustal development in the western Superior Province transect from Hf isotopes in zircons. Lithoprobe Western Superior Transect 2000 annual meeting volume pp. 38-44.

Defant, M.J., Drummond, M.S., 1990. Derivation of some modern arc magmas by melting of young subducted lithosphere. Nature 347, 662-665.

Defant, M.J., Kepezhinskas, P., 2001 Evidence suggests slab melting in arc magmas: Eos (Transactions, American Geophysical Union) 82, p. 67-70.

DePaolo, D.J., 1981. Trace elements and isotopic effects of combined wall-rock assimilation and fractional crystallization. Earth and Planetary Science Letters 53, 189-202.

Dautria, M., Dupuy, C., Takjerist, D., Dostal, J., 1992. Carbonate metasomatism in the lithospheric mantle: peridotitic xenoliths from a melilititic district of the Sahara basin. Contributions to Mineralogy and Petrology 111, 37-52.

Edward, A., Griffin, W.L., 1994. Application of proton-microprobe data tp trace-element partitioning in volcanic rocks. Chemical Geology 117, 251-284.

Ellam, R.M., Hawkesworth, C.J., 1988. Elemental and isotopic variations in subduction related basalts: Evidence for a three component model. Contributions to Mineralogy and Petrology 98, 72-80.

Elliot, T., Plank, T., Zindler, A., White. W., 1997. Element transport from slab to volcanic fromt at the Mariana arc. Journal of Geophysical Research 102, 14991-15019.

Evans, O.C., Hanson, G.N., 1997. Late- to post-kinematic Archaean granitoids of the S.W. Superior Province. In: De Wit, M., Ashwal, L. D (eds.) Greenstone belts. Oxford Monographs on Geology and Geophysics 35, 280-295.

Feng, R., Kerrich, R., 1992. Geochemical evolution of granitoids from the Archean Abitibi southern volcanic zone and the Pontiac subprovince, Superior Province, Canada: Implications for tectonic history and source regions. Chemical Geology 98, 23-70.

Foland, K.A., Landoli, J.D., Henderson, C.M.B., Jiangfeng, C., 1993. Formation of cogenetic quartz and nepheline syenites. Geochimica et Cosmochimica Acta 57, 697-704.

Foley, S.F., Barth, M.G., Jenner, G.A., 2000. Rutile/melt partition coefficients for trace element and an assessment of the influence of rutile on the trace element characteristics of subduction zone magmas. Geochimica et Cosmoshimica Acta 64, 933-938.

Fujimaki, H., Tatsumoto, M., Aoki, K., 1984. Partition coefficients of Hf, Zr and REE between phenocrysts and groundmasses. Proceedings of the fourteenth lunar and planetary science conference, Part 2. Journal of Geophysical Research 89, supplement B662-B672,

Gaetani, G.A., Grove, T.L., Bryan, W.B., 1993. The influence of water on the petrogenesis of subduction related igneous rocks. Nature 365, 332-334.

Gill, J.B., 1981. Orogenic Andesites and Plate Tectonics. Springer: Heidelberg, pp 390.

Green, T.H., Pearson, N.J., 1987. An experimental study of Nb and Ta partitioning between Ti-rich minerals and silicate liwuids at high pressures and temperatures. Geochimica et Cosmochimica Acta 51, 55-62.

Griffin, W.L., Pearson, N.J., Belousova, E., Jackson, S.E., O'Reilly, S.Y., van Agterberg, E., Shee, S.R., 2000. The Hf isotopic composition of the cratonic mantle: LAM-MC-ICPMS analysis of zircon megacrysts in kimberlites. Geochimica et Cosmochimica Acta 64, 133-147.

Grove, T.L., Kinzler, R.J., Bryan, W.B., 1992. Fractionation of mid-ocean ridge basalt (MORB). In: Morgan, J. P., Blackman, D.K., Sinton, J.M. (eds.) Mantle flow and

Melt Generation at Mid-Ocean Ridges. Geophysical Monograph, American Geophysical Union 71, 281-310.

Grove, T.L., Parman, S.W., Bowing, S.A., Price, T.C., Baker, M.B., 2002. The role of an H_2O-rich fluid component in the generation of primitive basaltic andesites and andesites from the Mt. Shasta region, N. California. Contributions to Mineralogy and Petrology 142, 375-396.

Hamilton, D.L., Bedson, P., Esson, J., 1989. The behavior of trce elements in the evolution of carbonatites. In: Bell K (ed.) Carbonatites: Genesis and Evolution. London: Unwin Hyman, pp 405-427.

Harmer, R.E., 1999. The petrogenetic association of carbonatite and alkaline magmatism: Constraints from the Spitskop Complex, South Africa. Journal of Petrology 40, 525-547.

Harmer, R.E., Gittins, J., 1998. The case for primary, mantle-derived carbonatite magma. Journal of Petrology 39, 1895-1903.

Hattori, K., Percival, J.A., 1999. Archean carbonate-bearing alkaline igneous complexes of the western Quetico metasedimentary belt, Superior Province, Ontario. Geological Survey of Canada Current Research 1999-C, 221-231.

Hawkesworth, C.J., Hergt, J.M., Ellam, R.M., McDermott, F., 1991. Element fluxes associated with subducyion related magmatism. Philosophical Transactions of the Royal Society of London, Series A 335, 393-405.

Hawkesworth, C.J., Turner, S.P., Peate, D.W., McDermott, F., van Calsteren, P.W., 1997. Elemental U and Th variations in island arc rocks: iomplications for u-series isotopes. Chemical Geology 139, 207-221.

Henry, P., Stevenson, R.K., Gariépy, C., 1998. Late Archean mantle composition and crustal growth in the Western Superior Province of Canada: Neodymium and lead isotopic evidence from the Wawa, Quetico and Wabigoon subprovinces. Geochemica et Cosmochimica. Acta 62, 143-157.

Hildreth, W., Moorbath, S., 1988. Crustal contributions to arc magmatism in the Andes of Central Chile. Contributions to Mineralogy and Petrology 98, 455-489.

Hirose, K., 1997. Melting experiments on lherzolite KLB-1 under hydrous conditions and generation of high-magnesian andesitic melts. Geology 25, 42-44.

Hofmann, A.W., Jochum, K.P., White, W.M., 1986. Nb and Pb in oceanic basalts: new constraints on mantle evolution. Earth and Planetary Science Letters 79, 297-314.

Hornig-Kjarsgaard, I., 1998. Rare earth elements in sovitic carbonatites and their mineral phases. Journal of Petrology 39, 2105-2121.

Hunter, R.H., McKenzie, D., 1989. The equilibrium geometry of carbonate melts in rocks of mantle composition. Earth and Planetary Science Letters 92, 347-356.

Ionov, D.A., Dupuy, C., O'Reilly, S.Y., Kopylova, M.G., Genshaft, Y.S., 1993. Carbonated peridotite xenoliths from Spitsbergen: implications for trace element signatures of mantle carbonate metasomatism. Earth and Planetary Science Letters 119, 283-97.

Ionov, D.A., Bodinier, J-L., Mukasa, S.B., Zanetti, A., 2002. Mechanisms and sources of mantle metasomatism: major and trace element composition of peridotite xenoliths from Spitsbergen of in the context of numerical modeling. Journal of Petrology 43, 2219-2260.

Ionov, D.A., O'Reilly, S.Y., Genshaft, Y.S., Kopylova, M.G., 1996. Carbonate-bearing mantle peridotite xenoliths from Spitsbergen: phase relationships, mineral compositions and trace-element residence. Contributions to Mineralogy and Petrology 125, 375-392.

Irvine, T.N., Barager, W.R.A., 1971. A guide to the chemical classification of the common volcanic rocks. Canadian Journal of Earth Sciences 8, 523-548.

Jenner, G.A., Foley, S.F., Jackson, S.E., Green, T.H., Fryer, B.J., Longerich, H.P., 1994. Determination of partition coefficients for trace elements in high pressure-temperature experimental run products by laser ablation microprobe-inductively coupled plasma-mass spectrometry (LAM-ICPMS). Geochimica et Cosmochimica Acta 58, 5099-5103.

Jones, J.H., Walker, D., Pickett, D.A., Murrell, M.T., Beattie, P., 1995. Experimental investigations of the partitioning of Nb, Mo, Ba, Ce, Pb, Ra, Th, Pa, and U between immiscible carbonate and silicate liquids. Geochimica Cosmochimica Acta. 59, 1307-1320.

Karsten, J.L., Klein, E.M., Sherman, S.B., 1996. Subduction zone geochemical characteristics in ocean ridge basalts from the southern Chile ridge: implications of modern ridge subduction systems for the Archean. Lithos 37, 143-161.

Kelemen, P.B., Yogodzinski, G.M., Scholl, D.W., 2001. Along-strike variation in lavas of the Aleutian island arc: implications for the genesis of high Mg# andesite and the continental crust. AGU Geophysical Monograph Series, submitted 2001.

Kepezhinskas, P., Defant., M.J., Drummond, M.S., 1996. Progressive enrichment of island arc mantle by melt-peridotite interaction inferred from Kamchatka xenoliths. Geochimica et Cosmochimica Acta 60, 1217-1229.

Keppler. H., 1996. Constrains from partitioning experiments on the composition of subduction-zone fluids. Nature 380, 237-240.

Kersting, A.B., Arculus, R.J., 1995. Pb isotope composition of Klyuchevskoy volcano, Kamchatka and North Pacific sediments: Implications for magma genesis and crustal recycling in the Kamchatkan arc. Earth and Planetary Science Letters 136, 133-148.

Kjarsgaard, B.A., Hamilton, D.L., 1988. Liquid immiscibility and the origin of alkali-poor carbonatites. Mineralogical Magazine 52, 43-55.

Kjarsgaard, B.A., Hamilton, D.L., 1989. The genesis of carbonatites by immiscibility. In Bell K (ed.) Carbonatites: Genesis and Evolution. London: Unwin Hyman, pp 388-404.

Kjarsgaard, B.A., 1998. Phase relations of carbonated high-CaO nephelinite at 0.2 and 0.5 GPa. Journal of Petrology 39, 2061-2075.

Kogarko, L.N., Henderson, C.M.B., Pacheco, H., 1995. Primary Ca-rich carbonatite magma and carbonatite-silicate-sulphide liquid immiscibility in the upper mantle. Contributions to Mineralogy and Petrology 121, 267-274.

Koster van Groos, A.F., Wyllie, P.J., 1963. Experimental data bearing on the role of liquid immiscibility in the genesis of carbonatites. Nature 199, 801-802.

Kretz, R., 1983. Symbols for rock forming minerals. American Mineralogist 68, 277-279.

Krogh, T.E., 1982. Improved accuracy of U-Pb ages by the creation of more concordant systems using an air abrasion technique. Geochimica et Cosmochimica Acta 46, 637-649.

Kwon, S-T., 1986. Lead-strontium-neodymium isotope study of the 100 to 2700 Ma old alkalic rock-carbonatite complexes in the Canadian shield: inferences on the geochemical and structural evolution of the mantle. Unpublished Ph.D. thesis University of California, Santa Barbara pp. 226.

Langmuir, C.H., Vocke, R.D., Hanson, G.N., 1978. A general mixing equation with application to Icelandic basalts. Earth and Planetary Science Letters 37, 380-392.

Lassen, B., Hattori, K., Percival, J.A., Wright, T., 2002. Unusually depleted Hf isotopic signatures in late Archean carbonatite, a result of carbonate metasomarism. Geochimica et Cosmochimica Acta 66, A433.

Le Maitre, R.W. (Ed.) 1989. A Classification of Igneous Rocks and Glossary of Terms. Blackwell, Oxford, 129 pp.

Lee, W-J, Wyllie, P.J., 1994. Experimental data bearing on liquid immiscibility, crystal fractionation and the origin of calciocarbonatites and natrocarbonatites. International Geology Review 36, 797-819.

Lee, W-J, Wyllie, P.J., 1998. Processes of crustal carbonatite formation by liquid immiscibility and differentiation, elucidated by modal systems. Journal of Petrology 39, 2005-2013.

MacKenzie, J.M., Canil, D., 1999. Composition and thermal evolution of cratonic mantle beneath the central Archean Slave Province, NWT, Canada. Contributions to Mineralogy and Petrology 134, 313-324.

Mahood, G.A., Baker, D.R.., 1986. Experimental constraints on depths of fractionation of mildly alkalic basalts and associated felsic rocks: Pantelleria, Strait of Sicily. Contributions to Mineralogy and Petrology 93, 251-264.

Martin, H., 1994. The Archean grey gneisses and the genesis of the continental crust. *In* Condie (ed.) Archean Crustal Evolution. Development in Precambrian Geology, 11. New York: Elsevier, pp. 205-258.

Maury, R.C., Defant, M.J., Joron, J-L., 1992. Metasomatism of the sub-arc mantle inferred from trace elements in Philippine xenoliths. Nature 360: 661-663.

McMurry, J., 2001. Crystal accumulation and shearing in a megacrystic quartz monzonite: Bodocó Pluton, Northeastern Brazil. Journal of Petrology 42, 251-276.

MacTavish, A.D., 1992. The geology, petrology, geochemistry of the Quetico intrusions, northwestern Ontario. Unpublished M.Sc. thesis, Lakehead University, Thunder Bay, Ontario, Canada, 219 pp.

Minarik, W., 1998. Complications to carbonate melt mobility due to the presence of an immiscible silicate melt. Journal of Petrology 39, 1965-1973.

Möller, P., Morteani, G., Schley, F., 1980. Dissolution of REE distribution patterns of carbonatites and alkalic rocks. Lithos 13, 171-179.

Moyen, J.–F., Martin, H., Jayananda, M., 2001. Multi-element geochemical modelling of crust-mantle interactions during late-Archean crustal growth : The Closepet granite (South India) : Precambrian Research112, 87-105.

Nelson, D.R., Chivas, A.R., Chappell, B.W., McCulloch, M.T., 1988. Geochemical and isotopic systematics in carbonatite and implications for the evolution of ocean-island sources. Geochimica et Cosmochimica Acta 52, 1-7.

Neumann, E.–R., Wulff-Pedersen, E., Simonsen, S.L., Pearson, N.J., Martí, J., Mitjavila, J., 1999. Evidence for fractional crystallization of periodically refilled magma chambers in Tenerife, Canary Islands. Journal of Petrology 40, 1089-1123.

Nixon, G., Johnston, A.D., 1997. Nature and origin of primitive magmas at subduction zones. Canadian Mineralogist 35, 253-256.

Pan, Y., Fleet, M.E., 1994. Granulite-facies metamorphism in the Quetico subprovince, north of Manitouwadage, Ontario. Canadian Journal of Earth Sciences 31, 1427-1439.

Pan, Y., Fleet, M.E., Heaman, L., 1998. Thermo-tectonic evolution of an Archean accretionary complex: U-Pb geochronological constrints on granulites from the Quetico Subprovince, Ontario, Canada. Precambrian Research 92, 117-128.

Paster, T.P., Schauwecker, D.S., Haskin, L.A., 1974. The behavior of some trace elements during solidification of the Skaergaard layered series. Geochimica et Cosmochimica Acta 38, 1549-1577.

Patchett, P.J., White, W.M., Feldmann, H., Kielinczuk, S., Hofmann, A.W., 1984. Hafnium/rare earth element fractionation in the sedimentary system and crustal recycling into the Earth's mantle. Earth and Planetary Science Letters 69, 365-378.

Peacock, S.M., 1990. Fluid processes in subduction zones. Science 248, 329-337.

Pecerillo, R., Taylor, S.R., 1976. Geochemistry of Eocene calc-alkaline volcanic rocks from the Kastamonu area, Northern Turkey. Contribution to Mineralogy and Petrology 58, 63-81.

Percival, J.A., 1989. A regional perspective of the Quetico metasedimentary belt, Superior Province, Canada. Canadian Journal of Earth Sciences 26, 677-693.

Percival, J.A., Sullivan, R.W., 1988. Age constraints on the origin of the Quetico belt, Superior Province, Canada. In: Radiogenic and isotope studies: Report 2; Geological Survey of Canada, Paper 88-2, 97-107.

Percival, J.A., Williams, H.R., 1989. Late Archean Quetico accretionary complex, Superior Province, Canada. Geology 17, 23-25.

Petford, N., Atherton, M., 1996. Na-rich partial melts of metabasalt at 8-32 kbar: Implications for continental growth and crust-mantle recycling. Journal of Petrology 36, 891-931.

Polat, A., Kerrich, R., 2001. Magnesian andesites, Nb-enriched basalts-andesites, and adakites from late Archean 2.7 Ga Wawa greenstone belts, Superior Province, Canada: Implications for late Archean subduction zone petrogenetic processes. Contributions to Mineralogy and Petrology 141, 36-52.

Polat, A., Kerrich, R., 2002. Nd-isotope systematics of ~2.7 Ga adakites, magnesian andesites, and arc basalts, Superior Province: evidence for shallow crustal recycling at Archean subduction zones. Earth and Planetary Science Letters 202, 345-360.

Presnall, D.C., Dixon, S.A., Dixon, J.R., O'Donnel, Y.H., Brenner, N.L., Schrock, R.L., Dycus, D.W., 1978. Liquidus phase relations on the join diopside-forsterite-anorthosite from 1 atm to 20 kbar: their being on the generation and crystallization of basaltic magmas. Contributions to Mineralogy and Petrology 66, 203-220.

Pyle, J.M., Haggerty, S.E., 1994. Silicate-carbonate liquid immiscibility in upper-mantle eclogites: Implications for natrosilicic and carbonatitic conjugate melts. Geochimica et Cosmochimica Acta 58, 2997-3011.

Rapp, R.P., Shimizu, N., Norman, M.D., Applegate, G.S., 1999. Reaction between slab-derived melts and peridotite in the mantle wedge: experimental constraints at 3.8 GPa. Chemical Geology 160, 335-356.

Ray, J.S., 1998. Trace element and isotope evolution during concurrent assimilation, fractional crystallization, and liquid immiscibility of a carbonated silicate magma. Geochimica et Cosmochimica Acta 52, 3301-3306.

Reagan, M.K., Gill, J.B., 1989. Coexisting calc-alkaline and high-niobium basalts from Turrialba volcano, Costa Rica: implications for residual titanites in arc magma source. Journal of Geophysical Research 94(B4), 4619-4633.

Reiners, W.P., Hammond, P.E. McKenna, J.M., Duncan, R.A., 2000. Young basalts of the central Washington Cascades, flux melting of the mantle, and trace element signatures of primary arc basalts. Contributions to Mineralogy and Petrology 138, 249-264.

Rollinson, H., 1993. Using geochemical data: Evaluation, Presentation, Interpretation. John Wiley and Sons, Inc., New York, 352 pp.

Rudnick, R.L., McDonough, W.F., Chappel, B.W., 1993. Carbonate metasomatism in the northern Tanzanian mantle: petrographic and geochemical characteristics. Earth and Planetary Science Letters 114, 463-475.

Ryerson, F.J., Watson, E.B., 1987. Rutile saturation in magmas: implications for Ti-Nb-Ta depletion in island-arc basalts. Earth and Planetary Science Letters 86, 225-239.

Sage, R.P., Lightfoot, P.C., Doherty, W., 1996. Bimodal cyclical Archean basalts and rhyolites from the Michipicoten (Wawa) greenstone belt, Ontario: geochemical evidence for magma contributions from the asthenospheric mantle and ancient

continental lithosphere near the southern margin of the Superior Province. Precambrian Research 76, 119-153.

Sajona, F.G., Maury, R.C., Pubellier, M., Leterrier, J., Bellon, H., Cotton, J., 2000. Magmatic source enrichment by slab-derived melts in a young post-collisional setting, central Mindanao (Philippines). Lithos 54, 173-206.

Samaniego, P., Martin, H. Robin, C., Monzier, M., 2002. Transition from calc-alkalic to adakitic magmatism at Cayambe volcano, Ecuador: Insights into slab melts and mantle wedge interactions. Geology 30, 967-970.

Saunders, A.D., Norry, M.J., Tarney, J., 1991. Fluid influence on the trace element composition of subduction zone magmas. In: Tarney, J., Pickering, K.T., Knipe, R.J., Dewey, J.F. (eds.) The Behavior and Influence of Fluids in Subduction Zones. London: The Royal Society, pp. 151-166.

Scherer, E., Münker, C., Mezger, K., 2001. Calibration of the Lutetium-Hafnium clock. Science 293, 683-687.

Sen, C., Dunn, T., 1994. Dehydration melting of a basaltic composition amphibolite at 1.5 and 2.0 GPa: implications for the origin of adakites. Contribution to Mineralogy and Petrology 117, 394-409.

Scherer, E., Münker, C., Mezger, K. 2001. Calibration of the Lutetium-Hafnium clock. Science 293, 683-687.

Schiano, P., Clocchiatti, R., Shimizu, N., Maury, R.C., Jochum, K.P., Hofmann, A.W., 1995. Hydrous, silica-rich melts in the sub-arc mantle and their relationship with erupted arc lavas. Nature 377, 595-600.

Shimoda, G., Tatsumu, Y., Nohda, S., Ishizaka, K., Jahn, B., 1998. Setouchi high-Mg andesites revisited: geochemical evidence for melting of subducted sediments. Earth and Planetary Science Letters 160, 479-492.

Shinjo, R., 1999. Geochemistry of high Mg andesites and the tectonic evolution of the Okinawa Trough-Ryukyu arc system. Chemical Geology 157, 69-88.

Shirey, S.B., Hanson, G.N., 1984. Mantle-derived Archean monzodiorite and trachyandesites. Nature 310, 222-224.

Shirey, S.B, Hanson, G.N., 1986. Mantle heterogeneity and crustal recycling in Archean granite-greenstone belts : evidence from Nd isotopes and trace elements in the Rainy Lake area, Superior Province, Ontario, Canada. Geochimica et Cosmochimica Acta 50, 2631-2651.

Sisson, T.W., Grove, T.L., 1993. Experimental investigations of the role of H2O in calc-alkaline differentiation and subduction zone magmatism. Contributions to Mineralogy and Petrology 113, 143-166.

Smith, I.E.M., Williams, I.G., 1978. Proceedings, 1978 Archean Geochemistry Conference, p. 369.

Smithies, R.H., Champion, D.C., 2000. The Archean high-Mg diorite suite: Links to tonalite-trondhjemite-granodiorite magmatism and implications for early Archean crustal growth. Journal of Petrology 41, 1655-1671.

Southwick, D.L., 1991. On the genesis of Archean granite through two-stage melting in the Quetico accretionary prism at a transpressional plate boundary. Geological Society of America Bulletin 103, 1385-1394.

Stacey, J.S., Kramers, J.D., 1975. Approximation of terrestrial lead isotopic evolution by a two-stage model. Earth and Planetary Science Letters 26, 207-221.

Stern, R.A., Hanson, G.N., 1991. Archean High-Mg granodiorite: A derivative of light rare earth element-enriched monzodiorite of mantle origin. Journal of Petrology 32, 201-238.

Stern, R., Hanson, G.N., Shirey, S.B., 1989. Petrogenesis of mantle-derived LILE-enriched Archean monzodiorite and trackyandesite (sanukitoids) in southwestern Superior Province. Canadian Journal of Earth Sciences 26, 1688-1712.

Stern, C.R., Kilian, R., 1996. Role of the subducted slab, mantle wedge and continental crust in the generation of adakites from the Andean Austral Volcanic Zone. Contributions to Mineralogy and Petrology 123, 263-281.

Stevenson, R., Henry, P., Gariépy, C., 1999. Assimilation-fractional crystallization origin of Archean sanukitoid suites: Western Superior Province, Canada. Precambrian Research 96, 83-99.

Steward, R.B., Price, R.C., Schmith, I.E.M., 1996. Evolution of high-K arc magma, Egmont volcano, Taranaki, New Zealand: evidence from mineral chemistry. Journal of Volcanology and Geothermal Research 74, 275-295.

Stoltz, A.J., Jochum, K.P., Spettel, B., Hofmann, A.W., 1996. Fluid- and melt-related enrichment in the subarc mantle: evidence from Nb/Ta variations in island-arc basalts. Geology 24, 587-590.

Strecheisen, A., 1976. To each plutonic rock its proper name. Earth-Science Reviews 12, 1-33.

Sun, S.S., McDonough, W.F., 1989. Magmatism in the ocean basins. Saunders, A.D., Norry, M.J. (eds.) Geological Society of America Special Publication 42, 313-345.

Sweeney, R.J., 1994. Carbonatite melt compositions in the Earths mantle. Earth and Planetary Science Letters 128, 259-270.

Tatsumi, Y., Eggins, S., 1995. *Subduction zone magmatism*. Cambridge, US: Blackwell Science, pp. 211.

Tatsumi, Y., 1981. Melting experiments on a high-magnesian andesite. Earth and Planetary Science Letters 54, 357-365.

Tatsumi, Y., 1982. Origin of high-magnesium andesites in the Setouchi volcanic belt, southwest Japan: II. Melting phase relations at high pressures. Earth and Planetary Science Letters 60, 305-317.

Tatsumi, Y., Ishizaka, K., 1982. Origin of high-Mg andesites in the Setouchi volcanic belt, southwest Japan, I. Petrographical and chemical characteristics. Earth and Planet Science Letters 60, 293-304.

Tatsumi, Y., 2001. Geochemical modeling of partial melting of subducting sediments and subsequent melt-mantle interaction: Generation of high-Mg andesites in the Setouchi volcanic belt, southwest Japan. Geology 29, 323-326.

Thirlwall, M.F., Upton, B.G.J., Jenkins, C., 1994. Interaction between continental lithosphere and the Iceland plume-Sr-Nd-Pb isotope geochemistry of Tertiary basalts, NE Greenland. Journal of Petrology 35, 839-879.

Tilton, G.R., Bell, K., 1994. Sr-Nd-Pb isotope relationships in late Archean carbonatites and alkaline complexes: Applications to the geochemical evolution of Archean mantle. Geochimica et Cosmochimica Acta 58, 3145-3154.

Thy, P., 1991. High and low pressure phase equilibria of a mildly alkalic lava from the 1965 Surtsey eruption: experimental results. Lithos 26, 223-243.

Tomlinson, K.Y., Stott, G.M., Percival, J.A., Stone, D. Basement terrane correlations and crustal recycling in the western Superior Province: Nd isotopic character of granitoid and felsic volcanic rocks in the Wabigoon subprovince, N. Ontario, Canada. Precambrian Research (in press.).

Turner, S., Hawkesworth, C., Rogers, N., Bartlett, J., Worthington, T., Hergt, J., Pearce, J., Smith, I., 1996. ^{238}U-^{230}Th disequilibria, magma petrogenesis and flux rates beneath the depleted Tonga-Kermadec island arc. Geochimica et Cosmochimica Acta 61, 4855-4884.

Twyman, J.D., Gittins, J., 1987. Alkalic carbonate magmas: Parental or derivative? In: Fitton JG, Upton BGL (eds.) Alkaline igneous rocks. Geological Society of London Special Publication 30, 85-94.

Veksler, I.V., Petibon, C., Jenner, G.A., Dorfman, A.M., Dingwell, D.B., 1998. Trace element partitioning in immiscible silicate-carbonate liquid systems: an initial experimental study using centrifuge autoclave. Journal of Petrology 39, 2095-2104.

Vervoort, J.D., Blichert-Toft, J., 1999. Evolution of the depleted mantle: Hf isotope evidence from juvenile rocks through time. Geochimica et Cosmochimica Acta 63, 533-556.

Vervoort, J.D., Patchett, P. J., Blichert-Toft, J., Albàrede, F., 1999. Relationships between Lu-Hf and Sm-Nd isotope systems in the global sedimentary system. Earth and Planetary Science Letters 168, 79-99.

Vroon, P.Z., van Bergen, M.J., Varecamp, J.C., 1993. Sr-Nd-Pb isotope systematics of the Banda arc, Indonesia. Combined subduction and assimilation of continental material. Journal of Geophysical Research 98, 22,349-22,366.

Wagner, C., Mokhtari, A., Deloule, E., Chabaux, F., 2003. Carbonatite and alkaline magmatism in Taourirt (Morocco): Petrological, geochemical and Sr-Nd isotope characteristics. Journal of Petrology 44, 937-965.

Wang, X., Griffin, W.L., O'Reilly, S.Y., Zhou, X., Xu, S., Jackson, S.E., Pearson, N.J., 2002. Morphology and geochemistry from late Mesozoic igneous complexes in coastal SE China. Mineralogical Magazine 66, 235-251.

Watson, E.B., Green, T.H., 1981. Apatite/liquid partition coefficients for the rare earth elements and strontium. Earth and Planetary Science Letters 56, 405-421.

Wendlandt, R.F., Harrison, W.J., 1979. Rare earth partitioning between immiscible carbonate and silicate liquids and CO_2 vapor: results and implications for the formation of light rare earth-enriched rocks. Contribution to Mineralogy and Petrology 69, 409-41.

Willingers, B., Baker, J.A, Krogstad, E.J., Peate, D.W., 2002. Precise and accurate in situ Pb-Pb dating of apatite, monazite and sphene by high-resolution laser ablation multicollector inductively coupled plasma mass spectrometry. Geochimica et Cosmochimica Acta 66, 1051-1066.

Woodhead, J.D., Hergt, J.M., Davidson, J.P., Eggins, S.M., 2001. Hafnium isotope evidence for "conservative" element mobility during subduction zone processes. Earth and Planetary Science Letters 192, 331-346.

Wooley, A.R., Kempe, D.R.C., 1989. Carbonatites: nomenclature, average chemical compositions, and element distribution. In: Bell K (ed.) Carbonatites: genesis and evolution. Unwin Hyman, London pp 1-14.

Wyllie, P.J., 1987. Transfer of subcratonic carbon into kimberlites and rare earth carbonatites. In: Mysen BO (ed.) Magmatic Processes: Physiochemical Principles. The Geochemical Society 107-120.

Wyllie, P.J., Lee, W,-J., 1998. Model system controls on conditions for formation of magnesiocarbonatite and calciocarbonatite magmas from the mantle. Journal of Petrology 39, 1885-1893.

Wyman, D.A., Ayer, J., Devaney, J.R.., 2000. Niobium-enriched basalts from the Wabigoon subprovince, Canada: evidence for adakitic metasomatism above an Archean subduction zone. Earth and Panetary Science Letters 179, 21-30.

Yogodzinski, G.M., Kay, R.W., Volynets, O.N., Koloskov, A.V., Kay, S.M., 1995. Magnesian andesite in the western Aleutian Komandorsky region: Implications for slab melting and processes in the mantle wedge: Geological Society of America Bulletin v. 107, p. 505-519.

Appendix 1

Geology and field relations

Field work in the Quetico subprovince was carried out during the summers of 1999 and 2000. This appendix presents a summary of the main field characteristics for each intrusion where samples were obtained. In general, exposure is good around lake shores, but dense vegetation obscures field relations elsewhere, leaving only small, isolated outcrops.

In the following the intrusions are ranked according to size starting with the largest intrusion. Rock names are assigned after the classification scheme of Streckeisen (1976).

A1.1. Linden intrusion

Linden Intrusion is located in northeastern Minnesota just north of the Quetico - Wawa subprovince boundary. It is approximately 90 km^2 based on interpretation of aeromagnetic data (Boerboom, 1994) but outcrops sparsely and has mainly been observed in drill cores. The complex consists of a main circular body, and a physically separate, but compositionally similar, smaller satellite body, which is elongated NE-SW. The exposed rocks are homogeneous and compositionally uniform syenites, but mela-syenitic units are present within drill cores (T. Boerboom, pers. comm. 2000). The syenite consists of pleochroic clinopyroxene, alkali-feldspar, plagioclase, titanite, biotite, apatite and Fe-Ti oxides ± quartz. Melanite garnet has been reported from some units (Boerboom, 1994). A moderate to strong penetrative igneous foliation is defined by the

preferred orientation of clinopyroxene and alkali-feldspar. There are virtually no magmatic, hydrated mineral phases within the intrusion, in strong contrast to the assemblages displayed by other intrusions in the area. Large titanite grains (up to 1 cm) are a widespread accessory constituent.

A1.2 Gheen intrusion

Gheen intrusion is a strongly elongate body, oriented NE-SW, approximately 10 km long and 1 to 2 km wide. It was described by Boerboom (1994) as a heterogeneous complex. It is located in northeastern Minnesota and is exposed mainly within road cuts. Rock types are highly variable and the major components of the complex include pyroxene hornblendite, monzodiorite, monzonite and monzosyenite, all of which are cut by late pink syenite dykes with straight contacts. It is the only intrusion included in this study which exposes volumetrically significant mafic and leucocratic rock types.

Where the contact to the host sedimentary rocks is exposed it is sharp. Large sedimentary xenoliths with preserved sedimentary textures and no visible sign of hybridization are common close to the margin. Three main phases are present within the intrusion: a leucocratic phase dominated by large alkali-feldspar megacrysts, a mafic phase with abundant clinopyroxene megacrysts and a mafic phase rich in biotite. The leucocratic phase has euhedral, blocky, perthitic alkali-feldspar megacrysts dispersed in a groundmass of clinopyroxene, plagioclase and minor hornblende, apatite and biotite. The megacrysts are mostly randomly distributed, but have locally been oriented into a foliation. Mutual cross cutting relationships are common and indicate coeval

emplacement of the various rock units. The presence of abundant circular to elongate enclaves of various sizes and compositions in the syenitic units as well as abundant round mafic enclaves in the mafic phases implies significant magma mingling. This is further corroborated by a preserved contact between the clinopyroxenite and the biotite-rich mafic phase with mutual inter-fingering textures, which suggests that the two liquids co-existed at the time of emplacement.

A1.3. Harnett Lake intrusion

Harnett Lake intrusion is a small elliptical intrusion approximately 5 km long and 3 km wide. It is dominated by leucocratic compositions and consists mainly of monzodiorite, monzosyenite and syenite. Heterogeneity on outcrop scale is expressed by significant variation in grain size and modal mineral modes. In the field, two main phases can be distinguished by color: grey and pink. There is clear field evidence that these two dominant rock types were constructed from more than one pulse of magma. In several localities the gray phase is clearly older and is broken up and intruded by the pink phase along a blocky joint system, although there is no indication for a major age difference between the two phases. Oriented trains of rounded, slightly elongate (cognate?) mafic enclaves are locally abundant and seem to be a result of magma mingling. The mafic enclaves are fine-grained and contain essentially the same minerals as the host, but have higher modal proportions of ferromagnesian minerals. Sharp outlines of the enclaves both macroscopically and microscopically indicate that the temperature difference between the two magmas was too small to permit significant mixing.

A wide band of sedimentary rock occurs within the intrusion and along its margins there is extensive mingling between sedimentary rocks and intrusive. In addition, small round sedimentary xenoliths occur within the center of the intrusion and these locally show physical evidence for hybridization along their margins. The felsic units are locally disturbed by thin (2-3 mm) quartz veins, and the intrusion is further cut by a number of narrow pink syenitic dikes (~30 cm), which are undeformed with straight contacts, suggesting that they intruded into brittle crust at a late tectonic stage.

A1.4. Beaverhouse Lake intrusion

The Beaverhouse Lake intrusion is circular in form and approximately 3 km in diameter. It is a heterogeneous body, which shows a wide range of textures with significant variation in grain size and modal mineral proportions on outcrop scale. Where the metasedimentary contact is exposed, it is sharp and only minor sedimentary enclaves occur within the intrusion. Rocks from the Beaverhouse Lake intrusion are predominantly composed of variable proportions of clinopyroxene, riebeckite and alkali-feldspar and have titanite, biotite, calcite and apatite as common accessory phases. Locally, there is well developed, but discontinuous, rhythmic mineral layering with individual layers tapering out laterally. The magmatic layering is defined by accumulation of mainly clinopyroxene, biotite and alkali-feldspar, giving rise to nearly monomineralic layers of biotite and alkali-feldspar. In places, there is evidence for intrusion of several batches of magma, with finer-grained units cutting compositionally similar but coarser-grained units giving rise to thin hornblende-rich reaction zones. Flow within the magma chamber is

inferred from the alignment of coarse alkali-feldspar megacrysts within slightly more mafic phases.

Carbonatite is present as a significant but minor phase. It is a sövite, which consists dominantly of coarse calcite, with variable, but lesser amounts of alkali-feldspar, riebeckite, aegirine augite, F-apatite, titanite, monazite and zircon. The sövite pod shows intrusive contacts with the syenite, has fine-grained margins, internal intrusive contacts, and contains small enclaves of the surrounding syenite. Ferromagnesian minerals are unevenly distributed within the sövite, forming clusters rich in silicate minerals.

In almost all outcrops thin syenitic dykes (2-30 cm) with straight contacts and no systematic orientation cut all other rock types. Net-veining by mm-thick quartz and alkali-feldspar veins is common.

A1.5. Whalen Lake intrusion

Whalen Lake intrusion is oval in shape, about 2 km wide and 3-4 km long. The intrusion comprises a wide lithological range and commonly displays conflicting field relationships within small exposures. The intrusion is dominantly leucocratic in composition, but also contains poorly exposed mafic to ultramafic units. Locally, the presence of a high proportion of elongate to round mafic enclaves within the felsic rock types suggests co-existence of two types of liquid at the time of crystallization.

The available field evidence indicates significant contamination by the surrounding metasedimentary rocks: Abundant, partly hybridized enclaves and rafts of metasedimentary rocks occur entrained in the syenitic phase, in particular near the margin

of the intrusion and testify to interaction between the magma and the host rock. In many areas sedimentary enclaves are transformed into elongate layers with flow structures and wispy tails due to flow during incorporation in a hot magma. In places, completely intermingled mafic and felsic units occur in a chaotic mixture of intrusive rocks and metasedimentary xenoliths.

The intrusion preserves discontinuous micro-rhythmic layering consisting of varying amounts of alkali-feldspar, plagioclase, hornblende, biotite and apatite on a scale of 1–5 cm. Movement within the magma chamber is evident from abundant flow banding of large alkali-feldspar grains within diorite (trachytoidal texture). Alternating layers of foliated intermediate and leucocratic phases indicate injection of several batches of magma during local flow within a small time frame. The leucocratic units contain numerous thin quartz- and feldspar-rich veins with random orientation. Fine grained syenitic dykes with straight contacts cut all other units, suggesting late stage emplacement during brittle conditions. A few dismembered lamprophyre dykes occur close to the margin of the intrusion.

A1.6. South Elbow Lake intrusion

South Elbow Lake intrusion is slightly oval in form and occupies an area of 5 km^2. The intrusion consists dominantly of foliated syenite containing minor sedimentary enclaves. A volumetrically subordinate, intermediate-mafic phase rich in hornblende and biotite is also present, but the contact between the two phases has not been established due to limited field exposure. Abundant, small (1-3 cm) mafic enclaves occur entrained

in the syenite in some localities, a texture which has been interpreted to result from magma mingling. Thin aplite dykes (~30 cm) with straight contacts crosscut all other units suggesting late stage emplacement into brittle crust, and numerous thin (2-3 mm) pink syenite veins cut the complex, especially towards its margin. The degree of deformation varies significantly within the intrusion and some outcrops are strongly foliated.

A1.7. North Elbow Lake intrusion

North Elbow Lake intrusion is an ultramafic to mafic body, which is dominated by hornblende-rich rock types. It was described by MacTavish (1992). The North Elbow Lake intrusion has a circular outline approximately two kilometres in diameter. The rocks range from fresh to strongly altered, where alteration occurs along fractures and as pervasive zones in some outcrops. The contact with the surrounding sediments is sharp, and the marginal units show very little evidence of deformation, suggesting that the intrusion was emplaced after the main deformation event. The intrusion is generally devoid of sedimentary xenoliths, although a few sedimentary rafts with no sign of hybridization occur within the mafic phases close to the margin. In the ultramafic units hornblende oikocrysts enclose chadacrysts of clinopyroxene, orthopyroxene and olivine, while large euhedral hornblende crystals with interstitial plagioclase dominate the mafic compositions. Ultramafic dykes with straight contacts cut the mafic units, but there is abundant field evidence for ultramafic enclaves and layers in the mafic phases as well as mafic enclaves and zones in the ultramafic phases, which indicates that the two types of

magmas coexisted at the time of crystallization. The mafic units are commonly net-veined by thin quartz-feldspar veins with random orientation, but the veins are not linked to any throughgoing fracture system. A few small pods and layers, up to 15 cm wide and mainly composed of feldspar, are present within the mafic bodies and a 30-40 cm wide "pegmatite" zone cuts the ultramafic phase. It has up to 10 cm long tabular hornblende grains oriented perpendicular to the margins and more equant hornblende crystals in the centre. The abundant poikilitic amphibole likely crystallized from a residual, relatively H_2O-rich liquid, while the coarse-grained pods and veins may represent filterpressed residual melt after fractionation of ferromagnesian minerals combined with the build-up of volatile components during advanced stages of solidification.

A1.8. Blalock intrusion

The Blalock Intrusion was described by Stern et al. (1989), Stern and Hanson (1991), as well as Smith and Williams (1978). The intrusion occupies an area of approximately 10 km^2 and has an overall elongate, but highly irregular outline. Rock types range from hornblende-clinopyroxenite to syenite, but intermediate rock types such as monzodiorite dominate, with local amethyst-bearing varieties. It is a composite body with a discontinuous marginal zone made up of monzodiorite, and an interior zone consisting of clinopyroxenite and less common tonalite. Minor sedimentary enclaves are present within the marginal phases. Locally, abundant mafic enclaves of a variety of sizes, shapes and compositions are entrained within the leucocratic units, which is indicative of magma mingling. The tonalitic phase is moderately to strongly foliated and contains small,

variably elongated mafic enclaves with aspect ratios between ~ 1:5 and 1:10. Several generations of undeformed felsic dykes with straight contacts cut the complex: the mafic phases are cut by one generation of pink dykes and both mafic and felsic phases are cut by a second generation of quartz-bearing pink dykes. Within the leucocratic units, the presence of mafic dykes fragmented into angular blocks as well as more rounded shapes is observed. The latter indicates that the dykes were transitional between brittle and ductile behavior at the time of fragmentation.

A1.9. Surprise Lake intrusion

Surprise Lake intrusion is circular in shape, 2.5 km in diameter, and mainly syenitic in composition. It is texturally and petrographically distinguished from other intrusions in the area by features such as plagioclase overgrowths on alkali-feldspar (rapakivi overgrowth) as well as alkali-feldspar overgrowth on plagioclase (anti-rapakivi) on the scale of a hand specimen and radiating alkali-feldspar crystals growing on foliation planes (macrospherulitic texture). The intrusion is not well exposed, but certain characteristics have been observed. It is composed of two main units: a leucocratic phase rich in alkali-feldspar and a volumetrically subordinate, slightly more mafic phase with higher modal hornblende contents. Crosscutting relationships suggest that the alkali-feldspar-rich phase is younger. Heterogeneity at outcrop scale is expressed as variations in grain size and modal mineral proportions and a weak igneous foliation is defined by the alignment of elongate hornblende and alkali-feldspar grains. There is evidence for intrusion of several batches of compositionally similar leucocratic magma, which gives

rise to internal intrusive boundaries with narrow chilled zones and thereby testifies to significant temperature difference between the magmas. Localized flow inference is expressed as thin zones of strongly oriented alkali-feldspar megacrysts occurring within leucocratic units with otherwise randomly oriented alkali-feldspar megacrysts.

A1.10. Heward intrusion

Heward intrusion is a small, oval shaped body, measuring 1.5 km in length, located in a forest covered, flat lying area, in which only small isolated patches are exposed. Based on the limited field evidence the intrusion appears entirely leucocratic and homogenous with respect to grain size and modal mineral proportions. It is composed of medium-grained, melanocratic syenite with alkali-feldspar, hornblende, quartz and biotite as the main minerals and epidote, titanite and apatite as common accessories. The observed limited variation in rock types and texture and the absence of sedimentary enclaves may not be characteristic for the intrusion as a whole, but could reflect only the units least susceptible to erosion.

A1.11. Kawene intrusion

Kawene is an elongate dyke-like intrusive body, which extends for about 500 m. It is a dominantly ultramafic body containing minor pegmatoidal veins of coarse-grained feldspathic material. The contact to the surrounding metasedimentary units is sharp with no observable chill. A volumetrically minor, poorly exposed, altered syenite phase is also

present. It contains abundant sedimentary enclaves, but the contact to the ultramafic unit has not been established due to limited field exposure. The syenite appears similar in composition to a dyke exposed elsewhere in the intrusion, which is clearly younger than the main ultramafic phase.

A1.12. South Kawene Lake intrusion

South Kawene Lake intrusion is a small, elongate, mafic to ultramafic body, two kilometers long, consisting of variably foliated hornblende-rich rock types. The margin of the complex is not well defined and the presence of abundant metasedimentary screens within the intrusion may indicate that it consists of a series of mafic dykes or small pods rather than a single body. Locally, coarser-grained phases with similar hornblende-rich assemblages but random mineral orientation are present and a few late stage granitic dykes with straight contacts cut the mafic units. Abundant small sedimentary enclaves along with thin quartz and calcite veins are present in some parts of the complex. Local breccias consist of expressed as angular fragments of intrusive rock surrounded by a leucocratic matrix presumed to be leucosome derived from the surrounding migmatitic metasedimentary rocks.

A1.13. Samuels Lake intrusion

Samuels Lake intrusion is a small, oval shaped complex, less than 500 m across, dominated by ultramafic compositions, which contains minor pods of coarse-grained

plagioclase-rich segregations. The intrusion can be divided into an outer rim, consisting of clinopyroxenite, and a core consisting of wehrlite and hornblendite. The various rock types range from almost fresh to intensively altered and thin calcite veins are common in some units. Significant grain size variation is observed on outcrop scale. Thin (~10 cm) dioritic dykes with straight contacts crosscut other rock types, and a few sedimentary enclaves with no sign of hybridization are present locally.

Sample no	Rock name	Geographic coordinates	Mineral mode	Description
A2.1. LINDEN INTRUSION				
BL0093	Alkali feldspar Syenite	47°51.48' N 92°56.32' W	70 % Kfs 10 % Pl 5-10 % Cpx 3-5 % Amp 3 % Bt 1-2 % Opq 1-2 % Chl 1 % Ttn <1 % Ap <1 % Zrn	Medium- to coarse-grained prophyritic rock with moderate foliation defined by aligned Kfs, Cpx and Bt. It consists of coarse, elongate perthite dispersed in a matrix of very fine-grained, moderately aligned Pl and microcline. Cpx (1-2 mm) is subhedral aegirine-augite with flecks of Bt and inclusions of Tnt and Oopq. The inclusions occur in zones, which parallel the foliation. Amp is subhedral and encloses fine-grained Bt and Ttn, veins of Chl and thin fibrous Chl overgrowths. Bt forms elongate oriented rows of ragged grains.
BL0094	Syenite	47°51.50' N 92°56.30' W	45 % Kfs 25 % Pl 20 % Cpx 5 % Bt 1-3 % Ap 1-3 % Ttn <1 % Opq	Medium- to coarse-grained porphyritic rock with moderate to strong foliation defined by aligned Kfs phenocrysts (5-7 mm) and Cpx. It consists of coarse elongate perthite with minor albite exolution dispersed in a groundmass of fine-grained, intergrown, untwinned Pl and faintly twinned microcline. Medium-grained Cpx is euhedral to subhedral, equant aegirine-augite with abundant inclusions of Bt, Ap, Ttn andOopq. It is bright green and strongly pleochroic. Euhedral to subhedral Ap occurs as inclusions in Cpx and less commonly interstitial to feldspar.
BL0095	Syenite	47°51.47' N 92°56.33' W	40-45 % Kfs 30-35 % Pl 15-20 % Cpx 1-3 % Bt 1-3 % Ttn 1-2 % Opq 1 % Ap	Medium- to coarse-grained porphyritic rock with moderate to strong foliation defined by aligned Cpx and Kfs phenocrysts. It is composed of coarse, elongate perthite with abundant albite exolution lamellae set in a groundmass of myriads of fine intergrown anhedral Pl and microcline. Cpx (1-3 mm) is bright green, pleochroic, euhedral to subhedral aegirine-augite with abundant inclusions of Bt, Ap, Ttn and Opq. Brown, euhedral to subhedral Bt occurs as discrete grains or as aggregates of ragged grains. Euhedral Tnt is present in many sizes (up to 2 mm). Anhedral Opq occurs along Cpx rims and in the feldspar groundmass.
A2.2. GHEEN INTRUSION				
BL0087	Kfs-feldspar bearing hornblendite	47°54.51' N 92°48.25' W	60-65 % Amp 15-20 % Kfs 10 % Pl (Ser) 5 % Chl 2-3 % Cal 1-3 % Ap 1-3 % Ep <1 % Opq <<1 % Ttn <<1 % Bt	Medium- to coarse-grained, strongly inequigranular rock essentially composed of large Amp (1 cm) set in a groundmass of medium-grained Kfs and Pl. Amp is euhedral to subhedral, partially replaced by Chl and contains abundant inclusions of Opq, Ap and Ttn. The rock is moderately to strongly altered and Amp is commonly fractured. Brown Tnt occurs as small, subhedral grains. Cal occurs as relatively large anhedral grains and as smaller irregular masses. Euhedral Ap is abundant.
BL0088	Plagioclase bearing hornblendite	47°55.08' N 92°48.30' W	75 % Amp 15 % Phl 5 % Pl <5 % Cal <1 % Qtz <1 % Opq	Medium-grained, massive rock essentially composed of subhedral amp (2-3 mm) with abundant flecks of Phl and interstitial pl. Fine-grained actinolitic Amp is present in some grain centers. Cal occurs as fine-grained needles in the groundmass. Pl occurs as medium-grained tabular crystals. A few brittle fractures are filled with Qtz.

Sample no	Rock name	Geographic coordinates	Mineral mode	Description
GHEEN INTRUSION				
BL0090	Monzodiorite	47°54.46' N 92°48.19' W	65-70 % Pl (Ser) 20 % Cpx 5 % Opq 3-5 % Bt 2 % Amp 1 % Ap <<1 % Ttn	Coarse-grained rock composed of large, euhedral Cpx (3-5 mm) set in a groundmass of tabular Pl. Cpx displays concentric zoning and sector zoning, has clean centers, and margins crowded with inclusions of Bt, Opq and rare Ttn. Large Opq in the groundmass replace Hbl and Cpx. Brown, randomly oriented Bt scatters throughout the feldspar groundmass. Ap is present as long needles within Pl.
BL0091	Monzosyenite	47°54.26' N 92°47.48' W	65-70 % Kfs 15 % Cpx 5-10 % Pl 5 % Amp 1-3 % Ap 1 % Bt 1 % Ttn 1 % Opq 1 % Cal <1 % Zrn	Medium- to very coarse-grained, inequigranular rock with minor flow lamination defined by alignment of Kfs megacrysts. The rock consists of blocky, subhedral megacrysts of perthite (~2 cm long and 1 cm wide) with megascopic oscillatory zoning dispersed in a matrix of medium-grained Cpx and Amp. Sporatic fractures within perthite are filled with microcrystalline microcline and Pl, and fine-grained, anhedral, faintly twinned Pl crystallize along grain boundaries. Cpx is subhedral, non pleocroic augite and contains abundant inclusions of coarse Ap, Ttn, Opq and miner irregular flecks of Amp.
BL0092	Monzonite	47°55.08' N 92°48.30' W	65-70 % Kfs 20 % Amp 5-10 % Pl 1 % Cpx 1 % Ttn <1 % Bt <1 % Ap	Medium-grained rock with weak to moderate foliation mainly defined by aligned Amp. It consists of medium-grained elongate perthite with interstitial Amp and Cpx. Cpx occurs as relict subhedral grains with many holes. Amp forms chains of medium-grained, subhedral to anhedral grains and has inclusions of Opq, Ttn and Bt.
BL0097	Monzonite	47°54.26' N 92°47.48' W	35-40 % Kfs 40-45 % Amp 10 % Pl (ser) 5 % Chl 2 % Ap 1-2 % Ttn <<1 % Cal <<1 % Bt	Medium-grained rock, which appears slightly banded due to differences in grain-size and modal mineralogy. It consists of bands of medium-grained anhedral Amp in a groundmass of microline and Pl, alternating with bands of slightly finer-grained tabular Amp within a feldspar groudmass. Ap occurs as small stubby grains and as thin needles within feldspar and amp. Euhedral Tnt have black alteration rims. Kfs varies from fresh to strongly altered grains.
BL0098	Monzo-syenite	48°54.46' N 92°48.19' W	55 % Kfs 20 % Amp 10 % Qtz 5 % Pl 3-5 % Ap 3 % Cpx 1-2 % Opq 1 % Ttn 1 % Cal <1 % Zrn	Medium to coarse-grained massive rock dominated by elongate Kfs with interstitial amp. Kfs has abundant albite exolution and minor fine-grained Pl and Qtz crystallizing along grain boundaries. Medium-grained, subhedral Cpx is partially replaced by Amp. Amp is anhedral and coarse-grained with many holes and inclusions of Opq, Ap and feldspar. Ap occurs as large, euhedral to subhedral grains (4 mm). Medium-grained opq occurs within feldspar and abundant very fine-grained rounded crystals occur within Amp.

Sample no	Rock name	Geographic coordinates	Mineral mode	Description
A2.3. HARNETT LAKE INTRUSION				
BL9930	Monzosyenite	48°38.96' N 92°18.22' W	50 % Pl 30-35 % Kfs 5 % Amp 5 % Bt 2-3 % Qtz 1-2 % Opq 1 % Ap 1 % Ttn <1 % Ep	Medium-grained rock with weak foliation due to preferred orientation of ferromagnesian minerals. It mainly consists of tabular Pl with concentric zoning and minor twinning. Slightly finer-grained, anhedral microcline and Qtz are interstitial to Pl. Subhedral amp encloses fine-grained Opq, Bt, Ap and Tnt and can be partially replaced by Bt and fine Ep and locally rimmed by Tnt. Bt is green, subhedral and has inclusions of Opq, Tnt and Ap. Opq is medium-grained and forms square, rounded and irregular grains locally mantled by Ttn.
BL9934	Alkali-feldspar Syenite	48°40.58' N 92°13.11' W	55-60 % Kfs 25 % Pl 5-10 % Qtz 5 % Amp <1 % Ttn <1 % Ep <<1 % Ap <<1 % Bt <<1 % Opq <<1 % Zrn	Fine- to medium-grained massive rock composed of a few large elongate sharply twinned Kfs in a medium-grained matrix of intergrown strongly twinned microcline and Pl and minor Qtz. Subhedral, green to bluish Amp, locally rimmed by Ttn, Ep or Opq, is interstitial to feldspar. Dark brown Tnt is euhedral to subhedral. Zrn is euhedral. Coarse Qtz occurs in patches, which may represent veins.
BL9939	Alkali-feldspar Syenite	48°41.12' N 92°13.16' W	75 % Kfs 15 % Pl 5 % Qtz 3-4 % Cpx 1 % Opq <1 % Amp <1 % Bt <1 % Cal <1 % Ap <1 % Ttn <1 % Ep <1 % Zrn	Fine- to medium-grained massive rock composed of anhedral perthite with abundant albite exolution lamellae dispersed in a matrix of fine-grained microcline with well-developed tartan plaid twinning, sharply twinned pl and qtz. Cpx is euhedral to subhedral aegirine-augite. It is bright green and strongly pleocroic and encloses numerous inclusions of Ap, Opq, Blue Amp, Pl and Kfs. Green Bt occurs as a few large grains, which are locally rimmed by small, euhedral Tnt. Amp is light blue and occurs as euhedral prisms next to Cpx and as a few larger grains within feldspar. Blocky Opq is locally rimmed by ttn. Cal forms large euhedral grains (primary phase) and smaller irregular aggregates (secondary phase).
BL9940	Monzosyenite	48°41.01' N 92°12.32' W	65 % Pl 15 % Kfs 5-10 % Bt 3-5 % Qtz 2-3 % Amp 2-3 % Ep 1 % Ap <<1 % Ttn <<1 % Opq	Medium-grained rock with weak foliation expressed as oriented rows of Amp and Bt. It is mainly composed of square to tabular Pl with concentric color zoning and occasional twinning and slightly finer-grained, anhedral microcline. Ragged Bt and Amp along with minor Ep, Opq and Ttn crystallize along feldspar grain boundaries. Ap occurs as small thin needles within feldspar.
BL9955	Monzosyenite	48°41.01' N 92°12.32' W	50 % Pl 30 % Kfs 5 % Amp 5 % Bt 2-3 % Opq 2-3 % Qtz 1-2 % Ep 1-2 % Ap <1 % Ttn <1 % Cal	Fine- to medium-grained, massive rock, mainly composed of intergrown faintly twinned microcline and Pl. Discrete grains of subhedral to anhedral Amp and subhedral Bt are common. Amp locally has Bt along grain margins and Bt can be mantled by Tnt. Blocky Opq is fine- to medium-grained. Ap is abundant within feldspar as a fine-grained, euhedral, elongate or stubby grains. Cal occurs as a few coarse grains.

Sample no	Rock name	Geographic coordinates	Mineral mode	Description
HARNETT LAKE INTRUSION				
BL0037	Syenite	48°40.46' N 92°13.25' W	60 % Pl 30 % Kfs 5-10 % Qtz 2-3 % Bt 1 % Ep <1 % Amp <1 % Oopq <1 % Ttn <<1 % Ap	Fine- to medium-grained rock, which is weakly foliated due to aligned rows of ragged Bt and euhedral Ep. It is mainly composed of intergrown microcline, Pl and Qtz, but also contains a few coarse, elongate perthite. Feldspar displays strong twinning. Amp is subhedral to anhedral with many pleocroic haloes. Bt occurs as green to reddish aggregates of ragged grains with Ep, and as single grains in the feldspar groundmass.
BL0040	Foid monzosyenite	48°41.01' N 92°12.32' W	60-65 % Pl 15-20 % Kfs 10-15 % Bt 3-5 % Amp 1-2 % Ep 1-2 % Ap <1 % Opq <<1 % Cal <<1 % Tnt	Fine-grained rock with ophitic texture, mainly composed of intergrown Pl and microcline with well developed twinning. Amp is euhedral to subhedral and locally contains flecks of Bt. Green Bt is euhedral to subhedral. Small, euhedral to subhedral Ep occurs along with Amp and Bt. Ap is a prominent phase and forms small, stubby prisms.
BL0044	Alkali-feldspar Syenite	48°40.35' N 92°12.39' W	65-70 % Kfs 15-20 % Pl 5 % Qtz 5 % Amp 1 % Ttn <1 % Ep <1 % Bt <<1 % Opq <<1 % Ap <<1 % Zrn	Medium-grained massive rock composed of intergrown, anhedral microcline and Pl with well developed twinning. Amp occurs as anhedral to subhedral grains with many holes and inclusions of Tnt and Opq and a few coarse inclusion-free plates. Ep is medium-grained and subhedral and occurs with Amp. Bt is as tabular grains mostly with Amp.
BL0047	The rock consists of fine-grained rounded mafic enclaves within syenite, these phases are described seperately below			
	Leucocratic phase	48°41.01' N 92°12.32' W	60 % Kfs 25 % Pl 5 % Amp 5 % Qtz 1-2 % Opq 1 % Cal 1 % Ep <1 % Ttn <1 % Ap	Medium-grained, fresh, massive rock essentially composed of anhedral perthite with abundant albite exolution lamellae dispersed in a matrix of intergrown sharply twinned microcline, untwinned Pl and minor qQtz. Anhedral Amp occurs along with fine-grained blocky Opq. Ttn is coarse-grained and euhedral.
	Mafic phase	48°41.01' N 92°12.32' W	50-55 % Pl 15-20 % Amp 10 % Bt 10 % Ep 5 % Ap 1 % Opq 1 % Ttn	Fine-grained rock with ophitic texture. Ferromagnesian minerals are concentrated in the border zone to the felsic phase. Pl is strongly twinned. Amp and Bt are elongate ragged grains. Ap is a prominent phase and occurs as small, stubby grains or long needles. Ep forms a few coarse, subhedral grains.

Sample no	Rock name	Geographic coordinates	Mineral mode	Description
A2.4. BEAVERHOUSE LAKE INTRUSION				
BL9999	Syenite	48°31.58' N 92°08.63' W	50-55 % Kfs 35-40 % Ppl 5 % Cpx 2 % Amp 1 % Ttn <1 % Ap <1 % Cal <<1 % Opq	Medium-grained fresh massive rock essentially composed of anhedral, sharply twinned microcline intergrown with faintly twinned Pl. It contains clusters composed of Cpx, elongate Tnt, blue Amp (riebeckite) and Ap. Riebekite is also found as smaller grains in the feldspar groundmass. Medium-grained Cal is interstitial to feldspar. Cpx is bright green, pleocroic aegirine-augite with minor inclusions of Ttn, Ap and Cal and flecks of blue Amp.
BL99101	Carbonatite	48°31.80' N 92°08.61' W	>95 % Cal 1 % Kfs 1 % Amp <1 % Mnz <1 % Opq <1 % Zrn	Medium- to coarse-grained, weakly foliated adcumulate. The rock consists almost entirely of cumulus Cal with some twinning. Coarse (early crystallized) Cal phenocrysts are dispersed in a groundmass of medium-grained Cal with minor interstitial blue Amp (riebeckite), Kfs and Mnz.
BL99103	alkali-feldspar syenite	48°31.80' N 92°08.61' W	60-65 % Kfs 20-25 % Pl 10 % Cpx 2-3 % Ap 1 % Amp <1 % Ttn <<1 % Cal <<1 % Opq	Medium-grained rock with heterogeneous appearance due to the presence of feldspar-rich clusters, which consists entirely of strongly twinned microcline and untwinned Pl. The remaining part of the rock is composed of elongate perthite with strong twinning and minor albite exolution in a groundmass of strongly twinned microcline, untwinned Pl and clusters of bright green aegirine-augite, minor blue Amp and coarse euhedral ap.
BL99104	Foid gabbro	48°31.31' N 92°08.64' W	40-45 % strongly altered, square grains, after Ne? 20-25 % Cpx 10 % Kfs 5-10 % Cal <5 % Chl <5 % Ppl 1 % Ap 1 % Amp <1 % Opq	Medium- to coarse-grained rock with moderate foliation defined by aligned Kfs and Cpx. Coarse rectangular perthite with abundant albite exolution and well-developed twinning are dispersed in a groundmass of bright green, subhedral, phleocroic aegirine-augite, Cal, Ap and an unidentified alteration mineral (presumably replacing ne). Chl occurs next to and within Cpx. Cal is a prominent phase, which mainly occurs as discrete euhedral grains, but also forms larger aggregates.
BL99108	alkali-feldspar syenite	48°31.78' N 92°08.63' W	50-55 % Kfs 35-40 % Pl 5 % Cpx 5 % Qtz 1 % Cal <1 % Amp <1 % Ttn < 1 % Ap <<1 % Oopq	Fine- to medium-grained, massive rock composed of intergrown, sharply twinned Pl and microcline. One very coarse elongate perthite is present. Euhedral to subhedral, bright green, pleocroic Cpx occurs along with minor blue Amp. Cal forms large grains in the feldspar groundmass and next to and within Cpx. Ap is common in the groundmass as small elongate prismatic crystals.

Sample no	Rock name	Geographic coordinates	Mineral mode	Description
BEAVERHOUSE LAKE INTRUSION				
BL0064	Carbonatite	48°31.80' N 92°08.61' W	90 % Cal 5 % Cpx 1-2 % Ap 1-2 % Kfs 1 % Amp <1 % Opq <1 % Qtz <1 % Zrn	Medium- to coarse-grained cumulate rock with heterogeneous appearance due to the presence of clusters rich in Cpx. It consists of a few very coarse rectangular Cal crystals in a matrix of medium-grained cumulate Cal with heterogeneous distribution (occasional clusters) of interstitial perthitic K-fs, blue Amp and Ap. Cpx is subhedral, bright green, strongly pleocroic and contains flecks of Amp and inclusions of Ttn, Ap, Cal and small Opq. Ap occurs as large euhedral inclusion-rich grains.
BL0065	Carbonatite	48°31.80' N 92°08.61' W	>95 % Cl 1-2 % Kfs 1 % Amp <1 % Phl <1 % Zrn <1 % Opq	Medium- to coarse-grained rock with erratic distribution of ferromagnesian minerals and textures close to adcumulate. It is composed of coarse Cal in a matrix of slightly finer Cal. Amp and Phl are small, ragged grains.
A2.5. WHALEN LAKE INTRUSION				
BL9984	Alkali-feldspar syenite	48°38.51' N 92°16.99' W	70 % Kfs 15-20 % Pl 5-10 % Cpx 3-4 % Ep 1 % Opq 1 % Ttn <1 % Bt <1 % Ap <1 % Cal	Fine- to medium-grained, unequigranular rock in which a few large, elongate grains of perthite and sharply twinned Pl are set in a groundmass of intergrown, sharply twinned microcline and faintly twinned Pl. Amp forms ragged, skeleton grains with random orientation and many inclusions of Ttn, Kfs, Opq and Ap. It is sometimes rimmed by anhedral Ep. Tnt is euhedral to subhedral. Cal forms rectangular grains in the feldspar groundmass.
BL99118	Monzonite	48°39.42' N 92°16.94' W	35-40 % Amp 30-35 % Kfs 20-25 % Pl 3 % Opq 2-3 % Ep 2 % Bt <1 % Ap <1 % Ttn	Medium-grained rock with moderate to strong foliation. It consists of Amp laths surrounding aligned Kfs. Amp is euhedral to subhedral with inclusions of Opq, Tnt, Ep, Bt and Ap. Green Bt forms large individual plates, which show evidence for deformation. Opq have many sizes and shapes (rounded or square or irregular shape) and can be rimmed by Tnt or Ep. Ep forms small clusters within feldspar, Amp and Bt. Ap is small, stubby grains.
BL99120	Alkali-feldspar syenite	48°38.84' N 92°18.20' W	85-90 % Kfs 5-10 % Pl 2-3 % Cpx 1 % Ttn <1 % Cal <<1 % Ap <<1 % Opq <<1 % Amp <<1 % Bt	Medium-grained rock with weak foliation. It is dominated by sharply twinned perthite with abundant albite exolution and minor fine-grained Pl and Qtz along grain boundaries. Cpx is light to bright green, pleocroic and euhedral to subhedral with inclusions of Pl, Opq, Tnt and Cal and a few flecks of Amp and Bt. Blue Amp occurs as strongly elongate ragged grains within Cpx. Ttn forms large, euhedral grains with occasional twinning. Cal is interstitial to Kfs.

Sample no	Rock name	Geographic coordinates	Mineral mode	Description
WHALEN LAKE INTRUSION				
BL99121	Monzosyenite	48°39.12' N 92°18.50' W	80-85 % Kfs 10 % Cpx <5 % Pl 2-3 % Cal 1 % Ttn <1 % Ap <<1 % Amp <<1 % Opq <<1 % Bt	Medium-grained rock with moderate foliation expressed as alignment of large Kfs and ferromagnesian minerals. It consists of subhedral, elongate, sharply twinned perthite with abundant albite exolution surrounded by minor fine-grained, elongate, faintly twinned Pl and Qtz. Cpx is subhedral, bright green, pleocroic and encloses inclusions of Opq, Cal, Pl and less commonly Ap, Tnt and flecks of Amp. Euhedral to anhedral Ap occurs close to ferromagnesian minerals and less commonly in the feldspar groundmass. Cal is a prominent mineral within and close to Cpx and in the feldspar groundmass. It is mostly euhedral, but also forms irregular masses.
BL99124	Granite	48°39.19' N 92°17.29' W	50 % Qtz 40-45 % Kfs 5-10 % Pl 2 % Bt 1 % Chl <1 % Cal <<1 % Ap <<1 % Opq <<1 % Zrn	Medium-grained, equigranular, massive rock composed of intergrown Pl, Qtz and microcline. Bt forms ragged grains and is commonly associated with Ap and Chl. It contains inclusions of feldspar, Qtz and flecks of Chl. Bt forms clusters and occasionally mantles Qtz. Ap is small, stubby, euhedral grains. Opq minerals are small, irregular grains in the quartzo-feldspatic groundmass. Cal forms irregular masses.
BL99160	Alkali-feldspar syenite	48°38.65' N 92°17.57' W	70-75 % Kfs 10-15 % Pl 5 % Qtz 5 % Amp 2-3 % Opq <1 % Bt <1 % Cal <<1 % Ap <<1 % Ttn	Medium- to coarse-grained massive rock, which displays textures close to orthocumulate. It is composed of coarse-grained perthite with abundant albite exolution and minor institial Pl. Amp is medium-grained and anhedral with many holes and inclusions of feldspar, Cal and Opq. Opq is fine- to coarse-grained and can have a variety of shapes.
BL0025	Monzo-syenite	48°39.21' N 92°16.59' W	65 % Kfs 10-15 % Pl 10 % Cpx 5-10 % Amp 1 % Cal 1-2 % Ap 1 % Ttn <1 % Opq <1 % bt	Medium- to coarse-grained massive rock essentially composed of coarse elongate perthite with interstitial Cpx, Amp, Ap and Tnt. Cpx is euhedral to subhedral, pleocroic and bright green and forms an interconnected framework along with Amp, coarse Cal and coarse, euhedral Ap. Amp is elongate, euhedral to subhedral with fine grained inclusions of Opq, Ap and Ttn. Ttn is medium to coarse-grained and subhedral to euhedral and occurs within Amp and interstitial to ferromagnesian minerals.
BL0028	Hornblendite	48°39.10' N 92°18.35' W	70-75 % Amp 10-15 % Phl 5-10 % Mus <5 % Opq 2-3 % Opx 1-2 % Pl 1-2 % Cal	Medium- to coarse-grained rock essentially composed of coarse anhedral oikocrysts enclosing medium-grained subhedral to rounded Opx, Cpx, Phl and minor Pl. Fine-grained Opq is scattered throughout the thin section.
BL0033	Monzo-syenite	48°39.25' N 92°49.53' W	60 % Kfs 15 % Pl 10 % Amp 5-10 % Qtz 5 % Pl 1-2 % Ep <1 % Ttn Ap <1 % Opq,Zrn	Fine- to coarse-grained (strongly unequigranular) rock. A few large rectangular perthite with abundant albite exolution are set in a groundmass consisting of fine- to medium-grained, sharply twinned microcline and Pl and minor Qtz. Amp occurs as coarse skeleton grains or as fine-grained aggregates with fine-grained Ep along margins and inclusions of Opq, Ap and Tnt. Ttn occurs as euhedral, rather coarse grains. Opq is fine to medium-grained and locally replaced by fine-grained Ep along margins.

Sample no	Rock name	Geographic coordinates	Mineral mode	Description
A2.6. SOUTH ELBOW LAKE INTRUSION				
BL99135	Monzonite	48°44.35' N 90°59.27' W	70-75 % Pl (Ser) 10 % Chl 5-10 % Cpx 5 % Amp 2-3 % Opq 1-2 % Ap 1 % Ep <1 % Cal	Medium- to coarse-grained massive rock, consisting of an interconnected framework of strongly altered Pl with interstitial large subhedral Cpx and Amp. Cpx is partly replaced by Amp and Chl, which again contain flecks of Ep and commonly have Ep and Opq along grain margins. Coarse Ap is common in the feldspar groundmass. Cal occurs as irregular grains with cChl and as larger grains in the feldspar-rich groundmass.
BL00111	Granite	48°44.37' N 91°01.30' W	40-45 % Pl (Ser) 35-40 % Kfs 10-15 % Qtz <1 % Oopq <1 % Chl <<1 % Ep <<1 % Ttn	Fine- to medium-grained rock with hypidiomorphic granular texture essentially composed of intergrown Pl, microcline (sharply twinned) and Qtz. A few ragged grains of Chl and small, irregular scattered grains of Opq occur.
A2.7. NORTH ELBOW LAKE INTRUSION				
BL9948	Hornblende pyroxenite	48°45.68' N 90°58.71' W	50-55 % Amp 20-25 % Opx 20-25 % Cpx 1-2 % Opq 1 % Ol <<1 % Phl <<1 % Ttn	Medium- to coarse-grained rock essentially composed of coarse Amp oikocrysts enclosing abundant medium-grained, euhedral to rounded Ol, Cpx and Oopx. Some Opx have concentric color zoning, and Ol has minor iddingsite alteration along cracks.
BL9950	Plagioclase bearing hornblendite	48°45.51' N 90°59.48' W	75-80 % Amp 10-15 % Mus 5 % Pl (Ser) 2-3 % Opq	Medium- to coarse-grained massive ortho-cumulate mainly composed of coarse amp with minor interstitial pl. Amp is commonly zoned and occurs as euhedral elongate or equant grains. It contains inclusions of pl, cal and opq and minor fibrous blue amp occurs in some grain centers. Pl is medium-grained with rare twinning. Opq occurs as small irregular grains.
BL9952	Hornblende gabbro	48°45.51' N 90°59.48' W	65-70 % Pl (Ser) 10-15 % Chl 10 % Amp 5 % Bt 3-5 % Opq	Medium-grained massive rock essentially composed of tabular Pl with oscillatory zoning and strong twinning, with interstitial Amp and Chl. Pl ranges from fresh to intensely altered. A few large partly resorbed Amp grains are present, while medium-grained ragged grains are common. Bt occurs as plates dotted with Opq and locally replaces Amp.
BL9953	Hornblende gabbro	48°45.51' N 90°59.48' W	60-65 % Amp 30-35 % Pl (Ser) 2-3 % Opq 2-3 % Ep 1 % Ap <1 % Chl	Medium- to coarse-grained rock with moderate foliation, which is mainly composed of coarse Pl phenocrysts enclosed by laths of medium-grained, euhedral Amp. Amp contains abundant inclusions of Opq and minor Ap and flecks of Chl. Ap and Opq are interstitial to Amp. Opq occurs as irregular grains, and some appear to be alteration products with rare fractures, which are filled with Chl.

Sample no	Rock name	Geographic coordinates	Mineral mode	Description
NORTH ELBOW LAKE INTRUSION				
BL9960	Plagioclase bearing hornblendite	48°45.68' N 90°59.41' W	75 % Amp 15-20 % Pl (Ser) <5 % Mus 1% Cal <1 % Ap <1 % Opq	Coarse-grained cumulate rock with intense alteration and veining and textures close to orthocumulate. It is essentially composed of coarse, subhedral, fractured Amp in a matrix of sericitized Pl, Ap, Chl and Mus. Veins occur both as pervasive veins and as minor fractures in ferromagnesian minerals and are filled with Mus. Pl is stongly altered to Cal and Ser.
BL99147	Plagioclase bearing hornblendite	48°46.01' N 91°09.10' W	70-75 % Amp 20-25 % Pl (Ser) 5 % Bt/Phl 1 % Opq <1 % Ap <1 % Chl	Medium-grained rock with moderate foliation defined by aligned Amp and Bt. It is weakly banded due to slight differences in modal proportion of Amp and Pl. It is composed of laths of subhedral, tabular Amp with interstitial Ppl. Amp contains flecks of Bt and abundant fine-grained exsolved Opq. Bt occurs as coarse inclusion-free plates and as medium-grained tabular crystals within Amp and in the groundmass.
BL99155	Pyroxene hornblende gabbronorite	48°45.43' N 90°59.87' W	40 % Cpx 30 % Amp 10 % Opx 10 % Pl 5-8 % unidentified alteration mineral 2-3 % Bt 1 % Opq <1 % Ap <1 % Chl	Medium to coarse-grained rock essentially composed of Amp megacrysts (up to 1 cm long) with interstitial Pl. Amp commonly have fine-grained inclusions of Opq and Pl and flecks or irregular grains of Bt and an unidentified alteration mineral. Euhedral to subhedral Cpx forms laths in the feldspar groundmass together with Opx. Opq is fine-grained and occurs as inclusions in ferromagnesian minerals and with Pl. Pl is almost completely transformed to an assemblage of fine-grained Ser, Ep and an unidentified alteration mineral.
BL0006	Hornblende gabbro	48°45.54' N 90°59.32' W	40-45 % Amp 40 % Pl (Ser) 10 % Chl 5-7 % Opq <3 % Bt	Medium-grained, inequigranular rock consisting of an interconnected framework of Amp with interstitial Ppl. The rock contains small pods of fine-grained material with similar texture and mineralogy. Pl ranges from unaltered with sharp twinning to completely altered. Amp is partly replaced by Chl and fine anhedral Opq and commonly has thin Amp overgrowths.
BL0017	Granodiorite	48°45.30' N 91°00.05' W	45-50 % Pl 30 % Qtz 10-15 % Kfs 5 % Bt <<1 % Ttn <<1 % Ap <<1 % Zrn	Fine- to medium-grained rock with weak to moderate foliation defined by Bt. It is composed of intergrown microcline (with well developed tartan twinning), faintly twinned Pl and Qtz. Bt is interstitial to feldspar and occurs as fine tabular crystals and as longer grains. Ap forms a few coarse euhedral grains.

Sample no	Rock name	Geographic coordinates	Mineral mode	Description
A2.8. BLALOCK INTRUSION				
BL0052	Foid gabbro	48°45.38' N 91°19.40' W	55 % Pl (Ser) 15 % Bt 10-15 % Amp 5-10 % Cpx 3 % Ep 2 % Ap <1 % Opq <<1 % Zrn	Medium-grained, massive rock composed of clusters of Cpx, Amp and Bt dispersed in a groundmass of medium-grained tabular Pl with strong twinning and altered centres. Equant, euhedral Cpx alters to Amp and contains flecks of Bt and inclusions of Ap and Opq. Microcrystalline Ep rims Amp. Plates of green Bt enclose fine-grained Ap and Opq.
BL0054	Foid monzo-diorite		65-70 % Kfs 10-15 % Pl 10 % Amp 5 % Bt 1-2 % Opq 1-2 % Qtz 1 % Tnt <1 % Ap	Medium-grained, massive, equigramular rock composed of clusters of Amp and Bt set in a groundmass of intergrown Pl, Kfs and minor Qtz. Amp and Bt are subhedral to anhedral. Amp contains myriads of very fine Opq and abundant very fine-grained, euhedral Tnt crystallize along the margins. Ap occurs as coarse tabular grains. Unaltered equigranular microcline has sharply developed tartan twinning, while Pl occurs as strongly elongate untwinned grains.
BL0076	Alkali-feldspar syenite		75-80 % Kfs 10-15 % Pl 5 % Cpx 2-3 % Bt 1 % Ttn <1 % Ap <<1 % Zrn Qtz ?	Medium-grained fresh rock with moderate foliation due to the preferred orientation of ferromagnesian minerals and Kfs phenocrysts. Anhedral perthite is set in a groundmass of fine intergrown microcline and Pl ± Qtz. Cpx is equant or elongate with flecks of Bt. Ttn forms euhedral grains in the feldspar groundmass and along Cpx margins. Zrn is euhedral.
BL0077	Monzonite		40-45 % Pl 30 % Kfs 10-15 % Amp 5-10 % Bt 2-3 % Ep 2 % Cpx 1-3 % Qtz <1 % Ap <1 % Ttn <1 % Opq <<1 % Cal <<1 % Zrn	Medium-grained rock composed of subhedral Amp and coarse plates of Bt set in a feldspar groundmass. Green Bt replaces Amp and commonly has Ep growing at or near the margins. Bt contains inclusions of Opq that have rims of Tnt. Ap forms small stubby euhedral grains in the feldspar groundmass and in Amp. Euhedral Ep occurs along with Bt. The groundmass consists of medium-grained equant to tabular Pl with interstitial, slightly finer-grained microcline.
BL0078	Syenite		40-45 % Kfs 35-40 % Pl 10 % Qtz 5-10 % Bt 1 % Oopq 1 % Ep <1 % Amp <1 % Cal <1 % Cpx <<1 % Ttn <<1 % Ap <<1 % Zrn	Medium- to coarse-grained rock with moderate to strong foliation, essentially composed of coarse, aligned perthite phenocrysts with well-developed twinning and abundant albite exolution. They are dispersed in a groundmass of medium-grained untwinned, moderately altered Pl with interstitial Qtz. Green Bt occurs as ragged grains along with Amp and has inclusions of Ep and Oopq and can be partly rimmed by Ep. Opq occurs as fine grains scattered within ferromagnesian minerals.

Sample no	Rock name	Geographic coordinates	Mineral mode	Description
BLALOCK INTRUSION				
BL0082	Syenite		40-45 % Kfs 25-30 % Pl (Ser) 15 % Qtz 5 % Bt 2-3 % Cpx 2-3 % Ep 1 % Amp 1 % Ttn <1 % Ap	Medium- to coarse-grained rock with moderate foliation defined by aligned Bt and to a lesser extent coarse aligned kfs. Perthite (5-10 mm) shows concentric zones of albite exolution and is set in a groundmass of medium-grained strongly twinned microcline, tabular, faintly twinned Pl and anhedral Qtz. Bt is red to green, elongate and subhedral and replaces Cpx along grain margins. Euhedral to anhedral small Tnt is abundant within Bt.
BL0084	Monzosyenite		35-40 % Kfs 25 % Pl 30-35 % Amp 2 % Bt 1-2 % Ep 1 % Ap <1 % Tnt <1 % Cpx <<1 % Opq <<1 % Zrn	Fine- to medium-grained rock with weak foliation defined by oriented aggregates of fine-grained Amp. It contains a few coarse perthite in a groundmass of myriads of fine-grained Pl, Amp and microcline. Amp contains flecks of Bt and has irregular margins. Coarse Tnt is euhedral to anhedral. Ap is common in the feldspar groundmass as small stubby grains and thin needles.
BL0085	Syenite		40 % Kfs 25 % Pl (Ser) 25 % Qtz 5 % Bt 3 % Amp 1 % Ep <1 % Oopq <1 % Tnt	Medium-grained massive rock. Anhedral perthite is surrounded by medium-grained rectangular Pl and finer anhedral Qtz. Ep forms euhedral equant grains. Bt occurs as irregular grains with small, subhedral Ttn crystallizing along the margins.
BL00103	Syenite		40-45 % Kfs 30 % Pl 10-15 % Qtz 5-10 % Amp 5 % Bt 2-3 % Ep <1 % Opq <1 % Ttn <<1 % Cal <<1 % Ap <<1 % Zrn	Medium- to coarse-grained rock defined by aligned amp and coarse aligned perthite (1 cm). Coarse pertite has abundant albite exolution and tantan twinning and is set in a groundmass of medium-grained intergrown Pl and Qtz. Amp is euhedral to subhedral and contains flecks of Bt and inclusions of Opq and Tnt. It is locally mantled by microcrystalline Ep. Euhedral Zrn has microscopically visible cores.
BL00104	Monzonite		40-45 % Kfs 25-30 % Pl (Ser) 15-20 % Amp 5 % Bt 5 % Ep <1 % Opq <1 % Ap Qtz ?	Medium-grained rock with weak foliation defined by faintly aligned Amp. It consists of anhedral, irregular grains of Amp in a groundmass of altered Pl and Kfs. Bt occurs as anhedral plates with rare Ep inclusions. Ep also occurs as discrete euhedral grains in the feldspar-rich groundmass.

Sample no	Rock name	Geographic coordinates	Mineral mode	Description
A2.9. SURPRISE LAKE INTRUSION				
BL9915	Syenite	48°38.45' N 92°03.42' W	85 % Pl 5 % Qtz <5 % Kfs 2-3 % Bt 1 % Amp <1 % Opq <1 % Ep <1 % Cal <1 % Ap <<1 % Ttn	Medium-grained rock, which appears slightly heterogeneous due to the presence of small Bt clusters. It is essentially composed of anhedral, intergrown Pl with minor Qtz. Bt occurs as irregular grains and larger masses and locally contains inclusions of Cal, Amp, Tnt, Qtz and Ep. Ap is small, elongate, euhedral grains. Cal occurs as fairly large grains next to and as inclusions in ferromagnesian minerals and as anhedral grains within the feldspar groundmass. Blocky Opq occurs within the feldspar-rich groundmass.
A2.10. HEWARD INTRUSION				
BL99145	Hornblende gabbro	48°46.17' N 91°08.75' W	60-65 % Pl (Ser) 25-30 % Amp 3-4 % Qtz 2-3 % Chl 1 % Ms 1 % Bt <1 % Ap <1 % Opq <<1 % Ttn <<1 % Ep	Medium- to coarse-grained rock containing a few brittle veinlets filled with Mus. It consists of coarse-grained, subhedral Amp dispersed in a matrix of altered Pl. Amp has inclusions of Pl, Opq and Chl and can be partially mantled by ragged Chl grains. Ap occurs as small, stubby grains in the Pl matrix and qtz forms fine-grained aggregates. A few coarse Bt grains are almost completely chloritized.
A2.11. SOUTH KAWENE INTRUSION				
BL9993	Plagioclase bearing pyroxene hornblendite	48°45.65' N 91°12.31' W	75-80 % Amp 5-10 % Pl 5-10 % Cpx 1-2 % Bt 1 % Ep <1 % Opq <1 % Ttn <1 % Qtz <1 % Ap <<1 % Cal <<1 % Chl	Coarse-grained rock composed of euhedral, equant Amp (~ 1 cm) set in a groundmass of medium-grained Pl, Cpx and Amp. Coarse Amp has inclusions of opq, tnt and ep and abundant flecks of euhedral bt and some grains have Ep along their margins and within cracks. Secondary Ttn occurs as small, stubby grains. Groundmass Pl encloses euhedral Cpx and Amp.
BL9995	Hornblende gabbro	48°45.69' N 91°11.91' W	80 % Amp 10-15 % Pl (Ser) 1-3 % Ep 2-3 % Bt 1-2 % Ap <1 % Ttn <<1 % Chl <<1 % Cal	Medium- to coarse-grained massive rock mainly composed of euhedral, elongate to equant Amp (5-10 mm) with interstitial Pl. The texture is close to orthocumulate with Amp as the cumulative phase. It encloses fine-grained Pl, Opq, and Bt, and is locally rimmed by Ep. Bt forms ragged grains and is locally replaced by Chl. Ap is abundant as small, stubby or long needle like grains within Pl.

Appendix 3

Mineral chemistry

Microprobe analyses have been obtained on the constituent minerals of a representative suite of samples. The QAS intrusions have a wide range of mineral compositions generally reflective of whole rock compositions. Major element variations of the main ferromagnesian minerals are illustrated along with whole rock data of all intrusions in Figure A3.1.

A3.1. Pyroxene

Low Ca-pyroxene is present in ultramafic units of the North Elbow Lake intrusion, where it locally exceeds clinopyroxene in abundance, but has not been observed in other intrusions. It has a narrow *mg*-number variation range between 0.80 and 0.82 [*mg*-number = $Mg/(Mg+Fe^{2+}$, assuming $Fe^{2+} = 0.85 \cdot Fe^{TOT}$], low Cr_2O_3 (< 0.2 wt %), relatively high Al_2O_3 (1.6 - 2.8 wt %) and classifies as bronzite (Table A3.1).

Clinopyroxene is present in most plutonic complexes in a wide variety of rock types. It ranges in composition from Cr-diopside and Mg-augite in mafic and ultramafic units to aegirine-augite in leucocratic units. All pyroxene analyses are illustrated in Figure A3.2. Clinopyroxene analyses not tabulated in Chapter 2 are listed in Table A2.2 and the data is illustrated in Fig. A.3.2. In mafic to ultramafic compositions clinopyroxene has Mg-number from 0.57 to 0.90, while clinopyroxene from leucocratic units has Mg-number

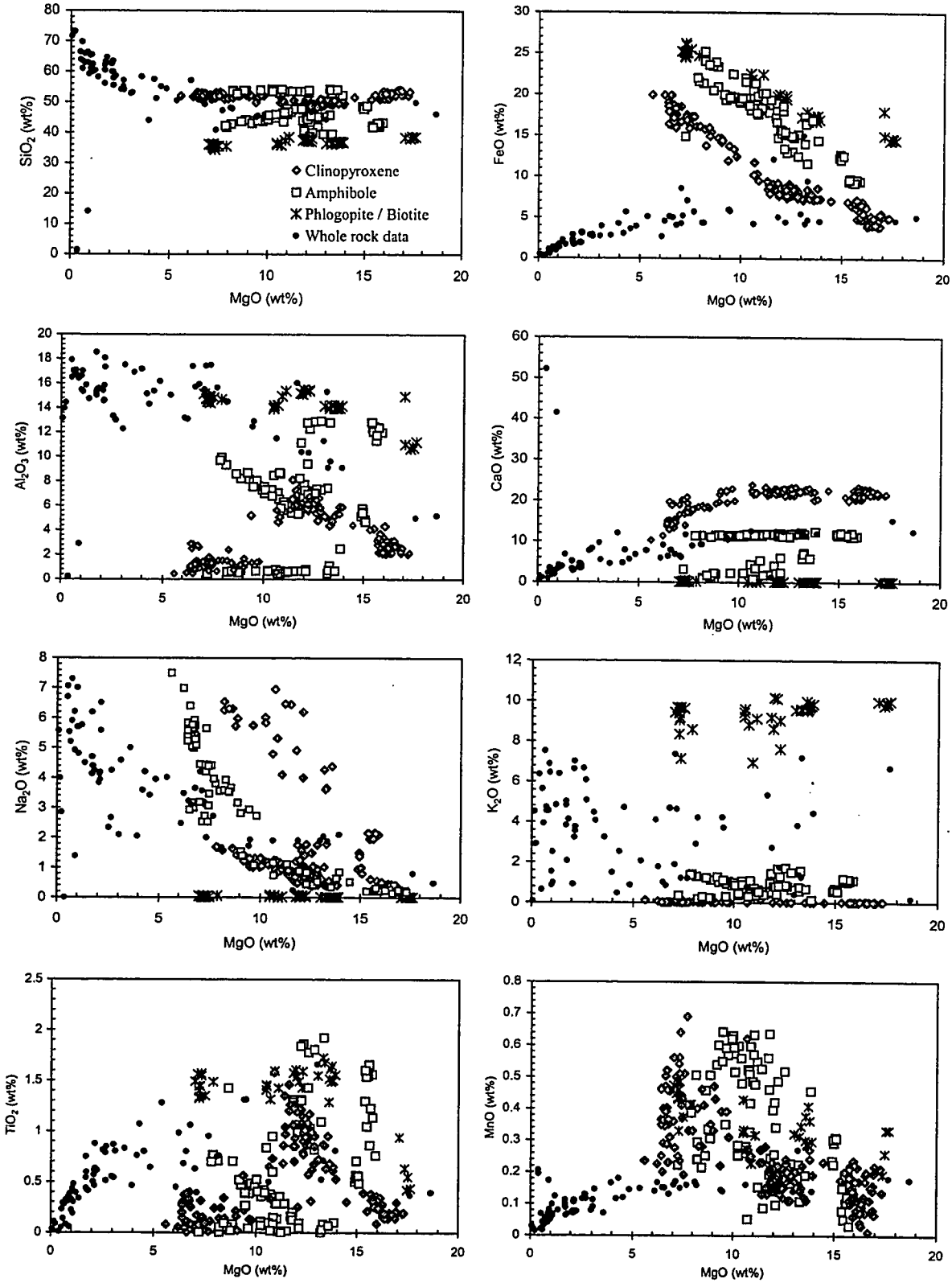
SiO2 (wt%)
MgO (wt%)
Clinopyroxene
Amphibole
Phlogopite / Biotite
Whole rock data
FeO (wt%)
MgO (wt%)
Al2O3 (wt%)
MgO (wt%)
CaO (wt%)
MgO (wt%)
Na2O (wt%)
MgO (wt%)
K2O (wt%)
MgO (wt%)
TiO2 (wt%)
MgO (wt%)
MnO (wt%)
MgO (wt%)

Figure A3.1

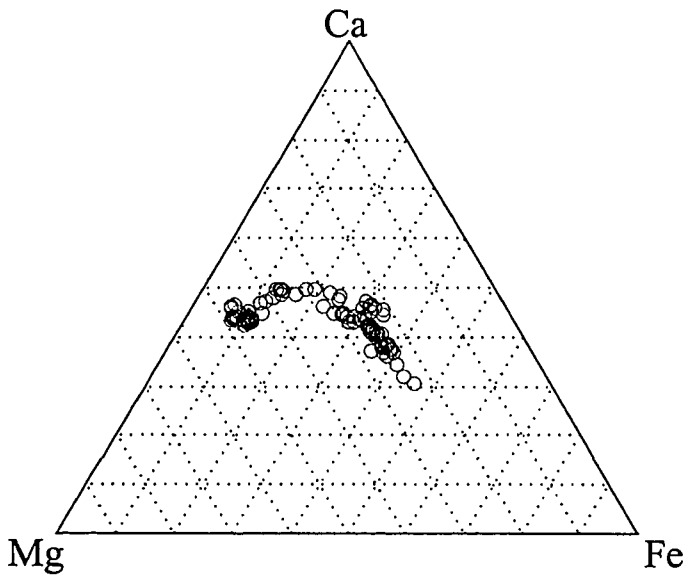

Fig. A3.2. Clinopyroxene from the QAS intrusions

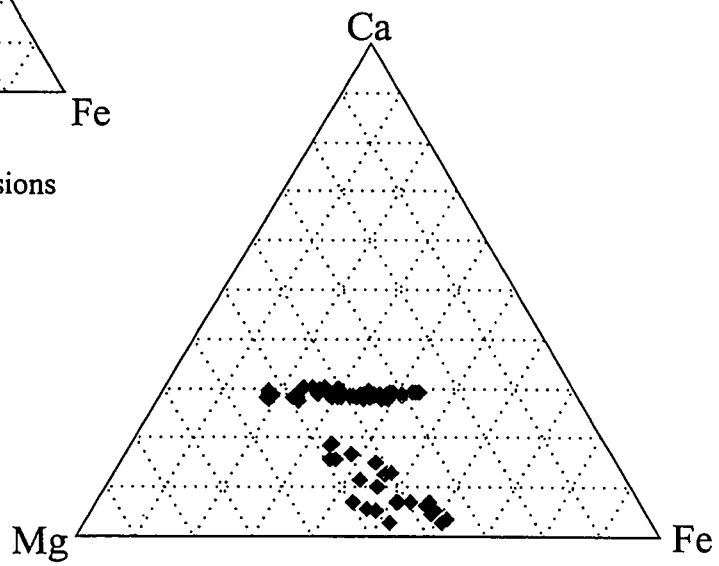

Fig. A3.3. Amphibole from the QAS intrusions

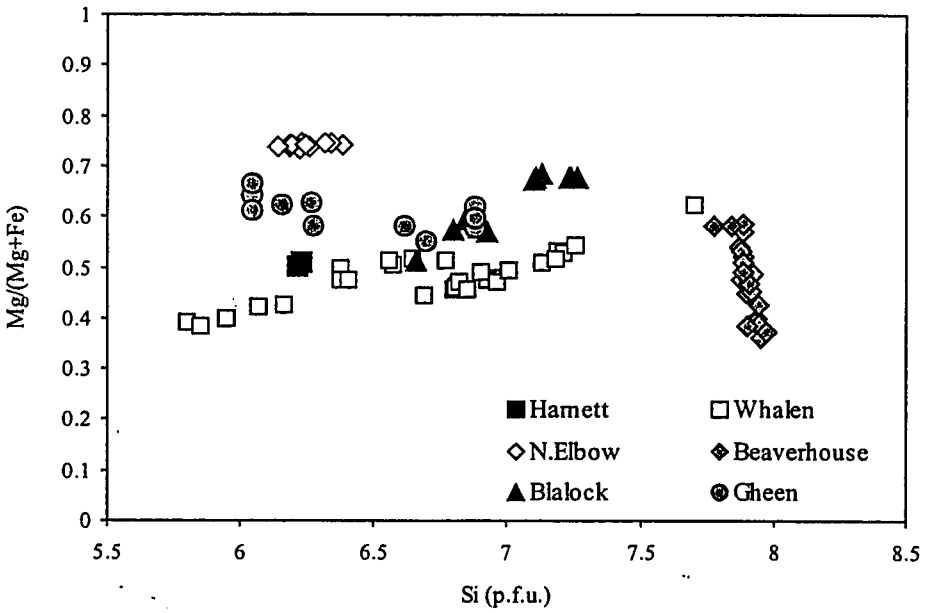

Fig. A3.4. Amphibole from the QAS intrusions

from 0.37 to 0.62. Relatively large amounts of Al appear in the octahedral sites in Cr-diopside and Mg-augite, whereas Al occurs solely in the tetrahedral sites within aegirine-augite. Using two different geobarometers [Thompson (1974) and Soescoo (1997)] clinopyroxene from mafic units have crystallized at pressures of 1.0 - 1.5 GPa (see Chapter 2). Zoned clinopyroxene is common in the Gheen intrusion. Leucocratic samples contain aegirine augite with distinctly low Al_2O_3 and up to 7 wt % Na_2O.

A3.2. Amphibole

All analysed amphiboles, except those from the Beaverhouse Lake intrusion, have $(Ca+Na)_{M4} > 1.34$ and $(Na)_{M4} < 0.67$ and thus classify as calcic amphiboles according to the classification scheme of Leake (1978). Amphiboles from North Elbow Lake intrusion range in composition from pargasite to pargasitic hornblende. Those from the Gheen intrusion trend from ferroan pargasite, through ferroan pargasitic hornblende to edenitic hornblende. Amphiboles from Blalock intrusion, Whalen Lake intrusion and Harnett Lake intrusion each define a trend from ferroan pargasite to edenite. Rocks from Beaverhouse Lake intrusion contains riebeckite, which trends separately on chemical diagrams, because of significantly higher SiO_2, FeO and Na_2O and low Al_2O_3 and CaO contents. Mg-number of all analyzed amphiboles varies significantly from 0.41 to 0.78. All amphiboles are plotted in Figure A3.3 and A3.4. *F* ranges between 0.1 and 0.9 wt % and shows no obvious correlation with other elements. Zoning within amphibole is microscopically evident in mafic units of North Elbow Lake intrusion and most analyzed grains show minor normal zoning. All amphibole analyses are listed in Table A3.3.

A3.3. Olivine

Olivine is a rare mineral within the QAS intrusions and occurs exclusively in mafic-ultramafic units of North Elbow Lake intrusion and in Samuels Lake intrusion. Unaltered olivine occur with clinopyroxene and low Ca-pyroxene as chadacrysts within hornblende oikocrysts in samples from North Elbow Lake intrusion, while serpentinized olivine is present in Samuels Lake intrusion. Olivine was analyzed in one sample (BL9948) from North Elbow Lake intrusion. The analyzed grains have a relatively low *mg*-number of ~ 0.78, low Ni (0.04 - 0.12 wt %) and relatively high MnO (0.28 - 0.35 wt %). A mantle origin for olivine is unlikely based on MgO, FeO and Ni contents. The scarcity of olivine in mafic to ultramafic units may imply that optimal conditions for olivine crystallization were not met during igneous activity. Olivine analyses are listed in Table A3.4.

A3.4. Feldspars

Within mafic and ultramafic compositions there is moderate to strong hydrothermal alteration of feldspars, such that the data set is biased toward the least altered leucocratic units. Feldspar analyses are listed in Table A3.5. In mafic compositions plagioclase occurs as a late crystallizing interstitial phase and is always normally zoned. Within leucocratic units alkali feldspar commonly occurs as medium-grained aligned crystals or less commonly as blocky megacrysts up to several centimeters in length. The megacrysts often have large (flow aligned) perthitic cores with oscillatory zoning, set in a

groundmass of fine-grained, faintly twinned plagioclase and more sharply developed tartan twinned microcline. In general, the FeO concentration of feldspars is low (< 0.3 wt %) whereas Ba contents vary from low to moderate. Alkali-feldspar megacrysts from Gheen intrusion are zoned with respect to Ba, which ranges from 0.9 to 1.8 wt %.

A3.5. Phlogopite and biotite

Each individual intrusion has a distinct range of mica compositions and there is very little overlap in mica compositions between intrusions probably reflecting crystallization under slightly different fO_2 and aH_2O conditions. Phlogopite and biotite analyses are listed in Table A3.6. K_2O varies from 6.9 to 10.1 wt %. *F* and Cl contents vary from below detection limit to maximum concentrations of 2.7 and 0.07 wt %, respectively, yielding very high F/Cl ratios. MgO varies between 7.0 wt % and 17.6 wt % and shows a strong positive correlation with *F*. Ti and Ba contents are uniformly low: TiO_2 varies between 0.4 wt % and 1.7 wt %, whereas BaO reaches maximum concentrations of 0.4 wt %. Judging from the compilations of Gaspar and Wyllie (1987) and Rosenbaum (1993), the low Ba - low Ti phlogopite is chemically similar to phlogopite in mantle rocks and in carbonatite. No significant zoning has been detected in mica, except in coarse phlogopite grains from a carbonatite plug within the Beaverhouse Lake intrusion, which have well-developed, visually evident, concentric zoning patterns, suggestive of a magmatic origin.

A3.6. Accessory minerals

A3.6.1 Calcite

Calcite analyses are close to end-member composition with Sr as the most important minor element. *Ca*-number [molar CaO/(CaO+MgO)] equals ~ 0.99, and SrO concentrations display a limited range between 1.0 and 1.2 wt %. MgO and FeO reach maximum concentrations of 0.3 and 0.6 wt %, respectively. Calcite also occurs as a secondary mineral in mafic and ultramafic rock types, mainly as infillings of fine-grained calcite in fracture zones and as replacement of plagioclase. Secondary calcite has not been analyzed. Calcite analyses are listed in Table A3.7.

A3.6.2. Apatite

Apatite is abundant in almost all leucocratic rock types and has been analyzed in four intrusions. The *F* content of all analyzed apatites is high (~ 3-5 wt %), while Cl concentration is minimal and mostly below detection limit. Fe, Si and Na occur in trace amounts (<0.2 wt % of the respective oxides). The presence of apatite intergrown with silicate minerals indicates participation early in the crystallizing sequence. Apatite analyses are listed in Table A3.8.

A3.6.3. Zircon

Primary magmatic features such as well-developed oscillatory zoning are preserved in many grains and sector zoning is a prominent feature in some zircons. The latter is an igneous phenomenon suggestive of rapid crystallization during disequilibrium conditions. It has been observed only in zircons from Harnett Lake intrusion and may reflect undercooling due to magma mingling. This explanation is consistent with elevated ThO_2 (<0.66 wt %) and Y_2O_3 (<0.37 wt %) concentrations in these zircons, as rapid growth during strong undercooling facilitates the entrance of Th and Y into the zircon lattice (Wang et al., 2002). HfO_2 concentrations of all analyzed zircons range from 0.34 to 1.38 wt %, and HfO_2/ZrO_2 varies between 0.005 and 0.022. Th/U is generally below 1, except in the outermost rims, confirming a magmatic origin of the zircons. The Gheen intrusion includes a small proportion of structure less grains, which may be metasomatic, although their Th/U ratios imply a magmatic origin. Most analyzed zircons have CaO concentration below detection limit, but one zircon from the Harnett Lake intrusion has distinct metamict zones with CaO contents up to 0.97 wt % (maximum concentration). Zircon analyses are listed in Table A3.9.

A3.6.4. Titanite

Titanite is present in almost all rock types except for ultramafic phases. It commonly occurs as wedge-shaped, euhedral grains and locally reaches 1 cm in length. Titanite contains considerable FeO and F, which maximum concentrations reaching 2.6 wt % and 1.0 wt %, respectively. Cl is very low and commonly below detectable levels. Titanite

with late stage titanite overgrowths was observed within the Harnett Lake intrusion. Titanite analyses are listed in Table A3.10.

Table A3.1. *Microprobe analyses of orthopyroxene from the QAS intrusions*

Sample #	IN	SiO_2	MgO	Al_2O_3	TiO_2	FeO	MnO	K_2O	CaO	Cr_2O_3	Total
BL9948	NEL	53.29	27.74	1.92	0.05	13.98	0.32	n.d.	1.12	0.06	98.66
BL9948	NEL	53.19	28.07	2.24	0.17	13.81	0.26	0.03	1.24	0.00	99.42
BL9948	NEL	53.35	27.77	2.33	0.15	13.01	0.24	n.d.	1.30	0.20	98.63
BL9948	NEL	53.30	27.46	2.32	0.10	12.80	0.35	0.01	1.39	0.06	98.27
BL9948	NEL	54.02	27.84	2.38	0.14	13.77	0.31	0.02	1.26	0.15	100.15
BL9948	NEL	54.06	28.09	1.67	0.07	14.13	0.27	0.02	1.14	n.d.	99.60
BL9948	NEL	54.06	28.33	2.58	0.17	13.05	0.29	n.d.	1.22	0.10	99.98
BL9948	NEL	54.24	28.17	2.16	0.14	13.17	0.31	0.01	1.28	0.17	99.78
BL9948	NEL	54.11	28.31	1.94	0.16	13.28	0.35	0.01	1.24	0.09	99.51
BL9948	NEL	53.52	27.97	2.26	0.15	13.27	0.32	n.d.	1.31	0.06	99.01
BL9948	NEL	52.98	27.65	2.49	0.17	13.72	0.26	n.d.	1.16	0.00	98.56
BL9948	NEL	53.38	28.43	2.23	0.19	13.11	0.28	n.d.	1.35	0.09	99.44
BL9948	NEL	53.85	28.14	1.95	0.11	13.35	0.27	n.d.	1.26	0.05	99.07
BL9948	NEL	53.15	27.83	2.78	0.16	13.79	0.18	n.d.	1.26	0.12	99.31
BL9948	NEL	54.48	28.20	1.81	0.13	13.69	0.29	n.d.	1.26	0.11	100.09
BL9948	NEL	53.36	28.35	2.49	0.13	13.22	0.24	0.01	1.11	0.17	99.29
BL9948	NEL	53.87	28.47	2.42	0.16	13.70	0.25	n.d.	1.24	n.d.	100.32

IN = intrusion. Abbreviations as in Figure 2.1.
n.d. = not detected

Table A3.2. *Microprobe analyses of clinopyroxene from the QAS intrusions*

Sample #	IN	SiO_2	Al_2O_3	TiO_2	FeO	MnO	MgO	K_2O	CaO	Na_2O	Cr_2O_3	Total
BL0091	LN	53.53	0.55	0.05	11.73	0.62	10.67	n.d.	23.80	0.74	0.08	101.77
BL0091	LN	52.19	1.35	0.13	13.31	0.39	9.68	0.01	22.81	1.08	n.d.	100.95
BL0091	LN	52.10	1.66	0.16	14.16	0.47	9.06	n.d.	21.45	1.54	0.01	100.61
BL0091	LN	52.17	1.26	0.02	14.39	0.43	9.12	n.d.	22.26	1.39	0.03	101.07
BL0094	LN	51.99	1.41	0.12	12.42	0.31	9.80	n.d.	19.88	2.73	n.d.	98.66
BL0094	LN	51.86	0.70	0.02	15.39	0.41	8.56	0.02	18.12	3.67	0.03	98.78
BL0094	LN	51.66	0.99	0.21	14.66	0.33	9.04	0.01	19.62	2.82	0.09	99.43
BL0094	LN	50.87	1.51	0.11	16.05	0.33	7.80	0.02	17.84	3.81	n.d.	98.34
BL0094	LN	52.13	1.16	0.07	14.67	0.35	8.89	0.01	19.18	3.16	n.d.	99.62
BL0094	LN	50.95	1.52	0.24	16.05	0.33	8.00	0.03	18.38	3.56	0.05	99.11
BL0094	LN	50.86	1.32	0.22	13.70	0.39	9.44	0.02	19.45	2.94	0.06	98.40
BL0094	LN	51.23	1.50	0.14	15.72	0.40	8.23	0.01	18.66	3.58	0.07	99.54
BL0094	LN	52.03	1.21	0.14	14.87	0.28	8.49	0.01	18.40	3.52	0.08	99.03
BL0094	LN	52.64	1.32	0.34	15.95	0.46	8.45	n.d.	18.40	3.54	0.22	101.31
BL0090	GH	49.49	5.88	0.53	7.26	0.19	13.94	n.d.	20.33	0.85	0.49	98.96
BL0090	GH	53.19	2.58	0.18	4.42	0.19	16.52	n.d.	22.85	0.34	0.44	100.71
BL0090	GH	51.53	4.39	0.30	7.02	0.23	14.47	n.d.	22.46	0.52	0.05	100.97
BL0090	GH	49.25	6.44	1.17	8.38	0.24	12.63	n.d.	22.86	0.41	0.20	101.58
BL0090	GH	49.47	6.50	0.90	7.68	0.16	12.30	0.03	22.87	0.83	0.10	100.84
BL0090	GH	50.48	5.63	0.68	9.42	0.23	11.32	0.15	21.96	1.11	0.03	100.01
BL0090	GH	50.47	5.13	0.95	7.84	0.12	13.53	0.01	23.02	0.35	0.14	101.56
BL0090	GH	50.70	5.29	0.61	7.25	0.27	13.79	n.d.	22.11	0.64	0.32	100.98
BL0090	GH	53.04	2.74	0.14	3.99	0.07	16.51	0.04	22.23	0.39	0.67	99.82
BL0090	GH	49.58	5.82	0.85	7.59	0.19	12.84	n.d.	23.32	0.53	0.13	100.85
BL0090	GH	49.68	5.62	0.65	10.19	0.27	10.65	0.01	22.36	1.16	n.d.	100.59
BL0090	GH	49.55	6.24	0.85	7.84	0.23	11.92	n.d.	22.35	0.88	0.37	100.23
BL0090	GH	53.83	2.79	0.17	4.07	0.01	16.66	0.02	22.33	0.41	0.38	100.67
BL0090	GH	48.32	6.74	1.14	8.39	0.14	12.28	0.01	22.9	0.44	0.23	100.59
BL0089	GH	53.43	2.20	0.26	5.10	0.14	15.93	–	22.27	0.32	0.25	99.90
BL0089	GH	48.13	5.58	1.21	8.11	0.20	12.22	–	22.70	0.48	0.14	98.77
BL0089	GH	48.32	6.27	1.35	9.02	0.27	11.39	–	21.74	0.77	0.01	99.14
BL0089	GH	48.20	5.96	1.46	9.07	0.28	11.59	–	21.82	0.87	0.01	99.26
BL0089	GH	48.90	6.08	0.95	8.17	0.18	12.67	–	21.98	0.66	0.11	99.70
BL0089	GH	49.43	6.08	0.97	7.63	0.15	12.34	–	22.44	0.68	0.11	99.83
BL0089	GH	49.43	5.77	0.99	7.35	0.17	12.31	–	22.68	0.68	0.09	99.47
BL0089	GH	50.23	5.88	0.65	8.58	0.24	13.81	–	20.19	0.64	0.07	100.29
BL0089	GH	47.35	7.24	1.20	9.07	0.15	11.61	–	21.90	0.60	0.06	99.18
BL0089	GH	49.20	6.08	0.88	8.05	0.21	12.50	–	22.22	0.72	n.d.	99.86
BL0089	GH	49.19	5.77	0.85	8.35	0.21	11.82	–	22.57	0.72	0.06	99.54
BL0089	GH	49.82	4.45	0.86	7.89	0.15	13.37	–	22.72	0.40	0.12	99.78
BL0089	GH	48.48	5.91	1.12	8.95	0.16	12.38	–	22.04	0.44	0.06	99.54
BL0089	GH	52.18	3.07	0.18	4.58	0.11	16.37	–	21.81	0.45	0.73	99.48
BL0089	GH	52.65	2.67	0.18	4.28	0.09	16.35	–	22.35	0.41	0.78	99.76
BL0089	GH	52.18	3.10	0.18	4.84	0.17	16.53	–	21.46	0.44	0.42	99.32
BL0089	GH	49.03	4.35	0.87	8.41	0.14	13.31	–	22.52	0.38	0.07	99.08
BL0089	GH	48.74	5.33	0.95	8.13	0.20	12.87	–	22.51	0.41	0.05	99.19
BL0089	GH	51.37	5.72	0.25	7.88	0.14	12.04	–	21.93	1.06	0.08	100.47
BL0089	GH	48.55	6.08	1.12	9.10	0.17	12.42	–	21.49	0.57	0.05	99.55
BL0089	GH	52.13	2.17	0.31	4.81	0.21	15.78	–	22.48	0.26	0.35	98.5
BL0090	GH	48.73	5.87	0.79	7.40	0.19	12.30	–	22.33	0.67	0.39	98.67
BL0090	GH	52.77	2.34	0.18	4.01	0.09	16.26	–	22.59	0.33	0.91	99.48
BL0090	GH	52.89	2.17	0.15	3.91	0.07	16.27	–	22.74	0.33	0.84	99.37
BL0090	GH	53.01	2.13	0.14	3.99	0.10	16.35	–	22.57	0.33	0.79	99.41
BL0090	GH	52.82	2.34	0.19	4.08	0.03	16.33	–	22.29	0.29	0.77	99.14
BL0090	GH	49.35	5.27	0.68	7.15	0.11	13.63	–	22.17	0.43	0.24	99.03
BL0090	GH	47.92	6.90	1.26	8.51	0.13	11.67	–	22.15	0.55	0.06	99.15
BL0090	GH	48.35	6.59	1.22	8.22	0.18	12.11	–	22.49	0.60	0.13	99.89
BL0090	GH	47.97	5.95	0.86	8.43	0.27	11.35	–	23.09	0.90	0.08	98.9
BL0090	GH	47.98	6.32	1.06	8.37	0.20	11.79	–	22.61	0.76	0.17	99.26
BL0090	GH	48.87	5.56	1.03	8.10	0.19	12.57	–	22.69	0.38	0.12	99.51
BL0090	GH	48.47	5.79	1.04	8.74	0.19	12.44	–	22.05	0.41	0.10	99.23
BL0090	GH	48.38	5.56	0.99	8.55	0.11	12.73	–	22.16	0.41	0.12	99.01
BL0090	GH	48.94	5.91	0.88	7.72	0.15	12.53	–	22.18	0.56	0.15	99.02
BL0090	GH	48.72	5.84	0.94	8.04	0.15	12.41	–	22.18	0.84	0.17	99.29
BL0090	GH	48.95	5.66	0.86	7.62	0.12	12.47	–	22.71	0.59	0.14	99.12
BL0090	GH	48.40	6.28	0.93	7.65	0.14	11.89	–	22.72	0.81	0.10	98.92

n.d. = not detected

Table A3.2. *Continued*

Sample #	IN	SiO_2	Al_2O_3	TiO_2	FeO	MnO	MgO	K_2O	CaO	Na_2O	Cr_2O_3	Total
BL0090	GH	49.86	5.57	0.57	7.76	0.20	12.56	–	21.37	0.95	0.44	99.28
BL0090	GH	48.72	6.52	1.04	8.79	0.13	11.42	–	21.93	0.87	0.17	99.59
BL0090	GH	48.74	6.36	1.58	9.50	0.25	10.89	–	21.80	1.00	n.d.	100.12
BL0090	GH	49.03	5.74	1.05	7.79	0.19	12.19	–	22.53	0.70	0.38	99.60
BL0090	GH	50.94	4.75	0.31	7.81	0.20	12.70	–	21.89	0.95	0.33	99.88
BL0090	GH	54.01	2.43	0.16	3.88	0.15	16.79	–	21.88	0.33	0.42	100.05
BL0090	GH	48.58	6.15	1.07	8.68	0.22	12.21	–	22.35	0.45	0.20	99.91
BL0090	GH	47.96	7.16	1.23	9.21	0.17	11.84	–	21.73	0.46	0.15	99.91
BL0090	GH	48.86	5.38	0.86	7.76	0.17	12.64	–	23.06	0.51	0.17	99.41
BL0090	GH	47.34	7.10	1.04	8.68	0.19	12.24	–	22.26	0.48	0.13	99.46
BL0090	GH	50.04	5.05	0.72	7.13	0.20	13.10	–	22.22	0.58	0.28	99.32
BL0090	GH	50.32	5.12	0.85	7.65	0.19	12.86	–	21.83	0.76	0.21	99.79
BL0090	GH	50.58	5.49	0.67	7.37	0.11	12.83	–	21.71	0.83	0.22	99.81
BL0090	GH	50.83	5.11	0.72	7.35	0.17	13.05	–	22.15	0.61	0.15	100.14
BL0090	GH	52.49	3.68	0.25	5.91	0.10	15.83	–	20.37	0.54	0.33	99.50
BL0090	GH	52.36	4.10	0.21	6.44	0.20	15.51	–	20.06	0.60	0.23	99.71
BL0090	GH	48.35	6.70	1.01	7.94	0.18	12.40	–	21.90	0.46	0.22	99.16
BL0090	GH	48.35	7.92	0.70	7.94	0.16	11.87	–	21.60	0.63	0.04	99.21
BL0090	GH	48.59	7.23	0.77	8.02	0.13	12.32	–	21.17	0.69	0.05	98.97
BL0090	GH	48.92	6.61	0.62	7.90	0.21	12.75	–	21.28	0.63	0.03	98.95
BL0090	GH	47.53	8.09	0.97	7.91	0.23	11.44	–	21.38	0.75	0.20	98.50
BL0090	GH	48.17	6.20	1.08	7.93	0.18	12.53	–	22.57	0.44	0.19	99.29
BL9939	HAR	53.03	1.18	0.05	16.94	0.64	7.36	n.d.	17.30	4.44	0.07	101.13
BL9939	HAR	53.20	1.32	0.09	17.29	0.51	7.59	n.d.	16.98	4.42	0.08	101.54
BL9939	HAR	51.44	1.01	0.09	16.93	0.56	7.32	0.02	16.86	4.43	n.d.	98.66
BL9939	HAR	52.67	0.64	0.01	17.27	0.69	7.71	n.d.	17.77	3.97	0.06	100.79
BL9939	HAR	52.49	0.65	0.04	17.51	0.51	7.32	n.d.	17.15	4.20	0.03	99.90
BL9939	HAR	52.19	0.97	0.07	18.49	0.56	7.04	0.02	16.48	4.45	0.01	100.28
BL9939	HAR	52.58	1.30	0.10	17.26	0.54	7.30	n.d.	16.66	4.43	0.06	100.23
BL9939	HAR	52.34	1.06	0.07	16.79	0.44	7.45	n.d.	16.97	4.39	0.01	99.52
BL99120	HAR	51.23	1.49	0.17	16.92	0.50	7.16	n.d.	20.04	2.53	0.10	101.14
BL99120	HAR	50.67	1.28	0.07	18.40	0.52	6.72	0.01	19.07	2.99	n.d.	99.73
BL99120	HAR	51.70	1.24	0.08	17.08	0.47	7.28	0.02	20.18	2.73	0.03	100.81
BL99120	HAR	51.67	1.68	0.15	16.52	0.41	7.42	n.d.	20.77	2.53	n.d.	101.15
BL99120	HAR	52.13	1.19	0.05	18.39	0.40	6.54	n.d.	19.64	2.93	0.04	101.31
BL9999	BHL	51.26	1.79	0.31	16.86	0.44	7.34	0.24	13.90	5.65	n.d.	98.03
BL9999	BHL	51.88	0.43	0.08	19.91	0.24	5.60	0.11	10.21	7.50	n.d.	96.28
BL9999	BHL	51.50	1.46	0.30	17.69	0.29	6.73	0.02	13.58	5.70	n.d.	97.42
BL9999	BHL	52.38	0.42	0.04	19.87	0.36	6.55	n.d.	12.80	6.40	n.d.	99.27
BL9999	BHL	51.68	1.10	0.33	18.26	0.46	6.76	n.d.	13.29	5.93	n.d.	98.22
BL9999	BHL	52.22	1.40	0.40	17.48	0.37	6.80	0.01	14.50	5.29	n.d.	98.74
BL9999	BHL	51.65	0.49	0.05	19.90	0.23	6.23	0.06	11.30	7.00	n.d.	97.36
BL9999	BHL	51.46	1.38	0.39	17.33	0.39	6.68	n.d.	13.88	5.67	n.d.	97.55
BL9999	BHL	51.76	1.17	0.38	17.12	0.39	6.66	0.01	14.06	5.76	n.d.	97.47
BL9999	BHL	51.41	1.06	0.27	17.89	0.46	6.44	n.d.	14.23	5.58	0.08	97.57
BL99103	BHL	52.84	0.82	0.10	18.50	0.40	6.72	n.d.	14.81	4.99	0.05	99.25
BL99103	BHL	53.02	0.89	0.09	18.53	0.50	6.65	n.d.	14.78	5.05	0.06	99.59
BL99103	BHL	52.69	0.89	0.08	18.41	0.46	6.86	0.01	14.54	5.10	0.07	99.15
BL99103	BHL	52.96	0.80	0.11	18.75	0.35	6.62	n.d.	14.23	5.38	0.05	99.25
BL99103	BHL	52.25	0.86	0.15	18.50	0.46	6.44	0.01	14.04	5.43	n.d.	98.17
BL99103	BHL	51.90	1.00	0.20	19.00	0.37	6.42	n.d.	13.79	5.37	n.d.	98.06
BL99103	BHL	52.10	0.97	0.20	18.56	0.35	6.43	n.d.	14.13	5.24	n.d.	98.03
BL99104	BHL	52.86	2.47	0.31	16.42	0.20	6.50	0.01	14.64	5.83	0.02	99.26
BL99104	BHL	52.63	2.85	0.37	16.28	0.29	6.54	n.d.	15.08	5.44	n.d.	99.48
BL99104	BHL	52.20	2.60	0.25	16.37	0.31	6.85	0.02	15.31	5.36	0.01	99.28
BL99104	BHL	52.81	2.71	0.31	16.78	0.35	6.79	0.02	14.89	5.75	n.d.	101.41
BL99104	BHL	52.54	2.68	0.27	15.90	0.23	6.78	n.d.	15.27	5.42	n.d.	99.09
BL99104	BHL	53.16	2.89	0.29	16.35	0.25	6.44	n.d.	14.95	5.84	n.d.	100.17
BL99104	BHL	52.38	2.37	0.24	13.74	0.28	8.30	0.01	18.11	3.93	n.d.	99.36
BL0064	BHL	51.76	1.01	0.08	17.16	0.24	7.33	0.05	14.78	5.28	0.05	98.47
BL0064	BHL	52.30	0.44	0.01	18.61	0.28	7.09	n.d.	13.37	6.20	n.d.	98.46
BL0064	BHL	51.71	1.06	0.07	16.83	0.25	7.26	n.d.	14.75	5.24	0.10	97.62
BL0064	BHL	52.02	1.09	0.09	16.93	0.19	7.55	n.d.	15.20	5.40	0.11	98.91
BL99121	WHL	52.17	1.09	0.03	16.27	0.43	7.49	n.d.	18.27	3.47	0.03	99.25
BL99121	WHL	52.69	1.29	0.02	15.86	0.37	7.46	0.01	19.28	3.07	n.d.	100.05

n.d. = not detected

Table A3.2. *Continued*

Sample #	IN	SiO_2	Al_2O_3	TiO_2	FeO	MnO	MgO	K_2O	CaO	Na_2O	Cr_2O_3	Total
BL99121	WHL	51.67	1.39	n.d.	16.66	0.47	6.66	0.01	18.77	3.16	n.d.	98.79
BL99121	WHL	52.17	1.41	0.05	16.67	0.36	7.03	0.05	18.86	3.18	n.d.	98.76
BL9948	NEL	51.87	2.65	0.26	6.31	0.11	16.19	0.02	21.37	0.27	0.27	99.64
BL9948	NEL	52.79	2.28	0.21	5.48	0.19	16.92	0.04	21.23	0.21	0.59	100.31
BL9948	NEL	51.51	2.81	0.32	6.17	0.20	15.71	n.d.	21.31	0.26	0.21	98.58
BL9948	NEL	51.74	2.91	0.36	6.82	0.17	15.96	n.d.	20.61	0.22	0.22	99.42
BL9948	NEL	51.09	3.16	0.34	6.55	0.22	16.13	n.d.	20.28	0.30	0.28	98.60
BL9948	NEL	51.67	3.04	0.33	6.77	0.22	15.80	0.03	20.73	0.28	n.d.	98.93
BL9948	NEL	51.52	2.96	0.28	6.83	0.18	15.87	n.d.	20.87	0.23	0.21	99.09
BL9948	NEL	51.46	3.14	0.38	6.76	0.21	15.68	n.d.	20.94	0.20	0.28	99.27
BL9948	NEL	52.55	2.15	0.16	5.14	0.12	16.44	0.03	21.99	0.28	0.26	99.39
BL9948	NEL	52.77	2.17	0.09	6.42	0.12	15.97	0.03	22.37	0.33	0.23	100.59
BL9948	NEL	51.34	2.80	0.31	6.56	0.24	15.97	n.d.	21.64	0.27	0.19	99.57
BL9948	NEL	52.31	2.51	0.19	5.19	0.22	16.97	n.d.	21.63	0.17	0.42	99.86
BL9948	NEL	50.83	3.34	0.31	7.18	0.11	15.74	0.02	20.78	0.27	0.29	99.13
BL9948	NEL	52.12	2.00	0.19	4.92	0.21	17.24	0.01	21.32	0.23	0.49	99.10
BL9948	NEL	52.47	2.08	0.20	5.14	0.16	16.89	n.d.	21.52	0.21	0.56	99.36
BL9948	NEL	51.62	3.41	0.31	6.90	0.22	16.01	n.d.	20.62	0.29	0.26	99.89
BL9948	NEL	53.30	2.11	0.19	4.94	0.13	17.32	0.02	21.50	0.18	0.46	100.62
BL9948	NEL	52.42	2.52	0.30	5.03	0.07	16.94	0.02	21.42	0.26	0.60	99.87
BL9948	NEL	50.81	4.04	0.39	6.92	0.17	15.32	0.03	20.90	0.20	0.07	99.11
BL9948	NEL	51.30	3.23	0.28	6.55	0.15	15.85	n.d.	20.90	0.24	0.45	99.09
BL9948	NEL	52.05	2.66	0.19	4.89	0.20	16.57	n.d.	21.27	0.14	0.70	99.02
BL9948	NEL	51.07	2.86	0.24	6.48	0.13	15.98	0.02	20.95	0.22	0.19	98.57
BL9948	NEL	51.21	2.56	0.28	6.17	0.17	16.21	0.03	21.03	0.24	0.35	98.29
BL9948	NEL	52.38	2.20	0.20	5.33	0.14	16.88	n.d.	21.80	0.25	0.59	99.79
BL9948	NEL	51.62	3.34	0.34	7.13	0.18	15.76	0.02	21.20	0.31	0.21	100.21

n.d. = not detected
IN = intrusion. Abbreviations as in Figure 2.1.

Table A3.3. *Microprobe analyses of amphibole from the QAS intrusions*

Sample #	IN	SiO_2	Al_2O_3	TiO_2	FeO	MgO	MnO	CaO	Na_2O	K_2O	Cr_2O_3	Total
BL9940	HAR	45.88	8.62	0.60	18.12	10.81	0.33	11.47	1.20	1.00	n.d.	98.18
BL99101	BHL	53.78	0.64	0.04	18.60	12.10	0.10	2.37	6.19	0.42	0.04	95.19
BL99101	BHL	54.09	0.47	0.02	21.35	10.72	0.05	0.85	6.95	0.31	n.d.	95.53
BL99101	BHL	53.49	0.67	0.02	19.37	11.48	0.09	1.80	6.45	0.39	0.03	94.77
BL99101	BHL	53.57	0.62	0.00	20.17	11.22	0.15	1.68	6.46	0.52	n.d.	95.14
BL99101	BHL	44.91	6.63	1.06	15.78	11.96	0.40	11.48	1.23	0.80	n.d.	95.16
BL99101	BHL	44.36	7.25	1.26	15.64	12.04	0.42	11.26	1.56	0.80	0.03	95.34
BL99101	BHL	43.51	8.68	0.95	17.76	10.80	0.51	11.47	1.23	1.09	0.11	97.13
BL99101	BHL	45.11	7.03	1.43	14.98	12.54	0.52	11.21	1.48	0.87	0.11	96.06
BL99101	BHL	45.39	6.92	1.30	15.46	12.20	0.49	11.17	1.40	0.84	0.05	96.30
BL9999	BHL	52.90	0.78	0.10	20.49	10.61	0.28	4.37	4.79	0.64	n.d.	95.57
BL9999	BHL	66.47	0.42	n.d.	14.87	7.25	0.22	3.15	3.15	0.36	n.d.	96.07
BL9999	BHL	53.74	0.72	0.08	23.36	8.88	0.31	1.99	5.97	0.22	0.02	95.77
BL9999	BHL	52.95	0.62	0.05	23.49	8.63	0.25	1.44	6.30	0.22	n.d.	94.26
BL9999	BHL	53.36	0.66	0.12	18.97	11.77	0.46	4.05	4.91	0.53	n.d.	95.37
BL9999	BHL	54.22	0.70	0.11	22.01	10.23	0.28	2.26	6.02	0.37	n.d.	95.59
BL9999	BHL	53.70	0.53	0.02	23.93	8.78	0.33	2.26	5.72	0.23	0.05	95.92
BL9999	BHL	53.77	0.57	0.01	25.23	8.23	0.29	1.11	6.25	0.16	n.d.	95.99
BL9999	BHL	53.18	0.78	0.09	18.01	12.10	0.34	6.04	4.00	0.58	n.d.	95.55
BL9999	BHL	53.87	0.66	0.04	22.48	9.62	0.35	2.24	5.74	0.31	n.d.	95.51
BL9999	BHL	53.34	0.69	0.08	19.83	10.84	0.42	3.35	5.31	0.44	0.03	94.89
BL9999	BHL	53.55	0.52	0.01	20.17	11.08	0.48	5.34	4.11	0.37	0.02	95.85
BL9999	BHL	53.57	0.67	0.07	21.55	10.24	0.25	2.31	5.84	0.45	n.d.	95.27
BL9999	BHL	53.57	0.58	0.06	24.07	8.23	0.24	0.84	6.53	0.19	n.d.	94.65
BL9999	BHL	52.74	0.64	0.09	23.60	8.45	0.21	1.67	6.30	0.28	0.07	94.59
BL0064	BHL	54.25	0.49	n.d.	17.30	13.18	0.21	5.81	4.27	0.59	0.08	97.31
BL0064	BHL	52.98	1.11	0.08	16.62	13.29	0.20	7.19	3.66	0.72	0.03	96.84
BL0064	BHL	53.95	0.72	0.03	16.40	13.24	0.22	6.87	3.61	0.57	0.07	96.16
BL0064	BHL	54.08	0.68	0.07	16.87	13.57	0.19	5.85	4.38	0.69	0.03	97.41
BL99118	WHL	44.09	8.23	0.71	20.90	8.88	0.51	11.46	1.41	1.12	n.d.	97.52
BL99118	WHL	43.58	8.61	1.42	20.49	8.65	0.46	11.03	1.63	1.22	n.d.	97.35
BL99118	WHL	42.79	9.32	0.71	21.33	8.16	0.51	11.40	1.57	1.30	n.d.	97.32
BL99118	WHL	41.71	9.92	0.77	21.57	7.93	0.39	11.29	1.67	1.42	n.d.	96.99
BL99118	WHL	42.23	9.70	0.70	22.01	7.85	0.41	11.37	1.68	1.37	n.d.	97.65
BL99118	WHL	47.85	5.62	0.29	18.09	10.97	0.49	11.50	1.17	0.62	n.d.	96.75
BL0084	WHL	48.59	5.14	0.50	12.29	14.90	0.24	11.79	0.94	0.57	0.12	95.80
BL9948	NEL	42.30	12.30	1.66	9.27	15.57	0.10	11.40	2.06	1.01	0.11	96.22
BL9948	NEL	41.99	12.39	1.56	9.49	15.71	0.18	11.12	2.16	1.05	0.17	95.99
BL9948	NEL	42.09	12.49	1.55	9.60	15.52	0.19	11.44	2.06	1.03	0.25	96.59
BL9948	NEL	43.01	11.31	0.86	9.52	15.61	0.10	11.07	2.01	1.01	0.27	94.92
BL9948	NEL	43.25	11.98	0.76	9.43	15.89	0.14	11.23	2.09	1.12	0.22	96.40
BL9948	NEL	42.25	12.32	1.54	9.73	15.43	0.15	11.42	2.14	1.05	0.06	96.32
BL9948	NEL	42.15	12.84	1.30	9.39	15.38	0.08	11.56	2.15	1.05	0.15	96.42
BL9948	NEL	41.95	12.06	1.05	9.55	15.46	0.05	11.32	1.95	1.09	0.26	95.17
BL9948	NEL	42.43	12.37	1.14	9.62	15.74	0.03	11.14	2.14	1.08	0.21	96.10
BL9948	NEL	43.08	11.76	1.23	9.25	15.64	0.12	11.93	1.95	1.15	0.21	96.75
BL9948	NEL	41.80	12.81	1.60	9.62	15.40	0.15	11.49	2.14	1.18	0.17	96.72
BL0084	BL	44.92	7.05	0.38	18.74	10.71	0.52	11.36	1.24	0.89	n.d.	96.23
BL0084	BL	46.43	6.54	0.35	18.35	10.77	0.52	11.34	0.93	0.69	n.d.	96.28
BL0084	BL	46.66	5.98	0.36	18.13	11.17	0.55	11.36	1.05	0.64	n.d.	96.03
BL0084	BL	45.12	7.21	0.36	19.57	10.25	0.60	11.21	1.19	0.98	n.d.	96.74
BL0084	BL	45.06	7.02	0.41	19.26	10.05	0.57	11.45	1.23	0.92	n.d.	96.28
BL0084	BL	45.93	6.31	0.29	18.16	11.00	0.57	11.76	0.91	0.72	n.d.	96.14
BL0084	BL	43.69	7.62	0.49	19.48	9.75	0.57	11.14	1.30	1.06	n.d.	95.28
BL0084	BL	43.84	8.15	0.47	19.33	9.28	0.60	11.44	1.35	1.01	n.d.	95.81
BL0084	BL	45.29	7.26	0.41	18.99	9.98	0.63	11.51	1.00	0.87	n.d.	96.06
BL0084	BL	44.02	7.95	0.27	19.78	9.49	0.64	11.38	1.02	1.11	n.d.	95.85
BL0084	BL	43.00	8.68	0.52	19.96	9.20	0.54	11.55	1.21	1.27	n.d.	96.14

n.d. = not detected

IN = intrusion. Abbreviations as in Figure 2.1.

Table A.5. Continued

Sample #	IN	SiO_2	Al_2O_3	TiO_2	FeO	MgO	MnO	CaO	Na_2O	K_2O	Cr_2O_3	Total
BL0084	BL	44.21	7.55	0.52	19.59	10.03	0.59	11.23	1.31	0.99	n.d.	96.32
BL0084	BL	44.79	7.30	0.42	18.78	10.39	0.56	11.36	1.17	1.06	n.d.	96.09
BL0084	BL	45.71	7.30	0.41	19.50	10.08	0.52	11.42	1.04	0.87	n.d.	97.05
BL0084	BL	43.80	7.54	0.39	19.62	9.48	0.55	11.14	1.29	1.11	n.d.	95.09
BL0084	BL	46.51	5.79	0.15	17.62	10.85	0.60	11.52	0.83	0.52	n.d.	94.78
BL0084	BL	45.92	6.79	0.40	18.65	10.43	0.48	11.72	1.08	0.89	n.d.	96.59
BL0084	BL	47.77	5.76	0.57	12.70	14.95	0.22	11.44	1.49	0.58	0.02	96.44
BL0084	BL	47.73	5.50	0.53	12.41	14.98	0.29	11.74	1.45	0.69	0.08	96.34
BL0084	BL	48.56	4.88	0.56	12.45	15.06	0.31	11.83	0.99	0.56	0.10	96.22
BL0084	BL	47.85	5.40	0.71	12.02	14.96	0.30	11.70	1.36	0.61	0.15	95.67
BL0084	BL	48.70	4.68	0.48	12.51	15.10	0.31	12.03	0.79	0.56	0.10	96.05
BL0087	BL	41.90	12.86	1.78	13.07	12.55	0.21	11.09	1.48	1.72	0.01	97.16
BL0087	BL	40.66	11.14	1.31	14.72	11.84	0.25	11.78	1.75	1.45	0.01	95.60
BL0087	BL	43.55	9.43	1.31	15.11	12.17	0.14	11.75	1.04	1.07	0.03	96.25
BL0087	BL	45.81	7.46	1.09	14.03	13.18	0.18	12.17	1.02	0.77	0.04	96.19
BL0087	BL	45.21	7.73	0.99	15.29	12.01	0.26	11.99	0.92	0.86	0.01	95.74
BL0087	BL	39.97	12.28	1.86	12.95	12.29	0.19	11.42	1.76	1.30	0.02	94.64
BL0087	BL	39.53	12.92	1.81	12.48	12.84	0.16	11.77	1.75	1.50	0.02	95.68
BL0087	BL	39.51	12.81	1.93	11.62	13.31	0.11	11.83	1.78	1.58	n.d.	95.02
BL0087	BL	45.20	7.29	0.82	15.14	12.85	0.23	11.95	0.94	0.66	n.d.	95.72
BL0087	BL	45.26	7.38	1.03	14.76	12.64	0.22	11.85	1.04	0.79	0.04	95.52
BL0087	BL	43.91	8.23	1.29	16.64	11.78	0.19	11.62	1.20	0.98	n.d.	96.76
BL0087	BL	38.77	12.76	1.84	13.42	12.16	0.17	11.61	1.41	1.69	n.d.	94.77

n.d. = not detected

IN = intrusion. Abbreviations as in Figure 2.1.

Table A3.4. *Microprobe analyses of olivine from the QAS intrusions*

Sample #	IN	SiO_2	Al_2O_3	TiO_2	Cr_2O_3	FeO	MgO	MnO	CaO	P_2O_5	Ni	BaO	Total
BL9948	NEL	37.61	0.04	0.04	n.d.	22.26	38.53	0.32	n.d.	0.02	0.06	0.12	99.09
BL9948	NEL	37.74	0.06	n.d.	n.d.	21.82	38.61	0.30	0.07	n.d.	0.08	0.02	98.78
BL9948	NEL	38.15	n.d.	n.d.	0.01	21.81	39.09	0.35	0.06	0.02	0.05	n.d.	99.67
BL9948	NEL	37.69	0.03	0.02	0.02	23.41	37.99	0.32	0.02	0.20	0.04	0.06	99.85
BL9948	NEL	37.57	0.06	0.02	0.08	22.64	38.74	0.28	0.03	n.d.	0.12	0.04	99.65

IN = intrusion. Abbreviations as in Figure 2.1.
n.d. = not detected

Table A3.5. *Microprobe analyses of feldspar from the QAS intrusions*

Sample #	IN	SiO_2	Al_2O_3	Cr_2O_3	FeO	MgO	K_2O	CaO	Na_2O	BaO	Total
BL0091	LN	62.66	18.96	–	0.05	n.d.	15.48	n.d.	0.33	1.83	99.31
BL0091	LN	62.93	19.09	–	n.d.	n.d.	15.05	0.01	0.37	1.72	99.17
BL0091	LN	62.18	18.87	–	0.20	0.02	15.41	0.05	0.41	1.21	98.35
BL0091	LN	62.08	18.93	–	0.04	0.02	15.41	0.01	0.65	0.86	98.00
BL0091	LN	64.55	19.54	–	0.09	0.01	15.39	n.d.	0.54	1.77	101.89
BL0091	LN	64.74	19.37	–	0.11	n.d.	16.09	0.01	0.47	1.53	102.32
BL0091	LN	65.25	19.21	–	0.12	n.d.	16.08	0.13	0.36	1.23	102.38
BL0091	LN	65.42	19.39	–	0.03	n.d.	16.15	n.d.	0.44	0.85	102.28
BL0094	LN	64.66	18.73	–	0.18	0.01	15.49	n.d.	0.49	0.75	100.31
BL0094	LN	64.20	18.81	–	0.18	n.d.	15.41	n.d.	0.30	0.84	99.74
BL0094	LN	64.87	18.95	–	0.27	n.d.	15.73	0.01	0.41	0.28	100.52
BL0094	LN	64.62	18.75	–	0.23	0.01	15.49	n.d.	0.30	0.31	99.71
BL0094	LN	64.82	19.02	–	0.14	n.d.	15.64	n.d.	0.32	0.43	100.37
BL0094	LN	63.45	18.36	–	0.23	n.d.	15.63	n.d.	0.43	0.68	98.78
BL0094	LN	63.50	18.59	–	0.15	n.d.	15.15	0.01	0.70	0.67	98.77
BL0094	LN	64.62	19.11	–	0.13	n.d.	15.14	0.03	0.46	1.49	100.98
BL0094	LN	64.28	18.92	–	0.18	n.d.	14.95	n.d.	0.40	1.61	100.34
BL9939	HAR	66.71	19.21	–	0.13	n.d.	12.74	n.d.	0.33	0.28	99.40
BL9939	HAR	64.76	18.79	–	0.13	n.d.	14.93	n.d.	0.28	0.17	99.06
BL9939	HAR	64.73	18.45	–	0.14	n.d.	14.36	0.01	0.25	0.17	98.11
BL9939	HAR	64.80	18.62	–	0.06	0.01	15.48	n.d.	0.44	0.21	99.62
BL9939	HAR	65.80	18.82	–	n.d.	0.01	16.40	n.d.	0.44	0.30	101.77
BL9939	HAR	65.35	18.87	–	0.03	n.d.	16.33	n.d.	0.28	0.31	101.17
BL9939	HAR	65.21	18.91	–	0.10	0.01	15.98	n.d.	0.48	0.25	100.94
BL99104	BHL	44.17	24.56	0.06	0.06	n.d.	0.07	27.52	0.04	n.d.	96.61
BL99104	BHL	65.72	18.74	n.d.	n.d.	n.d.	16.17	0.03	0.72	0.37	101.75
BL99120	WHL	65.18	18.59	–	0.10	0.02	16.20	n.d.	0.43	0.39	100.91
BL99120	WHL	66.21	18.96	–	n.d.	n.d.	15.81	n.d.	0.43	0.49	101.90
BL99120	WHL	66.18	19.30	–	0.17	0.01	15.74	n.d.	0.57	0.36	102.33
BL99121	WHL	66.01	18.92	–	0.11	n.d.	16.03	n.d.	0.59	0.43	102.09
BL99121	WHL	65.19	18.77	–	0.08	n.d.	16.15	n.d.	0.38	0.41	100.98
BL99121	WHL	65.03	18.70	–	0.10	0.01	15.39	n.d.	0.87	0.43	100.53
BL0076	BL	64.73	18.32	–	0.32	–	15.36	n.d.	0.36	0.62	98.61
BL0076	BL	64.34	18.58	–	0.29	–	15.40	n.d.	0.26	0.51	98.84
BL0076	BL	64.48	18.67	–	0.30	–	15.40	n.d.	0.30	0.81	98.68
BL0076	BL	64.21	18.75	–	0.25	–	15.48	n.d.	0.31	0.71	98.93
BL0084	BL	64.53	18.52	–	0.06	–	15.82	n.d.	0.26	0.47	99.61
BL0084	BL	65.02	18.80	–	0.09	–	15.71	n.d.	0.35	n.d.	98.26
BL0084	BL	64.18	18.58	–	0.07	–	15.44	n.d.	0.45	0.36	97.74
BL0084	BL	63.90	18.34	–	n.d.	–	15.48	n.d.	0.18	0.75	98.97
BL0084	BL	64.79	18.83	–	0.10	–	15.24	n.d.	0.44	0.19	98.71
BL0084	BL	64.77	18.60	–	0.08	–	15.26	n.d.	0.32	0.24	99.37
BL0084	BL	64.96	18.83	–	0.07	–	15.51	n.d.	0.33	0.58	98.57
BL0087	BL	64.35	18.56	–	n.d.	–	15.62	n.d.	0.40	0.60	98.38
BL0087	BL	64.28	18.78	–	n.d.	–	15.28	0.09	0.48	0.84	98.16
BL0087	BL	64.25	18.57	–	n.d.	–	15.30	0.06	0.69	0.62	98.97
BL0087	BL	64.85	18.72	–	0.12	–	15.29	0.08	0.87	0.19	88.10
BL0087	BL	68.18	19.83	–	n.d.	–	0.08	0.24	11.53	0.11	98.02
BL00103	BL	64.71	19.09	–	0.09	–	14.14	n.d.	1.25	0.96	98.27
BL00103	BL	64.19	18.77	–	0.26	–	15.05	n.d.	0.42	0.67	99.64
BL00103	BL	65.35	18.43	–	0.08	–	15.77	0.05	0.28	0.34	99.07
BL00103	BL	64.76	18.62	–	0.08	–	15.61	n.d.	0.40	0.99	98.42

IN = intrusion. Abbreviations as in Figure 2.1.
n.d. = not detected

Table A3.6. *Microprobe analyses of biotite/phlogopite from the QAS intrusions*

Sample #	IN	SiO_2	Al_2O_3	TiO_2	Cr_2O_3	FeO	MgO	MnO	K_2O	CaO	Na_2O	BaO	Cl	F	Total
BL9937	HAR	36.23	14.48	1.40	0.02	24.60	7.23	0.43	9.42	0.10	0.06	0.03	0.01	0.48	94.49
BL9937	HAR	35.39	14.67	1.49	n.d.	24.70	7.90	0.41	8.58	0.18	0.05	n.d.	n.d.	0.59	93.97
BL9937	HAR	34.82	14.94	1.45	n.d.	25.96	7.29	0.33	9.18	0.09	0.03	0.06	0.01	0.45	94.61
BL9937	HAR	35.92	14.53	1.32	0.03	24.53	7.24	0.43	9.65	0.05	0.03	0.14	n.d.	0.51	94.39
BL9937	HAR	36.11	15.13	1.49	0.02	25.23	7.04	0.47	9.43	0.04	0.04	0.13	0.02	0.54	95.69
BL9937	HAR	35.52	14.83	1.35	n.d.	25.44	7.52	0.37	9.62	0.05	0.02	0.08	0.01	0.46	95.27
BL9937	HAR	35.45	14.90	1.55	n.d.	25.10	7.35	0.49	9.67	0.01	0.03	0.09	n.d.	0.40	95.03
BL9937	HAR	34.34	14.40	1.57	n.d.	25.03	7.33	0.44	7.14	0.48	0.01	0.16	n.d.	0.39	91.30
BL9937	HAR	36.01	14.75	1.56	n.d.	25.12	7.16	0.45	9.67	0.04	0.02	0.20	n.d.	0.44	95.42
BL9937	HAR	35.32	14.82	1.34	0.02	25.05	7.25	0.48	9.06	0.12	0.03	0.10	n.d.	0.50	94.09
BL9937	HAR	35.17	14.54	1.45	n.d.	24.71	7.24	0.43	8.35	0.27	0.01	0.15	n.d.	0.46	92.78
BL9937	HAR	35.29	14.73	1.45	n.d.	26.22	7.26	0.43	9.39	0.05	0.01	0.21	n.d.	0.53	95.56
BL9940	HAR	37.03	15.35	1.49	n.d.	19.12	12.09	0.20	10.11	0.05	0.06	0.30	0.01	0.37	96.17
BL9940	HAR	37.10	15.45	1.43	0.02	19.84	12.24	0.15	9.03	0.03	0.02	0.22	0.02	0.37	95.90
BL9940	HAR	37.36	15.49	1.54	0.08	18.96	11.96	0.15	10.16	0.04	0.01	0.07	0.02	0.29	96.12
BL9940	HAR	37.36	14.95	1.59	0.07	19.32	10.90	0.23	6.94	0.01	n.d.	0.11	0.01	0.18	91.65
BL9940	HAR	38.07	15.38	1.59	0.01	19.42	12.26	0.17	7.62	0.03	0.05	0.15	0.01	0.32	95.08
BL9940	HAR	37.39	15.19	1.58	0.05	19.79	11.80	0.21	9.18	0.01	0.03	n.d.	n.d.	0.34	95.56
BL9940	HAR	37.89	15.12	1.61	0.03	20.01	11.92	0.15	8.62	n.d.	0.08	0.20	n.d.	0.33	95.94
BL99118	WHL	38.48	15.37	1.43	n.d.	22.43	11.08	0.32	9.11	0.13	0.02	n.d.	0.02	0.42	98.80
BL99118	WHL	36.07	13.91	1.46	n.d.	21.81	10.50	0.32	9.22	0.09	0.02	0.05	0.01	0.36	93.80
BL99118	WHL	36.45	14.00	1.41	n.d.	22.53	10.49	0.43	9.43	0.06	0.03	0.11	0.02	0.36	95.32
BL99118	WHL	36.00	14.18	1.44	0.02	21.81	10.51	0.33	9.58	0.02	0.08	0.15	n.d.	0.56	94.67
BL99118	WHL	35.85	14.20	1.32	0.05	21.47	10.69	0.27	8.81	0.15	0.06	0.13	n.d.	0.58	93.56
BL0076	BL	38.06	10.66	0.63	0.01	14.36	17.36	0.19	9.78	0.05	n.d.	0.06	n.d.	2.72	94.09
BL0076	BL	38.36	10.72	0.55	n.d.	14.52	17.52	0.33	9.90	0.01	n.d.	0.04	n.d.	2.54	94.91
BL0076	BL	38.56	11.20	0.44	0.01	14.38	17.65	0.33	9.97	0.04	n.d.	n.d.	0.03	2.74	95.54
BL0076	BL	38.72	10.85	0.42	0.02	14.65	17.46	0.26	9.83	0.10	n.d.	0.23	0.02	2.28	95.02
BL0076	BL	38.39	10.99	0.94	0.03	14.93	17.07	0.21	9.96	n.d.	n.d.	n.d.	0.04	2.57	95.33
BL00103	BL	36.73	14.15	1.56	0.07	16.91	13.89	0.30	9.84	n.d.	n.d.	0.26	0.03	1.25	95.21
BL00103	BL	36.41	14.14	1.55	0.01	17.26	13.03	0.32	9.54	0.04	n.d.	0.41	0.05	0.95	93.89
BL00103	BL	36.63	14.21	1.49	0.06	16.94	13.69	0.28	9.86	n.d.	n.d.	0.41	0.03	1.14	94.96
BL00103	BL	36.72	13.93	1.51	0.02	17.09	13.59	0.38	9.52	0.04	n.d.	n.d.	0.00	1.16	94.17
BL00103	BL	36.96	14.01	1.64	n.d.	16.73	13.72	0.41	9.68	0.01	n.d.	0.06	0.05	1.20	94.54
BL00103	BL	36.83	13.97	1.50	0.09	17.39	13.80	0.36	9.75	n.d.	n.d.	0.26	0.07	1.15	95.33
BL00103	BL	36.73	14.22	1.68	0.06	16.71	13.36	0.34	9.56	0.01	n.d.	0.08	0.06	1.12	94.17
BL00103	BL	36.97	13.93	1.62	0.06	17.33	13.65	0.29	9.59	n.d.	n.d.	0.41	0.02	1.24	95.21
BL00103	BL	36.26	13.94	1.72	0.01	17.87	13.28	0.31	9.59	n.d.	n.d.	0.26	0.05	1.11	94.57
BL00103	BL	36.40	14.01	1.29	0.10	16.98	13.58	0.30	9.98	n.d.	n.d.	0.24	0.02	1.18	94.28

IN = intrusion. Abbreviations as in Figure 2.1.
n.d. = not detected

Table A3.7. *Microprobe analyses of calcite from the QAS intrusions*

Sample #	IN	CaO	MgO	FeO	MnO	ZnO	SrO	BaO	SO_3	As_2O_3	CO_2	Total
BL99101	BHL	52.30	0.36	0.51	0.27	n.d.	1.16	0.09	0.12	n.d.	44.07	98.88
BL99101	BHL	50.77	0.34	0.59	0.19	n.d.	0.97	n.d.	0.11	n.d.	44.55	97.53
BL99101	BHL	51.11	0.34	0.52	0.16	n.d.	1.05	n.d.	n.d.	n.d.	44.46	97.70
BL99101	BHL	51.67	0.34	0.45	0.25	n.d.	1.11	n.d.	n.d.	n.d.	44.29	98.12
BL99101	BHL	52.34	0.29	0.36	0.28	n.d.	1.00	n.d.	n.d.	n.d.	44.21	98.53
BL99101	BHL	51.54	0.27	0.36	0.25	n.d.	1.00	0.12	n.d.	n.d.	44.35	97.88
BL99101	BHL	51.29	0.33	0.37	0.22	n.d.	1.03	n.d.	n.d.	n.d.	44.45	97.73
BL0064	BHL	54.54	0.16	0.29	0.29	n.d.	1.05	0.14	n.d.	n.d.	43.64	100.15
BL0087	BL	54.00	0.10	0.10	0.20	n.d.	0.20	0.10	n.d.	n.d.	44.30	98.80
BL0087	BL	53.90	0.10	0.10	0.10	n.d.	0.10	0.10	0.10	n.d.	44.30	98.70
BL0087	BL	53.70	0.10	0.10	0.10	0.10	0.20	n.d.	n.d.	n.d.	44.30	98.60

IN = intrusion. Abbreviations as in Figure 2.1.
n.d. = not detected

Table A3.8. *Microprobe analyses of apatite from the QAS intrusions*

Sample #	IN	SiO_2	Al_2O_3	TiO_2	Cr_2O_3	FeO	MgO	MnO	CaO	Na_2O	K_2O	P_2O_5	NiO	BaO	V_2O_5	F	Cl	Total
BL99103	BHL	0.46	n.d.	n.d.	n.d.	0.16	0.03	0.07	55.46	n.d.	n.d.	41.36	0.06	0.05	0.01	3.59	0.01	99.89
BL0064	BHL	0.13	n.d.	n.d.	n.d.	0.01	n.d.	n.d.	54.80	0.13	n.d.	41.11	0.03	0.02	0.04	4.58	n.d.	101.49
BL0064	BHL	0.11	n.d.	n.d.	0.06	0.06	n.d.	0.03	55.17	0.17	n.d.	40.84	0.02	0.14	n.d.	3.89	n.d.	101.18
BL0064	BHL	0.07	n.d.	n.d.	0.03	0.05	0.03	0.05	55.18	0.04	0.01	40.69	0.07	0.02	0.04	3.66	n.d.	100.58
BL0076	BL	0.87	0.04	n.d.	0.05	0.01	0.01	0.08	52.40	0.20	n.d.	39.39	0.03	0.09	n.d.	5.14	0.02	99.70
BL0076	BL	1.19	0.01	n.d.	n.d.	n.d.	n.d.	0.06	52.63	0.26	0.10	37.98	0.01	0.32	n.d.	3.90	0.01	98.11
BL0076	BL	0.28	0.02	n.d.	n.d.	0.13	n.d.	0.06	53.88	0.18	n.d.	40.29	n.d.	0.05	n.d.	3.79	0.02	100.17
BL0076	BL	0.84	0.01	n.d.	n.d.	n.d.	0.01	n.d.	53.15	0.33	n.d.	39.03	0.02	0.25	n.d.	3.81	n.d.	98.85
BL0084	BL	0.50	n.d.	n.d.	0.01	0.08	0.02	n.d.	54.97	0.22	0.03	41.13	n.d.	n.d.	0.01	4.53	n.d.	99.69
BL0084	BL	0.68	0.04	n.d.	0.13	0.03	n.d.	0.10	54.66	0.12	0.14	40.69	0.02	0.07	n.d.	5.03	0.02	99.68
BL0087	BL	0.23	n.d.	n.d.	0.03	n.d.	n.d.	0.02	55.51	0.11	n.d.	41.63	0.08	n.d.	0.10	5.42	0.01	100.92
BL0087	BL	0.25	0.04	n.d.	0.11	0.01	0.01	0.05	55.91	0.01	n.d.	41.70	0.03	n.d.	0.05	3.71	0.05	100.43

IN = intrusion. Abbreviations as in Figure 2.1.
n.d. = not detected

Table A3.9. *Microprobe analyses of zircon from the QAS intrusions*

Sample #	IN	SiO_2	Al_2O3	Fe_2O_3	CaO	MgO	MnO	P_2O_5	ZrO_2	HfO_2	ThO_2	UO_2	PbO	Y_2O_3	Ce_2O_3	Total
ZR-1-1	GH	32.60	0.01	n.d	n.d.	0.01	n.d.	n.d.	65.74	1.24	0.02	0.02	0.01	n.d.	n.d.	99.65
ZR-1-2	GH	32.70	n.d.	n.d.	n.d.	n.d.	n.d.	0.28	65.83	1.21	0.04	0.06	0.07	n.d.	n.d.	100.19
ZR-1-3	GH	32.61	n.d.	n.d.	n.d.	n.d.	0.03	0.19	66.70	1.05	n.d.	0.04	0.05	0.01	n.d.	100.68
ZR-1-4	GH	32.59	n.d.	0.07	n.d.	0.02	n.d.	0.23	65.56	0.73	0.22	0.11	0.11	0.12	0.04	99.80
ZR-1-4	GH	33.13	n.d.	n.d.	n.d.	0.01	0.04	0.20	66.69	0.71	n.d.	n.d.	n.d.	n.d.	n.d.	100.78
ZR-2-1	GH	32.82	0.01	n.d.	n.d.	0.01	n.d.	0.23	67.09	0.87	n.d.	0.04	0.05	0.10	0.04	101.26
ZR-2-2	GH	33.01	n.d.	n.d.	n.d.	n.d.	n.d.	0.10	66.31	1.05	0.05	n.d.	0.09	n.d.	n.d.	100.61
ZR-3-1	HAR	32.26	0.06	0.21	0.10	0.03	0.01	0.18	66.16	1.27	0.07	0.18	0.06	n.d.	0.07	100.66
ZR-3-2	HAR	30.14	n.d.	0.16	0.67	n.d.	0.01	0.11	62.26	1.01	0.05	0.24	0.03	n.d.	n.d.	94.68
ZR-3-3	HAR	29.99	0.15	0.38	0.97	n.d.	n.d.	0.20	61.10	0.87	0.10	0.39	0.01	0.05	n.d.	94.21
ZR-3-4	HAR	29.71	0.08	0.26	0.88	n.d.	0.02	0.28	60.66	1.38	0.02	0.38	n.d.	0.05	n.d.	93.72
ZR-3-4	HAR	30.07	0.05	0.12	0.45	n.d.	0.05	0.26	60.69	0.42	0.34	0.33	0.17	0.63	0.05	93.63
ZR-5-1	HAR	30.88	0.13	n.d.	0.51	n.d.	0.10	0.16	62.31	0.34	0.20	0.19	0.22	0.14	n.d.	95.18
ZR-5-2	HAR	31.96	n.d.	0.02	0.03	0.01	0.03	0.18	66.07	0.83	0.04	0.21	0.18	0.07	n.d.	99.63
ZR-5-3	HAR	32.56	n.d.	0.01	0.09	n.d.	0.04	0.17	65.34	0.87	0.01	0.10	0.11	0.06	n.d.	99.36
ZR-5-4	HAR	31.93	n.d.	0.04	0.19	0.02	0.05	0.19	66.16	1.05	0.07	0.16	0.06	0.04	0.01	99.97
ZR-5-5	HAR	31.63	0.02	0.17	0.47	0.02	n.d.	0.13	64.56	1.09	0.08	0.38	0.08	0.13	0.01	98.77
ZR-6-1	HAR	32.56	n.d.	0.04	0.04	n.d.	n.d.	0.12	66.30	1.24	n.d.	0.09	0.04	0.06	n.d.	100.49
ZR-6-2	HAR	32.86	0.02	0.03	n.d.	0.02	n.d.	0.08	66.08	0.76	n.d.	0.06	0.11	0.05	n.d.	100.07
ZR-7-1	GH	32.99	n.d.	n.d.	n.d.	n.d.	0.01	0.17	67.31	0.74	0.03	0.02	n.d.	n.d.	n.d.	101.27
ZR-7-2	GH	32.57	n.d.	0.12	0.02	n.d.	0.06	0.19	66.11	1.00	0.06	0.11	0.11	0.14	n.d.	100.49
ZR-8-1	GH	33.45	n.d.	n.d.	n.d.	n.d.	n.d.	n.d.	67.17	0.97	n.d.	n.d.	n.d.	0.10	n.d.	101.69
ZR-8-2	GH	32.98	n.d.	n.d.	n.d.	0.01	0.04	0.08	67.72	0.53	0.08	0.06	0.12	0.06	n.d.	101.68
ZR-8-3	GH	33.26	0.01	0.02	n.d.	n.d.	0.04	n.d.	67.07	0.99	0.04	n.d.	0.09	n.d.	n.d.	101.52
ZR-8-4	GH	32.86	n.d.	0.01	0.02	n.d.	n.d.	0.03	66.34	1.36	0.07	0.08	n.d.	0.01	n.d.	100.78
ZR-9-1	GH	32.78	n.d.	n.d.	n.d.	n.d.	0.03	0.14	65.80	1.04	n.d.	0.01	n.d.	0.04	0.01	99.85
ZR-9-2	GH	32.92	n.d.	0.02	n.d.	n.d.	n.d.	0.27	66.70	0.50	n.d.	n.d.	0.04	0.09	0.02	100.56
ZR-9-3	GH	32.61	n.d.	0.01	0.01	n.d.	n.d.	0.15	66.44	1.00	n.d.	0.03	0.01	n.d.	n.d.	100.26

n.d. = not detected
IN = intrusion. Abbreviations as in Figure 2.1.

Table A3.10. *Microprobe analyses of titanite from the QAS intrusions*

Sample #	IN	SiO_2	Al_2O_3	TiO_2	Cr_2O_3	FeO	MgO	MnO	CaO	Na_2O	K_2O	P_2O_5	NiO	BaO	V_2O_5	F	Cl	Total
BL9999	BHL	29.65	0.98	33.20	n.d.	1.68	0.03	0.01	27.42	0.09	0.03	0.06	0.03	0.13	0.08	0.82	0.01	94.21
BL9999	BHL	29.41	1.31	31.56	0.30	2.38	0.05	0.03	25.42	0.14	0.04	0.01	0.01	0.13	0.10	0.64	0.02	91.29
BL0064	BHL	29.10	0.80	36.80	0.10	2.30	n.d.	0.10	26.80	n.d.	n.d.	n.d.	n.d.	0.20	0.30	0.90	n.d.	97.50
BL0076	BL	28.80	0.80	35.60	n.d.	2.60	0.10	0.10	26.20	n.d.	n.d.	0.10	n.d.	n.d.	0.30	1.00	n.d.	95.70
BL0076	BL	28.70	0.90	35.50	n.d.	2.40	0.10	0.10	25.80	n.d.	n.d.	0.10	0.10	n.d.	0.20	0.90	n.d.	95.00
BL0084	BL	29.68	1.61	32.01	n.d.	2.26	0.01	0.08	27.11	0.02	0.04	0.19	0.07	0.33	0.19	0.30	0.01	93.99
BL0084	BL	29.60	1.56	32.30	0.50	1.91	0.02	0.06	26.84	0.01	n.d.	0.14	0.05	0.35	0.22	0.42	n.d.	93.54
BL0084	BL	29.61	1.66	31.56	n.d.	2.47	0.02	n.d.	27.52	n.d.	n.d.	0.04	0.07	0.31	0.12	0.90	0.05	94.36
BL0084	BL	29.75	1.75	32.36	n.d.	2.05	0.03	0.13	28.10	0.06	0.02	0.06	0.13	0.09	0.08	0.16	0.02	94.86
BL00103	BL	29.00	1.30	35.50	0.10	1.70	n.d.	0.20	26.20	n.d.	n.d.	0.10	n.d.	n.d.	0.10	0.90	n.d.	95.30
BL00103	BL	29.30	1.40	35.70	n.d.	1.70	n.d.	0.20	27.30	n.d.	n.d.	0.10	n.d.	0.40	0.20	0.80	n.d.	97.20
BL99103	BL	30.11	0.73	37.58	n.d.	1.65	n.d.	0.05	26.77	0.23	0.01	n.d.	n.d.	n.d.	n.d.	0.53	0.03	97.68